# High Rayleigh Number Convection in a Porous Medium

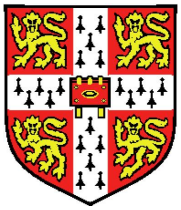

Duncan Robin Hewitt

Department of Applied Mathematics and Theoretical Physics

University of Cambridge

A thesis submitted for the degree of

*Doctor of Philosophy*

November 11, 2013

This dissertation has been submitted as part of an application for a Junior Research Fellowship at Trinity College, Cambridge. All the work is my own, and has been carried out over the course of my Ph.D. under the supervision of Professor John Lister and Dr. Jerome Neufeld, at the Department of Applied Mathematics and Theoretical Physics, University of Cambridge.

The work contained in chapters 2, 3, 5, and 6 has been published or accepted for publication, as noted at the start of each chapter. The work in chapter 4 is in preparation for submission.

Duncan Hewitt

November 11, 2013

# Abstract

Convection in a fluid-saturated porous medium is of widespread importance in a variety of geophysical and industrial settings. A range of porous convective systems are investigated at high Rayleigh number $Ra$, using numerical, theoretical, and experimental techniques.

After an introductory chapter in which the relevance of this work to the long-term storage of $CO_2$ is discussed, well resolved direct numerical simulations of two-dimensional Rayleigh–Bénard convection in a porous medium ('Rayleigh–Darcy convection') are presented for Rayleigh numbers $Ra \leqslant 4\times10^4$. Measurements of the convective flux, as described by the Nusselt number $Nu$, for $1300 \leqslant Ra \leqslant 4 \times 10^4$ are extremely well fitted by $Nu = \alpha\, Ra + \beta$, for $\alpha = 6.9 \times 10^{-3}$ and $\beta = 2.75$, which indicates that, contrary to some previous indications, the linear classical scaling $Nu \sim Ra$ is attained asymptotically. The flow dynamics are analysed, and the interior of the vigorously convecting system is shown to be increasingly well-described as $Ra \to \infty$ by a simple columnar 'heat-exchanger' model with a single horizontal wavenumber $k$ and a linear background temperature field. Numerical measurements are approximately fitted by $k \sim Ra^{0.4}$.

In chapter 3, the stability of this heat-exchanger flow is examined, with the aim of uncovering the mechanism that controls the horizontal lengthscale of the columnar flow. The dimensionless heat-exchanger flow comprises interleaving columns of horizontal wavenumber $k$ that are driven by a steady balance between vertical advection of a background linear density stratification and horizontal diffusion between the columns. The flow is always unstable in an unbounded domain: the growth rate and structure of the most unstable mode are found

using a Floquet stability analysis; the physical mechanism of instability is investigated by a matched asymptotic expansion of the linear-stability problem; and the non-linear evolution is examined using direct numerical simulations. The results of the stability analysis are applied to the columnar flow in a two-dimensional Rayleigh–Darcy cell at high $Ra$: a balance of time scales for growth and propagation suggests that the flow is unstable for horizontal wavenumbers $k$ greater than $k \sim Ra^{5/14}$ as $Ra \to \infty$. This stability criterion is consistent with the hitherto unexplained numerical measurements of $k$ presented in chapter 2.

Geological porous formations are commonly interspersed with thin, roughly horizontal, low-permeability layers. In chapter 4, statistically steady high-$Ra$ porous convection in the presence of a thin, low-permeability, horizontal layer is investigated. The flow depends only on the ratio of the height and relative permeability of the interior layer, given by the impedance $\Omega$. Two particularly notable features are observed as $\Omega$ is increased: the dominant horizontal lengthscale of the flow increases dramatically; and $Nu$ can increase, before decreasing markedly for larger values of $\Omega$. The dependence of the flow on $Ra$ is explored, and simple 'toy' models are developed to describe some of the observed behaviour.

Convection in a closed porous domain, driven by a dense buoyancy source along the upper boundary only, soon starts to wane due to the increase of the average interior density. In chapter 5, theoretical and numerical models are developed of subsequent long period of shutdown of convection at high $Ra$. The relationship between this slowly evolving 'one-sided' shutdown system and the statistically steady 'two-sided' Rayleigh–Darcy cell is investigated. Measurements of $Nu(Ra)$ from chapter 2 are used in theoretical box models of the one-sided shutdown system and found to give excellent agreement with high-resolution numerical simulations of this system. The dynamical structure of shutdown can also be accurately predicted by measure-

ments from a Rayleigh-Darcy cell. Results are presented for a general power-law equation of state.

In chapter 6, these ideas are extended to model the shutdown of convection in different physical one-sided systems, which comprise two fluid layers with an equation of state such that the solution which forms at the (moving) interface is more dense than either layer. The two fluids are either immiscible or miscible. Theoretical box models compare well with numerical simulations in the case of a flat interface between the fluids. Experimental results from a Hele–Shaw cell and numerical simulations both show that interfacial deformation can dramatically enhance the convective flux for miscible fluids.

In chapter 7, high-resolution direct numerical simulations of three-dimensional statistically steady porous convection are presented for $Ra \leqslant 2 \times 10^4$, and measurements of $Nu$ are very well described over the range $1500 \lesssim Ra \leqslant 2 \times 10^4$ by the relationship $Nu = \alpha_3 \, Ra + \beta_3$, for $\alpha_3 = 9.6 \times 10^{-3}$ and $\beta_3 = 4.28$. This fit strongly suggests that, as in two dimensions, the classical linear scaling is attained as $Ra \to \infty$. The magnitude of the flux is roughly 40% higher than in two-dimensions. The dynamical structure of the flow is analysed, and the interior flow is again found to be increasingly well described by a heat-exchanger model. Numerical measurements of the dominant wavenumber $k$ are approximately fitted by $k \sim Ra^{0.54}$, which is a notably larger exponent than in two dimensions.

This work is summarized in chapter **??**, and the applicability of the results to the convective dissolution of geologically sequestered $CO_2$ in a saline aquifer is discussed.

# Contents

# Chapter 1

# Introduction

Convection plays a central role in an enormous range of environmental processes. It is responsible for much of the Earth's weather: on a large scale, convection drives atmospheric and oceanic circulation; on a smaller scale, the formation of clouds and storms. Flow in the Earth's mantle, which fuels the geodynamo and the motion of tectonic plates, is driven by convection. The freezing of the polar oceans, the motion of volcanic plumes, and the rate at which a kettle boils or a radiator heats a room are all controlled by convection. In addition, from a mathematical viewpoint, convection is a complex nonlinear process that provides an archetypal fluid-dynamical setting for the study of chaotic and turbulent dynamics, bifurcations, and emergent patterns (Cross & Hohenberg, 1993; Kadanoff, 2001).

Convection can be broadly defined as the motion of fluid due to gravity acting on an unstable density profile. The density of a fluid is determined by the distribution of internal energy, which is typically set by differences in temperature or in the concentration of a solute. If dense fluid lies above less dense fluid, such that the fluid is unstably stratified, then, under the action of gravitational forces, the dense fluid sinks and the less dense fluid rises; potential energy is converted into kinetic energy, and convection ensues.

In this dissertation, we explore in detail a range of physically motivated problems involving convection in a fluid-saturated porous medium. Convection in porous media has widespread importance in a plethora of geophysical and industrial processes (Nield & Bejan, 2006). Heat from deep within the Earth drives

underground hydrothermal convection that is crucial for the extraction of geothermal energy (Cheng, 1978), while convective currents in both the continental and the oceanic lithosphere play a major role in the heat budget of the Earth (Stein, 1995; Cherkaouim & Wilcock, 1999). Density differences that drive convection may also be due to variations in salinity, as in the flow of saline groundwater due to evaporation from the surface (Wooding *et al.*, 1997*a*,*b*). The convective gravity drainage of brine from sea ice in the polar oceans has important implications for global oceanic circulation and mixing (Notz & Worster, 2009), while a similar process is responsible for the formation of freckles in industrial alloy castings (Fowler, 1985). In recent years, there has been particular interest in the effect of porous convection on the long-term storage of $CO_2$ by geological sequestration (Orr Jr., 2009), which has been widely proposed as a technological means of stabilizing the rising concentration of atmospheric $CO_2$ (Metz *et al.*, 2005). The importance of convection for the long-term sequestration of $CO_2$ is the primary motivation for this work, and is discussed in more detail in §1.1 below.

For the sake of clarity, throughout this dissertation we refer to convection in a porous medium as 'porous convection', in contrast to 'pure-fluid' convection, not in a porous medium. Porous convection, which is governed by Darcy's law rather than the full Navier–Stokes equations, provides a more tractable system than pure-fluid convection in which to study the nonlinear dynamics and pattern formation of convective flows (Graham & Steen, 1994), owing primarily to the absence of inertia in Darcy's law.

The vigour of convection and the associated dynamics of the flow depend in large part on the driving strength of buoyancy and the inhibiting dissipative effects of diffusion and viscosity in the system. The ratio of driving and inhibiting effects is given by a dimensionless parameter called the Rayleigh number $Ra$. The aim of this dissertation is to provide a thorough exploration of convection in a porous medium at high $Ra$, in a range of physical systems. In particular, we examine in detail the complex nonlinear dynamics of high-$Ra$ convection, and we characterize the dependence of the convective transport of buoyancy, which is perhaps the most physically important measure of convection, on the physical parameters and geometry of different systems. We also develop physically motivated reduced models of convection that can be applied to different systems.

In §1.1, we outline the details of geological $CO_2$ sequestration and the importance of convective transport for the long-term security of sequestered $CO_2$. In §1.2, we discuss the basic equations and modelling assumptions which underlie the work throughout this dissertation, and in §1.3 we give a brief overview of some previous studies of porous convection. In §1.4, we lay out the structure of the dissertation.

## 1.1 Geological $CO_2$ sequestration

There has been recent resurgent interest in the subject of convection in a porous medium, owing to its relevance to the long-term storage of geologically sequestered $CO_2$. Geological sequestration entails the underground storage of pressurized $CO_2$ in underground porous rock. With growing global demand for energy, it seems probable that sequestration will need to play a major role as a part of attempts to curb the rising anthropogenic emissions of $CO_2$, which are now higher than 30 gigtons a year (Metz *et al.*, 2005; Friedlingstein *et al.*, 2010). Estimates of the subterranean storage capacity of $CO_2$ range from 1700 to 14000 gigatons or higher (Metz *et al.*, 2005; Orr Jr., 2009). This wide range reflects both the large uncertainty in the properties that constitute a suitable storage site, and the lack of sufficiently accurate geological data of potential sites. Sequestration has been tested on large scales in various locations around the world; the longest-running industrial example is at the offshore Sleipner gas fields in the North sea, where roughly one million tons of $CO_2$ have been sequestered in the nearby Utsira sand reservoir every year since 1996 (Kongsjorden *et al.*, 1997).

After capturing and compressing $CO_2$ into a supercritical liquid at its source (e.g. a power plant), geological storage is achieved by injecting the supercritical $CO_2$ down into deep porous formations that are typically located at depths $\gtrsim$ 800 m below the Earth's surface. The most abundant potential storage sites are deep saline aquifers (brine-saturated porous rock), and it is these that are the focus of this work; other possible sites include depleted oil and gas reservoirs, coal beds, and seabed sediments. Under storage conditions in a saline aquifer, supercritical $CO_2$ is significantly less dense ($\sim 700\,\mathrm{kg\,m^{-3}}$) than the ambient brine ($\sim 1000\,\mathrm{kg\,m^{-3}}$), and will rise through the aquifer after injection.

From the point of view of both viability and safety, it is essential that the long-term ($\sim 10^4$ years) underground storage of sequestered $CO_2$ can be assured. Therefore, since the injected $CO_2$ is buoyant, the presence of a bounding impermeable caprock (typically a shale or clay layer) below which the $CO_2$ can pool and spread under gravity, is vital for any storage site. This 'topographic' trapping of $CO_2$ may not necessarily result in secure long-term storage, because fractures in the caprock or migration due to its topography can lead to undesired leakage of the buoyant $CO_2$ plume (Pritchard, 2007; Neufeld *et al.*, 2011; Vella *et al.*, 2011). There are, however, other mechanical and geochemical processes which take place over different timescales. Three main process are: 'residual trapping', in which small pockets of $CO_2$ are immobilized in the brine by capillary forces; 'mineral trapping', in which chemical reactions with minerals in the host rock lead to the precipitation of $CO_2$; and 'dissolution trapping', in which $CO_2$ dissolves into the host brine (Metz *et al.*, 2005).

Residual or capillary trapping, well known to oil engineers and hydrologists (Bear, 1988), takes place whenever the porous medium is initially saturated with one fluid, which is then displaced by another immiscible fluid. Such is the case with brine and $CO_2$, where capillary forces act to trap pockets of $CO_2$ in the wake of the injected current over relatively short time scales (Hesse & Tchelepi, 2008; Golding *et al.*, 2011). Mineral trapping, on the other hand, is anticipated to take place over extremely long time scales (typically much longer than the timescales over which the injected $CO_2$ might leak to the surface), and is very dependent on the properties of the host rock (Orr Jr., 2009).

Dissolution trapping, or convective dissolution, forms the primary motivation for this dissertation. Supercritical $CO_2$ is roughly $3-5\%$ soluble by weight in brine under typical storage conditions (van der Meer, 2005). Although $CO_2$ is significantly less dense than brine, this weak dissolution forms a solution that is denser than brine. The dense solution is, therefore, unstable to downwelling convection, which enhances the transport of $CO_2$ away from the injected current, and leads to more secure storage. Geochemical field observations in natural $CO_2$ reservoirs suggest that convective dissolution provides a very significant and persistent mechanism for the transport of $CO_2$ (Gilfillan *et al.*, 2009).

Typical values of the Rayleigh number (more formally defined in §1.2.3 below)

for convective dissolution can vary significantly, and can be very high owing to the relatively small diffusivity of $CO_2$ in brine ($\approx 10^{-9}\,\mathrm{m^2 s^{-1}}$), the potentially large permeability of the rock ($10^{-15}$ to $10^{-11}\,\mathrm{m^2}$), and the large spatial scales of subsurface saline aquifers ($\sim 10^2$ m). These parameter values give rise to Rayleigh numbers in the range $10 < Ra < 10^5$. If $Ra$ is small, convective dissolution will not have a significant impact; for $Ra > O(1000)$, on the other hand, convective dissolution is expected to play a major role in the long-term stability of stored $CO_2$. It is this parameter range that is the focus of this dissertation.

## 1.2 Governing equations and modelling assumptions

### 1.2.1 Darcy velocity and Darcy's law

The porosity $\phi$ of a porous medium is defined as the fraction of the medium that is made up of pore space. Flow in the pore space is typically modelled by taking the average of quantities like the local velocity and pressure in each pore over a representative volume that encapsulates many pores (known as a 'representative elementary volume' or REV; Bear 1988). The interstitial velocity $\boldsymbol{v}$ is defined to be the mean velocity over all the pore space in a REV. The average volume flux or Darcy velocity, $\boldsymbol{u}$, is the average velocity over both the solid matrix and the pore space in a REV, and is therefore given by $\boldsymbol{u} = \phi \boldsymbol{v}$.

The fluid is assumed to be incompressible, which gives

$$\boldsymbol{\nabla} \cdot \boldsymbol{u} = 0. \tag{1.1}$$

The Darcy velocity $\boldsymbol{u}$ is governed by Darcy's law (Bear, 1988; Phillips, 2009), which relates the driving pressure and buoyancy forces to the viscous drag imparted by the medium on the pore scale. The driving forces are given by the pressure gradient $-\nabla p$ and buoyancy $-\rho \boldsymbol{g}$, where $p$ is the pressure, $\rho$ is the density, and $\boldsymbol{g}$ is the gravitational acceleration. The viscous drag scales with $\mu \nabla^2 \boldsymbol{v} \sim \mu \boldsymbol{v}/\delta_p^2$, where $\mu$ is the viscosity of the fluid and $\delta_p$ is the typical length-

scale of the pores. A balance of driving and drag forces gives Darcy's law,

$$\boldsymbol{u} = -\frac{K}{\mu}\left(\boldsymbol{\nabla} p - \rho \boldsymbol{g}\right), \tag{1.2}$$

where $K \sim \phi\,\delta_p^2$ is the permeability. As well as depending on both the fraction of pore space ($\phi$) and the typical pore size ($\delta_p$), the permeability typically depends on properties of the complex pore network, like the tortuosity and the 'connectedness' of the pores.

Darcy's law (1.2) rests on a number of assumptions. The medium is assumed to be fully saturated by the fluid, so there are no effects of partial saturation. On the pore scale, inertia is assumed to be negligible compared to viscous drag, such that the pore-scale Reynolds number $Re_p$ is small[1]. The lengthscales of the flow are also assumed to remain larger than the typical scale of the REV. The latter two assumptions are discussed in more detail in §1.2.4 below.

Throughout this dissertation, we also make the assumption that density variations are small relative to the magnitude of the density itself; this is the (porous equivalent of the) Boussinesq approximation. Mathematically, the assumption is contained within the condition of incompressibility (1.1): variations in the density affect the buoyancy term in (1.2), but have a negligible effect on the velocity via conservation of mass.

### 1.2.2 Transport of solute or heat

The equation of state describes the dependence of the density $\rho$ either on the concentration $C$ of a solute, $\rho(C)$ (as in the case of $CO_2$ and brine), or on the temperature $T$, $\rho(T)$. In the former case, the concentration field in the liquid phase of the medium evolves by advection and diffusion, as described by

$$\phi\frac{\partial C}{\partial t} + \boldsymbol{u}\cdot\boldsymbol{\nabla} C = \phi\nabla\cdot\left(D\nabla C\right), \tag{1.3}$$

[1]There have been numerous attempts to extend Darcy's law or to re-derive the momentum equation for $Re_p > O(1)$. These include simply appending inertial terms to Darcy's law (e.g. Wooding 1957), or adding a quadratic drag term (the 'Forchheimer equation'; see e.g. Joseph *et al.* 1982). In general, it is difficult to find a robust physical basis for these alternative momentum equations, and they are not considered in this dissertation.

where $D$ is the solutal diffusivity, which we assume is constant.

In the case of thermal convection, one needs to consider the conservation of heat in both the solid and the liquid phases of the medium, which are coupled by the transfer of heat between the phases. In general, the transport equations for the temperature $T_s$ of the solid phase and $T_l$ of the liquid phase are given by

$$(1-\phi)\,\rho_s c_s \frac{\partial T_s}{\partial t} = (1-\phi)\,\nabla\cdot(\alpha_s \nabla T_s) + \mathcal{H}\,(T_s - T_l)\,, \tag{1.4a}$$

$$\phi\rho_l c_l \frac{\partial T_l}{\partial t} + \rho_l c_l\, \boldsymbol{u}\cdot\boldsymbol{\nabla} T_l = \phi\nabla\cdot(\alpha_l \nabla T_l) - \mathcal{H}\,(T_s - T_l)\,, \tag{1.4b}$$

where $\rho_{s,l}$, $c_{s,l}$, and $\alpha_{s,l}$ are the density, the specific heat capacity, and the thermal conductivity of the solid and liquid phases, respectively, and $\mathcal{H}$ is the volumetric heat-transfer coefficient between the phases. Throughout this dissertation, we will make the simplifying assumption that there is no heat transfer to the solid phase ($\mathcal{H} = 0$); as such, the temperature of the liquid and solid are decoupled. The validity of this assumption is discussed in §1.2.4 below. We therefore need only model the evolution of the temperature field in the liquid region (1.4b), which, on setting $T_l = T$, reduces to

$$\phi\frac{\partial T}{\partial t} + \boldsymbol{u}\cdot\boldsymbol{\nabla} T = \phi\nabla\cdot(\kappa\nabla T)\,. \tag{1.5}$$

Here, $\kappa = \alpha_l/(\rho_l c_l)$ is the thermal diffusivity of the liquid, which we assume is constant. Equations (1.3) and (1.5) therefore have an identical form, and so, under the assumption of negligible heat transfer to the solid phase, any analysis of thermal convection (for which $\rho$ is a function of $T$ alone) will be directly applicable to solutal convection (for which $\rho$ is a function of $C$ alone). For simplicity, both for solutal and thermal convection, we have neglected the effects of dispersion in the medium.

### 1.2.3 Dimensionless parameters

The ratio of the driving strength of buoyancy to the dissipative effects of diffusion and viscosity is given by the Rayleigh number $Ra$, defined in the case of thermal

convection by

$$Ra = \frac{UH}{\phi\kappa} = \frac{\Delta\rho\, g\, KH}{\phi\kappa\mu}, \tag{1.6}$$

where $U = \Delta\rho\, gK/\mu$ is the buoyancy velocity, $\Delta\rho$ is the driving density difference and $H$ is a typical length scale. For solutal convection, $\kappa$ is replaced by $D$ in (1.6). The Rayleigh number can alternatively be thought of as the ratio of diffusive and convective time scales; in this sense, it is also a Peclét number. In this dissertation, we focus on convective systems in which $Ra$ is large, and thus advection, rather than diffusion, provides the dominant transport mechanism.

The dimensionless measure of the convective transport, or flux, of buoyancy is given by the Nusselt number $Nu$. The Nusselt number is the ratio of the total flux $F^*$ of buoyancy to the diffusive flux that would occur if there were no convection. In the case of thermal convection driven by a temperature contrast $\Delta T$ across a depth $H$, the Nusselt number is given by

$$Nu = \frac{F^*}{\phi\kappa\,(\Delta T/H)}. \tag{1.7}$$

If there is no convection, $Nu = 1$. Based on dimensional analysis, $Nu = Nu(Ra)$, and the form of this relationship has been widely studied. One of the main results presented in chapter 2 is the characterization of this relationship for $Ra \gg 1$. We note that, for solutal convection, the Nusselt number is sometimes referred to as the Sherwood number; for simplicity, throughout the dissertation it will be referred to as the Nusselt number.

### 1.2.4 Discussion of assumptions at high $Ra$

We recall that a number of assumptions lie behind Darcy's law (1.2). Two assumptions need particular consideration when the Rayleigh number is large. First, viscous terms are assumed to dominate inertial terms on the pore-scale; i.e., the pore-scale Reynolds number $Re_p$ is assumed to be small. Although this condition cannot hold for arbitrarily large values of $Ra$, because $Ra$ is proportional to the buoyancy velocity, it can hold for $Ra \gg 1$ provided the pore scale remains small. More formally, we recall that the typical pore size $\delta_p \sim K^{1/2}$, and define both the Darcy number $Da = K/H^2 \sim (\delta_p/H)^2$ to be a dimensionless

measure of the pore size, and the Prandtl number $Pr = \mu/(\rho\kappa)$ to be the ratio of viscous and thermal/solutal diffusivity. Darcy's law is expected to remain valid if

$$Re_p = \frac{Ra\, Da^{1/2}}{Pr} < O(1). \tag{1.8}$$

Second, Darcy's law is based on an assumption that the lengthscales of the flow are larger than the scale of the REV, and therefore much larger than the pore scale. At high $Ra$, the smallest lengthscales are diffusive, and are anticipated to scale like $H/Ra$ (see chapter 2). A comparison of the diffusive lengthscale with the pore scale $\delta_p \sim K^{1/2}$ suggests that Darcy's law should remain valid if

$$Ra\, Da^{1/2} \ll O(1). \tag{1.9}$$

Throughout this dissertation, we assume that (1.8) and (1.9) apply. For a $CO_2$ sequestration site, typical values of $Da$ lie in the range $10^{-19} \lesssim Da \lesssim 10^{-15}$, while $Pr > 1$, which suggests that Darcy's law remains valid for at least $Ra \lesssim 10^6$. The majority of geophysical values of $Ra$ in a porous medium, and all the values considered in this dissertation, lie below this bound.

Thus the work in this dissertation is directly relevant to solutal convection at high $Ra$. To aid intuition, and in common with the many previous studies of convection, however, we will use the terminology of thermally driven convection, except in chapters 5 and 6. As mentioned above, analysis of thermal convection is equally applicable to solutal convection under the assumption that there is no heat transfer to the solid phase of the medium. It should be noted that, in a physical system, this assumption is likely to break down at large values of $Ra$, particularly when the temperature contrasts are large. However, while the specific physics of a particular system may vary, the results detailed in this dissertation provide the tools to systematically understand the dynamics of high-Rayleigh-number porous convection in a wide variety of physical settings.

## 1.3 Introduction to two-dimensional convection in a porous Rayleigh–Bénard ('Rayleigh–Darcy') cell

The Rayleigh–Bénard cell provides a canonical system for the study of convection. The cell has lower and upper boundaries held at fixed hot and cold temperatures, respectively, and thus attains a statistically steady state, which allows for accurate characterization of both the convective flux through the system and the associated nonlinear dynamics. The study of convection in a pure-fluid Rayleigh–Bénard cell has a long and rich history, and remains an enduring and active subject of fundamental interest in fluid dynamics (Siggia, 1994; Ahlers *et al.*, 2009). Of particular physical importance is the relationship between the convective flux of buoyancy, as described by the Nusselt number $Nu$, and the relative 'strength' of convection, as described by the Rayleigh number $Ra$.

In comparison to pure fluid convection, convection in a porous version of the Rayleigh–Bénard cell has received rather less attention, particularly at high values of $Ra$. In order to avoid confusion with the pure-fluid Rayleigh–Bénard cell, throughout this dissertation we refer to this porous cell as a Rayleigh–Darcy cell. The Rayleigh–Darcy cell is a 'two-sided' convective system, because there is convective transport away from both the upper and the lower boundaries. Natural convective systems in porous media are often driven by a source of buoyancy on only one boundary, and we refer to such systems as 'one-sided'. Convection in one-sided systems is discussed in detail in chapter 5.

Convection in a two-dimensional Rayleigh–Darcy cell has been widely studied for $Ra \lesssim 1300$ (see Nield & Bejan 2006). For $Ra < Ra_{\text{crit}} = 4\pi^2$, a vertically linear and horizontally uniform temperature field is stable; there is no flow (Lapwood, 1948), and all the buoyancy transfer is diffusive ($Nu = 1$). For $4\pi^2 < Ra \lesssim 382$, the convective flow takes the form of large-scale convective rolls, which are steady and stable. The Nusselt number increases with $Ra$, and the relationship $Nu(Ra)$ can be well predicted by a weakly non-linear analysis (Nield & Bejan, 2006). For $382 \lesssim Ra \lesssim 1300$, convective instabilities in the boundary layers result in a series of bifurcations that perturb, but do not completely break down, the background

cellular structure of the flow (Robinson & O'Sullivan, 1976; Kimura *et al.*, 1986; Graham & Steen, 1994). The perturbations take the form of 'dripping' plumes which grow from the boundary layers but are washed around with the background circulation. The growth and migration of these plumes gives rise to periodic, doubly periodic, or chaotic oscillations in the time-dependent Nusselt number. The dynamics exhibit significant hysteresis in this regime, and so the values of $Ra$ at which bifurcations occur are approximate.

Above $Ra \approx 1300$, the quasisteady background rolls are completely broken down by the growth of destabilizing plumes from the upper and lower boundaries (Otero *et al.*, 2004). The change in the dynamical structure marks the transition to the 'turbulent' high-$Ra$ regime. Curiously, there is a sharp drop in $Nu(Ra)$ across the transition (Graham & Steen, 1994; Otero *et al.*, 2004), which is presumably attributable to the reorganization of the flow structure. The high-$Ra$ regime in a Rayleigh–Darcy cell, which has been very little studied in the past, is examined in detail in chapter 2, as discussed below.

## 1.4 Layout

The layout of the dissertation is as follows. In chapter 2, we present direct numerical simulations of convection in a two-dimensional Rayleigh–Darcy cell for $Ra \leqslant 4 \times 10^4$, and examine in detail the convective dynamics at high $Ra$, which have been largely unexplored until now. In particular, our measurements of the Nusselt number $Nu$ are extremely well fitted in the high-$Ra$ regime ($Ra \gtrsim 1300$) by an expression of the form $Nu = \alpha\, Ra + \beta$, where $\alpha = 6.9 \times 10^{-3}$ and $\beta = 2.75$. This fit strongly suggests that the linear 'classical' scaling $Nu \sim Ra$ (discussed in §2.1) is attained asymptotically. We show that the interior of the vigorously convecting system is dominated by persistent vertical columnar flow. Remarkably, the columnar flow is increasingly well described as $Ra \to \infty$ by a steady columnar 'heat-exchanger' solution with a single horizontal wavenumber $k$. The wavenumber increases with $Ra$, and measurements of $k$ are approximately fitted by $k \sim Ra^{0.4}$.

In chapter 3, we examine the stability of columnar convection in a porous medium. This work is motivated by the strikingly persistent quasisteady colum-

nar flow observed in the previous chapter, and by the unexplained physical mechanism that controls the horizontal wavenumber $k$ of this flow. We investigate the hypothesis that the stability of the columnar flow provides the mechanism for wavelength selection, by studying the linear stability of an unbounded 'heat-exchanger' flow. The dimensionless flow comprises interleaving vertical columns of horizontal wavenumber $k$ and amplitude $\widehat{A}$ that are driven by a steady balance between vertical advection of a background linear density stratification and horizontal diffusion between the columns. We use a Floquet linear-stability analysis to show that the unbounded flow is always unstable, and determine the largest growth rate in the limit $Ra \gg k/\widehat{A}$ using a matched asymptotic expansion. The most unstable perturbation in this limit takes the form of vertically propagating pulses on the background columns. Direct numerical simulations show that the non-linear evolution of the instability results in a coarsening of the columnar flow. We apply the results of the stability analysis to the columnar flow in a two-dimensional Rayleigh–Darcy cell, by balancing time scales of propagation and growth. This scaling argument suggests that the columnar flow would be unstable if the wavenumber $k$ were greater than $k \sim Ra^{5/14}$, as $Ra \to \infty$. A correction to this scaling for finite $Ra$ gives a slightly stronger dependence on $Ra$, in good agreement with the numerical measurements from chapter 2. The agreement demonstrated suggests that stability of the columnar flow may provide the hitherto unexplained mechanism that controls the horizontal structure of high-$Ra$ porous convection.

In chapter 4, we present a numerical investigation of the flow in a porous cell containing a thin horizontal layer of much lower permeability than the rest of the cell. This work is motivated by the common occurrence of thin, roughly horizontal, low-permeability layering in geophysical aquifers. We show that, if both the height $h$ and permeability $\Pi$ of the interior layer are small compared with the height and permeability of the rest of the cell, the flow is a function of their ratio, $\Omega = h/\Pi$, only. This observation is corroborated by direct numerical results. We characterize the dependence of the convective flux and the associated dynamical structure of the flow on $\Omega$, which can be thought of as the impedance due to the low-permeability layer. Two observations are particularly striking: first, the horizontal lengthscale of the plumes in the interior of the cell increases dramatically

as $\Omega$ is increased; and second, the presence of an interior low-permeability layer can cause the Nusselt number $Nu$ to increase appreciably from the value in a homogeneous cell with no interior layer. We explore the dependence of $Nu(\Omega)$ and the structure of the flow on $Ra$, and develop simple reduced models of the system to describe some of the observed features.

In chapter 5 and chapter 6, we extend our previous work on 'two-sided' statistically steady Rayleigh–Darcy convection to consider the evolution of convection in a 'one-sided' system. A one-sided system has a source of buoyancy on one boundary alone, and there is no steady state. In a closed domain, driven by a dense source on an upper boundary, convection gradually 'shuts down' owing to the increase in the average interior density. In chapter 5, we show that the evolution of the convective flux in this one-sided shutdown system can be directly calculated from the relationship $Nu(Ra)$ in a two-sided statistically steady Rayleigh–Darcy cell (studied in chapter 2). We develop simple 'box' models that give excellent agreement with high-resolution numerical calculations. We also find a remarkable similarity in the dynamical structure of convection between the one-sided evolving system and the two-sided statistically steady system; vertical columnar plumes reach across the height of the domain, and their lateral scale evolves in very good qualitative agreement with measurements of $k(Ra)$ from chapter 2. We extend this work to model the shutdown of convection with a general power-law equation of state.

In chapter 6, we build on the work of the previous chapter to consider different, more complex, physical systems, which comprise two fluid layers with an equation of state such that the solution that forms at the interface is more dense than either layer (as in the case of supercritical $CO_2$ overlying brine). We consider both immiscible and miscible fluids; in each case, the predictions of theoretical box models agree well with the results of high-resolution numerical simulations. We undertake both laboratory experiments and numerical simulations which show that interfacial deformation can dramatically enhance the convective flux.

In chapter 7, we present the first numerical study of high-$Ra$ Rayleigh–Darcy convection in three dimensions. We give a brief overview and discussion of the features of the flow below the transition to the high-$Ra$ regime, as the system has been very little studied previously except for the range $Ra \lesssim 300$ in which the

convection is steady. Measurements of $Nu(Ra)$ over the range $1500 \leqslant 2 \times 10^4$ are very well fitted by $Nu = \alpha_3 \, Ra + \beta_3$, for $\alpha_3 = 9.6 \times 10^{-3}$ and $\beta_3 = 4.28$. This fit strongly suggests that the classical linear scaling $Nu \sim Ra$ is attained asymptotically, as in two dimensions (chapter 2). We also measure the dynamical structure of the flow, and show that a steady heat-exchanger model provides an increasingly good description of the interior exchange flow as $Ra \to \infty$. The dominant horizontal wavenumber of the interior flow is roughly fitted by $k \sim Ra^{0.54}$ over this range of $Ra$.

Finally, in chapter 8, we summarize all of this work. We discuss some of the implications of our results for the geological storage of $CO_2$, and directions for future work. In appendix A, we give a detailed description of the numerical schemes that were developed and used throughout the dissertation.

# Chapter 2

# Two-dimensional Rayleigh–Darcy convection at high Rayleigh number

The material contained in this chapter has been published in *Physical Review Letters*, under the title 'Ultimate regime of high Rayleigh number convection in a porous medium' (Hewitt *et al.*, 2012).

## 2.1 Introduction

The Rayleigh–Darcy cell (porous Rayleigh–Bénard cell) provides an archetypal configuration in which to study convection in a porous medium. The cell has imposed temperatures on its upper and lower boundaries and thus attains a statistically steady state, which allows both for a detailed investigation of the convective dynamics and for an accurate measurement of the convective flux, as described by the Nusselt number $Nu$.

As discussed in the introduction, various authors have studied and characterized the convective dynamics of the two-dimensional Rayleigh–Darcy cell for low and moderate values of the Rayleigh number $Ra$ (see Nield & Bejan 2006). We recall that, for $Ra < 4\pi^2$, there is no convection (Lapwood, 1948), while for $4\pi^2 < Ra \lesssim 1300$, the flow exhibits convective rolls, which undergo a series of

bifurcations that perturb the background flow as $Ra$ is increased (Kimura *et al.*, 1986; Graham & Steen, 1994). For $Ra \gtrsim 1300$, this quasisteady background flow breaks down completely, marking a transition to the high-$Ra$ regime of interest here. Although this transition was observed in a numerical study by Otero *et al.* (2004), who measured $Nu(Ra)$ for $Ra \leqslant 10^4$, the dynamics of the flow in the high-$Ra$ regime have not previously been explored.

The Nusselt number, which describes the transport of buoyancy in a system, provides perhaps the most physically important measure of convection. Characterization of the relationship $Nu(Ra)$ has been the subject of extensive research. The famous 'classical' scaling argument (Howard, 1964) for convection in a pure-fluid Rayleigh–Bénard cell claims that, for sufficiently large $Ra$, the heat transfer into the domain becomes independent of the height $H$ of the domain, because the the structure of the flow is dominated by plume shedding from thin boundary layers into a turbulent interior. This argument predicts a scaling of $Nu \sim Ra^{1/3}$ in a pure fluid.[1]

For porous convection in a Rayleigh–Darcy cell at high $Ra$, the classical argument instead predicts a linear scaling $Nu \sim Ra$. In agreement with this prediction, a linear scaling has been shown to be a rigorous upper bound for the the flux (Busse & Joseph, 1972; Doering & Constantin, 1998; Otero *et al.*, 2004; Wen *et al.*, 2012). However, in their direct numerical study of the high-$Ra$ regime, Otero *et al.* (2004) found a slightly reduced exponent $Nu \sim Ra^{0.9}$ for $1300 \lesssim Ra \leq 10^4$. Experimental results from a one-sided system with a convecting upper boundary and a deep or no-flux bottom boundary have given scalings closer to $Nu \sim Ra^{0.8}$ (Neufeld *et al.*, 2010; Backhaus *et al.*, 2011).

In this chapter, we use well-resolved direct numerical simulations of a two-dimensional Rayleigh–Darcy cell over the range $1300 < Ra \leq 4 \times 10^4$ to examine

[1]The turbulent nonlinear dynamics of pure-fluid convection, together with dependence on the Prandtl number, give rise to a system of rather more complexity than this simple argument suggests (Siggia, 1994; Ahlers *et al.*, 2009). For example, the widely cited (if no longer widely believed) theory of Castaing *et al.* (1989) suggested that shear in the boundary layers due to large-scale circulation could re-introduce a dependence on the height $H$ at larger $Ra$, to give a reduced scaling $Nu \sim Ra^{2/7}$, while the so-called 'ultimate' scaling of $Nu \sim Ra^{1/2}$, in which the flux is controlled entirely by the turbulent interior dynamics, has been hypothesized by rigorous upper bounds (Kraichnan, 1962; Doering & Constantin, 1996; Plasting & Kerswell, 2003), and observed in numerical simulations (Lohse & Toschi, 2003; Calzavarini *et al.*, 2005) and experiments (Chavanne *et al.*, 1997; He *et al.*, 2012) at very high values of $Ra$.

the dynamics and behaviour of the flux in the high-$Ra$ regime. In §2.2, we present the governing equations and non-dimensionalization, and briefly outline the numerical scheme that we employed (the numerical scheme is discussed in detail in appendix A). In §2.3, we present the numerical results, which reveal that, contrary to previous indications of a sub-linear scaling, the linear classical scaling $Nu \sim Ra$ is attained asymptotically. In §2.4, we explore the dynamics of the flow in the high-$Ra$ regime; the dynamical structure of the flow is dominated by vertical columnar 'megaplumes' that extend across the interior of the domain, and are driven by entrainment and mixing of small 'protoplumes' near the upper and lower boundaries. The flow in the interior is increasingly well described as $Ra \to \infty$ by a simple steady 'heat-exchanger' solution with a single horizontal wavenumber $k$. Measurements of $k$ give an approximate scaling of $k \sim Ra^{0.4}$.

In §2.5, we summarize and discuss our results.

## 2.2 Governing equations and numerical method

### 2.2.1 Dimensional equations

We consider the flow of a Boussinesq fluid in a two-dimensional homogeneous and isotropic porous medium, with horizontal and vertical coordinates $x^*$ and $z^*$, respectively (dimensional variables are denoted with a $^*$). We assume that the flow $\boldsymbol{u}^*$ obeys Darcy's law and is incompressible,

$$\boldsymbol{u}^* = -\frac{K}{\mu}\left(\nabla p^* + \rho^* g \hat{\boldsymbol{z}}^*\right), \tag{2.1}$$

$$\nabla \cdot \boldsymbol{u}^* = 0, \tag{2.2}$$

where $K$ is the permeability of the porous medium and $\mu$ is the fluid viscosity, both of which are assumed to be constant, $p^*$ is the pressure field, $g$ is the acceleration due to gravity, and $\hat{\boldsymbol{z}}^*$ is a unit vector in the positive $z^*$ direction. The density $\rho^*$ satisfies a linear equation of state with respect to the temperature field $T^*$,

$$\rho^* = \rho_0\left[1 - a\left(T^* - T_0\right)\right], \tag{2.3}$$

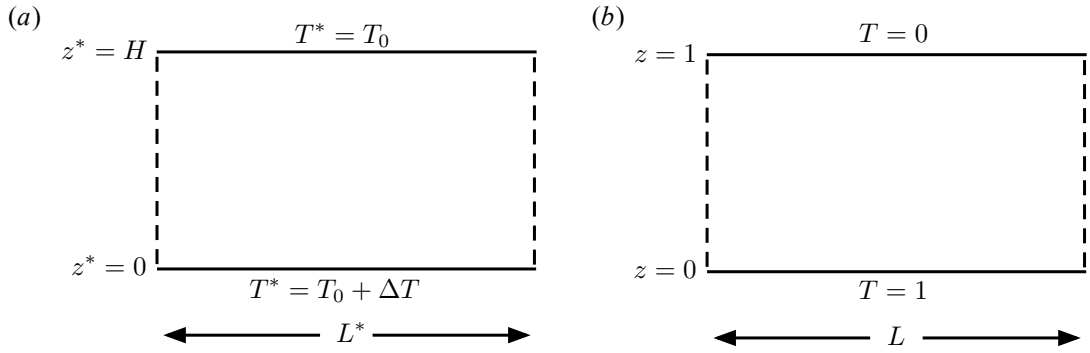


Figure 2.1: A schematic of the setup for the $(a)$ dimensional and $(b)$ dimensionless Rayleigh Darcy cell.

with constant coefficient of thermal expansion $a$ and constant reference density and temperature $\rho_0$ and $T_0$ respectively. The temperature field evolves in time $t^*$ by advection and diffusion,

$$\phi \frac{\partial T^*}{\partial t^*} + \boldsymbol{u}^* \cdot \nabla T^* = \phi \kappa \nabla^2 T^*, \tag{2.4}$$

where $\phi$ is the porosity of the porous medium and $\kappa$ is the thermal diffusivity, both again assumed to be constant. Note that we have neglected heat transfer to the solid phase of the medium in (2.4) (see §1.2).

We consider a domain of depth $H$ and width $L^*$, with periodic boundary conditions on the sides $x^* = 0, L^*$ (figure 2.1$a$). We impose zero mass flux and fixed temperature on the top and bottom of the domain:

$$T^* = T_0 + \Delta T, \quad w^* = 0 \quad \text{at} \qquad z^* = 0, \tag{2.5a}$$

$$T^* = T_0, \quad w^* = 0 \quad \text{at} \qquad z^* = H. \tag{2.5b}$$

### 2.2.2 Dimensionless equations

We define the density scale $\Delta\rho = \rho_0 a \Delta T$ and the convective velocity scale $U = Kg\Delta\rho/\mu$. Lengths are scaled with $H$, velocity with $U$, pressure with $gH\Delta\rho$, and

time with $\phi H/U$; we also introduce a rescaled dimensionless temperature $T$ given by

$$T = \frac{T^* - T_0}{\Delta T}. \tag{2.6}$$

This rescaling gives dimensionless equations

$$\boldsymbol{u} = -\left(\nabla P - T\hat{\boldsymbol{z}}\right), \tag{2.7}$$

$$\nabla \cdot \boldsymbol{u} = 0, \tag{2.8}$$

$$\frac{\partial T}{\partial t} + \boldsymbol{u} \cdot \nabla T = \frac{1}{Ra}\nabla^2 T, \tag{2.9}$$

where $P = p + z\,\rho_0/\Delta\rho$ is a reduced pressure, and the Rayleigh number is given by

$$Ra = \frac{UH}{\phi\kappa} = \frac{\rho_0 a \Delta T g K H}{\phi\kappa\mu}. \tag{2.10}$$

The thermal boundary conditions in (2.5) become

$$T = 1 \quad \text{at} \quad z = 0, \qquad \text{and} \qquad T = 0 \quad \text{at} \quad z = 1. \tag{2.11}$$

The dimensionless system is shown schematically in figure 2.1($b$).

Non-dimensionalizing in this way gives rise to $O(1)$ dimensionless temperature and convective velocity and time scales, while diffusive time and length scales are $O(Ra^{-1})$. The Rayleigh number takes the role of an inverse diffusivity in (2.9). This choice of dimensionless variables aids numerical calculations by leaving the timescales for convergence to a statistically-steady state independent of $Ra$.

The Nusselt number $Nu$ is the dimensionless average heat flux though the system, scaled by the flux due to steady conduction alone. The heat flux can be determined by the diffusive flux through the lower boundary of the domain, which gives

$$Nu = \langle nu(t) \rangle = \left\langle -\frac{1}{L}\int_0^L \left.\frac{\partial T}{\partial z}\right|_{z=0} \mathrm{d}x \right\rangle, \tag{2.12}$$

where angle brackets $\langle\ \rangle$ denote a long-time average and $L = L^*/H$ is the dimen-

sionless width of the domain. We define the expression inside the angle brackets of (2.12) to be the time dependent Nusselt number $nu(t)$.

### 2.2.3 Numerical method

The requirement of incompressibility (2.8) can be satisfied by introducing a streamfunction $\psi$, with $(u, w) = (\psi_z, -\psi_x)$. We eliminate the pressure field $P$ by taking the curl of (2.7), which gives

$$\nabla^2 \psi = -\frac{\partial T}{\partial x}. \tag{2.13}$$

Equations (2.9) and (2.13) were solved numerically. The numerical method is outlined very briefly below, and is discussed in detail in appendix A.

Equation (2.13) was solved using a spectral method, and (2.9) with an alternating-direction implicit method. The diffusion and advection operators in (2.8) were discretised using standard second-order finite differences and flux-conservative techniques respectively. We used a vertical co-ordinate transformation in order to resolve the diffusive boundary layers at $z = 0, 1$ which have an anticipated depth $\delta \sim Ra^{-1}$. The numerical simulations are second order in space and time, and have been extensively benchmarked against previous numerical results at lower values of $Ra$ (Graham & Steen, 1994; Otero *et al.*, 2004), as discussed in appendix A.

The numerical simulations were initialised in one of two ways: either with a small (random) perturbation to the steady conduction solution $T = 1 - z$, $\boldsymbol{u} = 0$, or with the statistically-steady output from a simulation at a lower or similar $Ra$. After some initial transient dynamics, which depend on the initialisation method, the system settles into a statistically steady state. Unlike at lower values of $Ra$ (see, e.g., Otero *et al.* 2004), we have seen no evidence that the initial conditions play a role in the long-term behaviour of the system in the high-$Ra$ regime.

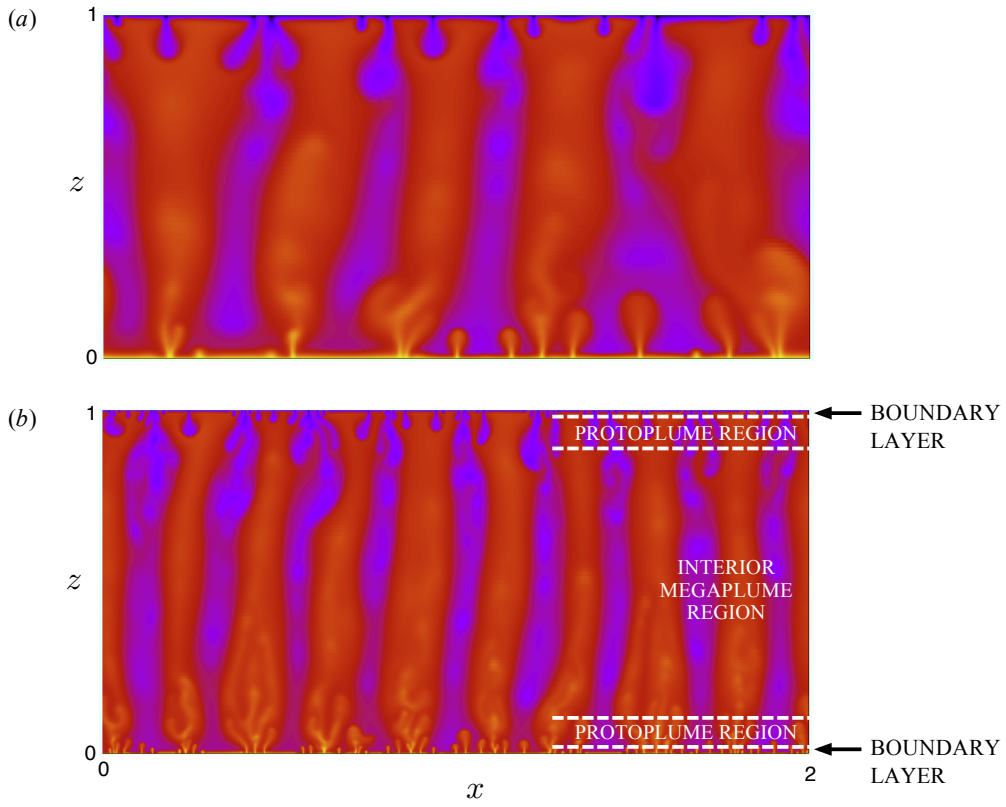


Figure 2.2: Snapshots of the temperature field for $L = 2$ at: $(a)$ $Ra = 5000$; and $(b)$ $Ra = 2 \times 10^4$, which highlights the three regions of differing dynamics, as discussed in the main text.

## 2.3 Numerical results

### 2.3.1 Structure of the flow

For $Ra \gtrsim 1300$, the system cannot sustain the large-scale quasi-periodic roll structure found at lower $Ra$, which is broken down as unsteady plumes from the boundaries drive a vigorous columnar exchange flow across the height of the domain. This transition in the dynamics marks the start of the 'high-$Ra$' regime, which is studied here.

The flow can be divided into three regions of differing dynamics, as illustrated in figure 2.2, which shows snapshots of the temperature field for $Ra = 5000$ and $Ra = 2 \times 10^4$. The interior region is dominated by predominantly vertical

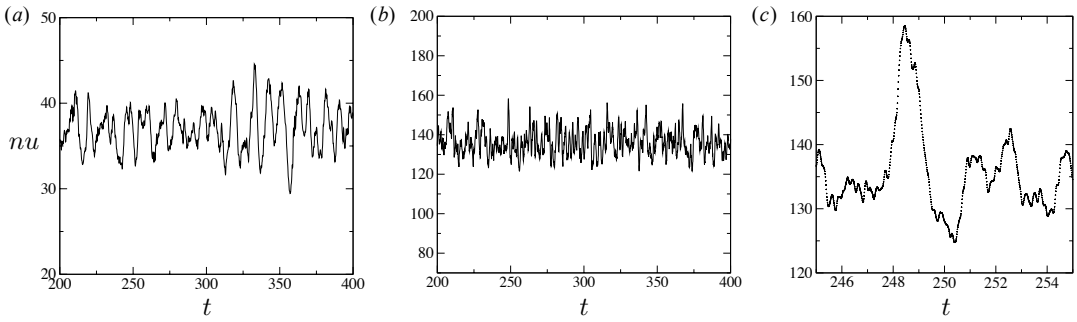


Figure 2.3: The instantaneous Nusselt number $nu(t) = \int \partial T/\partial z|_{z=0}\, \mathrm{d}x$ for: $(a)$ $Ra = 5000$; and $(b)$ $Ra = 2 \times 10^4$, with the vertical axis showing the range $[Nu/2, 3Nu/2]$. Panel $(c)$ shows the same data as $(b)$ on an expanded sale; the individual data points shown are separated by ten time steps $\Delta t$, illustrating that the measurements are well resolved in time.

exchange flow, carried in columns or 'megaplumes' of a fairly regular and $Ra$-dependent wavelength. At the very top and bottom of the domain are thin diffusive boundary layers, where intermittent short-wavelength instabilities drive the growth of small 'protoplumes'. Between the boundary layers and the interior columnar flow is a region where the dynamics are characterised by the rapid growth and vigorous mixing of protoplumes. Lateral flushing by the large-scale flow drives entrainment of the protoplumes into the interior megaplumes. As can be observed by a comparison of figure 2.2$(a)$ and $(b)$, the horizontal scale of both the protoplumes and the interior megaplumes decreases as $Ra$ increases.

### 2.3.2 The Nusselt number

For $Ra \gtrsim 1300$, the time-dependent Nusselt number, $nu(t)$, of the statistically steady state exhibits chaotic fluctuations about the time-averaged Nusselt number $Nu$. The typical frequency scales of these fluctuations increase with $Ra$, while their relative amplitude decreases, as shown for $Ra = 5000$ and $Ra = 2 \times 10^4$ in figure 2.3. A numerical estimate of $Nu$ is obtained by time-averaging until statistical uncertainty in the mean of $nu(t)$ is reduced to within 0.25%. The details of this averaging technique are given in appendix 2.A.

Figure 2.4 shows $Nu(Ra)$ for $Ra \leqslant 4 \times 10^4$. The transition to the high-$Ra$ regime is marked by a sharp discontinuity in $Nu$ at $Ra \approx 1300$. A least-squares fit

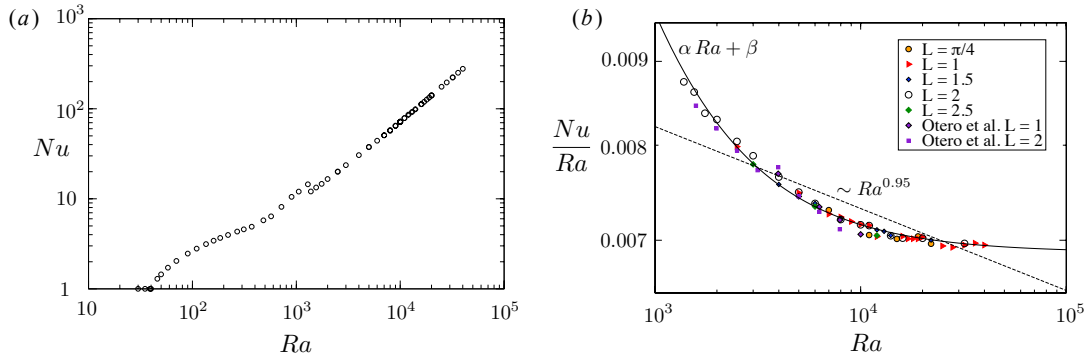


Figure 2.4: $(a)$ The time-averaged Nusselt number $Nu(Ra)$, showing the onset of convection at $Ra = 4\pi^2$ and the transition to the high-$Ra$ regime at $Ra \approx 1300$. $(b)$ The scaled Nusselt number $Nu/Ra$ in the high-$Ra$ regime, for different aspect ratios $L$, together with the data from Otero *et al.* (2004) for $Ra \leqslant 10^4$ for comparison. The best-fit power law $Nu \sim Ra^{0.95}$ (dotted line) does not capture the trend as $Ra$ increases; instead, the measurements are very well described by $Nu = \alpha Ra + \beta$, for $\alpha = 6.88 \times 10^{-3}$ and $\beta = 2.75$ (solid line).

of the data beyond this point gives a scaling of $Ra \sim Nu^{0.95\pm0.01}$, in approximate agreement with previous results (Otero *et al.*, 2004). However, the numerical measurements for $1300 \leqslant Ra \leqslant 4 \times 10^4$ are much more accurately fitted by an equation of the form

$$Nu = \alpha Ra + \beta, \tag{2.14}$$

where $\alpha \approx 6.9 \times 10^{-3}$ and $\beta \approx 2.75$ are constants. Figure 2.4$(b)$ shows a plot of $Nu/Ra$ against $Ra$, together with (2.14) and the best-fit power-law curve $Nu \sim Ra^{0.95}$. We find that the linear fit (2.14) deviates from the data by less than 0.6%, while the power-law fit deviates by more than 2%, over the range shown. The excellent fit provided by (2.14) strongly suggests that the classical linear scaling is attained asymptotically, and so the flux is asymptotically independent of the height of the domain. This result is perhaps surprising, given that the system is dominated by columnar exchange flow across the whole domain (fig. 2.2) which, we might imagine, could provide a mechanism by which information could be propagated between the upper and lower boundaries. We find that $Nu$ exhibits no systematic dependence on the aspect ratio $L$; the slight scatter in the measurements of fig. 2.4$(b)$ is the result of extremely long-timescale

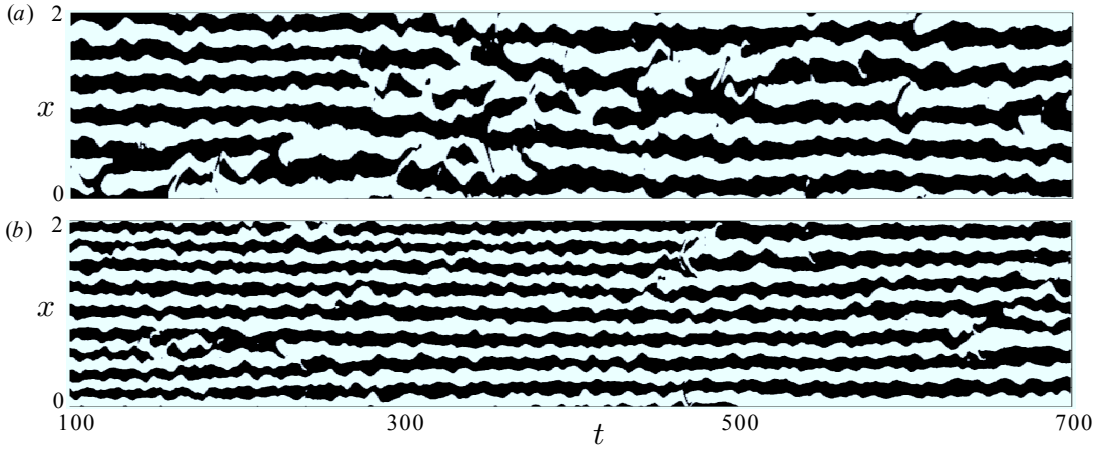


Figure 2.5: The sign of the vertical velocity at $z = 0.5$ over time: $(a)$ $Ra = 5000$; and $(b)$ $Ra = 2 \times 10^4$. White and black signify positive and negative vertical velocity respectively.

fluctuations in the number of megaplumes in the domain, as discussed in §2.4.1 below.

## 2.4 Dynamics of the flow

### 2.4.1 The interior region

We observed in figure 2.2 that the interior of the flow is dominated by vertical columnar megaplumes in the high-$Ra$ regime. Space-time plots of the sign of the vertical velocity at $z = 0.5$ (figure 2.5) reveal the remarkable persistence of this columnar structure, particularly at higher $Ra$. The location of the columnar megaplumes appears to be almost steady in time, despite significant short-timescale fluctuations in the position of the edges of the columns. There is some slight variability in the number of columns over extremely long timescales, which could be due to weak mode restriction imposed by the horizontal periodicity, although similar long-timescale variability is observed in calculations with larger aspect ratios $L$.

#### 2.4.1.1 Heat-exchanger solution

Based on the observed persistence of the megaplumes in figure 2.5, we can develop a simple, steady model of the columnar flow in the interior. There is an exact 'heat-exchanger' solution to (2.9) and (2.13) in an unbounded domain, in which vertical advection of a background linear temperature gradient is exactly balanced by horizontal diffusion between neighbouring megaplumes, giving a steady solution,

$$T = \widehat{A}\cos(kx) - \frac{k^2}{Ra}\,z, \tag{2.15a}$$

$$u = 0, \tag{2.15b}$$

$$w = \widehat{A}\cos(kx). \tag{2.15c}$$

The solution comprises interlocking columnar flow with amplitude $\widehat{A}$ and a regular horizontal wavenumber $k$.

Equation (2.15$a$) shows that the horizontally averaged temperature profile is vertically linear. Numerical measurements of the temporally and horizontally averaged temperature $\langle\overline{T}\rangle$ (figure 2.6) agree with this linear behaviour in the interior region. The gradient of $\langle\overline{T}\rangle$ decreases as $Ra$ increases. We compare the amplitude of the columnar flow in the heat-exchanger model with the numerical calculations by measuring the root-mean-square (rms) temperature perturbations and velocity components, $T_{\rm rms}$, $w_{\rm rms}$ and $u_{\rm rms}$. In the heat-exchanger model, $T_{\rm rms} = w_{\rm rms} = \widehat{A}/\sqrt{2}$ and $u_{\rm rms} = 0$, independent of $z$. Numerical measurements of $T_{\rm rms}$, $w_{\rm rms}$ and $u_{\rm rms}$ at different values of $Ra$ (figure 2.7$a$) show very good agreement with this behaviour asymptotically: $u_{\rm rms}$ decreases as $Ra$ increases, and $T_{\rm rms}$ appears to tend towards $w_{\rm rms}$, which is itself roughly independent of $Ra$, as $Ra \to \infty$.

These measurements indicate that the vigorously convecting system is dominated by a remarkably persistent columnar flow that becomes increasingly ordered and increasingly well-described by the steady heat-exchanger solution as $Ra$ increases. Moreover, the measurements presented in figure 2.7($a$) suggest that $\widehat{A}$ is asymptotically independent of $Ra$ and given by $\widehat{A} = \sqrt{2}T_{\rm rms} \approx \sqrt{2}\,(0.083) \approx$

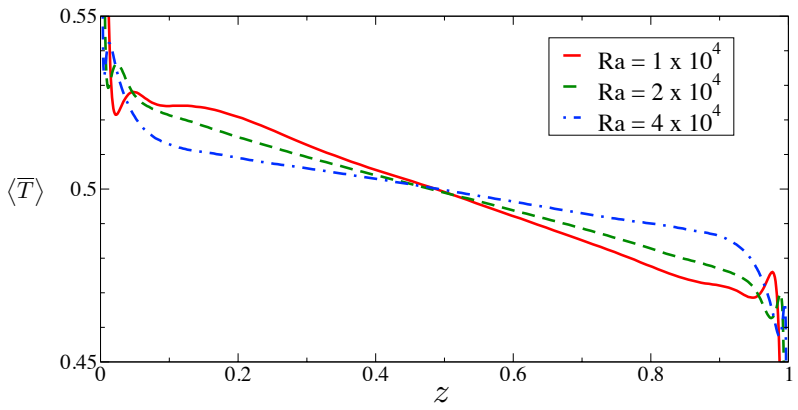


Figure 2.6: The temporally and horizontally averaged temperature profile $\langle\overline{T}\rangle$ for $Ra = 1, 2, 4 \times 10^4$, as marked. The profiles are approximately linear through the interior of the domain, with a gradient that decreases with $Ra$.

0.117 as $Ra \to \infty$. This observation agrees with the indications from figure 2.4 that the classical linear scaling for $Nu(Ra)$ is attained asymptotically, and corroborates the validity of the heat-exchanger model for the interior flow: since the heat flux is dominated by advection in the interior at high $Ra$, the heat-exchanger model (2.15) gives $Nu \approx Ra\widehat{A}^2/2 \approx 0.0069Ra$ as $Ra \to \infty$, in very good agreement with the measured value of the coefficient $\alpha$ in (2.14). [1]

Figure 2.7($b$) shows the variation in the rms temperature and velocity fields with $z$ for a selection of values of $Ra$. The heat-exchanger solution requires the rms values to be independent of $z$, and so we expect it to be valid across the interior, where the measured quantities vary slowly and $T_{\rm rms} \approx w_{\rm rms}$. Near to the upper and lower boundaries of the domain, however, the rms quantities vary significantly: $T_{\rm rms}$ and $w_{\rm rms}$ differ appreciably, and $u_{\rm rms}$ grows. These observations signify that the heat-exchanger solution breaks down near to the upper and lower boundaries of the domain, where protoplumes dominate the dynamics of the flow.

We have also adapted the unbounded heat-exchanger solution (2.15) to model the effect of circulation in a finite domain, by including vertical variation with a wavenumber $m \ll k$. The adapted model is discussed in appendix 2.B. The model, which includes a non-zero horizontal velocity, gives good quantitative

[1] Interestingly, the average advective heat flux depends only on the amplitude $\widehat{A}$, and is independent of the wavenumber $k$.

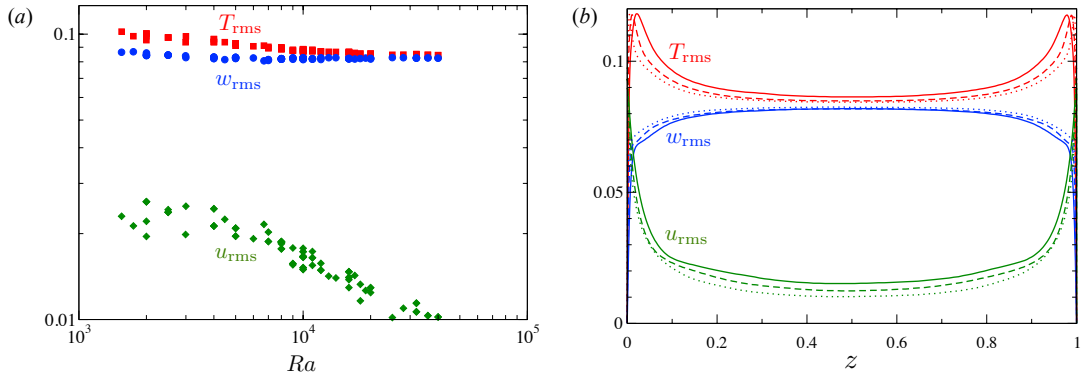


Figure 2.7: The temporally average root-mean-square temperature $T_{\rm rms}$ (red), vertical velocity $w_{\rm rms}$ (blue) and horizontal velocity $u_{\rm rms}$ (green): $(a)$ measured at $z = 0.5$; and $(b)$ plotted against $z$, for $Ra = 10^4$ (solid), $Ra = 2\times10^4$ (dashed), and $Ra = 4 \times 10^4$ (dotted).

agreement with the behaviour of the rms temperature and velocity perturbations in figure 2.7$(a)$, and reduces to the simple heat-exchanger solution (2.15) as $Ra \to \infty$.

#### 2.4.1.2 Measurements of the dominant wavenumber $k$

The heat-exchanger model *per se* leaves the wavenumber $k$ of the columnar flow undetermined. We measured $k$ using a time-average of the Fourier transform of the temperature field at $z = 0.5$, and these measurements are presented in figure 2.8$(a)$. We obtained very similar results by applying the same method to the vertical velocity field. The measurements of $k$ can be fitted by an approximate scaling

$$k = 0.48Ra^{0.4}, \tag{2.16}$$

(figure 2.8$b$), although the data also hints at a possible decrease in the exponent for $Ra \gtrsim 2 \times 10^4$ [1]. There is some variation between different calculations, even for the same aspect ratio $L$, which is likely due to fluctuations in the dominant wavenumber over extremely long timescales (as observed in figure 2.5).

[1] A larger range of $Ra$ would be required to verify any change in exponent. However, results from a stability analysis of the heat-exchanger solution (presented in chapter 3) are consistent with the measurements presented here and suggest an asymptotic scaling of $k \sim Ra^{5/14}$ ($5/14 \approx 0.357$).

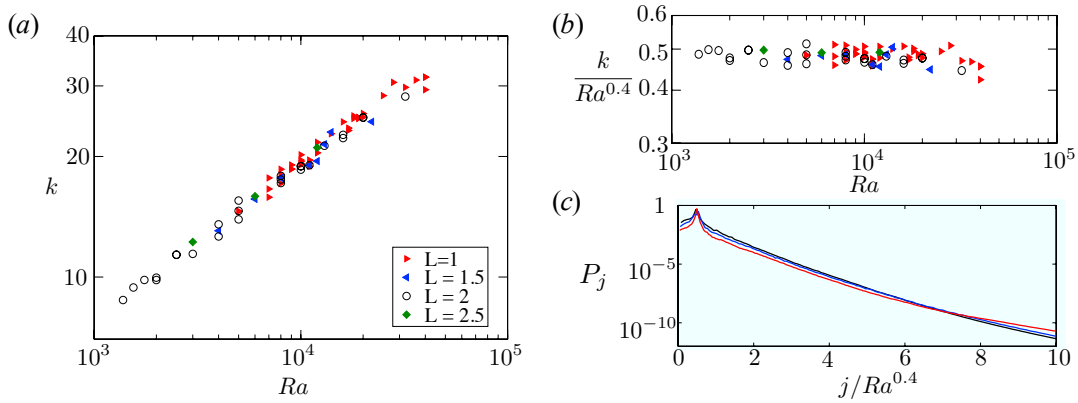


Figure 2.8: Measurements of the temporally averaged horizontal wavenumber: $(a)$ the dominant wavenumber $k$, measured from a Fourier transform at $z = 0.5$, for different aspect ratios $L$ as marked; $(b)$ the dominant wavenumber scaled by $Ra^{0.4}$; and $(c)$ the time-averaged power spectra $P_j$ against the scaled wavenumber $j/Ra^{0.4}$, for $Ra = 1, 2, 4 \times 10^4$ (black, blue, and red, respectively), showing exponential decay for large wavenumbers and a clear peak at $j = k$. We attribute the variability in the measurements of $k$ in $(a)$ and $(b)$ to very long timescale fluctuations in the dominant wavenumber that are not fully time-averaged.

The time-averaged power spectra $P_j$, which are given as a function of the wavenumber $j$ by the square of the magnitude of the Fourier transform, show a clear peak at the dominant wavenumber $k$, and an exponential decay for large wavenumbers (figure 2.8$c$). While relatively low wavenumbers appear to exhibit the same approximate scaling with $Ra$ as $k$, larger wavenumbers seem to display a stronger scaling, as can be seen by examining the measurements of $P_j$ for large wavenumbers in figure 2.8$(c)$.

### 2.4.2 The proto-plume region

In a bounded domain, the interior columnar-exchange flow feeds into and is fed by protoplumes near to the upper and lower boundaries. A plausible hypothesis is that the horizontal wavenumber $k$ and the amplitude $\widehat{A}$ of the interior flow are determined by the interaction between the megaplumes and the protoplume regions. To examine the dynamics in these regions, we constructed space-time diagrams of the temperature in a slice at a fixed height just above the bottom boundary layer (which exhibits behaviour that is mirrored at the top). Figure

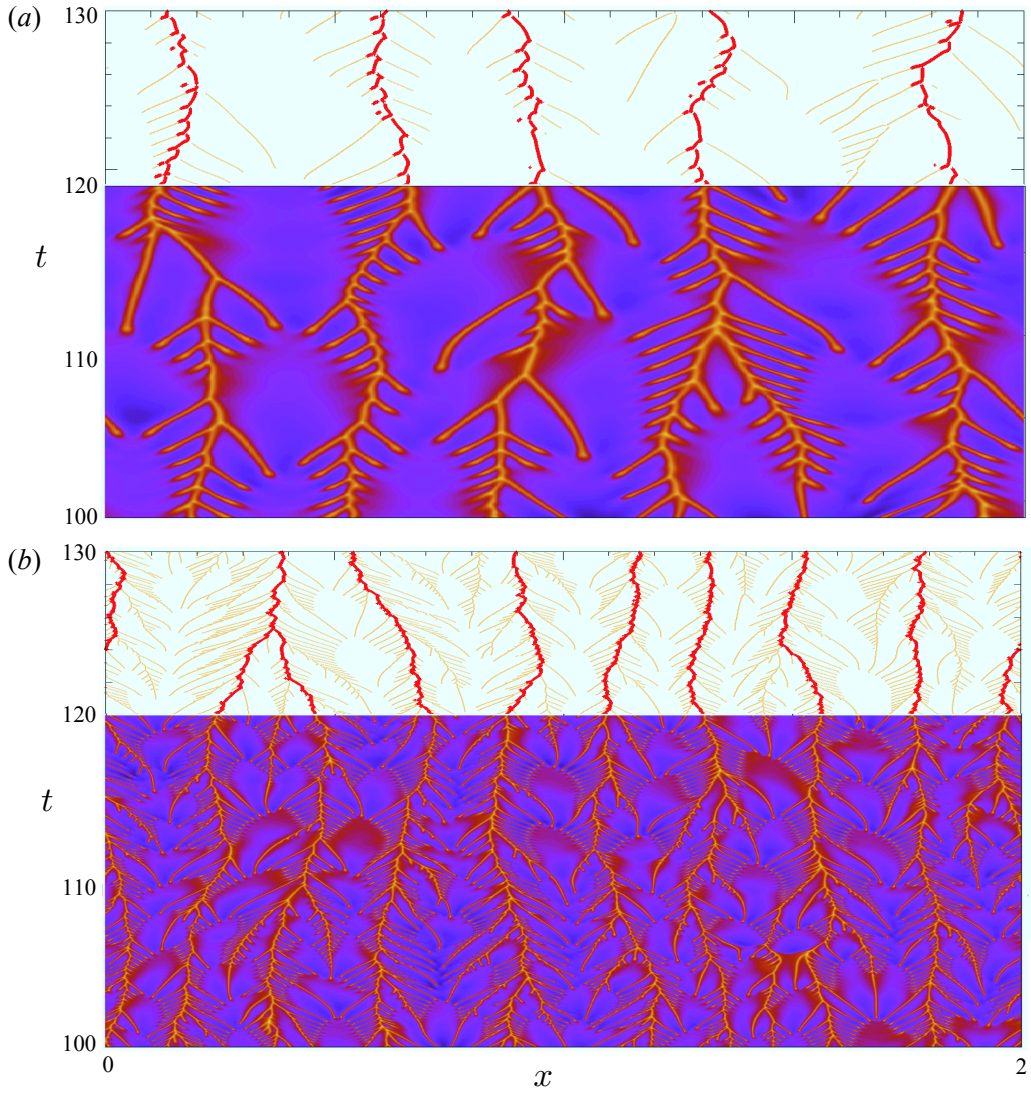


Figure 2.9: Space-time plots of the temperature in a slice just above the lower boundary layer at $z = 100/Ra$, for: $(a)$ $Ra = 5000$; and $(b)$ $Ra = 2 \times 10^4$. These plots show both the directly measured temperature ($t < 120$) and the results of a plume-tracking algorithm ($t > 120$), which gives a way to analyse the dynamics of plumes in more detail. Megaplume roots are highlighted, and the 'ribs' of the fishbone structures (see the text) mark the formation and entrainment of protoplumes.

2.9 reveals a characteristic repeating 'fish-bone' pattern, which corresponds to persistent mega-plume roots (the 'backbones') together with transient formation and entrainment of protoplumes on either side (the 'ribs').

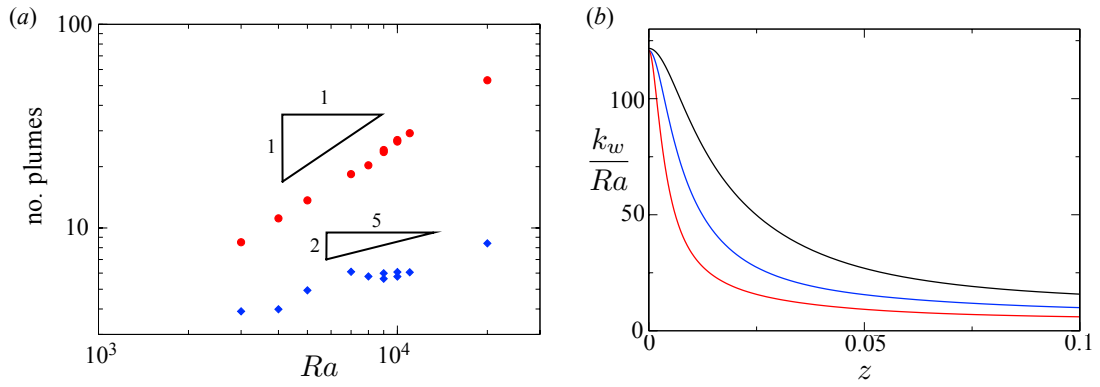


Figure 2.10: $(a)$ The temporally averaged number of plumes in the boundary layer for $L = 2$, counted by a plume-tracking algorithm: the total number of plumes (red) is best fit by a scaling of $Ra^{0.97\pm0.05}$, while the number of megaplumes alone is best fit by a scaling of $Ra^{0.39\pm0.06}$, in rough agreement with the measurements of $k$ in the interior (figure 2.8). $(b)$ The dominant wavenumber $k_w(z)$ of the vertical velocity, measured by a Fourier transform and scaled by $Ra$, for $Ra = 1, 2, 4\times10^4$ (black, blue, and red, respectively). The wavenumber has a linear scaling with $Ra$ near the boundary, in contrast to the much weaker scaling of $k$ in the interior.

The pattern of ribs shows bursts of protoplumes that typically commence near a larger established plume, while later proto-plumes in the burst originate successively further away. We interpret this as propagation of instability along the boundary layer which drains the buoyancy accumulated since the previous burst. Concomitantly each new proto-plume is entrained back towards the larger established plume. This coupled mechanism of instability and entrainment leads to episodic and highly time-dependent patterns of plume growth and flushing.

Counts from a plume-tracking algorithm of the number of plumes in the boundary layer (figure 2.10$a$) and measurements of the dominant wavenumber as a function of $z$ (figure 2.10$b$) both strongly suggest that the typical lateral lengthscale of the protoplumes scale like $Ra^{-1}$, which is a much stronger scaling than the megaplume spacing $k^{-1}$ (2.16). This means that there are more proto-plumes being entrained into each megaplume at higher values of $Ra$. In addition, visual comparison and rescaling of plots like fig. 2.9$(a)$ and $(b)$ suggests that the typical timescales and lateral lengthscales of the 'ribs' in the fish-bone structures scale approximately like $Ra^{-1}$. The lengthscales certainly decrease significantly more rapidly with $Ra$ than the mega-plume spacing, as can be seen by comparing

the number of 'ribs' in fig. 2.9. We also observe that the patterns of 'ribs' are increasingly initiated by protoplumes, as well as megaplumes, as $Ra$ is increased, which leads to increasingly ramified fish-bone patterns at higher $Ra$, and is suggestive of a hierarchy of coarsening as $Ra$ is increased. All of these observations strongly suggest that the horizontal wavenumber $k$ of the interior flow is not directly governed by the dynamics of protoplumes at the top and bottom of the domain.

## 2.5 Conclusions

We have found that numerical measurements of the Nusselt number in a Rayleigh–Darcy cell over the range $1300 < Ra \leqslant 4 \times 10^4$ are extremely well fitted by $Nu = \alpha Ra + \beta$, with $\alpha = 6.9 \times 10^3$ and $\beta = 2.75$. This fit strongly suggests that the classical linear scaling $Nu \sim Ra$ is attained asymptotically, in contrast to previous indications of a sub-linear scaling (Otero *et al.*, 2004). An implication of this linear scaling is that the dimensional flux is asymptotically independent of the height of the domain.

Given the increasingly vigorous nature of the dynamics at the boundaries, it is striking that the interior columnar flow displays such persistent regular structure as $Ra$ increases. Indeed, despite highly time-dependent forcing from the protoplume regions, we have shown that the *steady* heat-exchanger solution, which comprises purely vertical flow, provides a remarkably good description of the dynamics of the interior region asymptotically. This increasingly ordered behaviour as $Ra$ is increased is quite unlike the disordered turbulent dynamics in the interior of a pure-fluid Rayleigh–Bénard cell at high $Ra$ (e.g. Ahlers *et al.* 2009). The dominant horizontal wavenumber $k$ of the interior flow increases with $Ra$, and can be approximately fitted by a scaling of $k \sim Ra^{0.4}$ for $1300 < Ra \leqslant 4 \times 10^4$.

The episodic bursting and propagation of boundary-layer instabilities near the upper and lower boundaries of the domain give rise to the fish-bone structures shown in figure 2.9. The typical horizontal lengthscale of the resultant protoplumes approximately scales with $Ra^{-1}$, which is a much stronger than the dominant interior lengthscale $k^{-1}$. The difference in scalings suggests that the protoplumes do not govern the interior wavenumber $k$ directly.

Motivated by this intriguing observation, in chapter 3 we examine in detail whether the interior wavenumber is determined instead by the stability of the columnar flow itself. The results of the stability analysis are consistent with the numerical measurements of $k(Ra)$ presented in figure 2.8, and suggest an asymptotic scaling for the wavenumber of $k \sim Ra^{5/14}$.

The measurements of the flux $Nu(Ra)$ and the surprising dynamical structure of the flow discussed in this chapter provide a basis for a wide range of buoyancy-driven flows in porous media, some of which are discussed in the remainder of this dissertation. In particular, the results of this chapter have implications for the long-term stabilization of sequestered $CO_2$ through dissolution-driven convection.

# Appendices

## 2.A Averaging the Nusselt number

The local time-dependent Nusselt number, $nu(t)$, is given by

$$nu(t) = -\frac{1}{L}\int_0^L \left.\frac{\partial T}{\partial z}\right|_{z=0} \mathrm{d}x = -\frac{1}{L}\frac{\partial \zeta}{\partial z}\int_0^L \left.\frac{\partial T}{\partial \zeta}\right|_{\zeta=0} \mathrm{d}x, \tag{2.17}$$

where $\zeta(z)$ is the rescaled vertical coordinate (see appendix A). In the statistically steady high-$Ra$ regime, $nu(t)$ exhibits chaotic fluctuations about a mean (see figure 2.3). We measured and averaged $nu(t)$ until the average had converged to a suitably defined tolerance. To reduce computation time, we used a 'quadratic-box' running average to reduce the convergence time.

We define the 'quadratic-box' (QB) average of length $L$, $Q_L(t)$, to be the weighted average,

$$Q_L(t) = \frac{15}{16L^5}\int_{t-L}^{t+L} \left(L^2 - [\tau - t]^2\right)^2 nu(\tau)\,\mathrm{d}\tau. \tag{2.18}$$

We generate a running QB average $\overline{Q}_L$ by averaging (2.18) over all previous time

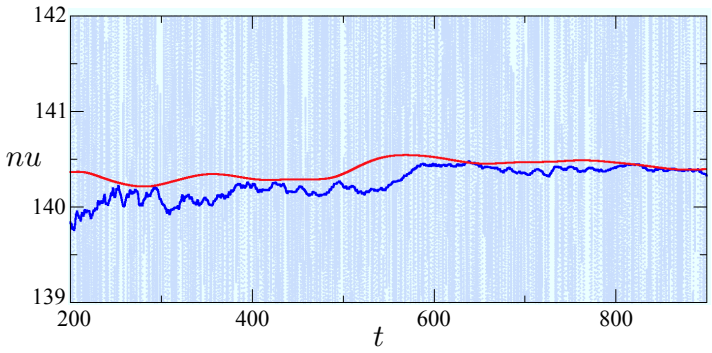


Figure 2.11: The instantaneous Nusselt number $nu(t)$ at $Ra = 2 \times 10^4$ (grey; taken from figure 2.3($b$) and plotted on a much larger scale), together with a standard running average (blue) and the 'quadratic box' running average $\overline{Q}_L(t)$ (red) as defined in the text.

(for the sake of this discussion, $t = 0$ is taken to correspond to a time after all initial transients have decayed and the system is in a statistically steady state), to give

$$\overline{Q}_L(t) = \frac{1}{t - 2L} \int_L^{t-L} Q_L(\tau)\, \mathrm{d}\tau. \tag{2.19}$$

Figure 2.11 shows an example of measurements of $nu(t)$ at $Ra = 2 \times 10^4$, together with the standard running average (which simply averages all previous data points equally) and the QB running average. The QB average gives a much smoother signal than a standard running average. A QB will also give smoother convergence than a simple unweighted box average would, because the averaging function in (2.18) is only discontinuous in the second derivative rather than the zeroth at $t \pm L$, which gives much more rapidly decaying Fourier modes.

The convergence of $\overline{Q}_L(t)$ is determined by specifying a convergence timescale $t_{\mathrm{conv}}$ and tolerance $\varepsilon$. We consider $\overline{Q}_L(t)$ to have converged to $Nu$ if

$$\left|\overline{Q}_L(t_1) - \overline{Q}_L(t_2)\right| < \varepsilon \left( \frac{\overline{Q}_L(t_1) + \overline{Q}_L(t_2)}{2} \right) \quad \text{for all} \quad t_1, t_2 \in [t - t_{\mathrm{conv}}, t]. \tag{2.20}$$

We typically used values of $\varepsilon = 2.5 \times 10^{-3}$ (i.e. convergence to 0.25%) and $t_{\mathrm{conv}} = 100$.

## 2.B The adapted heat-exchanger solution

In §2.4.1.1, we found that the flow in the interior of the Rayleigh–Darcy cell is increasingly well described by a simple heat-exchanger solution as $Ra \to \infty$. The heat-exchanger solution (2.15) comprises purely vertical columnar flow in an unbounded domain. In this appendix, we adapt the unbounded heat-exchanger solution to model the effect of circulation in a finite domain, by including vertical variation with a wavenumber $m \ll k$. The adapted heat-exchanger model takes the form

$$T = \hat{T}\cos(kx)\sin(mz) - \frac{k^2}{Ra}\left(1 + \frac{m^2}{k^2}\right)z, \tag{2.21a}$$

$$u = \hat{u}\sin(kx)\cos(mz), \tag{2.21b}$$

$$w = \hat{w}\cos(kx)\sin(mz), \tag{2.21c}$$

where

$$\hat{u} = \frac{km}{k^2+m^2}\hat{T}, \qquad \text{and} \qquad \hat{w} = \frac{k^2}{k^2+m^2}\hat{T}. \tag{2.22$a$, $b$}$$

Horizontal advection of temperature is neglected in this model, which is a valid approximation as long as $\hat{T}m \ll k^2$. We expect that $m$ is related to the height of the domain, which implies that the more rapid horizontal variations with wavenumber $k$ dominate as $Ra$ increases; hence the simple heat-exchanger solution (2.15) is recovered asymptotically.

Equations (2.21)–(2.22) provide three relationships which link five measurable unknowns, $\hat{T}$, $\hat{w}$, $\hat{u}$, $k$, and $\partial\overline{T}/\partial z$, together with one less easily measured, $m$. These relationships allow us to test the accuracy of the model. Two comparisons, for $\hat{u}$ and for $\partial\overline{T}/\partial z$, are presented below.

First, we consider the horizontal velocity $\hat{u}$. Elimination of $m$ from (2.22) gives an alternative expression for $\hat{u}$,

$$\hat{u} = \hat{w}\left(\frac{\hat{T}}{\hat{w}} - 1\right)^{1/2}. \tag{2.23}$$

We also recall the relationships $T_{\mathrm{rms}} = \hat{T}/\sqrt{2}$, $w_{\mathrm{rms}} = \hat{w}/\sqrt{2}$, and $u_{\mathrm{rms}} = \hat{u}/\sqrt{2}$.

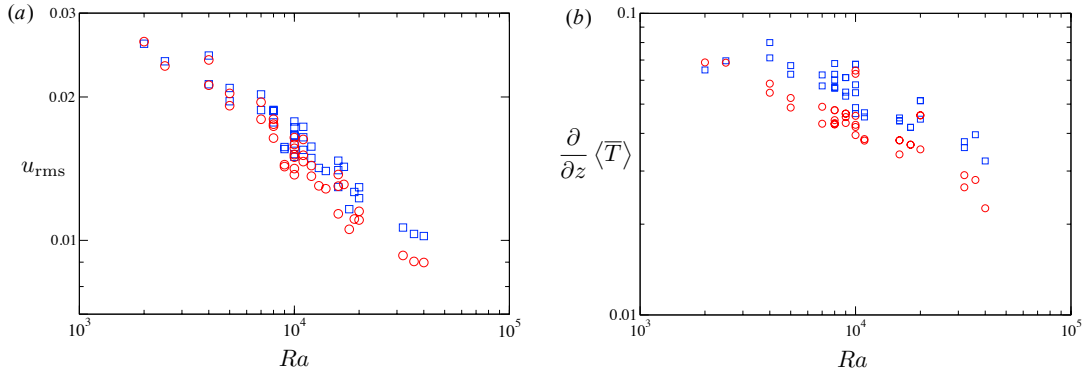


Figure 2.12: Measurements of: $(a)$ the average rms horizontal velocity $u_{\rm rms}$ at $z = 0.5$, from direct numerical measurements (blue squares) and calculated from the adapted heat-exchanger model using (2.23) (red circles); and $(b)$ the magnitude of the temporally and horizontally averaged vertical temperature gradient, from direct numerical measurements (blue squares), and calculated from the adapted heat-exchanger model using (2.24) (red circles).

Figure 2.12$(a)$ shows directly measured values of $u_{\rm rms}$ together with the theoretical values obtained from (2.23) and the measured values of $T_{\rm rms}$ and $w_{\rm rms}$. The measurements suggests a very reasonable agreement with the adapted heat-exchanger model, although there is roughly a 10% difference in magnitude.

Second, we consider the magnitude of the linear gradient of the temporally and horizontally averaged temperature profile, $\partial\left\langle\overline{T}\right\rangle/\partial z$, that was shown in figure 2.6. Elimination of $m$ from the theoretical expression for the gradient in (2.21$a$) using (2.22$a$), gives

$$\left|\frac{\partial\overline{T}}{\partial z}\right| = \frac{k^2}{Ra}\frac{\hat{T}^2}{\hat{w}^2}. \tag{2.24}$$

Figure 2.12$(b)$ shows a comparison of direct measurements of the interior gradient with the calculated value obtained from (2.24) (together with measurements of $T_{\rm rms}$ and $w_{\rm rms}$). Again, we see a good qualitative fit, although with a difference in magnitude of $\sim 15\%$. A power-law fit of the measured data gives a $Ra$ exponent of $-0.27 \pm 0.05$, while the theory (2.24) predicts an asymptotic scaling of approximately $Ra^{-0.2}$, based on the approximate fit $k \sim Ra^{0.4}$ in §2.4.1.2. The variation in the data shown in figure 2.12 is related to the variation in the measurements of $k$ (figure 2.8), and is predominantly due to long-timescale variations in the

number of plumes in the domain, as discussed in §2.4.1.2.

There are at least two plausible reasons for the slight difference between theory and measurements in figure 2.12. First, the measurements of $k^2$ that we have used in (2.24) are calculated from measurements of $k$; however, since the true solution contains more than one Fourier mode, this calculation will yield an underestimate the true value of $k^2$. Second, there will be more horizontal heat transfer than the purely diffusive transfer that the model predicts, because of mixing due to transient dynamics in the interior of the Rayleigh–Darcy cell. So vertical advection of heat, and therefore the background gradient of the flow, will be slightly larger than the model predicts, in order to balance this increased horizontal transfer.

# Chapter 3

# Stability of columnar convection in a porous medium

The material contained in this chapter has been accepted for publication in the *Journal of Fluid Mechanics*, under the title 'Stability of columnar convection in a porous medium' (Hewitt *et al.*, 2013*b*).

## 3.1 Introduction

In chapter 2, we found that vertical columnar flow dominates the flow in a two-dimensional Rayleigh–Darcy cell at high Rayleigh number $Ra$. Curiously, the columnar flow not only persists, but becomes increasingly well organized as $Ra$ is increased, in striking contrast to the disordered dynamics in a pure fluid Rayleigh–Bénard cell at high $Ra$ (e.g. Ahlers *et al.* 2009). We found that, as $Ra$ increases, the interior columnar flow becomes increasingly well described by a steady 'heat-exchanger' solution, in which vertical advection of a background temperature gradient exactly balances horizontal diffusion (figure 3.1). The numerical measurements presented in chapter 2 gave an approximate scaling for the wavenumber $k$ of the columnar flow of $k \sim Ra^{0.4}$ over the range $1300 < Ra \leqslant 4\times10^4$ (see figure 2.8), although it was noted that there was some suggestion of a slightly smaller exponent asymptotically. While $k$ clearly increases with $Ra$, the amplitude $\widehat{A}$ of the columnar flow tends towards a constant (see figure 2.7), consistent with an

asymptotic Nusselt-number scaling $Nu \sim Ra$.

Columnar structures are also very widely observed in two and three-dimensional convective flow driven by a source of buoyancy on one boundary only. Following the onset of convection, flow below a dense source (or, equivalently, above a buoyant source) is marked by vigorous mixing at the boundary which feeds into persistent downwelling plumes, as observed in several experimental (Neufeld *et al.*, 2010; Backhaus *et al.*, 2011; Slim *et al.*, 2013) and numerical (Pau *et al.*, 2010; Hidalgo *et al.*, 2012; Fu *et al.*, 2013) studies. If the boundaries of the domain are impermeable then, over longer times, the convective flow weakens as the density in the interior increases towards that of the upper boundary. This 'shutdown' regime is studied in chapters 5 and 6: we will show in these chapters that the columnar flow across the interior of the domain persists throughout, with a wavenumber $k$ that decreases slowly as the average interior density increased and the effective Rayleigh number decreased. The relationship between $k(t)$ and $Ra(t)$ gives excellent quantitative agreement with results from the Rayleigh–Darcy cell presented in chapter 2.

The physical mechanism that governs the wavenumber $k(Ra)$ has so far remained elusive. In chapter 2 we argued that $k$ is not controlled directly by the small-scale dynamics of proto-plumes near the boundary, since these have a lateral scale of $Ra^{-1}$, which is a much stronger dependence on $Ra$ than the observed wavenumber exponent of about 0.4. It has been suggested by Wen *et al.* (2012, 2013) that the wavenumber is determined by the size of a 'minimal flow unit', which is set by the largest wavenumber $k$ for which the buoyancy flux remains independent of $k$. Solutions for steady convective flow in a narrow Rayleigh–Darcy cell (Corson, 2011) give a scaling of $k \sim Ra^{1/2}$ for the minimal flow unit, while recent numerical measurements of the minimal flow unit for unsteady flow suggest a slightly weaker dependence on $Ra$ (Wen *et al.*, 2013), in rough agreement with the observed wavenumber scaling of $Ra \sim k^{0.4}$. This observation does not, however, provide a mechanism for the physical control of wavenumber. The aim of this chapter is to explore whether the wavenumber might be determined by the stability of the columnar flow.

Columnar 'heat-exchanger' flows are not only observed in porous media; similar flow is found in double-diffusive systems, in the form of 'salt fingers'. These

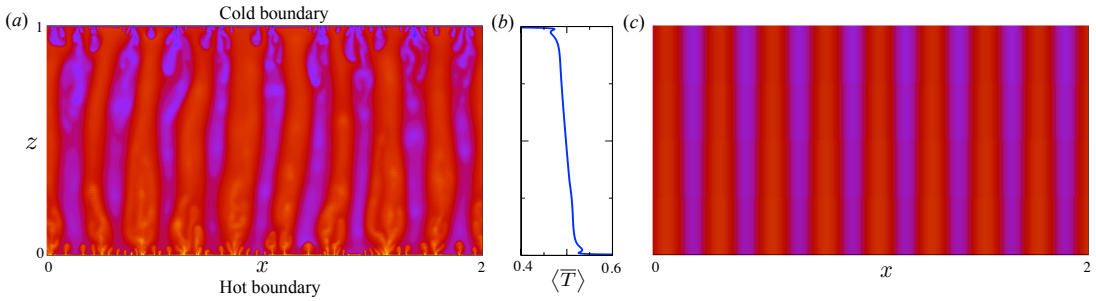


Figure 3.1: $(a)$ A snapshot of the temperature field in a Rayleigh–Darcy cell at $Ra = 2 \times 10^4$ (see chapter 2), which is dominated by vertical columnar exchange flow across the domain; $(b)$ the corresponding temporally and horizontally averaged temperature $\langle \overline{T} \rangle (z)$, which shows the relatively weak linear temperature gradient across the interior of the domain; and $(c)$ the temperature field of steady heat-exchanger flow with the same wavelength and background temperature gradient as $(a)$.

fingers can occur when the density is a function of two components with different molecular diffusivities, such as heat and salt, provided that the unstably distributed component (salt) has a lower diffusivity than the stably distributed component (heat) (Huppert & Turner, 1981). Stability of the salt fingers has long been suggested as the controlling mechanism for their dynamical structure (Stern, 1969); it was explored in detail by Holyer (1981, 1984), and remains an active area of study (Schmitt, 2012; Radko & Smith, 2012). The Floquet analysis employed by Holyer (1984) to solve the linear-stability problem provides a starting point for our approach here.

In this chapter, we examine the stability of two-dimensional columnar heat-exchanger flow in a porous medium. The flow is driven by temperature differences between the columns, but the analysis is equally applicable to compositional convection (see §1.2). In §3.2, we set out the governing equations for heat-exchanger flow in an unbounded medium, and find that the flow is controlled by a single parameter, the rescaled amplitude $A$. In §3.3, we use Floquet theory to perform a linear-stability analysis of this flow. We show that the dominant instability for $A \gtrsim 17.2$ has double the horizontal wavelength of the background columns and a relatively small vertical wavenumber, and we determine the dependence on $A$ of the vertical wavenumber and growth rate of this mode. In §3.4, we present an

asymptotic analysis of the most unstable perturbation for $A \gg 1$, and discuss the physical mechanism of instability. In §3.5, we explore the non-linear evolution of the instability for large $A$ using direct numerical simulations.

In §3.6, we discuss the relevance of all these results for the scaling of the columnar wavenumber $k$ in a Rayleigh–Darcy cell at high $Ra$. A balance of the time scale for instability and the time scale for advection of perturbations across the domain suggests that the columnar flow should be unstable for wavenumbers $k \sim Ra^{5/14}$ as $Ra \to \infty$, while a correction to this asymptotic estimate gives a slightly stronger dependence on $Ra$ for $Ra < O(10^5)$. These scalings give good agreement with numerical measurements of the dominant wavenumber $k$ from the interior of a Rayleigh–Darcy cell.

We conclude with a summary of the main results and their implications in §3.7.

## 3.2 Governing equations

### 3.2.1 Dimensionless equations

We consider flow in a homogeneous, isotropic and unbounded two-dimensional porous medium, with horizontal and vertical coordinates $x$ and $z$, respectively. As in chapter 2, the flow $\boldsymbol{u} = (u, w)$ is incompressible and satisfies Darcy's law, and the density $\rho$ of the fluid is linearly related to the temperature $T$, which satisfies a transport equation. These equations are given in dimensionless variables by

$$\boldsymbol{\nabla} \cdot \boldsymbol{u} = 0, \qquad \boldsymbol{u} = -\left(\boldsymbol{\nabla} P + \rho \hat{\boldsymbol{z}}\right), \tag{3.1a, b}$$

$$\rho = 1 - T, \qquad \frac{\partial T}{\partial t} + \boldsymbol{u} \cdot \boldsymbol{\nabla} T = \frac{1}{Ra} \nabla^2 T, \tag{3.2a, b}$$

where $P$ is the reduced pressure (see §2.2.2). The Rayleigh number $Ra$ is given by

$$Ra = \frac{\rho_0 a \, \Delta T \, g \Pi H}{\phi \kappa \mu}, \tag{3.3}$$

where $\Pi$ is the permeability, $\phi$ is the porosity, $g$ is the gravitational acceleration, $\rho_0$ is a reference density, $a$ is the coefficient of thermal expansion, $\kappa$ is the thermal diffusivity and $\mu$ is the viscosity of the fluid, all of which are assumed to be constant. In common with the rest of this dissertation, we have assumed that there is negligible heat transfer to the solid phase of the medium, and, as such, these equations are equally applicable to compositional convection. We have non-dimensionalized with respect to a temperature scale $\Delta T$, which determines the buoyancy-velocity scale $U = \rho_0 \beta \, \Delta T g \Pi / \mu$, and with respect to a length scale $H$, which determines the convective time scale $\phi H / U$. In the case of a Rayleigh–Darcy cell, these scales would correspond to the driving temperature difference across the domain and the height of the domain, respectively, as in chapter 2.

We satisfy (3.1$a$) by introducing a streamfunction $\psi$, where $(u, w) = (\partial\psi/\partial z, -\partial\psi/\partial x)$. We take the curl of (3.1$b$) to eliminate the pressure, and combine with the equation of state (3.2$a$) to obtain

$$\nabla^2 \psi = -\frac{\partial T}{\partial x}. \tag{3.4}$$

Equations (3.2$b$) and (3.4) govern the flow.

There is an exact solution of (3.2$b$) and (3.4) given by a steady 'heat-exchanger' flow (see chapter 2; §2.4.1.1), in which vertical advection of a background linear temperature gradient by interleaving columns of exchange flow balances horizontal diffusion between the columns; the horizontal velocity is zero, and the vertical velocity is directly proportional to the sinusoidal variation of temperature across the columns. The heat-exchanger solution $[\psi_0, T_0]$ is characterized by a wavenumber $k$ and amplitude $\widehat{A}$, and is given by

$$T_0 = \widehat{A} \cos kx - \frac{k^2}{Ra} z, \quad \psi_0 = -\frac{\widehat{A}}{k} \sin kx, \quad u_0 = 0, \quad w_0 = \widehat{A} \cos kx, \tag{3.5$a$, $b$, $c$, $d$}$$

(cf. (2.15)), where $u_0 = \partial\psi_0/\partial z$ and $w_0 = -\partial\psi_0/\partial x$ are the corresponding horizontal and vertical velocity of the flow. The average vertical advective heat flux for heat-exchanger flow scales with $\widehat{A}^2$, and is independent of the wavenumber $k$.

### 3.2.2 Re-scaled equations

The heat-exchanger flow (3.5) is governed by three parameters $k$, $\widehat{A}$, and $Ra$, which describe the wavenumber, the amplitude, and the relative strength of advection and diffusion, respectively. We can scale out two of these apparent degrees of freedom by setting

$$\boldsymbol{X} = k\boldsymbol{x}; \qquad \Theta = \frac{Ra}{k}T; \qquad \Psi = Ra\,\psi; \qquad \tau = \frac{k^2}{Ra}t. \tag{3.6}$$

The governing equations (3.4) and (3.2$b$) become

$$\nabla^2\Psi = -\frac{\partial\Theta}{\partial X}, \qquad \frac{\partial\Theta}{\partial\tau} + \frac{\partial\Psi}{\partial Z}\frac{\partial\Theta}{\partial X} - \frac{\partial\Psi}{\partial X}\frac{\partial\Theta}{\partial Z} = \nabla^2\Theta, \tag{3.7$a$, $b$}$$

and the heat-exchanger solution (3.5) becomes

$$\Theta_0 = A\cos X - Z, \quad \Psi_0 = -A\sin X, \quad U_0 = 0, \quad W_0 = A\cos X. \tag{3.8$a$, $b$, $c$, $d$}$$

The rescaled strength of the flow

$$A = \frac{\widehat{A}Ra}{k}, \tag{3.9}$$

is now the only free parameter. Equation (3.8) gives the background flow for the stability analysis of the subsequent sections of this chapter.

## 3.3 Linear-stability analysis

### 3.3.1 Theory

We consider small perturbations $[\widetilde{\Psi}, \widetilde{\Theta}]$ to the background heat-exchanger flow of the form

$$\widetilde{\Psi} = \mathrm{Re}\left\{F(X)\exp\left(\sigma t + \mathrm{i}\alpha Z\right)\right\}, \qquad \widetilde{\Theta} = \mathrm{Re}\left\{G(X)\exp\left(\sigma t + \mathrm{i}\alpha Z\right)\right\}, \tag{3.10$a$, $b$}$$

where $|F|, |G| \ll 1$. By retaining only terms that are linear in $F$ and $G$, the governing equations (3.7) become

$$F'' - \alpha^2 F = -G', \qquad (\sigma + \mathrm{i}\alpha A \cos X)\, G + F' - \mathrm{i}\alpha A \sin X F = G'' - \alpha^2 G. \tag{3.11a, b}$$

Owing to the spatial dependence of the coefficients in (3.11$b$), we cannot assume a simple-harmonic normal-mode form for $F$ and $G$. Instead, we utilise the periodicity of the equations: the coefficients are periodic in $X$ with period $2\pi$, and, therefore, (3.11) forms a Floquet system. Floquet theory (see Jordan & Smith 1999, for example) implies that the eigenmodes $\boldsymbol{y}_j(X)$ of any homogeneous system of linear ordinary differential equations that has periodic coefficients with period $\lambda$ can be written in the form $\boldsymbol{y}_j(X) = \boldsymbol{p}_j(X) \exp(\mathrm{i}\beta_j X)$, where $\boldsymbol{p}_j$ is periodic with period $\lambda$, and $\beta_j$ is a (possibly complex) constant. If the eigenmodes are also required to be spatially periodic, then $\beta_j$ must be real. In (3.11), $\lambda = 2\pi$, and so the function $\boldsymbol{p}_j(X)$ can be written as a sum of complex exponentials of the form $\exp(\mathrm{i}nX)$ for integer $n$ (Beaumont, 1981). We therefore look for spatially periodic eigenmodes of the form

$$\begin{pmatrix} F \\ G \end{pmatrix} = \mathrm{Re}\left\{ \exp(\mathrm{i}\beta X) \sum_{n=-\infty}^{\infty} \begin{pmatrix} F_n \\ G_n \end{pmatrix} \exp(\mathrm{i}nX) \right\}, \tag{3.12}$$

where $\beta$ is real. Due to the invariance of (3.12) under integer shifts in $\beta$ and under reflection $\beta \to -\beta$, we can pick $0 \leqslant \beta \leqslant 1/2$ without loss of generality. We refer to $\beta$ as the horizontal wavenumber of the perturbation; strictly, $\beta$ is the wavenumber of the largest horizontal scale, and the infinite sum allows for perturbations on smaller scales.

The eigenvalue $\sigma$ is given as a function of $\alpha$ and $\beta$ by substituting the Fourier sum (3.12) into (3.11) and rewriting $\sin X$ and $\cos X$ in terms of complex exponentials. Equation (3.11) becomes

$$\mathrm{i}\gamma_n^2 F_n = -(\beta + n)\, G_n, \tag{3.13a}$$

$$\mathrm{i}\,(\beta+n)\,F_n - \frac{\alpha A}{2}\,(F_{n-1}-F_{n+1}) = -\left(\gamma_n^2+\sigma\right)G_n - \frac{\mathrm{i}\alpha A}{2}\,(G_{n-1}+G_{n+1})\,, \quad (3.13b)$$

where $\gamma_n^2 = (\beta+n)^2+\alpha^2$, and eliminating $F$ between (3.13a) and (3.13b) gives

$$\left[\frac{(\beta+n)^2}{\gamma_n^2} - \gamma_n^2 - \sigma\right] G_n = \frac{\mathrm{i}\alpha A}{2}\left[\left(1+\frac{\beta+n+1}{\gamma_{n+1}^2}\right)G_{n+1} + \left(1-\frac{\beta+n-1}{\gamma_{n-1}^2}\right)G_{n-1}\right]. \quad (3.14)$$

Equation (3.14) can be written as an infinite matrix equation of the form

$$M\boldsymbol{G} = \sigma\boldsymbol{G}, \quad (3.15)$$

where the vector $\boldsymbol{G} = (\cdots G_{n-1}, G_n, G_{n+1}, \cdots)$, and $M$ is an infinite (tridiagonal) matrix. Solutions to (3.15) are found by looking for eigenvectors $\boldsymbol{G}$ of $M$ with eigenvalues $\sigma$. The real part of $\sigma$ gives the growth rate of perturbations.

### 3.3.2 Solutions

#### 3.3.2.1 The limit of large horizontal scales

The equations simplify dramatically if we only consider perturbations on the largest horizontal scales, which is achieved by severely truncating the infinite sum in (3.12) such that $G_n = 0$ for all $n \neq 0$. In this long-wavelength limit, the columnar flow is completely decoupled from the perturbation, which is equivalent to setting $A = 0$ and losing the effect of flow on stability. Equation (3.14) reduces to the standard linear-stability analysis of a linear background temperature field about rest (Nield & Bejan, 2006), and the growth rate is given by the usual Rayleigh modes,

$$\sigma = \frac{\beta^2}{\beta^2+\alpha^2} - \left(\beta^2+\alpha^2\right). \quad (3.16)$$

The flow is unstable if $\beta > \beta^2+\alpha^2$. If there is no constraint on the size of the domain, then the growth rate is maximized by $\alpha \ll \beta \ll 1$, which gives a limiting growth rate $\mathrm{Re}\{\sigma\} = 1$. If the perturbation is constrained in a finite domain, then the instability takes the form of one or more large convective rolls.

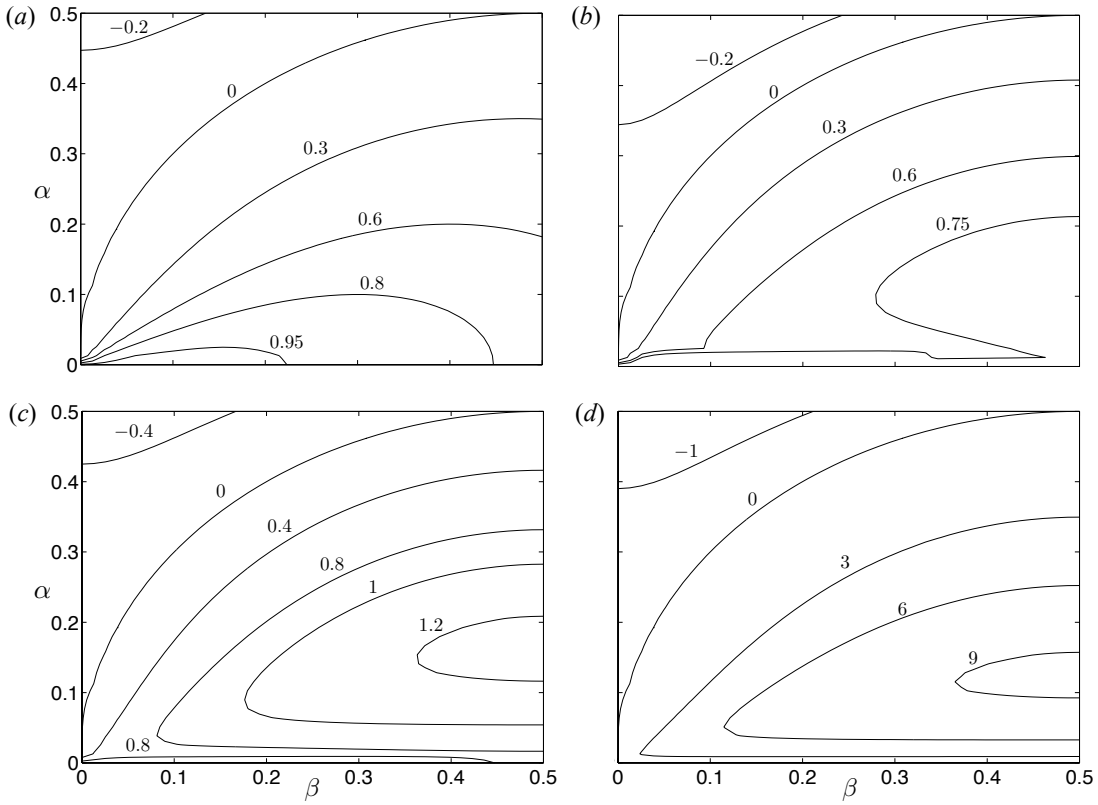


Figure 3.2: Contours of the growth rate $\mathrm{Re}\{\hat{\sigma}\}$ (as marked) against the horizontal wavenumber $\beta$ and the vertical wavenumber $\alpha$ at amplitudes: $(a)$ $A = 0$; $(b)$ $A = 2^3$; $(c)$ $A = 2^5$; and $(d)$ $A = 2^{12}$. The marginal-stability curve is independent of $A$ (§3.3.2.3). The maximum growth rate is initially $\mathrm{Re}\{\hat{\sigma}\} = 1$, which is attained at $\alpha = \beta = 0$. As $A$ increases, a mode with horizontal wavenumber $\beta = 0.5$ and $\alpha > 0$ becomes increasingly unstable. For $A \gtrsim 17.2$ $(c,d)$, this mode has a growth rate that is greater than 1.

#### 3.3.2.2 Numerical solutions that incorporate smaller scales

We incorporated the effects of smaller horizontal modes on the stability of the flow by retaining more terms in the Fourier sum in (3.12) and solving (3.15) numerically. We found eigenvalues $\sigma$ by truncating the infinite sum in (3.15) to $-N \leqslant n \leqslant N$, for some integer $N(\alpha, \beta, A)$, which was increased until the relative error in the eigenvalue with the largest real part (growth rate) was less than $10^{-5}$. We denote the eigenvalue with the largest real part $\hat{\sigma}(\alpha, \beta, A)$.

Figure 3.2 shows contour plots of the growth rate $\mathrm{Re}\{\hat{\sigma}\}$ against the vertical

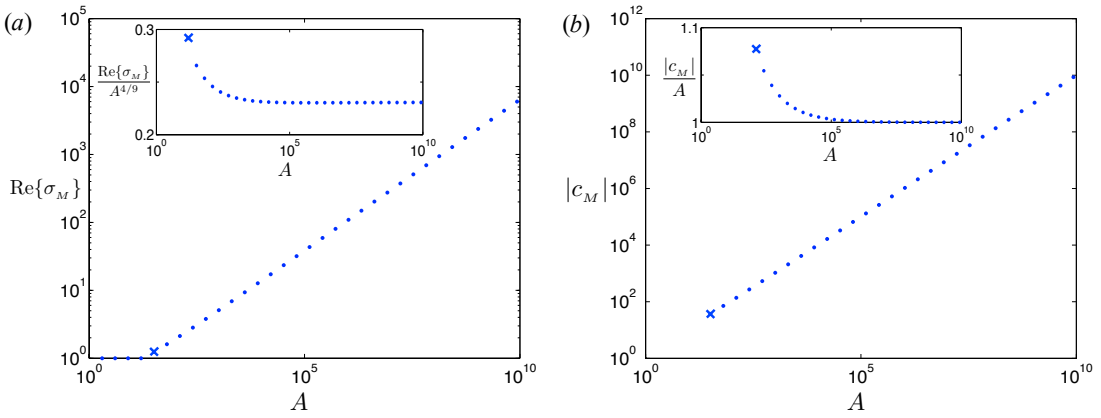


Figure 3.3: $(a)$ The maximum growth rate $\mathrm{Re}\{\sigma_{_M}\}$, which asymptotically scales like $A^{4/9}$ as shown in the inset, and $(b)$ the magnitude of the corresponding phase speed $c_{_M} = -\mathrm{Im}\{\sigma_{_M}\}/\alpha_{_M}$, which tends to the maximum background velocity $A$ asymptotically, as shown in the inset. The cross signifies the first data point after the change of most unstable mode at $A \approx 17.2$.

and horizontal wavenumbers $\alpha$ and $\beta$, for different values of $A$. For all $A$, we find that the growth rate is negative for $\alpha > 1/2$, and this range is therefore not shown. We also recall that we only need to consider values of $\beta$ in the range $0 \leqslant \beta \leqslant 1/2$ due to the symmetries of the system.

Figure 3.2 reveals three interesting features. First, the marginal-stability curve $\mathrm{Re}\{\hat{\sigma}\} = 0$ appears to be independent of the amplitude $A$. This observation is confirmed analytically in §3.3.2.3. Second, for $A \lesssim 17.2$, the most unstable mode occurs at $\alpha = \beta = 0$ and has constant growth rate $\mathrm{Re}\{\hat{\sigma}\} = 1$, which is the same as the case $A = 0$ discussed above in §3.3.2.1. Third, a new mode with $\beta = 1/2$ and $\alpha > 0$ becomes increasingly unstable as $A$ is increased, and, for $A \gtrsim 17.2$ (figure 3.2*c,d*), the new mode has a growth rate that exceeds that of the zero-wavenumber mode. For all higher values of $A$, this mode is the most unstable.

The most unstable mode is defined by the wavenumbers $(\alpha_{_M}(A), \beta_{_M}(A))$ that maximize the growth rate $\mathrm{Re}\{\hat{\sigma}(\alpha, \beta, A)\}$ over $\alpha$ and $\beta$. We label the most unstable mode as $\sigma_{_M}(A) = \hat{\sigma}(\alpha_{_M}, \beta_{_M}, A)$, and the corresponding cut-off value for convergence of the Fourier sum in (3.12) as $N_{_M}(A) = N(\alpha_{_M}, \beta_{_M}, A)$.

The maximum growth rate $\mathrm{Re}\{\sigma_{_M}\}$ and the phase speed $c_{_M} = -\mathrm{Im}\{\sigma_{_M}\}/\alpha_{_M}$

are shown in figure 3.3. The change in the most unstable mode at $A \approx 17.2$ can be observed as the point where the maximum growth rate begins to increase and the phase speed becomes non-zero. Both $\mathrm{Re}\{\sigma_{_M}\}$ and $|c_{_M}|$ show an asymptotic power-law dependence on $A$, which is very well fitted by

$$\mathrm{Re}\{\sigma_{_M}\} = 0.231A^{4/9}, \qquad c_{_M} = \pm A \qquad \text{as} \quad A \to \infty. \tag{3.17a, b}$$

The most unstable mode, therefore, propagates at the maximum speed of the background flow, either up or down depending on the alignment of the perturbation (see §3.3.2.4 below). (In fact, we find that the magnitude of the phase speed for all unstable modes with $\alpha > 0$ is asymptotically given by $A$, while that of the stable modes is zero.)

The wavenumbers of the most unstable mode are both zero for $A \lesssim 17.2$. At $A \approx 17.2$, the vertical wavenumber $\alpha_{_M}$ becomes non-zero, and gradually decreases as $A$ increases further (figure 3.4*a*). Asymptotically, $\alpha_{_M}$ is very well fitted by

$$\alpha_{_M} = 0.332A^{-1/9} \quad \text{as} \quad A \to \infty. \tag{3.18}$$

The corresponding horizontal wavenumber $\beta_{_M}$ is $1/2$ for all $A \gtrsim 17.2$, as suggested by the results of figure 3.2, which means that the most unstable perturbation has twice the wavelength of the background flow.

The cut-off value $N_{_M} = N(\alpha_{_M}, \beta_{_M}, A)$ increases like $A^{2/9}$ for large $A$ (figure 3.4*b*). Since larger wavenumbers in the Fourier sum in (3.12) describe shorter horizontal scales, the need to increase $N_{_M}$ for convergence suggests that the smallest horizontal scales of the most unstable perturbation decrease like

$$N_{_M}^{-1} \sim A^{-2/9} \quad \text{as} \quad A \to \infty. \tag{3.19}$$

In §3.4, we confirm that the truncated Fourier sum remains an accurate representation of the solution by comparison with an asymptotic expansion of the differential equations (3.11).

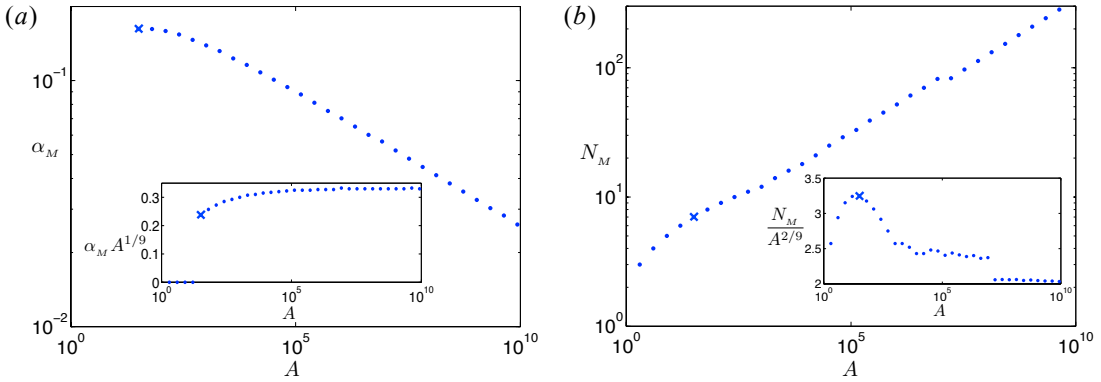


Figure 3.4: $(a)$ The vertical wavenumber $\alpha_{_M}$ of the most unstable mode, which asymptotically scales like $A^{-1/9}$ as shown in the inset, and $(b)$ the cut-off $N_{_M} = N(\alpha_{_M}, \beta_{_M}, A)$ for the Fourier sum in (3.12), which asymptotically scales like $A^{2/9}$ as shown in the inset. The origin of the discontinuity at $A \approx 10^7$ is unclear. The cross signifies the first data point after the change of most unstable mode at $A \approx 17.2$.

#### 3.3.2.3 Marginal stability

The results of figure 3.2 suggest that the marginal-stability curve is independent of the amplitude $A$. Here we verify this suggestion analytically.

Marginal stability occurs when $\mathrm{Re}\{\hat{\sigma}\} = 0$. Numerical results for general $A > 0$ suggest that the eigenvector $\boldsymbol{G}$ corresponding to the marginally stable modes takes the simple form $G_{-1} = \pm G_0$, and $G_n = 0$ for $n \neq 0, -1$. Motivated by this observation, and the corresponding form of $F_n$ from (3.13a), we consider eigenvectors $[F, G]$ of the form

$$F = \pm\left[\sin\beta X + \sin(1-\beta)X\right], \qquad G = \mp\left[\cos\beta X + \cos(1-\beta)X\right]. \quad (3.20a, b)$$

On substituting (3.20) into the advection-diffusion equation (3.11$b$), we obtain

$$\left[\sigma + \left(\beta^2 + \alpha^2 - \beta\right)\right] G = \mathrm{i}\alpha A\left[\sin X F - \cos X G\right], \quad (3.21)$$

which, by using double-angle formulae and (3.20), reduces to

$$\left[\sigma + \left(\beta^2 + \alpha^2 - \beta\right)\right] = \pm\mathrm{i}\alpha A. \quad (3.22)$$

The eigenfunctions (3.20) must also satisfy Poisson's equation (3.11*a*); this gives the requirement that

$$\beta = \beta^2 + \alpha^2, \tag{3.23}$$

which is precisely the marginal-stability relationship for $A = 0$ given in (3.16). Combining (3.22) and (3.23) gives

$$\sigma = \pm \mathrm{i}\alpha A, \tag{3.24}$$

which corresponds to a phase speed of $|c| = A$ and a growth rate of zero.

The marginal-stability curve (3.23) is, therefore, independent of $A$, as are the corresponding eigenfunctions $[F, G]$ (3.20), provided $A > 0$. Interestingly, the eigenfunctions do differ from those for $A = 0$, which are pure Fourier modes with wavenumber $\beta$; the presence of background flow with unit wavenumber introduces an additional component to the marginally stable perturbation with wavenumber $1 - \beta$.

#### 3.3.2.4 Structure of the most unstable perturbation

For $A \lesssim 17.2$, the most unstable mode has $\alpha_{_M} = \beta_{_M} = 0$, growth rate $\mathrm{Re}\{\sigma_{_M}\} = 1$ and phase speed $c_{_M} = 0$. The instability takes the form of a roll-like perturbation of the background temperature gradient, with a wavelength that is independent of the background columnar flow. At $A \approx 17.2$, a different mode becomes the most unstable, which has half the horizontal wavenumber of the background flow $\beta_{_M} = 1/2$. The vertical wavenumber and phase speed of this mode are also both non-zero.

Figure 3.5 shows the structure of the most unstable mode for $A = 2^5 = 32$ (figure 3.5*a,c*) and $A = 2^{20} \approx 10^6$ (figure 3.5*b,d*). The perturbation takes the form of tall, thin, counter-rotating rolls (figure 3.5*a,b*; right-hand plots). Each roll has width $2\pi$, and is centred on a downwelling of the background columnar flow. The whole perturbation has horizontal period $4\pi$. The temperature perturbation $\widetilde{\Theta}$ takes the form of claw-shaped pulses centred on the upwellings of the background flow (figure 3.5*a*; left-hand plot), which, for larger amplitudes (figure 3.5*b*; left-hand plot), split into two neighbouring pulses of the same sign.

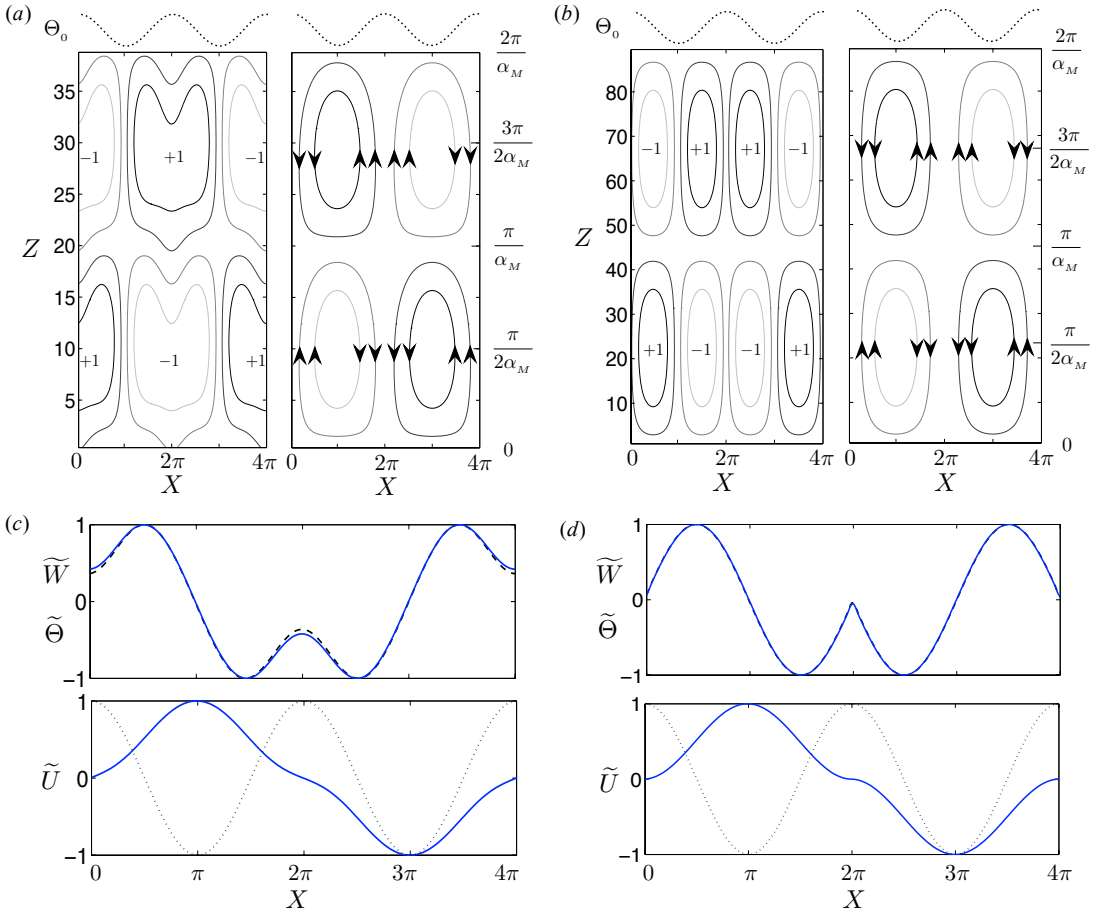


Figure 3.5: The structure of the most unstable perturbation $(a,c)$ for $A = 2^5$ and $(b,d)$ for $A = 2^{20}$. Panels $(a)$ and $(b)$ show contours of the perturbation temperature $\widetilde{\Theta}$ (left) (scaled to unit amplitude), at intervals of 0.4, and streamlines (right) with arrows showing the direction of the flow, together with schematic profiles of the background flow $\Theta_0 = W_0$ (top). The perturbation is doubly periodic, with horizontal period $4\pi$ and vertical period $2\pi/\alpha_{_M}$. Panels $(c)$ and $(d)$ show horizontal profiles of the perturbation quantities (scaled to unit amplitude): upper plots show the temperature $\widetilde{\Theta}$ (solid) and vertical velocity $\widetilde{W} = -\partial\widetilde{\Psi}/\partial X$ (dashed) at $Z = \pi/2\alpha_{_M}$; lower plots show the horizontal velocity $\widetilde{U} = \partial\widetilde{\Psi}/\partial Z$ (solid) at $Z = \pi/\alpha_{_M}$ together with the background columnar flow $\Theta_0$ (dotted) scaled by $A$. The vertical velocity and temperature perturbations are almost indistinguishable. The perturbations shown here propagate upwards; the same perturbations shifted horizontally by $\pi$ would propagate downwards and have the same growth rate.

The vertical velocity $\widetilde{W}$ and temperature $\widetilde{\Theta}$ of the dominant perturbation (figure 3.5*c,d*) are symmetric about $X = 2n\pi$ for integer $n$, and are almost indistinguishable from each other. As $A$ increases, the profiles of $\widetilde{\Theta}$ and $\widetilde{W}$ become increasingly sinusoidal in the intervals $(2n\pi, 2(n+1)\pi)$, but their gradients change by an $O(1)$ amount through increasingly narrow regions centred on $X = 2n\pi$. The horizontal velocity $\widetilde{U}$ either diverges away from or converges into these regions.

The perturbations shown in figure 3.5 have a phase speed $c_{_M} = A$ to leading order, and thus move upwards at the maximum speed of the background flow. If the perturbation were shifted horizontally by $\pi$, the pulses would be centred on the downwellings of the background flow and the phase speed would be $c_{_M} = -A$; the growth rate and vertical wavenumber would be unchanged.

## 3.4 Asymptotic analysis of linear stability for $A \gg 1$

Motivated by the structure of the most unstable perturbation as just described, and in order to understand the physical balances behind the instability, we examine the linear stability of heat-exchanger flow in the asymptotic limit $A \gg 1$. In this limit, the dominant balance in the advection–diffusion equation (3.11*b*) is most obviously between horizontal advection of the background temperature by the perturbation $\sim \alpha A \sin XF$ and vertical advection of the perturbation flow by the background velocity $\sim \alpha A \cos XG$. However, the perturbation plotted in figure 3.5(*d*) shows that advection cannot dominate everywhere; the temperature gradient changes by an $O(1)$ amount through regions centred on $X = 2n\pi$ for integer $n$, which suggests the presence of boundary layers in which horizontal diffusion enters the leading-order balance.

We first observe that the linearized governing equations (3.11) exhibit a number of symmetries. Suppose that, for a given eigenvalue $\sigma(A, \alpha)$, we have solutions $[F(X), G(X)]$. It is clear from the form of (3.11) that $[-F(-X), G(-X)]$, $[F(2\pi + X), G(2\pi + X)]$, and $[-F(2\pi - X), G(2\pi - X)]$ are all also solutions, as are any linear combinations of these. Thus we are free to construct solutions with any given reflectional symmetry around $X = 0$ and $X = \pm\pi$. Therefore,

motivated by the symmetries of the most unstable mode shown in figure 3.5, we consider a solution $[F, G]$ in which $G$ is even under reflection about $X = 0$ and odd under reflection about $X = \pm\pi$, and $F$ is odd under reflection about $X = 0$ and even under reflection about $X = \pm\pi$. Such a solution is periodic with period $4\pi$.

As discussed above, we anticipate boundary-layer regions located near $X = 2n\pi$, for integer $n$, in which horizontal diffusion ($G''$) enters the leading-order balance in (3.11$b$). We therefore look for an asymptotic solution over the range $0 \leqslant X \leqslant 2\pi$, which has the symmetries of $[F, G]$ discussed above, with an inner region near $X = 0$ where diffusion is important, and an outer region away from $X = 0$ where the advection terms dominate.

In order to motivate the asymptotic scalings, we also recall the measured scalings from the full Floquet analysis of §3.3 for the growth rate $\mathrm{Re}\{\sigma\} \sim A^{4/9}$, the phase speed $c_{_M} = -\mathrm{Im}\{\sigma\}/\alpha_{_M} = A$, and the vertical wavenumber $\alpha_{_M} \sim A^{-1/9}$ (see 3.17 and 3.18).

### 3.4.1 Asymptotic expansion

We consider the limit of large amplitude $A$ and of small vertical wavenumber $\alpha$, such that $\alpha A \gg 1$ and $\alpha \ll 1$, and we try

$$\sigma = -\mathrm{i}\sigma_0 \alpha A + \sigma^*, \tag{3.25}$$

where $|\sigma^*| \ll \alpha A$, and $\sigma_0$ is an $O(1)$ constant to be determined. The perturbation equations (3.11) can be rewritten as

$$F'' + G' = \alpha^2 F, \qquad \mathrm{i}\alpha A\,(\cos X - \sigma_0)\,G - \mathrm{i}\alpha A \sin X F + \sigma^* G + F' = G'' - \alpha^2 G. \tag{3.26$a$, $b$}$$

The boundary conditions come from the symmetries of the solution as discussed above, and are given by

$$F(0) = G'(0) = G(\pi) = F'(\pi) = 0. \tag{3.27}$$

Based on the limits $\alpha A \gg 1$, $\alpha \ll 1$, the leading-order behaviour of (3.26)

away from $X = 0$ is given by

$$F' + G = c_0, \qquad (\cos X - \sigma_0)\, G - \sin X F = 0, \tag{3.28a, b}$$

where $c_0$ is a constant of integration that comes from the first integral of (3.26$a$). Equation (3.28) has solutions

$$F = (\cos X - \sigma_0)\left(1 + c_0 \int \frac{dX}{\cos X - \sigma_0}\right), \quad G = \sin X \left(1 + c_0 \int \frac{dX}{\cos X - \sigma_0}\right), \tag{3.29a, b}$$

where, without loss of generality, the arbitrary amplitude of the perturbations has been scaled to unity. Based on the form of the numerical solutions in figure 3.5, we assume that there are no leading-order discontinuities in $F$ at $X = 0$ or in $G$ at $X = \pi$. The boundary conditions (3.27) thus imply that $\sigma_0 = 1$ and that $c_0 = 0$, such that the leading-order outer solutions are given by

$$F = \cos X - 1, \qquad G = \sin X. \tag{3.30a, b}$$

The leading-order phase speed $c = -\mathrm{Im}\{\sigma\}/\alpha = \sigma_0 A$ is given by $c = A$, as we found numerically in (3.17$b$)

Since $\sigma_0 = 1$, the coefficients $\cos X - \sigma_0$ and $\sin X$ of the $O(\alpha A)$ terms in (3.26$b$) both vanish as $X \to 0$, which suggests an inner boundary-layer region there, as indicated by the numerical solutions. We look for a balance in (3.26$b$) between the advection terms, horizontal diffusion $G''$ and growth $\sigma^* G$. This balance gives $\alpha A X^2 G \sim \alpha A X F \sim \sigma^* G \sim G/X^2$. From (3.30$b$), we also have that $G \sim X$ as $X \to 0$. Based on these balances, we define the following inner variables:

$$\xi = (\alpha A)^{1/4} X; \quad s = (\alpha A)^{-1/2} \sigma^*; \quad g(\xi) = (\alpha A)^{1/4} G(X); \quad f(\xi) = (\alpha A)^{1/2} F(X). \tag{3.31a, b, c, d}$$

Rewritten in terms of the inner variables, the governing equations (3.26) be-

come

$$f'' + g' = \alpha^2 (\alpha A)^{-1/2} f, \qquad g'' - \left( s - \frac{\mathrm{i}\xi^2}{2} \right) g + \mathrm{i}\xi f = (\alpha A)^{-1/2} \left( f' + \alpha^2 g \right). \tag{3.32a, b}$$

At leading-order,

$$f' + g = \gamma_0, \qquad g'' - \left( s - \frac{\mathrm{i}\xi^2}{2} \right) g + \mathrm{i}\xi f = 0. \tag{3.33a, b}$$

The constant of integration $\gamma_0$ in (3.33$a$) is determined by matching with the outer region: by integrating (3.26$a$) and substituting from (3.30$a$), we obtain to leading order

$$F' + G = \alpha^2 \int_{\pi}^{X} (\cos X - 1) \, \mathrm{d}X = \alpha^2 (\sin X - X + \pi), \tag{3.34}$$

where the lower limit of the integral has been determined from the boundary conditions (3.27$c$,$d$). The right-hand side of (3.34) is given by $\alpha^2 \pi$ to leading order as $X \to 0$, which, together with the inner scalings (3.31$c$,$d$), determines the constant of integration in (3.33$a$) as

$$\gamma_0 = \alpha^2 (\alpha A)^{1/4} \pi = \left( \alpha A^{1/9} \right)^{9/4} \pi. \tag{3.35}$$

The boundary conditions for (3.33) are given by the two symmetry conditions (3.27$a$,$b$) $f(0) = g'(0) = 0$ and a matching condition that $g \to \xi$ as $\xi \to \infty$. In appendix 3.A, we consider the generic behaviour of the solutions of (3.33), and find that the matching condition constitutes two constraints on the differential equation; we therefore have four conditions on a third-order system, which is sufficient to determine the unknown eigenvalue $s$. We solve (3.33) numerically, and determine $s$ as a function of the rescaled vertical wavenumber

$$\alpha^* \equiv \alpha A^{1/9}, \tag{3.36}$$

(cf. 3.35). The leading-order growth rate is then given by $\mathrm{Re}\{\sigma^*\} =$

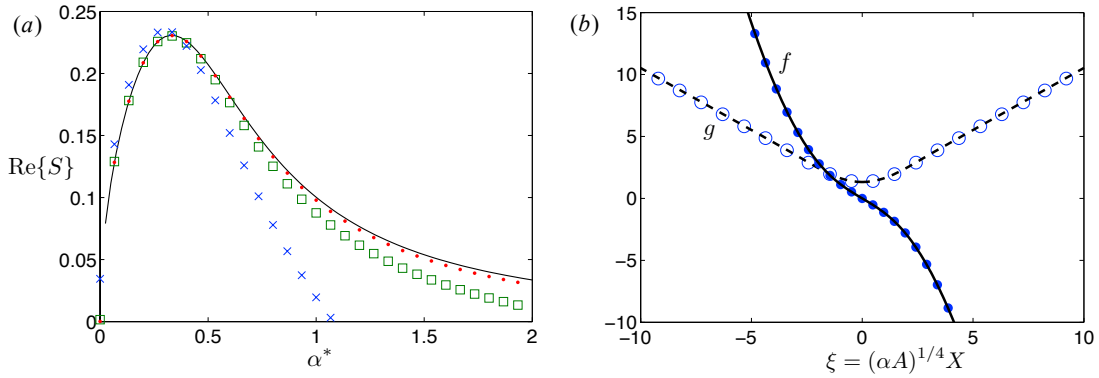


Figure 3.6: Asymptotic solutions ($A \gg 1$) and full numerical solutions of the eigenvalue problem (3.15). ($a$) The leading-order scaled growth rate $\mathrm{Re}\{S\} = \alpha^{*1/2}\mathrm{Re}\{s\} = A^{-4/9}\mathrm{Re}\{\sigma^*\}$ against the scaled vertical wavenumber $\alpha^* = \alpha A^{1/9}$: the asymptotic solution (line), and the full numerical solutions for $A = 2^{10}$ (crosses), $A = 2^{20}$ (squares), and $A = 2^{30}$ (dots). ($b$) The solution $[f, g] = [(\alpha A)^{1/2}F, (\alpha A)^{1/4}G]$ (solid and dashed lines, respectively) of (3.33), together with full solutions of (3.15) for $A = 2^{30}$ (solid and hollow circles, respectively).

$(\alpha A)^{1/2}\,\mathrm{Re}\{s(\alpha^*)\}$ from (3.31$b$), or alternatively

$$\mathrm{Re}\{\sigma^*\} = A^{4/9}\mathrm{Re}\{S(\alpha^*)\}, \quad \text{where} \quad S(\alpha^*) = \alpha^{*1/2}s(\alpha^*). \tag{3.37}$$

Numerical solutions for the leading-order scaled growth rate $\mathrm{Re}\{S(\alpha^*)\}$ are shown in figure 3.6($a$). The eigenvalue with the maximum growth rate is given by $S = 0.2308 - 0.182\mathrm{i}$ and occurs at $\alpha^* = 0.332$, such that $\mathrm{Re}\{\sigma^*\} = 0.2308A^{4/9}$ at $\alpha = 0.332A^{-1/9}$. These values agree extremely well with the measurements presented in figures 3.3($a$) and 3.4($a$) for the maximum growth rate $\mathrm{Re}\{\sigma_{_M}\}$ and the corresponding vertical wavenumber $\alpha_{_M}$, respectively. Since the imaginary part of $S$ is negative, the second-order correction to the phase speed is positive, and is given by $-\mathrm{Im}\{\sigma^*\}/\alpha = 0.55A^{5/9}$. The dependence of $\mathrm{Re}\{S\}$ on the wavenumber $\alpha^*$ (figure 3.6$a$) shows very good agreement between the asymptotic analysis and the full solutions of the Floquet analysis for large $A$, as do the eigenfunctions $[f, g]$ of (3.33), which give the leading-order behaviour of $[F, G]$ near $X = 0$ (figure 3.6$b$).

The leading-order growth rate $\mathrm{Re}\{S(\alpha^*)\}$ increases for small $\alpha^*$ and decreases

for large $\alpha^*$ (figure 3.6*a*). In appendix 3.B, in order to understand this behaviour, we analyse the leading-order equations for the inner region (3.33) in the asymptotic limits $\alpha^* \ll 1$ and $\alpha^* \gg 1$. The physical basis for the decay in the growth rate at small and large $\alpha^*$ is discussed below.

### 3.4.2 Physical mechanism of instability for $A \gg 1$

It has proved difficult to unravel the precise details of the physical mechanism of instability, largely owing to the fact that the growth rate depends on a subtle second-order interaction between boundary-layer regions and the main flow. However, based on the form of the asymptotic equations, we can make various observations about the relevant physical components that control the propagation and growth of perturbations.

The leading-order evolution of the most unstable perturbation for $A \gg 1$ is neutral propagation at speed $c = \pm A$, which is the maximum speed of the background flow. The neutral propagation is the result of a leading-order advective balance between two processes: horizontal advection of the background temperature field $\Theta_0$ by the perturbation velocity $\widetilde{U}$, and vertical advection of the perturbation temperature field $\widetilde{\Theta}$ by the background velocity $W_0$. We illustrate this balance by working in a frame of reference moving with the perturbation, as sketched in figure 3.7. We consider an upwards propagating perturbation ($c = +A$), but the discussion equally applies to downwards propagating perturbations. Since the vertical wavenumber $\alpha^*$ is small, Darcy's law implies that the perturbation temperature $\widetilde{\Theta}$ and vertical velocity $\widetilde{W}$ are proportional. By mass conservation, the horizontal velocity $\widetilde{U}$ is strongest where the vertical variation of $\widetilde{W}$ is largest, which occurs where $\widetilde{W}$ vanishes. The perturbation flow therefore takes the form of tall thin circulating cells. Horizontal advection of $\Theta_0$ by $\widetilde{U}$ leads to an induced temperature perturbation (shown dashed on the right-hand side of figure 3.7) that is vertically out of phase with the original temperature perturbation. Downwards vertical advection of the induced temperature perturbation by the background flow $W_0$ (in this propagating frame) balances the horizontal advection in such a way that the original perturbation is sustained.

The leading-order advective balance gives a neutrally propagating mode.

Growth occurs because of horizontal diffusion in the thin boundary-layer regions centred on the lines $X = 2n\pi$, across which the temperature gradient changes significantly. The importance of diffusion can be seen by an examination of (3.33$b$), which shows that the two advective processes described above are balanced by diffusion ($g''$) and growth ($sg$) in these boundary-layer regions. Indeed, (3.33$b$) also shows that the advective processes, which have imaginary coefficients, and diffusion, which has a real coefficient, are vertically out of phase, so that we might expect the rescaled eigenvalue $s$ to have both a non-zero imaginary part, which gives a correction to the phase speed, and a non-zero real part, which gives growth.

The strength of diffusion, which must determine the growth rate, depends on the rescaled vertical wavenumber $\alpha^*$. We found in §3.4.1 that the growth rate decreases at both large and small $\alpha^*$ (figure figure 3.6$a$). For $\alpha^* \ll 1$, the perturbation cells are very long, and, by continuity, the horizontal velocity is weak. The boundary-layer regions, which have a width that is set by the strength of the horizontal advection, are therefore wider (as in (3.31$a$)), so the diffusive flux is weaker, and the growth rate decreases. Conversely, for $\alpha^* \gg 1$, the horizontal velocity is strong. In this limit, the perturbation in the boundary-layer regions takes a different form: the temperature is smoothed out by strong horizontal advection, and the leading-order advective balance no longer gives discontinuities in the temperature gradient (see appendix 3.B). Owing to this smoothed temperature profile, diffusion only enters the balance at higher order, and so both the diffusive flux and the growth rate decrease. We therefore find that there is a balance between diffusion being too weak for $\alpha^* \ll 1$ and horizontal velocity being too strong for $\alpha^* \gg 1$, which gives rise to an optimal wavenumber $\alpha^* = 0.332$ at which the growth rate is maximum.

Interestingly, the instability process discussed above is independent of the background linear temperature gradient. Indeed, the analysis of §3.4.1 shows that the term describing advection of the background temperature gradient ($F'$) does not enter the asymptotic equations. This contrasts with the control of the instability for small $A$ by the background temperature gradient.

Another interesting implication of the above discussion is that thermal diffusion provides a destabilizing mechanism for the flow. In appendix 3.C, we examine

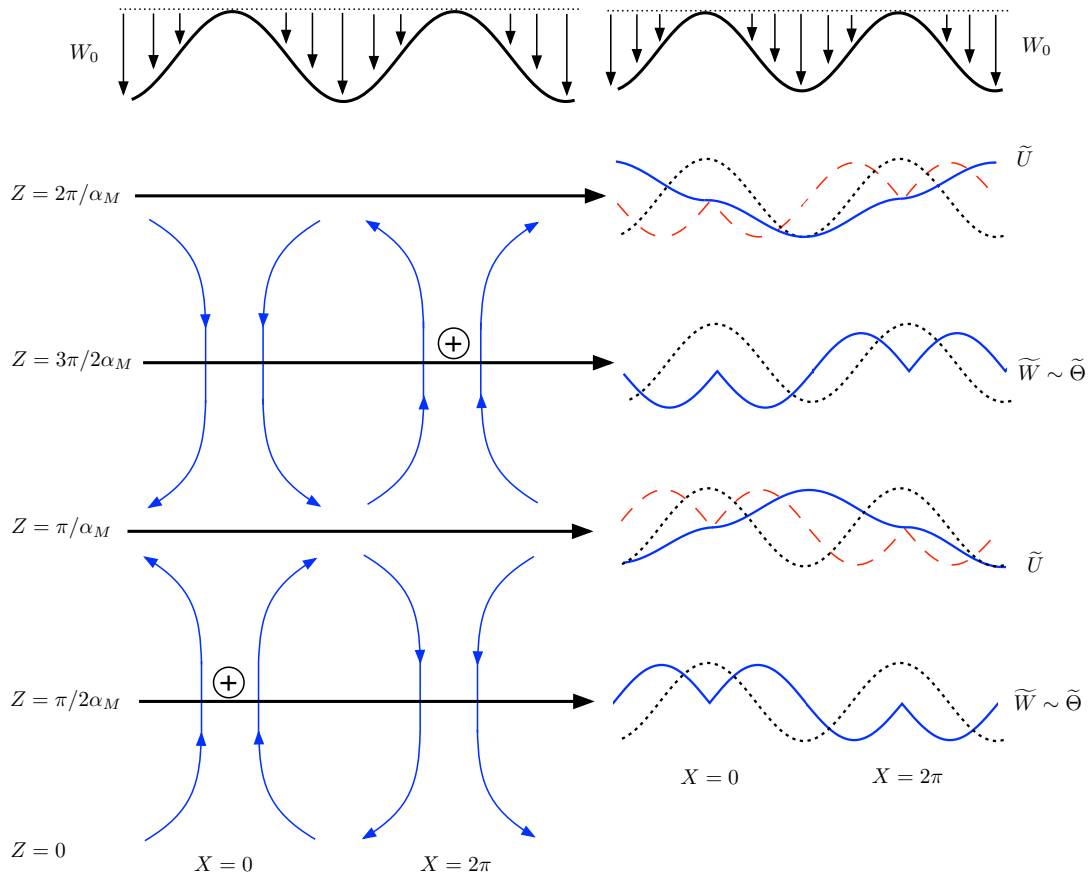


Figure 3.7: A schematic of the instability for $A \gg 1$, in a frame of reference moving with the perturbation. The background vertical velocity $W_0 = A\cos X - A$ in this frame is shown at the top. The left-hand side shows streamlines of the perturbation flow; the perturbation temperature $\widetilde{\Theta}$ is proportional to the vertical velocity $\widetilde{W}$, and locations at which pulses form on the background columns as a result of the instability are marked with a $\oplus$. The right-hand side shows horizontal profiles (all scaled to unit amplitude) along the lines of constant $z$ as marked. Each plot shows the background temperature field $\Theta_0$ (dotted), together with one of the perturbation velocities (solid) as labelled on the right; in each plot, the velocity not shown is zero. The plots at $Z = \pi/\alpha_{_M}$ and $Z = 2\pi/\alpha_{_M}$ also show the induced temperature perturbations (dashed) that result from horizontal advection of the background field $\Theta_0$ by $\widetilde{U}$. The neutral propagation of the perturbation is sustained by downwards advection of the induced temperature perturbation by the background velocity $W_0$.

a related system of columnar-exchange flow of two fluids of different densities in the absence of diffusion, and we find that the flow is always neutrally stable. This observation supports the idea that diffusion is required for the growth of perturbations. There is some parallel between the role of thermal diffusion here and the role of viscosity in the stability of plane Poiseuille flow (e.g. Drazin 2002), where the flow is linearly unstable for sufficiently large Reynolds numbers, but is linearly stable in the inviscid limit.

## 3.5 Evolution of the instability in the non-linear regime

In order to explore the development of the instability beyond the linear regime, we examined heat-exchanger flow using high-resolution direct numerical simulations. We set the temperature $\Theta = \Theta_0 + \widetilde{\Theta}$ to be the steady heat-exchanger solution $\Theta_0 = A\cos X - Z$, as in (3.8$a$), plus an initially small perturbation $\widetilde{\Theta}(X, Z, \tau)$, and then solved the non-linear governing equations (3.7) for the evolution of $\widetilde{\Theta}$ numerically. In order to clearly observe the non-linear evolution of the instability, we used doubly periodic boundary conditions for $\widetilde{\Theta}$ and for the corresponding streamfunction $\widetilde{\Psi}$ (given by 3.7$a$). We used a vertical period of $2\pi/\alpha_{_M} \approx 18.9A^{1/9}$, which is the height of the most unstable mode calculated in §3.3. The initial value of $\widetilde{\Theta}$ was proportional to the most unstable mode.

Snapshots of the temperature field $\Theta$ at different times for $A = 2^8 = 256$ and horizontal period $L = 8\pi$ are shown in figure 3.8($a$–$d$), together with the corresponding magnitude of the perturbation over time (figure 3.8$e$) and dominant wavenumber of the flow (figure 3.8$f$). The linear growth of the instability leads to the formation of pulses (figure 3.8$a$) which move with the background flow. Once the pulses have reached a certain size, the amplitude stops growing, and the flow becomes unstable to a secondary instability, which breaks the symmetry of the solution and results in less regular motion (figure 3.8$b$,$c$). The system gradually re-organizes into columnar flow with a quarter of the wavenumber of the original flow (figure 3.8$d$), but the same background temperature gradient, which remains imposed by the representation $\Theta = \Theta_0 + \widetilde{\Theta}$.

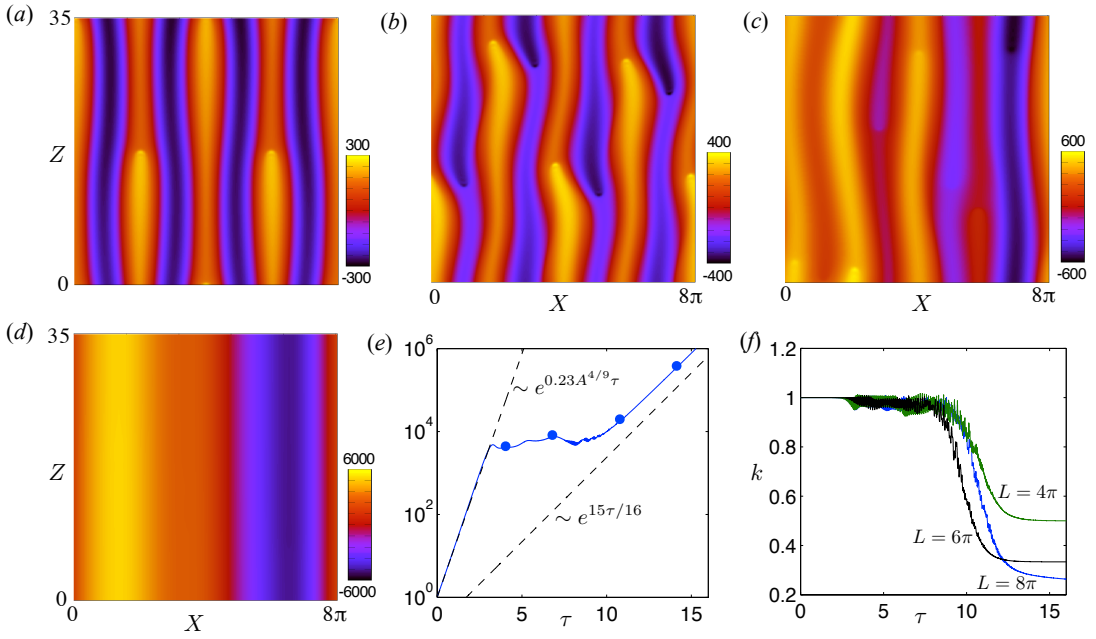


Figure 3.8: Nonlinear dependence of the instability for $A = 2^8$ and horizontal period $L = 8\pi$. Snapshots of the temperature field $\Theta(X, Z, \tau)$ at times: $(a)$ $\tau = 4$, the growth of pulses on the background flow that result from linear instability; $(b)$ $\tau = 7$ and $(c)$ $\tau = 11$, the secondary instability; and $(d)$ $\tau = 14$, the growing heat-exchanger flow with a quarter of the original wavenumber (3.38). Panel $(e)$ shows the magnitude of the perturbation over time, as measured by the L2 norm and scaled by the initial magnitude; dots correspond to the pictures in the previous panels. The asymptotic growth of the most unstable mode (from (3.17$a$)) and the growth of the unsteady exchange flow (3.38) are also shown, for comparison. Panel $(f)$ shows the dominant wavenumber $k$ of the flow (measured by a Fourier transform of the temperature field at $Z = 0.5$), for simulations with different horizontal periods $L$ as marked; in each case, the wavenumber decreases towards the fundamental mode $2\pi/L$.

However, the wavenumber and background gradient of a steady heat-exchanger flow are linked by (3.5$a$); hence if the wavenumber decreases and the gradient is fixed, the flow can no longer be a steady solution of the governing equations. Instead, we find that the amplitude of the flow grows exponentially (figure 3.8$e$). It is straightforward to show that the governing equations permit unsteady columnar flow with a fixed background temperature gradient for any

wavenumber $\kappa$; this generalized time-dependent columnar flow is given by

$$\Theta = Ae^{(1-\kappa^2)\tau}\cos\kappa X - Z, \qquad W = Ae^{(1-\kappa^2)\tau}\cos\kappa X, \tag{3.38$a$, $b$}$$

for any amplitude $A$. The steady solution $\kappa = 1$ (3.8) can be thought of as the marginally stable solution: if $\kappa > 1$, horizontal diffusion dominates and the amplitude decays; if $\kappa < 1$, advection dominates and the amplitude grows. In the results of figure 3.8, the system ultimately adopts a wavenumber $\kappa = 1/4$, and the magnitude of the flow grows like $e^{15\tau/16}$ (figure 3.8$e$). We note that the continued exponential growth at late times only arises because it can feed off the fixed background temperature gradient that is imposed in an effectively infinite domain.

The main conclusion from this calculation is that the non-linear evolution of the instability leads to a reduction of the wavenumber of the flow. We have also carried out simulations in domains with different horizontal periods $L$; in each case the flow coarsened due to a secondary instability, leaving one upwelling and one downwelling column in the domain (figure 3.8$f$).

## 3.6 Implications for two-dimensional convection in a porous medium

In this section, we return to the linear-stability analysis of §3.3 and consider the implications of this analysis for columnar flow in a vertically confined domain. Specifically, we investigate whether stability might provide the mechanism that controls the horizontal scale of the columnar flow in the interior of a two-dimensional Rayleigh–Darcy cell at high $Ra$.

### 3.6.1 The wavenumber of columnar flow in a Rayleigh–Darcy cell at high $Ra$

Flow in a Rayleigh–Darcy cell for $Ra \gtrsim 1300$ is dominated in the interior by columnar flow. This nearly steady interior flow is fed from the upper and lower boundaries of the cell by vigorous mixing and merging of short-wavelength pro-

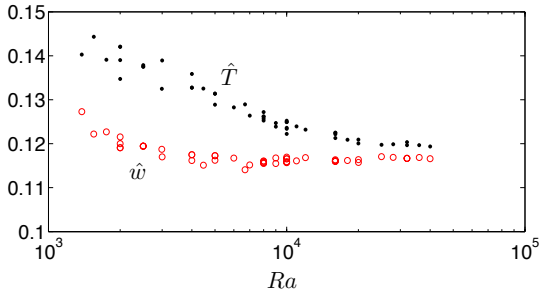


Figure 3.9: Measurements of the amplitude of the temperature $\hat{T}$ (dots) and vertical velocity $\hat{w}$ (circles) of the columnar flow in the interior of a Rayleigh–Darcy cell (adapted from figure 2.7). The amplitudes appear to tend to approximately the same constant value, $\hat{T}, \hat{w} \to 0.117$, as $Ra \to \infty$. (This result is directly equivalent to the asymptotic 'classical' linear scaling of the Nusselt number with $Ra$, as observed in chapter 2) For comparison with the linear-stability analysis, we choose $\widehat{A} = \hat{w}$.

toplumes (see figure 3.1*a*). The numerical measurements presented in chapter 2, which are taken from a cell of height $H = 1$ for the range $1300 \leqslant Ra \leqslant 4 \times 10^4$, suggest that the columnar flow in the interior of the cell is increasingly well described by the steady heat-exchanger solution in (3.5) as $Ra \to \infty$. Measurements of the dominant wavenumber $k$ over the same range were approximated by $k \approx 0.47 Ra^{0.4}$, although there are significant fluctuations in the data, and there is some suggestion of a slightly weaker exponent at very large $Ra$ (see §2.4.1.2).

It is important to note that there are some significant differences between the columnar flow in a Rayleigh–Darcy cell at high $Ra$ and the steady unconfined heat-exchanger flow that has been the subject of this paper so far. Most notably, the cell has a finite height, and the flow in the interior is fed by time-dependent proto-plumes at the upper and lower boundaries as discussed above, whereas the heat-exchanger flow (3.5) has an infinite height, and any disturbances propagate indefinitely. It is, nonetheless, interesting to try applying some of the results from the stability of unconfined heat-exchanger flow to the flow in a vertically confined domain, and to compare the resultant scalings of this simple analysis with numerical measurements of the dominant wavenumber $k$.

In ideal heat-exchanger flow, the amplitude of the temperature and vertical velocity are equal, as in (3.5). In a Rayleigh–Darcy cell, the numerical measure-

ments presented in chapter 2 show that the amplitude of the temperature $\hat{T}$ and vertical velocity $\hat{w}$ tend to approximately the same constant value, $\hat{T}, \hat{w} \to 0.117$, as $Ra \to \infty$. However, for finite $Ra$, $\hat{T}$ is somewhat larger than $\hat{w}$ (figure 3.9). There is, therefore, an ambiguity about which measurement to use. Since $\hat{w}$ varies less than $\hat{T}$ over the measured range of $Ra$, we choose to set $\widehat{A} = \hat{w}$ for the following analysis (although, in fact, we find very little difference if $\hat{T}$ is used instead).

In a vertically confined domain, we hypothesize that a perturbation to the steady columnar flow will destabilize the flow if the time scale for growth of the perturbation is shorter than the time scale for the perturbation to advect from one boundary to the other. We assume that the regions of proto-plumes at the upper and lower boundaries provide perturbations to the columnar flow on a range of scales. Since the height of the Rayleigh–Darcy cell in rescaled co-ordinates (§3.2.2) is $H = k$, the time scale for advection of the most unstable perturbation across the domain for $A \gg 1$ is $H/c_{_M} = k/A$ (from 3.17$b$), and the time scale for growth of the most unstable perturbation is $1/\mathrm{Re}\{\sigma_{_M}\} = 1/(0.231A^{4/9})$ (from 3.17$a$). A comparison of these time scales, which is the hypothesized condition for instability, gives

$$\frac{k}{A} \gtrsim \frac{1}{0.231A^{4/9}} \quad \text{for} \quad A \gg 1, \tag{3.39}$$

which reduces to

$$k \gtrsim 2.6\,(\hat{w}Ra)^{5/14} \gtrsim 1.2\,Ra^{5/14} \quad \text{for} \quad Ra \gg 1, \tag{3.40}$$

on using $A = \widehat{A}Ra/k = \hat{w}Ra/k$ and the observation that $\hat{w} \to 0.117$ as $Ra \to \infty$. We note that, since (3.40) is simply obtained by a comparison of time scales, we would not expect the numerical pre-factor in (3.40) to be accurate, beyond giving a rough estimate of the order of magnitude.

For $A \lesssim O(10^4)$, both the growth rate and the phase speed of the most unstable mode are found numerically to be slightly larger than the asymptotic scalings (3.17) (see inset to figure 3.3). In addition, for $Ra \lesssim O(10^4)$, the amplitude $\hat{w}$ is slightly larger than its asymptotic value (see figure 3.9). We found simple empirical fits $\mathrm{Re}\{\sigma_{_M}\} \approx 0.231A^{4/9} + 0.34A^{-0.2}$ and $c_{_M} \approx A + 0.55A^{0.55}$ to the numerical data for $A \gtrsim 17.2$, and $\hat{w} \approx 0.117 + 2900Ra^{-1.8}$ to the amplitude for

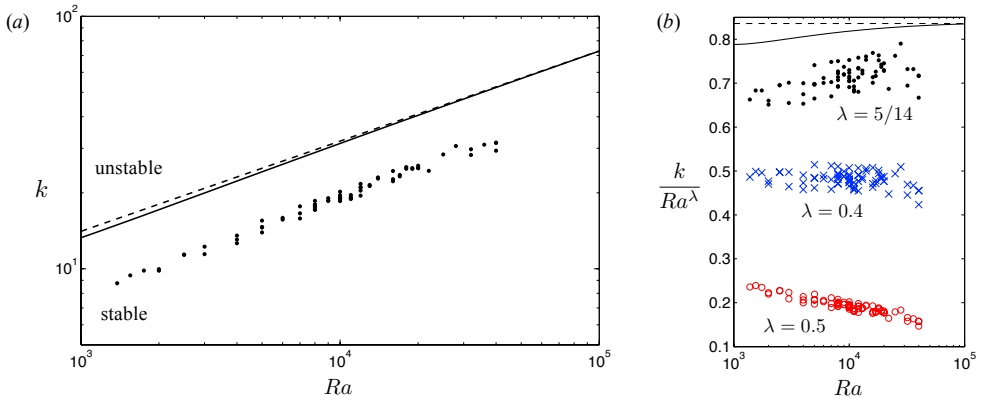


Figure 3.10: Measurements of the wavenumber $k$ from a Rayleigh–Darcy cell of height $H = 1$ and aspect ratio either $L = 1$ or $L = 2$, taken from figure 2.8: $(a)$ the wavenumber $k(Ra)$ (dots) together with the asymptotic stability estimate (3.40) (dashed line) and the approximate correction to the asymptotic scaling for finite $Ra$ and $A$ from (3.41) (solid line); and $(b)$ the scaled wavenumber $k/Ra^{\lambda}$ for trial exponents $\lambda = 5/14$ (dots), $\lambda = 0.4$ (crosses), and $\lambda = 0.5$ (circles), together with the asymptotic stability estimate (3.40) (dashed line) and the correction from (3.41) (solid line), both scaled by $0.7Ra^{5/14}$. The measured data follows the trend of the correction (solid line) over this range of $Ra$.

$Ra \geqslant 1300$. By using these fits in the balance of time scales $k/c_{_M} \sim 1/\mathrm{Re}\{\sigma_{_M}\}$, as above, with $A = \hat{w}Ra/k$, we obtain a correction for finite $Ra$ and $A$ to the asymptotic stability estimate (3.40). This approximate correction $k(Ra)$ is given implicitly by the equations

$$k = \frac{A + 0.55A^{0.55}}{0.231A^{4/9} + 0.34A^{-0.2}}; \qquad kA = Ra\left(0.117 + 2900Ra^{-1.8}\right). \tag{3.41}$$

Figure 3.10$(a)$ shows measurements of the time-averaged dominant wavenumber $k(Ra)$ from a Rayleigh–Darcy cell for $1300 < Ra \leqslant 4 \times 10^4$, together with the asymptotic stability estimate (3.40) (dashed line), and the approximate correction to the asymptotic scaling, given by the solution of (3.41) (solid line). The measured data lies inside the stable region, and appears to give good agreement with the trend of the stability estimates.

In order to examine this agreement more closely, we can rescale the wavenumber and the stability estimates by different trial powers of $Ra$ (figure 3.10$b$). As a preliminary observation, we can see from this rescaling that the measured data

exhibits a distinctly weaker scaling than $k \sim Ra^{1/2}$, which was identified as the 'minimal flow unit' for steady convection (Corson, 2011). Instead, it appears that the data is fairly well described by the scaling $k \sim Ra^{0.4}$ over this range of $Ra$, which is slightly stronger than the asymptotic stability estimate $k \sim Ra^{5/14}$. However, it is also evident that the estimate corrected for finite $Ra$ and $A$ (solid line) differs appreciably from the asymptotic estimate (dashed line) over this range of $Ra$, and that the measured data follows the trend of the correction. (The parameter $A$ for the data shown lies in the range $25 \lesssim A \lesssim 150$.) In particular, the data appears to show a slight trend towards a lower exponent at the highest values of $Ra$, in agreement with the prediction of the stability estimate.

The measured data does, therefore, appear to be consistent with the theoretical stability estimate. Given the very different boundary conditions between the Rayleigh–Darcy cell and the unconfined heat-exchanger flow, this qualitative agreement is notable. Figure 3.10($b$) suggests that the Rayleigh number for the measured data is still too low to observe the hypothesized asymptotic scaling $k \sim Ra^{5/14}$; numerical measurements of $k$ at higher values of $Ra$ would be needed to confirm this suggestion.

### 3.6.2 The onset of the high-$Ra$ regime in a Rayleigh–Darcy cell

Working on the hypothesis that stability controls the horizontal scale of the interior flow in a Rayleigh–Darcy cell, it is natural to consider what happens as $Ra$ decreases, or, equivalently, as the re-scaled amplitude of the flow $A$ decreases. In §3.3.2, we found that the nature of the dominant instability in an unbounded domain changes completely when $A \lesssim 17.2$. A similar dramatic change is observed in the dynamics of the Rayleigh–Darcy cell as $Ra$ decreases below $Ra \approx 1300$ (Graham & Steen, 1994; Otero *et al.*, 2004), from columnar-exchange flow in the interior for $Ra \gtrsim 1300$ to large-scale convective rolls for $Ra \lesssim 1300$.

Numerical measurements of $k$ and $\widehat{A} = \hat{w}$ at $Ra = 1380$, which is just above the transition point, give a value of $A \approx 14.5$ (alternatively, using $\widehat{A} = \hat{T}$ gives $A \approx 15.6$), which is remarkably close to the bifurcation value $A \approx 17.2$ in the linear-stability problem. In fact, since the most unstable mode of the unbounded

flow for $A < 17.2$ has zero wavenumber in both directions, which is not physically achievable in a finite domain, we would expect the Rayleigh–Darcy cell to have a slightly lower bifurcation value of $A$. The rough agreement demonstrated here provides an intriguing direction for further investigation, and again suggests that stability criteria may play an important role in the dynamical structure of the Rayleigh–Darcy cell.

## 3.7 Conclusions

We have examined the stability of columnar convection in a porous medium. The flow is characterized by dimensionless horizontal wavenumber $k$, amplitude $\widehat{A}$, and background temperature gradient $-k^2/Ra$. The stability of the flow in an unbounded domain is then a function of the parameter $A = \widehat{A}Ra/k$ alone.

We used a Floquet analysis to determine the eigenvalues $\sigma$ of the linear-stability problem (3.11) numerically. Somewhat surprisingly, the marginal-stability curve $\mathrm{Re}\{\sigma\} = 0$ is independent of $A$ and thus given by the usual criterion $\beta = \beta^2 + \alpha^2$ for stability of a linear temperature field, where $\beta$ and $\alpha$ are the horizontal and vertical wavenumbers, respectively. For small $A$, the most unstable mode is given by $\alpha = \beta = 0$, and has growth rate $\mathrm{Re}\{\sigma\} = 1$; this mode is an instability of the background linear temperature gradient, and is independent of the columnar flow. However, at $A \approx 17.2$, a different mode becomes the most unstable. This mode has double the horizontal period of the background flow ($\beta = 1/2$), takes the form of vertically propagating pulses on the background columns, and has a growth rate that increases with $A$. Asymptotically, the vertical wavenumber of the most unstable mode is given by $\alpha = 0.332A^{-1/9}$, the growth rate by $\mathrm{Re}\{\sigma\} = 0.2308A^{4/9}$, and the vertical phase speed by $|c| = A$. The sign of $c$ changes if the perturbation is shifted horizontally by $\pi$ (a quarter period).

For $A \gg 1$, advective processes dominate the flow across almost all of the domain: horizontal advection of the background temperature by the perturbation flow balances vertical advection of the perturbation temperature by the background flow. In the absence of any diffusion, this advective balance would simply give a neutrally stable propagating mode. However, the temperature gradient

changes significantly across thin boundary-layer regions that are centred on the maxima (for upwelling perturbations) or minima (for downwelling perturbations) of the background flow. Horizontal diffusion in these boundary-layer regions provides a mechanism for growth, as discussed in §3.4.2. Interestingly, the instability is independent of the background vertical temperature gradient in the limit $A \gg 1$, and is driven entirely by the columnar flow.

Numerical simulations of the non-linear evolution of the instability for $A \gtrsim 17.2$ in a periodic domain show that perturbations initially grows in accordance with linear theory, before the flow undergoes a secondary instability. After a period of reorganization, the system evolves into a new columnar flow with a smaller wavenumber than the original flow.

Persistent vertical columnar structures have also been observed in three-dimensional porous convection (e.g. Pau *et al.* 2010; Fu *et al.* 2013, and chapter 7 below), and it seems likely that many of the ideas discussed in this chapter could be extended to three dimensions. However, while it is straightforward to write down three-dimensional heat-exchanger base flows, the linear-stability analysis of such flows is much more complicated than in two dimensions (primarily owing to the double expansion in the Floquet analysis). In fact, even the leading-order advection–propagation balance for $A \gg 1$ does not yield analytic solutions in three-dimensions, unlike in two dimensions (see (3.30)). A three-dimensional stability analysis is left for future work, while a detailed investigation of the interior flow of statistically steady three-dimensional porous convection is presented in chapter 7.

This work was motivated by the hitherto unexplained mechanism that controls the horizontal wavenumber of the columnar flow in the interior of a two-dimensional Rayleigh–Darcy cell at high $Ra$. Numerical measurements of this flow suggest that it is increasingly well described by the steady heat-exchanger solution as $Ra \to \infty$ (chapter 2). By a comparison of the time scales for growth and propagation of the most unstable mode, we derived an asymptotic stability estimate $k \sim (\widehat{A}Ra)^{5/14}$ for the wavenumber $k$ of vertically confined heat-exchanger flow. In a Rayleigh-Darcy cell, the amplitude $\widehat{A}$ is given by the amplitude of the temperature $\hat{T}$ or the vertical velocity $\hat{w}$, which numerical measurements suggest are asymptotically equal and independent of $Ra$. The estimated stability bound-

ary thus reduces to $k \sim Ra^{5/14}$ as $Ra \to \infty$. For $Ra < O(10^5)$, the stability boundary has a slightly stronger dependence on $Ra$ than this asymptotic scaling. Although numerical measurements in a Rayleigh–Darcy cell at higher $Ra$ would be required to verify the asymptotic scaling $k \sim Ra^{5/14}$, the stability boundary gives good agreement with the previously unexplained trend of numerical measurements of $k(Ra)$ over the range $1300 < Ra \leqslant 4 \times 10^4$.

The results of this chapter, therefore, support the hypothesis that the stability of the interior columnar flow provides the mechanism that controls the wavenumber $k$ in Rayleigh–Darcy convection. The vigorous large-wavenumber dynamics of protoplume formation at the upper and lower boundaries force the system over a range of small scales, and the columnar flow adopts the smallest scale for which it can remain stable over the height of the domain, which is given by $k \sim Ra^{5/14}$ as $Ra \to \infty$. Any smaller scale of columnar flow would be unstable, and the resulting instability would lead to a coarsening of the flow.

# Appendices

## 3.A Generic behaviour of solutions of (3.33)

Equation (3.33) can be re-written as a single differential equation for $f$ by substituting $g = \gamma_0 - f'$ into (3.33$b$) to to obtain

$$f''' + \left(\frac{\mathrm{i}\xi^2}{2} - s\right) f' - \mathrm{i}\xi f = \gamma_0 \left(\frac{\mathrm{i}\xi^2}{2} - s\right) \tag{3.42}$$

We seek solutions that satisfy $f(0) = f''(0) = 0$ and the matching condition $f \to -\xi^2/2$ (equivalently $g \to \xi$) as $\xi \to \infty$. In order to determine the unknown eigenvalue $s$, we require four boundary conditions for the third-order system (3.42). It is not clear, *per se*, whether the matching condition constitutes one or two constraints; this depends on the generic behaviour of the solutions as $\xi \to \infty$.

A WKB approximation to (3.42) in the limit $\xi \to \infty$ gives leading-order

solutions of the form

$$f \sim c\,\xi^2 - \gamma_0\xi + d_\pm\,\xi^b \exp\left[\pm\frac{(1-\mathrm{i})}{4}\xi^2\right] + O(1) \quad \text{as} \quad \xi \to \infty, \tag{3.43}$$

where $b$ would be determined at the next order, and $c$ and $d_\pm$ are constants. The matching condition $f \to -\xi^2/2$ requires both that $c = -1/2$ and that $d_+ = 0$. It therefore constitutes two constraints, and we have sufficient conditions to determine the eigenvalue $s$ in (3.33).

## 3.B Variation of the growth rate Re$\{S\}$ for $\alpha^* \ll 1$ and $\alpha^* \gg 1$

In §3.4.1, we determined the leading-order growth rate $\mathrm{Re}\{\sigma^*\} = A^{4/9}\mathrm{Re}\{S\}$ as a function of the rescaled vertical wavenumber $\alpha^*$, and found that $\mathrm{Re}\{S(\alpha^*)\}$ increased for small $\alpha^*$ and decreased for large $\alpha^*$ (figure 3.6*a*). In this appendix, in order to understand this behaviour, we examine the limits $\alpha^* \ll 1$ and $\alpha^* \gg 1$. For clarity, we re-write (3.33) and (3.37) here as

$$f' + g = \alpha^{*9/4}\pi, \qquad g'' - \left(s - \frac{\mathrm{i}\xi^2}{2}\right) g + \mathrm{i}\xi f = 0, \qquad S = \alpha^{*1/2} s. \quad (3.44a, b, c)$$

The boundary conditions are $f(0) = g'(0) = 0$ and $g \to \xi$ as $\xi \to \infty$.

In the limit $\alpha^* \ll 1$, (3.44*a*) becomes $f' = -g$ to leading order, while (3.44*b*) remains unchanged; the solution to these equations gives an eigenvalue $s = (1 - \mathrm{i})/2$ that is independent of $\alpha^*$ to leading order. (The corresponding expression for the eigenfunction $f$ can be found analytically in integral form, but the expression is not elucidating.) Hence

$$\mathrm{Re}\{S\} = \frac{1}{2}\alpha^{*1/2} \quad \text{for} \quad \alpha^* \ll 1. \tag{3.45}$$

In the limit $\alpha^* \gg 1$, the balance in (3.44*a*) requires that the eigenfunctions $[f, g]$ are $O(\alpha^{*9/4})$ to leading-order. We write $g = \alpha^{*9/4} g_0 + g_1 + O(\alpha^{*-9/4})$ and $f = \alpha^{*9/4} f_0 + f_1 + O(\alpha^{*-9/4})$, and expand $s = s_0 + \alpha^{*-9/4} s_1 + O(\alpha^{*-9/2})$. The matching condition as $\xi \to \infty$ only applies at second order and is given by $g_1 \to \xi$;

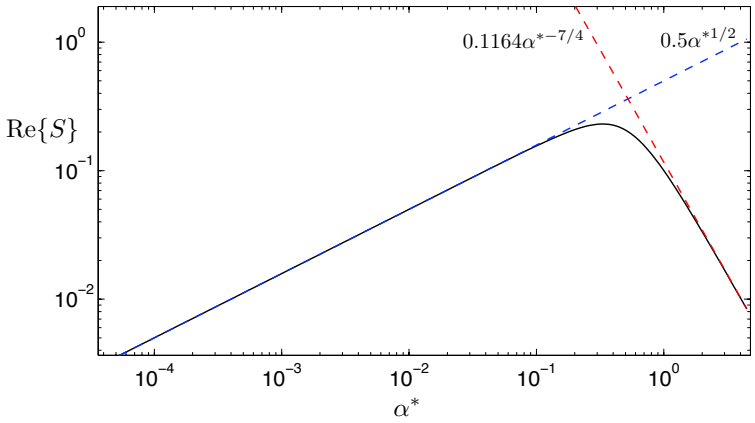


Figure 3.11: The leading-order growth rate Re{$S$} (solid) as a function of the scaled vertical wavenumber $\alpha^*$, together with the predictions from the asymptotic analysis for $\alpha^* \ll 1$ (3.45) and $\alpha^* \gg 1$ (3.47) (dashed).

the first-order condition is instead given by $g_0 \to 2\pi$ (or, equivalently, $f_0 \to -\pi\xi$), which comes from the form of the solution as $\xi \to \infty$ given by (3.43$b$) in appendix 3.A.

The solution of (3.44$a$,$b$) at leading order is simply given by $[f_0, g_0] = [-\pi\xi, 2\pi]$ and $s_0 = 0$; neither diffusion ($g''$) or growth ($sg$) enter the leading-order balance, which is instead simply between the advective terms. At second order, (3.44$a$,$b$) become

$$f_1' = -g_1, \qquad g_1'' + \frac{\mathrm{i}\xi^2}{2} g_1 - 2\pi s_1 + \mathrm{i}\xi f_1 = 0, \tag{3.46$a$, $b$}$$

which can be solved numerically, together with boundary conditions $f_1(0) = g_1'(0) = 0$ and $g_1 \to \xi$ as $\xi \to \infty$, to give an eigenvalue $s_1 = 0.1164 - 0.048i$. Thus

$$\mathrm{Re}\{S\} = 0.1164\,\alpha^{*-7/4} \quad \text{for} \quad \alpha^* \gg 1. \tag{3.47}$$

Figure 3.11 shows that the leading-order asymptotic predictions of Re{$S(\alpha^*)$} for small and large wavenumber from (3.45) and (3.47) give very good agreement with the full solution of figure 3.6($a$). The physical basis for the decay in the growth rate at small and large $\alpha^*$ is discussed in §3.4.2.

## 3.C Stability of piecewise uniform exchange flow in the absence of diffusion

In the main text of this chapter, we examined the stability of density-driven heat-exchanger flow, in which vertical advection balanced horizontal diffusion between the interleaving columns. Motivated by the interesting observation in §3.4.2 that diffusion acts as a destabilizing mechanism for the columnar flow, in this appendix we examine the related system of exchange flow of two distinct fluids of different densities in the limit of negligible diffusion. The fluids again flow in interleaving columns, as shown in figure 3.12.

The governing equations for the flow are incompressibility and Darcy's law (5.7). The system is horizontally periodic, and each period contains an upwelling column of unit width and uniform velocity $w$ and a downwelling column of width $\lambda^{-1}$ and velocity $-\lambda w$ by continuity (figure 3.12). The interface between the $j^{\text{th}}$ and $(j+1)^{\text{th}}$ columns is labelled by $X_j$. The density is piecewise uniform, and so the governing equations combine to give

$$\nabla^2 p = 0, \tag{3.48}$$

in each column.

We look for a pressure perturbation $\widetilde{p}_j$ in the $j^{\text{th}}$ column and a corresponding interfacial perturbation $\widetilde{X_j}$ of the form

$$\widetilde{p}_j = \pi_j(x)\exp(\sigma t + \mathrm{i}\alpha z), \qquad \widetilde{X}_j = \xi_j \exp(\sigma t + \mathrm{i}\alpha z). \tag{3.49}$$

The horizontal variation $\pi_j$ of the perturbed pressure is found by solving (3.48), which gives

$$\pi_j(x) = A_j \cosh[\alpha(x - X_j)] + B_j \sinh[\alpha(x - X_j)]. \tag{3.50}$$

The constants $A_j$, $B_j$ and $\xi_j$ are determined by continuity of pressure and a kinematic condition for each column at $X_j + \widetilde{X}_j$, which are linearized to give

$$\pi_j(X_j) = \pi_{j-1}(X_j), \tag{3.51a}$$

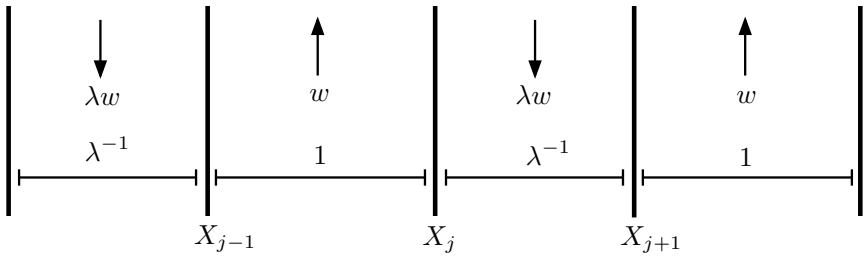


Figure 3.12: A schematic showing the interleaving flow of two distinct fluids of different densities, in columns with width ratio $\lambda$.

$$\left(\frac{\partial}{\partial t}+w_j\frac{\partial}{\partial z}\right)\widetilde{X}_j=-\left.\frac{\partial\widetilde{p}_j}{\partial z}\right|_{x=X_j},\qquad \left(\frac{\partial}{\partial t}+w_{j-1}\frac{\partial}{\partial z}\right)\widetilde{X}_j=-\left.\frac{\partial\widetilde{p}_{j-1}}{\partial z}\right|_{x=X_j}. \tag{3.51b}$$

By substituting (3.49) into (3.51) and eliminating $\xi_j$, we obtain

$$A_{j+1}=A_j\cosh\alpha d_j+B_j\sinh\alpha d_j, \tag{3.52a}$$

$$B_{j+1}=\frac{\sigma+\mathrm{i}\alpha w_{j+1}}{\sigma+\mathrm{i}\alpha w_j}\left(A_j\sinh\alpha d_j+B_j\cosh\alpha d_j\right), \tag{3.52b}$$

where $[d_j,w_j]$ are the width and velocity of the $j^{\text{th}}$ column, given by $[1,w]$ for even $j$ and $[\lambda^{-1},-\lambda w]$ for odd $j$.

We consider perturbations that are periodic over $2N$ columns, for some integer $N$. Therefore, we equate the perturbations to the interface at $X_{2N}$ with those at $X_0$. The application of (3.52) $2N$ times gives a dispersion relation for $\sigma$ of the form

$$\det\left(M^N-I\right)=0, \tag{3.53}$$

where $I$ is the identity matrix. The matrix $M$ is given by

$$M=\begin{pmatrix}C_\lambda & S_\lambda\\ \Gamma S_\lambda & \Gamma C_\lambda\end{pmatrix}\begin{pmatrix}C_1 & S_1\\ \Gamma^{-1}S_1 & \Gamma^{-1}C_1\end{pmatrix};\qquad \Gamma=\frac{\sigma+\mathrm{i}\alpha w}{\sigma-\mathrm{i}\alpha\lambda w}, \tag{3.54$a$, $b$}$$

where $C_1=\cosh\alpha$, $S_1=\sinh\alpha$, $C_\lambda=\cosh(\alpha/\lambda)$, and $S_\lambda=\sinh(\alpha/\lambda)$.

Equation (3.53) has solutions if and only if $M^N$ has eigenvalue 1, or equiv-

alently $M$ has an eigenvalue that is an $N^{\text{th}}$ root of unity. Moreover, it is easily shown that the determinant of $M$ is 1, and so the product of the eigenvalues of $M$ is 1. Thus, (3.53) has solutions if and only if the eigenvalues of $M$ are a conjugate pair of $N^{\text{th}}$ roots of unity. We label these eigenvalues $\mu_\pm = a \pm \mathrm{i}b$, for some real $a$ and $b$ with $|a| \leq 1$, $|b| \leq 1$. Then (3.53) is equivalent to

$$\det\left(M - \mu_\pm I\right) = 0, \tag{3.55}$$

which can be reduced to

$$\left(1 + \Gamma^2\right) S_1 S_\lambda + 2\left(C_1 C_\lambda - a\right)\Gamma = 0, \tag{3.56}$$

Equation (3.56) is a quadratic for $\Gamma$, which has discriminant

$$\Delta = 4\left[\left(C_1 - C_\lambda\right)^2 + 2(1-a)C_\lambda C_1 + a^2 - 1\right]. \tag{3.57}$$

Since $C_1 C_\lambda \geqslant 1$ and $|a| \leqslant 1$, (3.57) implies that $\Delta \geqslant (a-1)^2 \geqslant 0$, and so solutions $\Gamma$ of (3.56) must be real. This constraint, together with (3.54*b*), requires that $\sigma$ is pure imaginary, which holds for any width ratio $\lambda$, velocity $w$, periodicity $N$, or wavenumber $\alpha$. Therefore, in the absence of diffusion, the columnar exchange flow of two distinct fluids of different densities is neutrally stable to all wavelengths; perturbations are advected by the flow without growth or decay. This result is similar to the observation in §3.4.2 that the leading-order advection balance for heat-exchanger flow gives neutral propagation, and growth is only possible because of diffusion.

# Chapter 4

# High-Rayleigh-number convection in a porous medium containing a thin low-permeability layer

The material contained in this chapter is in preparation for submission to the *Journal of Fluid Mechanics*.

## 4.1 Introduction

Porous media are often modelled as homogeneous (as in the rest of this dissertation), and described by uniform averaged properties like the porosity and permeability. Natural porous media, however, are rarely homogeneous. In particular, geophysical aquifers commonly consist of a series of roughly horizontal layers of rock of distinctly different permeabilities (Monkhouse, 1970; Phillips, 2009). Layering of this sort can frequently be observed on exposed rock faces in quarries or coastal cliffs, such as the Jurassic sandstone cliffs at Bridport in Dorset, UK (Morris & Shepperd, 1982). Both the permeability and the depth of layers can be much smaller than those of the main formation: the exposed Aztec sandstone in Nevada, for example, at over a kilometre in depth, is charac-

terized by multiple very thin ($\sim$ 1 cm) horizontal layers that are several orders of magnitude less permeable than the main formation (Sternlof *et al.*, 2006). An important example for the geological storage of $CO_2$ is the Utsira sand formation at the Sleipner field in the North Sea, where roughly 1 million tonnes of $CO_2$ have been sequestered every year since 1996 (Bickle *et al.*, 2007; Boait *et al.*, 2012). Seismic images have revealed that the flow of injected $CO_2$ is significantly affected by the presence of nine low-permeability roughly horizontal mudstone layers which intersperse the formation, and are much thinner (roughly $1 - 5$ m deep) than the formation itself (roughly 200 m deep) (Bickle *et al.*, 2007).

The study of convection in inhomogeneous or anisotropic media has tended to focus on the onset of convection and the subsequent dynamics of the flow at low Rayleigh numbers (Simmons *et al.*, 2001; Ennis-King *et al.*, 2005; Nield & Bejan, 2006). In media comprising layers of high and low permeability, McKibben & O'Sullivan (1980, 1981) found that, as the permeability contrast between the layers is increased, there is a transition in the flow dynamics from large-scale convective rolls to local convective structures confined to the higher-permeability layers. McKibben & Tyvand (1983) examined the flow at low $Ra$ in a medium with thin low-permeability layers, and found that the presence of these layers can significantly increase the critical Rayleigh number for the onset of convection. They modelled the flow under the assumption that both the height and permeability of the low-permeability layers were small but their ratio was $O(1)$; we adopt a similar approach here for the case of vigorous high-$Ra$ convection.

In this chapter, we use high-resolution numerical simulations to examine the impact of a thin, horizontal, low-permeability layer on the strength and dynamical structure of high-$Ra$ convection in a porous medium. We consider a cell comprising an identical upper and lower layer, between which there is a thin interior layer of a lower permeability. The whole cell is heated from below and cooled from above. The flow thus attains a statistically steady state, which allows for a systematic examination of the effect of a thin low-permeability layer on the heat flux through the cell and on the associated flow structure. In the limit in which there is no interior layer, the cell is identical to the homogeneous Rayleigh–Darcy cell discussed in chapter 2. All physical properties of the fluid and the medium except the permeability are assumed to be constant throughout the cell; in par-

ticular, we assume for simplicity that the porosity $\phi$ of the medium is uniform, and is thus independent of the permeability (see appendix 4.A for a discussion of this assumption).

The chapter is laid out as follows. In §4.2, we present the governing equations and non-dimensionalization. In §4.3, we discuss our numerical results. We show that, in the limit that both the dimensionless height $h$ and permeability $\Pi$ of the low-permeability interior layer are small, the flow can be described solely by their ratio $\Omega = h/\Pi$. The dominant horizontal lengthscale of the flow increases dramatically as $\Omega$ is increased, and the Nusselt number can increase for small values of $\Omega$, before decreasing significantly for larger values of $\Omega$. Motivated by these observations, in §4.4 we develop simple one-dimensional models of the system, and discuss future directions and challenges for modelling. Finally, in §4.5, we summarize and discuss our main results.

## 4.2 Governing equations

We consider the flow of a Boussinesq fluid in a two-dimensional porous medium, with horizontal and vertical coordinates $x^*$ and $z^*$ respectively. The medium comprises a thin interior layer between a relatively deep upper and lower layer (figure 4.1*a*). The combined depth of the three layers is $z^* = H$. The upper and lower layers have uniform permeability $K_1$, while the thin interior layer has uniform permeability $K_2 < K_1$ and depth $h^* \ll H$, and lies between $z_1^* = (H - h^*)/2$ and $z_2^* = (H + h^*)/2$. Within each layer, the medium is homogeneous and isotropic.

We assume that the flow $\boldsymbol{u}^* = (u^*, w^*)$ in all three layers is incompressible and is governed by Darcy's law. The equation of state $\rho^*(T^*)$ is linear, and the temperature field $T^*$ satisfies an advection–diffusion transport equation. These equations are given by

$$\boldsymbol{\nabla} \cdot \boldsymbol{u^*} = 0, \tag{4.1a}$$

$$\mu \boldsymbol{u} = \begin{cases} -K_1 \left(\nabla p^* + \rho^* g \hat{\boldsymbol{z}}^*\right) & 0 \leqslant z^* \leqslant z_1^*, \ z_2^* \leqslant z^* \leqslant H, \\ -K_2 \left(\nabla p^* + \rho^* g \hat{\boldsymbol{z}}^*\right) & z_1^* < z^* < z_2^*, \end{cases} \tag{4.1b}$$

$$\rho^* = \rho_0 \left[1 - a\left(T^* - T_0\right)\right], \tag{4.1c}$$

$$\phi \frac{\partial T^*}{\partial t^*} + \boldsymbol{u^*} \cdot \boldsymbol{\nabla} T^* = \phi D \nabla^2 T^*, \tag{4.1d}$$

where $\mu$ is the viscosity, $p^*$ is the pressure, $g$ is the gravitational acceleration, $\hat{\boldsymbol{z}}^*$ is a unit vector in the $z^*$ direction, $\rho_0$ and $T_0$ are a constant reference density and temperature, respectively, $a$ is the coefficient of thermal expansion, $\phi$ is the porosity of the medium, and $D$ is the constant thermal diffusivity in the liquid phase. As in the rest of this dissertation (see §1.2), heat transfer to the solid phase of the medium is neglected; as such, these equations are equally applicable to compositionally driven convection.

On the upper and the lower boundaries of the domain, the vertical velocity vanishes and a fixed temperature is imposed, such that

$$T^*\big|_{z^*=0} = T_0 + \Delta T, \qquad T^*\big|_{z^*=H} = T_0, \qquad w^*\big|_{z^*=0,H} = 0, \tag{4.2}$$

where $\Delta T$ is a fixed unstable (positive) temperature difference. The pressure, temperature and normal velocity are continuous at the internal boundaries $z^* = z^*_{1,2}$. The domain is periodic in the $x^*$ direction, with period $x^* = L^*$.

We non-dimensionalize the system with respect to the depth $H$ of the whole domain, the permeability $K_1$ of the upper and lower layers, the density difference across the domain $\Delta\rho = \rho_0 a \Delta T$, and the convective time scale $\phi H \mu / (g \Delta \rho K_1)$. The dimensionless rescaled temperature is given by $T = (T^* - T_0)/\Delta T$.

In dimensionless variables, the governing equations (4.1) reduce to

$$\boldsymbol{\nabla} \cdot \boldsymbol{u} = 0, \tag{4.3a}$$

$$\boldsymbol{u} = \begin{cases} -\left(\nabla p - T\hat{\boldsymbol{z}}\right) & 0 \leqslant z \leqslant z_1,\ z_2 \leqslant z \leqslant 1, \\ -\Pi\left(\nabla p - T\hat{\boldsymbol{z}}\right) & z_1 < z < z_2, \end{cases} \tag{4.3b}$$

$$\frac{\partial T}{\partial t} + \boldsymbol{u} \cdot \boldsymbol{\nabla} T = \frac{1}{Ra} \nabla^2 T, \tag{4.3c}$$

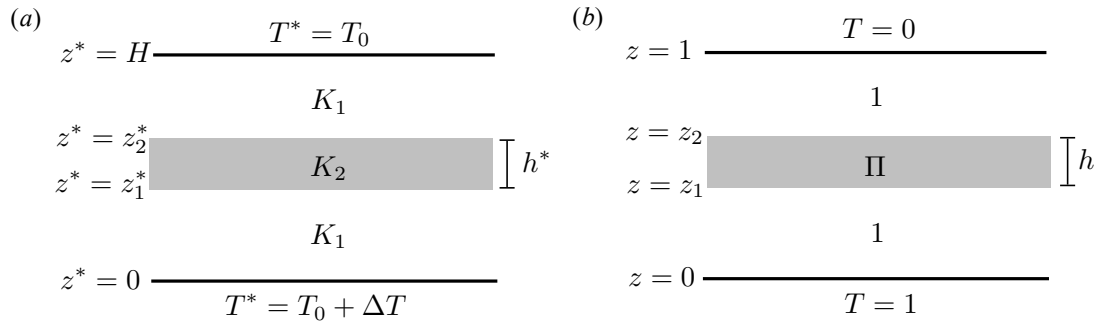


Figure 4.1: A schematic showing the system under consideration, with the permeability of each layer and the thermal boundary conditions marked, for $(a)$ dimensional and $(b)$ dimensionless variables.

where $p = [p^*/(Hg) + \rho_0 z]/\Delta\rho$ is a reduced pressure, $\Pi = K_2/K_1 < 1$ is the ratio of the two permeabilities, and we have combined the equation of state (4.1$c$) with Darcy's law (4.1$b$). The dimensionless edges of the interior layer are given by $z_{1,2} = (1 \mp h)/2$. The parameter $Ra$ is the Rayleigh number, which is the ratio of the driving strength of buoyancy to inhibiting dissipative effects of viscosity and diffusion, given by

$$Ra = \frac{g\Delta\rho K_1 H}{\phi D\mu}. \tag{4.4}$$

The dimensionless boundary conditions on the upper and lower boundaries of the domain are given from (4.2) by

$$T|_{z=0} = 1, \qquad T|_{z=1} = 0, \qquad w|_{z=0,1} = 0, \tag{4.5}$$

(figure 4.1$b$). The conditions at the internal interfaces between the different layers are given by continuity of temperature, pressure and normal velocity,

$$[T] = [p] = [w] = 0 \quad \text{at} \quad z = z_1, z_2. \tag{4.6}$$

As in chapter 2, incompressibility (4.3$a$) is satisfied by the introduction of a streamfunction $\psi$ which obeys $(u, w) = (\partial\psi/\partial z, -\partial\psi/\partial x)$. We eliminate the

pressure field by taking the curl of (4.3$b$), which gives

$$\nabla^2\psi = \begin{cases} -\partial T/\partial x & 0 \leqslant z \leqslant z_1,\ z_2 \leqslant z \leqslant 1, \\ -\Pi\ \partial T/\partial x & z_1 < z < z_2. \end{cases} \tag{4.7}$$

We incorporate the boundary condition for the pressure at the interfaces with the interior layer by combining (4.6) with Darcy's law (4.3b), to give the boundary conditions in terms of discontinuities of the horizontal velocity:

$$u|_{z=z_1^+} = \Pi\ u|_{z=z_1^-}\,, \qquad u|_{z=z_2^-} = \Pi\ u|_{z=z_2^+}\,. \tag{4.8}$$

The flow is described by four dimensionless parameters: the Rayleigh number $Ra$; the permeability ratio $\Pi$; the relative depth of the interior layer $h = h^*/H$; and the width of the domain $L = L^*/H$. Unless otherwise stated, all the numerical results presented in this chapter have $L = 4$.

The statistically steady convective flux, or, in dimensionless variables, the Nusselt number $Nu(Ra, \Pi, h)$, can be defined as the temporally and horizontally averaged heat flux across the lower boundary of the domain:

$$Nu = \langle nu(t) \rangle = \left\langle -\frac{1}{L}\int_0^L \left.\frac{\partial T}{\partial z}\right|_{z=0} \mathrm{d}x \right\rangle, \tag{4.9}$$

where $nu(t)$ is the instantaneous flux through the lower boundary at a given time $t$. The angle brackets $\langle\,\rangle$ signify a long-time average.

We solved (4.3b) and (4.7) numerically. The numerical method is discussed very briefly here, and is described in more detail in appendix A, §A.2.1. We employed a vertical coordinate transformation in order to fully resolve both the thin boundary layers at the upper and lower boundaries of the domain, and the interfaces between the different layers inside the cell. Unless explicitly noted in the text below, the initial condition for all calculations was given by a linear vertical temperature gradient with a small random perturbation. After an initial reorganization period, the flow attains a statistically steady state (although this state is affected by hysteresis; see §4.3.4.2 below). At high $Ra$, the local flux through the boundary $nu(t)$ exhibits chaotic fluctuations about a mean in this state, and the computations are continued until the Nusselt number (4.9) has

converged to within 0.25% of its mean.

## 4.3 Numerical results

We begin by presenting our numerical measurements and discussing the observations. We focus initially on simulations at $Ra = 5000$, which is appreciably higher than the onset of the high-$Ra$ regime for homogeneous Rayleigh-Darcy convection at $Ra \approx 1300$ (Otero *et al.*, 2004). We then examine the dependence of the system on $Ra$ in §4.3.5.

### 4.3.1 Numerical results for $Ra = 5000$

Snapshots of the statistically steady temperature field for different values of the height $h$ of the interior layer and two different permeability ratios $\Pi$ are shown in figures 4.2 and 4.3, together with profiles of the temporally and horizontally averaged temperature $\langle\overline{T}\rangle(z)$. The homogeneous case $h = 0$ (equivalently $\Pi = 1$) is shown in figure 4.2($a$).

These figures show that the structure of the flow changes significantly as the height of the interior layer increases. For homogenous convection (figure 4.2$a$), the flow is dominated in the interior by columnar megaplumes with a roughly regular horizontal wavelength (see chapter 2). The most evident change in the flow structure as the height $h$ of the interior layer is increased (figure 4.2$b$–$f$) is a remarkably significant increase in the horizontal scale of these plumes. The widths of upwelling and downwelling plumes become increasingly different on either side of the interior low-permeability layer, and the flow increasingly resembles an ordered array of cells; each cell is half the height of the domain and comprises a thin vertical plume flowing up/down and a much wider plume carrying the return flow. The horizontally averaged temperature $\langle\overline{T}\rangle$ profiles also change appreciably as $h$ is increased. For homogeneous convection (figure 4.2$a$), the profile has a very weak negative gradient throughout the interior of the domain. As $h$ is increased, (figure 4.2$b$–$f$), the profiles appear to 'double back' in the upper and lower halves of the domain and the gradient becomes positive, giving an apparent stable background stratification in each layer. The

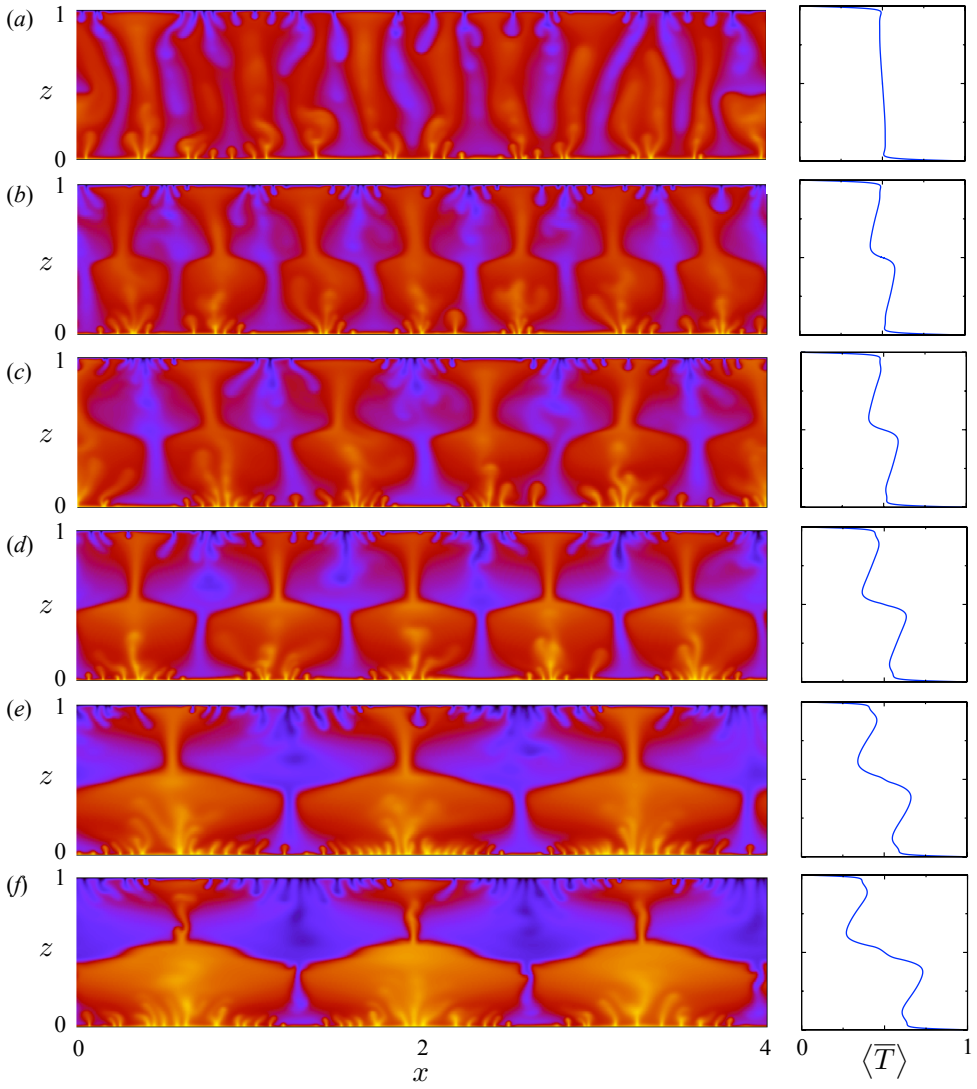


Figure 4.2: Snapshots of the temperature field $T \in [0, 1]$ for $Ra = 5000$, $\Pi = 0.04$, and height $h$ of the interior layer: $(a)$ $h = 0$ (no interior layer); $(b)$ $h = 0.005$; $(c)$ $h = 0.01$; $(d)$ $h = 0.02$; $(e)$ $h = 0.04$; and $(f)$ $h = 0.08$. The temporally and horizontally averaged temperature $\langle \overline{T} \rangle$ is shown on the right-hand side.

temperature difference across the interior low-permeability layer increases with $h$.

For a smaller value of $\Pi$ (figure 4.3), we find that the horizontal scale increases even more rapidly as $h$ is increased. In fact, for sufficiently large values of $h$, the horizontal scale of the plumes appears to have become so broad that protoplumes

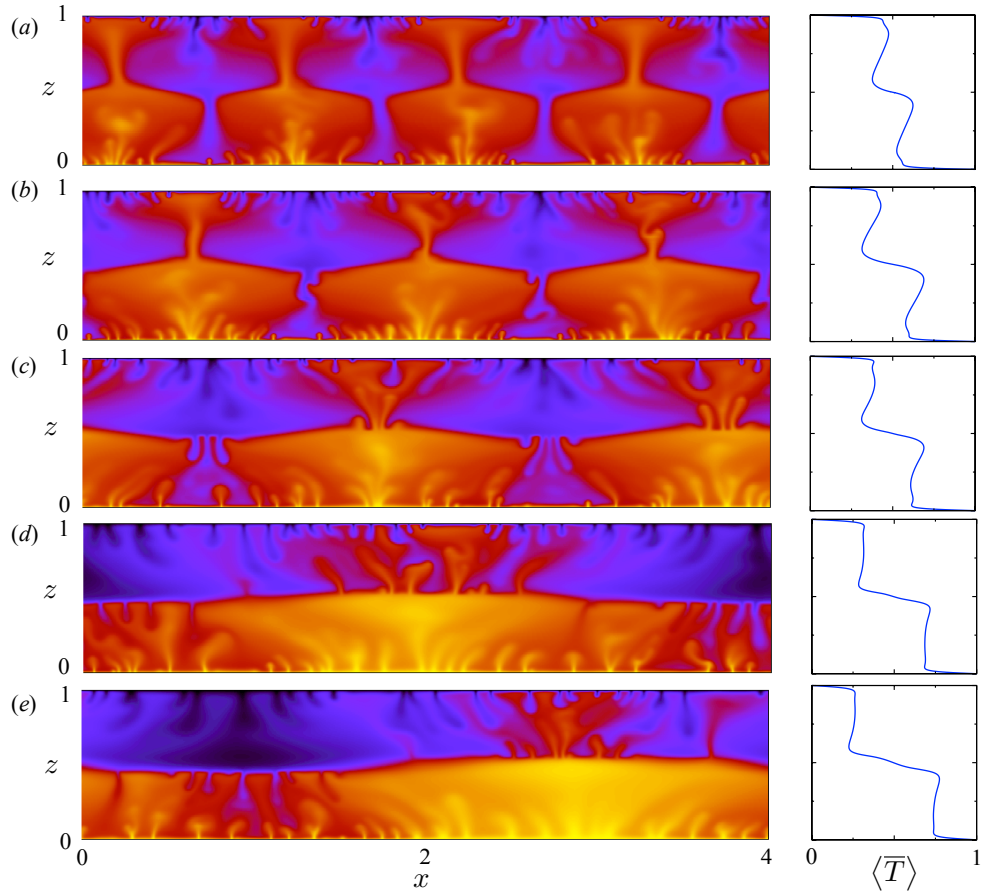


Figure 4.3: Snapshots of the temperature field $T \in [0, 1]$ for $Ra = 5000$, $\Pi = 0.01$, and height of the interior layer: $(a)$ $h = 0.005$; $(b)$ $h = 0.01$; $(c)$ $h = 0.02$;, $(d)$ $h = 0.04$; and $(e)$ $h = 0.08$. The temporally and horizontally averaged temperature $\langle \overline{T} \rangle$ is shown on the right-hand side.

form near the interior low-permeability layer (figures 4.3$d$,$e$). In these cases with only a few megaplumes in the domain, it is likely that the dominant horizontal scale is affected by the aspect ratio $L$. The profiles of $\langle \overline{T} \rangle$ again show an increasing temperature difference across the interior layer as $h$ is increased, although the apparent stratification that we observed in figure 4.2 appears to decrease for large $h$. The structure of the flow is discussed in more detail in §4.3.4 below.

Figure 4.4($a$) shows measurements of the Nusselt number as a function of the height $h$ of the interior layer for different values of $\Pi$. Surprisingly, the Nusselt number does not decreases monotonically as $h$ increases; rather, it increases for

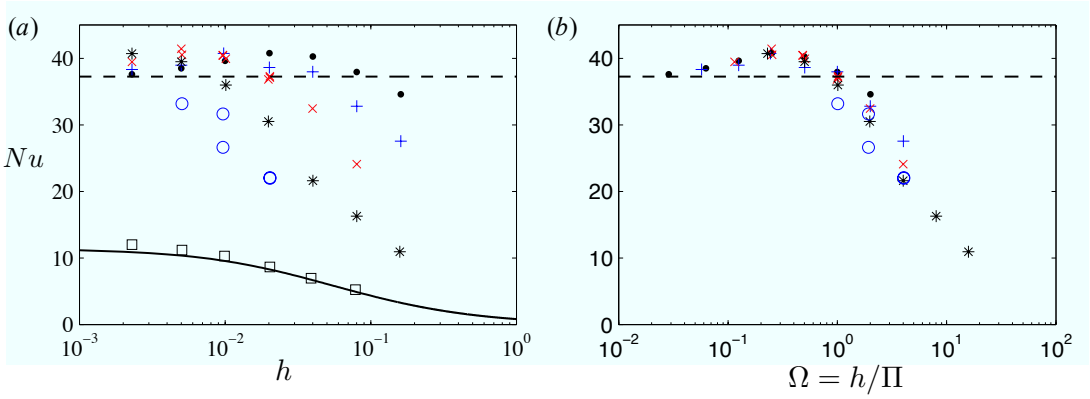


Figure 4.4: The Nusselt number $Nu$ for $Ra = 5000$: $(a)$ as a function of the height of the low permeability layer $h$; and $(b)$ as a function of the parameter $\Omega = h/\Pi$. Measurements are shown for different values of the permeability ratio $\Pi$: $\Pi = 0$ (squares); $\Pi = 0.005$ (circles); $\Pi = 0.01$ (stars); $\Pi = 0.02$ (crosses); $\Pi = 0.04$ (pluses); $\Pi = 0.08$ (dots). The solid line in $(a)$ is the theoretical prediction for an impermeable interior layer (see §4.4.2). For homogeneous Rayleigh–Darcy convection (i.e. the limit $h \to 0$), $Nu = 37.25$ (dashed line). Surprisingly, the Nusselt number initially increases with $\Omega$, before decreasing for $\Omega \gtrsim 0.25$.

small $h$ and non-zero $\Pi$. It is also notable that, even if $\Pi \ll 1$ (but $\Pi \neq 0$), the flux can remain close to the value for homogeneous convection if $h$ is sufficiently small. The measurements roughly collapse onto a single curve when plotted as a function of the quantity $\Omega = h/\Pi$ (figure 4.4$b$), as discussed in the following section.

### 4.3.2 Dependence on $\Omega = h/\Pi$

The measurements of $Nu$ presented in figure 4.4$(b)$ appear to collapse onto a single curve as a function of $\Omega = h/\Pi$. This dependence can be understood by a simple examination of the governing equations in the limit $h, \Pi \ll 1$. In this limit, Darcy's law (4.3b) implies that the horizontal velocity in the interior layer is small ($O(\Pi)$), while the vertical velocity is given by

$$w = -\Pi \left( \frac{\partial p}{\partial z} - T \right) = -\frac{\Pi}{h} \left[ p(z_2) - p(z_1) + O(h) \right]. \tag{4.10}$$

The flow through the interior layer is therefore predominantly vertical if $h, \Pi \ll 1$ and $\Pi/h \sim O(1)$, and is driven by pressure differences, rather than by buoyancy. In this limit, the flow is controlled by the parameter $\Omega = h/\Pi$, which is an impedance or resistance, being a ratio of pressure and Darcy velocity.

We can parameterize the effect of the interior layer by manipulating (4.10) and working in the distinguished limit $h, \Pi \to 0$ such that $\Omega = h/\Pi$ remains finite. The derivative of (4.10) with respect to $x$, together with the continuity conditions for $w$ and $p$ from (4.6), gives

$$\Omega \frac{\partial w}{\partial x} \approx u(z_{2+}) - u(z_{1-}). \tag{4.11}$$

We note that there is no requirement of continuity for the horizontal velocity at $z = z_{1,2}$. In the limit $h, \Pi \to 0$, (4.11) reduces to a jump condition for the horizontal velocity, given by

$$\Omega \left. \frac{\partial w}{\partial x} \right|_{z=0.5} = [u]_{z=0.5_-}^{z=0.5_+}. \tag{4.12}$$

The temperature and vertical velocity are continuous at $z = 0.5$ in this limit.

### 4.3.3 Reduced numerical simulations

Motivated by the results of the previous section, we developed a simplified numerical scheme in which the thin interior layer is parameterized by the jump condition (4.12), together with continuity of temperature and vertical velocity, at $z = 0.5$ (see appendix A for details). This parameterization both simplifies the numerical computations and appreciably reduces the numerical cost, as there is no longer an interior layer to be resolved. We refer to these simulations as 'reduced', to distinguish from 'full simulations' in which the interior layer is fully resolved.

Measurements of $Nu(\Omega)$ from reduced simulations give good agreement with results from full simulations for different values of $h$ and $\Pi$ (figure 4.5). There appears to be a slight difference in some of the measurements for large values of $\Omega$; this is likely owing in part to the relatively large values of $h$ in some of the

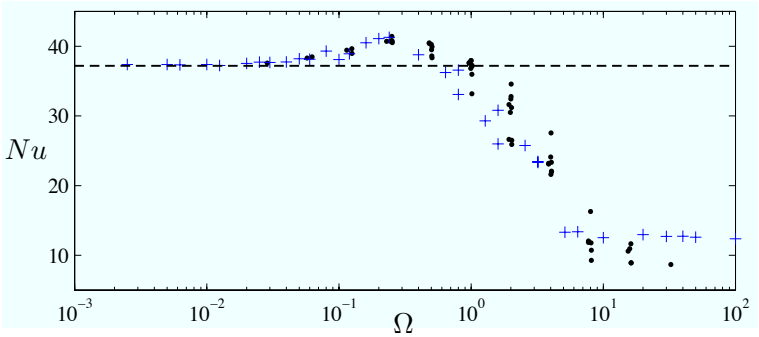


Figure 4.5: The Nusselt number $Nu(\Omega)$ from full simulations for $10^{-3} \leqslant h \leqslant 0.2$ and $10^{-4} \leqslant \Pi \leqslant 0.1$ (dots; includes the data from figure 4.4), and from reduced simulations (crosses), for $Ra = 5000$. The results give very good agreement, and tend to the homogeneous value of $Nu = 37.25$ (dashed line) in the limit $\Omega \to 0$. The slight discrepancy that can be observed at large values of $\Omega$ is because of the relatively large values of $h$ in some of the full simulations; in fact, the relatively small difference in the measurements suggests that the reduced framework provides a reasonable approximation even when, as in some of the full simulations, the interior layer is as much as half of the height of the upper and lower layers.

full simulations. There is also significant variability in the measurements of $Nu$, which is related to variability in the horizontal structure of the flow, as discussed in §4.3.4.2 below.

Figure 4.5 shows that $Nu$ increases gradually with $\Omega$, to give a maximum of $Nu \approx 41.2$ at $\Omega \approx 0.25$. This is an increase of approximately 10% from the value of $Nu$ for homogeneous convection. For $\Omega \gtrsim 0.25$, $Nu$ decreases rapidly. For $\Omega \gtrsim 5$, measurements from reduced simulations level off at roughly a quarter of the value of $Nu$ for homogeneous convection, while measurements from full simulations appear to continue to decrease slowly. The difference in behaviour is discussed in §4.4.2.

### 4.3.4 The dynamical structure of the flow

We have previously observed in figures 4.2 and 4.3 that the dynamics of the flow change dramatically for different values of $h$ and $\Pi$, and we showed in §4.3.2 that the flow is a function of $\Omega = h/\Pi$ only, for $h, \Pi \ll 1$. In this section we describe

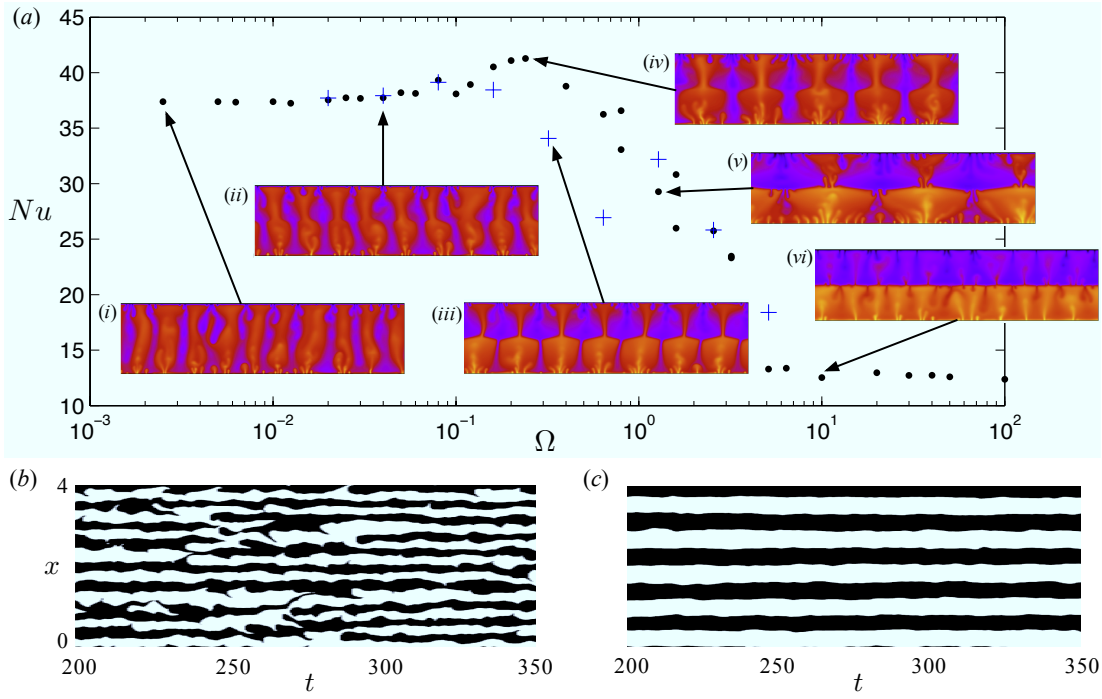


Figure 4.6: $(a)$ Measurements of $Nu(\Omega)$ from reduced simulations for $Ra = 5000$, from figure 4.5 (dots), and from a series of simulations for increasing $\Omega$ in which the initial condition for each value of $\Omega$ was given by the final state from the previous value (crosses). Snapshots $(i)$–$(vi)$ of the statistically steady-state temperature field for different values of $\Omega$ demonstrate both the increase in the wavenumber with $\Omega$, and the effects of hysteresis on the structure and on $Nu$ (discussed in §4.3.4.2). Panels $(b)$ and $(c)$ show space-time plots of the sign of the vertical velocity at $z = 0.5$, for: $(b)$ $\Omega = 2.5 \times 10^{-3}$, corresponding to snapshot $(i)$; and $(c)$ $\Omega = 0.25$, corresponding to snapshot $(iv)$.

in detail the change in the dynamical structure with $\Omega$, and the corresponding form of $Nu(\Omega)$.

#### 4.3.4.1 Dependence on $\Omega$

Figure 4.6$(a)$ shows measurements of $Nu(\Omega)$ from reduced simulations, together with snapshots of the temperature field which show how the dynamical structure of the flow varies with $\Omega$. For $\Omega \lesssim 0.05$ (figure 4.6$a$: $i$ and $ii$), the dynamics are dominated by columnar flow across the full height of the domain with a fairly small wavelength, as in the case of homogeneous flow. The flow in the interior of

the cell is predominantly vertical, and the widths of upwelling and downwelling plumes appear to be roughly equal throughout the domain. The interior flow is also noticeably affected by transient dynamics, as can be observed in a spatio-temporal plot of the sign of the vertical velocity at $z = 0.5$ in figure 4.6($b$). This plot shows variability in the size and location of the edges of the megaplumes. The Nusselt number does not change appreciably for $\Omega \lesssim 0.05$.

For $0.05 \lesssim \Omega \lesssim 0.3$ (figure 4.6$a$: *iii* and *iv*), the flow structure appears to be increasingly cellular. The horizontal lengthscale of the flow increases dramatically in this range. The flow resembles a series of cells of half the height of the domain; in the lower half of the domain, for example, these cells take the form of a thin cold downwelling plume neighbouring a much wider hot upwelling plume, which impinges on the inner boundary and 'leaks' through into the upper half of the domain, feeding the base of a thin upwelling plume there. The effect of transient dynamics on the flow appears to decrease, and the flow becomes increasingly 'ordered'; in particular, there is much less variability in the location and width of the plumes than at lower values of $\Omega$ (figure 4.6$c$). Somewhat unexpectedly, the Nusselt number increases over this range of $\Omega$. For fixed height $h$, this observation implies that the flux increases as the permeability of the interior layer is decreased.

For $0.3 \lesssim \Omega \lesssim 5$ (figure 4.6$a$: *v*), the horizontal lengthscale of the flow continues to increase. In this range, the flow near to the interior boundary appears to be unstable to the growth of protoplumes, which perturb the cellular structure that dominated the flow at lower values of $\Omega$. The Nusselt number decreases markedly in this range of $\Omega$.

At $\Omega \approx 5$, the structure of the flow changes completely. For $\Omega \gtrsim 5$ (figure 4.6$a$: *vi*), the flow resembles two independent cells, each of half the original height and half the original temperature contrast, placed one on top of the other. Unlike at lower values of $\Omega$, there are no plumes that reach across the full height of the domain. The Nusselt number appears to be roughly constant for $\Omega \gtrsim 5$.

Figure 4.7 shows four sets of a selection of temporally averaged measurements of the flow, with each set corresponding to a different range of $\Omega$ discussed above. For each set, the figure shows three panels corresponding to profiles of the average temperature (left), the asymmetry between the widths of upwelling and downwelling plumes (centre), and the magnitudes of horizontal temperature contrasts

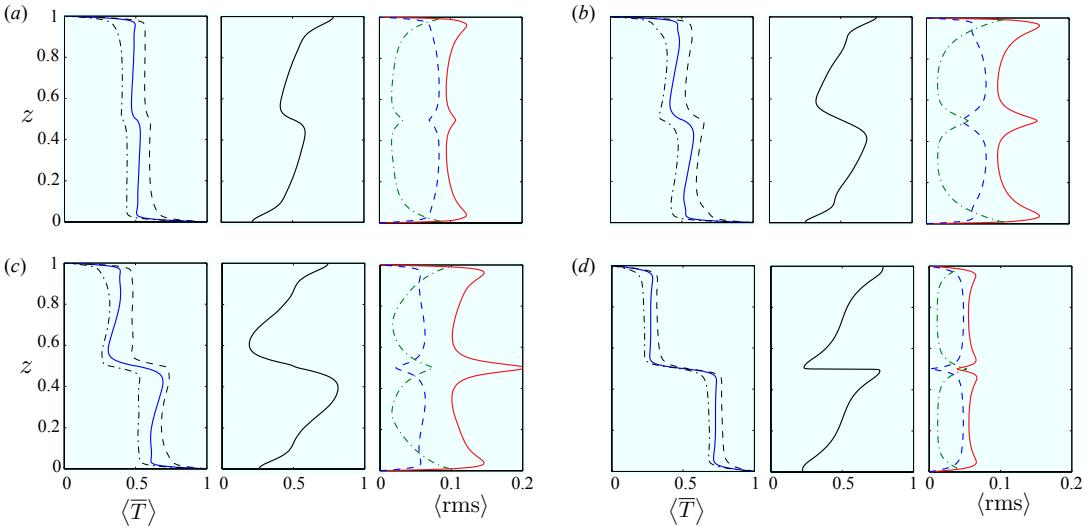


Figure 4.7: Measurements from reduced simulations: left panels show $\langle \overline{T} \rangle (z)$ (solid), together with the average temperature of upwelling fluid (dashed) and the average temperature of downwelling fluid (dot-dashed); centre panels show the proportion of the fluid with $w > 0$, which gives a measure of the asymmetry between the widths of upwelling and downwelling plumes; and right panels show the temporally averaged rms temperature perturbations and velocities $T_{\mathrm{rms}}(z)$ (red, solid), $w_{\mathrm{rms}}(z)$ (blue, dashed), and $u_{\mathrm{rms}}(z)$ (green, dot-dashed). Measurements are shown for: $(a)$ $\Omega = 0.04$, corresponding to figure 4.6($a$:$ii$); $(b)$ $\Omega = 0.25$, corresponding to figure 4.6($a$:$iv$); $(c)$ $\Omega = 1.28$, corresponding to figure 4.6($a$:$v$); and $(d)$ $\Omega = 10$, corresponding to figure 4.6($a$:$vi$).

and velocities provided by the root-mean-square (rms) quantities $T_{\mathrm{rms}}$, $w_{\mathrm{rms}}$, and $u_{\mathrm{rms}}$ (right).

For $\Omega = 0.04$ (figure 4.7$a$), $\langle \overline{T} \rangle$ is roughly uniform in the interior of the domain, except for a small temperature difference across the interior boundary at $z = 0.5$. Similarly, the rms quantities are fairly uniform, with small deviations in the vicinity of $z = 0.5$.

For $\Omega = 0.25$ (figure 4.7$b$), which corresponds to the maximum value of $Nu$, the average temperature field appears to have a weak stable stratification in the upper and lower layers of the domain. The temperature difference across the interior low-permeability layer is larger than in figure 4.7($a$), and the rms quantities vary appreciably near $z = 0.5$. For $\Omega = 1.28$ (figure 4.7$c$), much of this behaviour is more pronounced: there is still an apparent stable stratification

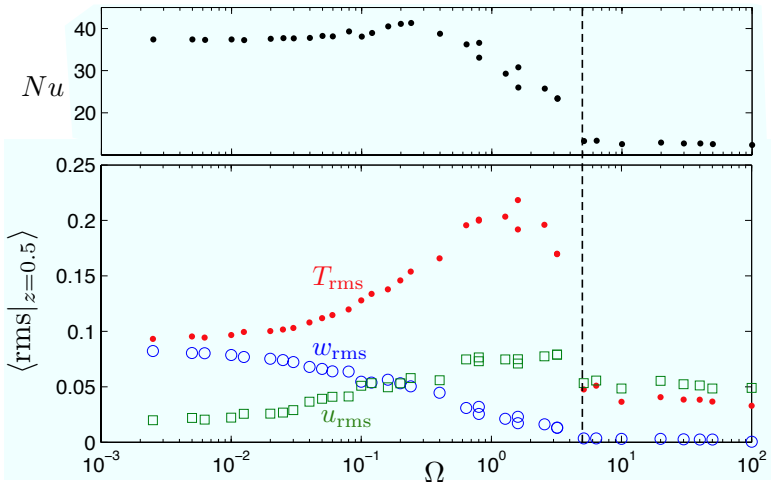


Figure 4.8: Measurements from reduced simulations of the temporally averaged rms temperature perturbations and velocities at $z = 0.5$, as marked. The Nusselt number $Nu(\Omega)$ from figure 4.5 is shown above for comparison. The vertical velocity at $z = 0.5$ is approximately zero for $\Omega \gtrsim 5$; this reflects the transition from advective to diffusive transport across the interior low-permeability layer, marked by the dashed line.

in each layer, the temperature difference across the interior layer is larger again, and there is even greater variation in the rms quantities near $z = 0.5$.

At both $\Omega = 0.25$ and $\Omega = 1.28$ (figure 4.7*b,c*), however, there is a significant asymmetry between upwelling and downwelling plumes, that changes with depth, and which corresponds to the visual impression from figure 4.6(*a:iv,v*) of interleaving plumes with different widths. In addition, we observe that the average temperature restricted to either upwellings or downwellings alone does not display as strong a stratification as $\langle \overline{T} \rangle$. These observations suggest that the measured stratification in the average temperature does not so much indicate a 'true' background stratification throughout the flow (although there is a weak stratification in the wider plume; see figure 4.7*c*), but is predominantly a reflection of the fact that the widths of the hot and cold plumes vary with height.

For $\Omega = 10$ (figure 4.7*d*), the profiles look quite different to those at lower values of $\Omega$. There is no apparent stratification in either layer; the vertical velocity appears to vanish at $z = 0.5$; the temperature variations decrease, rather than increase, near $z = 0.5$; and the magnitude of the rms quantities throughout the

domain is much less than at lower values of $\Omega$.

Figure 4.8 shows measurements of the rms quantities at $z = 0.5$, for different values of $\Omega$. As $\Omega$ is increased, $w_{\mathrm{rms}}$ decreases, while $u_{\mathrm{rms}}$ and $T_{\mathrm{rms}}$ increase. There is, however, a clear change in the trend of these measurements at $\Omega \approx 5$, which corresponds to the transition in the dynamics that we observed in figure 4.6($a$), and to the difference in the profiles in figure 4.7($d$) discussed in the previous paragraph. In particular, $w_{\mathrm{rms}} \approx 0$ for $\Omega \gtrsim 5$, which means that there is no appreciable advective flux through the low-permeability layer. We interpret the change in the dynamics as a transition from advection to diffusion as the dominant transport mechanism across the interior layer. The diffusive transport across the layer is independent of $\Omega$, since it is independent of the permeability, and so $Nu(\Omega)$ should become constant in this regime, as we observed in figure 4.6($a$). The flow resembles two separate Rayleigh–Darcy cells with roughly a quarter of the original Rayleigh number, since both the height and the temperature contrast across each cell are half the original value. For ease of notation, we will refer to this regime for $\Omega \gtrsim 5$ as the 'diffusion regime', and to the regime for $\Omega \lesssim 5$ as the 'advection regime'.

#### 4.3.4.2 Hysteresis

We also observed significant hysteresis in the dynamical structure of the flow, which affects the value of $Nu(\Omega)$. In order to demonstrate this effect, measurements from two different series of simulations with different initial conditions were included in figure 4.6($a$). In the first series of simulations (dots), the initial condition was given by a random perturbation to a linear base state, as in all the other measurements presented in this paper. In the second (crosses), the final state of each simulation was used as the initial condition for the next simulation at a higher value of $\Omega$. Both the measurements of $Nu(\Omega)$ and the horizontal structure of the flow show significant variability between the different simulations, as can be seen by a comparison of the statistically steady-state dynamics in figure 4.6($a$: *iii* and *iv*). This comparison suggests that multiple statistically steady (or at least quasi-steady) states exist for a given value of $\Omega$. The hysteresis is likely due in large part to restriction imposed by the horizontal periodicity of the domain,

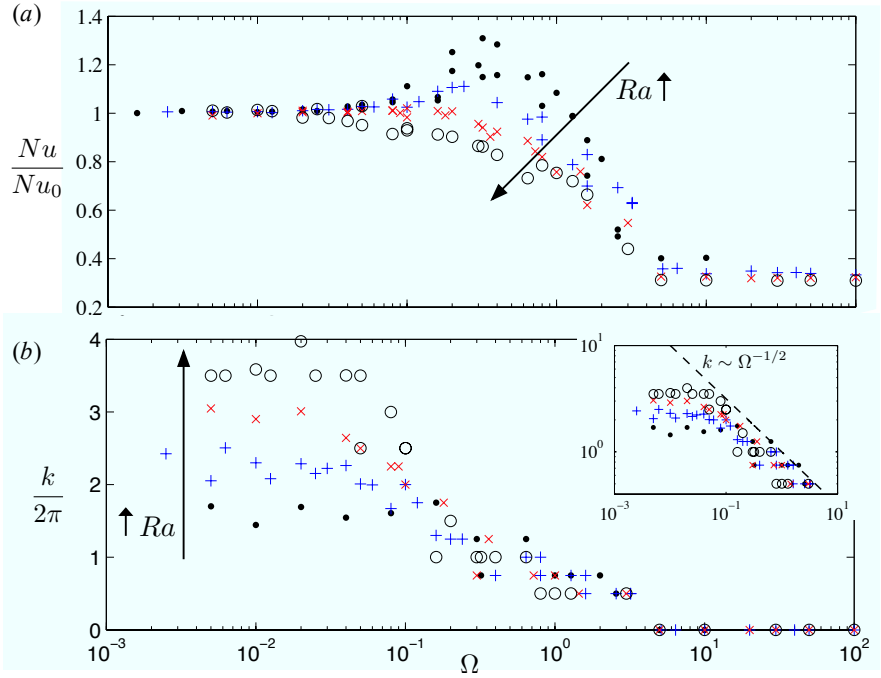


Figure 4.9: Measurements from reduced simulations, for $Ra = 2500$ (dots), $Ra = 5000$ (pluses), $Ra = 10^4$ (crosses), and $Ra = 2 \times 10^4$ (circles), of: $(a)$ the Nusselt number $Nu(\Omega)$, scaled by the Nusselt number $Nu_0$ for homogeneous convection (from chapter 2); and $(b)$ the average wavenumber $k$ scaled by $2\pi$, measured by the temporally averaged mode of the wavenumbers from a Fourier transform of the temperature field at $z = 0.5$. The inset shows the same data on a log-log scale, together with the scaling $k \sim \Omega^{-1/2}$. Note that the simulations at $Ra = 2 \times 10^4$ have aspect ratio $L = 2$.

rather than to initial conditions alone; we have also observed the flow attain quite different statistically steady states in simulations with the same initial conditions.

### 4.3.5 Dependence on $Ra$

We have, thus far, focused on the flow at a fixed value of $Ra = 5000$. Figure 4.9$(a)$ shows measurements of $Nu(\Omega)$ for different values of $Ra$ in the range $2500 \leqslant Ra \leqslant 2 \times 10^4$, scaled by the Nusselt number $Nu_0(Ra)$ for homogeneous Rayleigh–Darcy convection. The values of $Nu_0$ are taken directly from the measurements in chapter 2. There are two particularly interesting features of this plot. First, we observe that the initial trend in $Nu(\Omega)$ as $\Omega$ is increased changes with the

value of $Ra$; at $Ra = 2500$, $Nu$ increases by over 30% before then decreasing, while at $Ra = 2 \times 10^4$, $Nu$ decreases monotonically. Second, as we observed in the previous section, $Nu$ is approximately constant for large $\Omega$ in the diffusion regime. Figure 4.9($a$) suggests that the transition to this regime occurs at a value of $\Omega$ that is roughly independent of $Ra$. This observation is perhaps surprising, given that the Rayleigh number can be interpreted as a measure of the relative strengths of advection and diffusion.

The corresponding average horizontal wavenumber $k(\Omega)$ of the statistically steady flow at $z = 0.5$ is shown in figure 4.9($b$). The data is somewhat noisy, which reflects the degree of hysteresis that can affect the flow. The wavenumber for small $\Omega$ tends to the value for homogeneous Rayleigh–Darcy convection (measurements of which are approximately fitted by $k = 0.48Ra^{0.4}$; see figure 2.8 of chapter 2). The wavenumber decreases dramatically for $\Omega \gtrsim 0.1$ and the value of $\Omega$ at which the wavenumber begins to decrease roughly coincides with the value at which $Nu/Nu_0$ begins to differ appreciably from 1. The subsequent decrease in $k$ has an approximate scaling of $k \sim \Omega^{-1/2}$ (figure 4.9$b$ inset). This scaling in discussed in §4.4.3. There is some suggestion from these measurements that $k$ becomes independent of $Ra$ as $\Omega$ increases.

A comparison of snapshots of the flow for different values of $Ra$ at $\Omega = 0.1$ and $\Omega = 0.3$ is shown in figure 4.10. For $\Omega = 0.1$, the dominant horizontal lengthscale of the flow decreases as $Ra$ is increased. For $\Omega = 0.3$, the difference in the horizontal lengthscale is less clear, but the dynamical structure of the flow exhibits a strong dependence on $Ra$. In particular, the flow for larger $Ra$ (figure 4.10$c$,$d$) is affected by the formation of protoplumes near the inner boundary. As a result, the flow appears more 'disordered' than the cellular flow at smaller values of $Ra$ (figure 4.10$a$, $b$). The presence of protoplumes near the interior boundary is also reflected in the proportion of fluid with positive vertical velocity (figure 4.10, right column). At smaller values of $Ra$ (e.g. figure 4.10$a$), the variation in the proportion of upwelling and downwelling fluid with height is bigger at $\Omega = 0.3$ than it is at $\Omega = 0.1$, and, as a consequence, the apparent stratification in the upper and lower layers is larger. In contrast, at higher values of $Ra$ (e.g. figure 4.10$c$,$d$), the variation is less at $\Omega = 0.3$ than at $\Omega = 0.1$, presumably owing to the presence of protoplumes near the interior boundary.

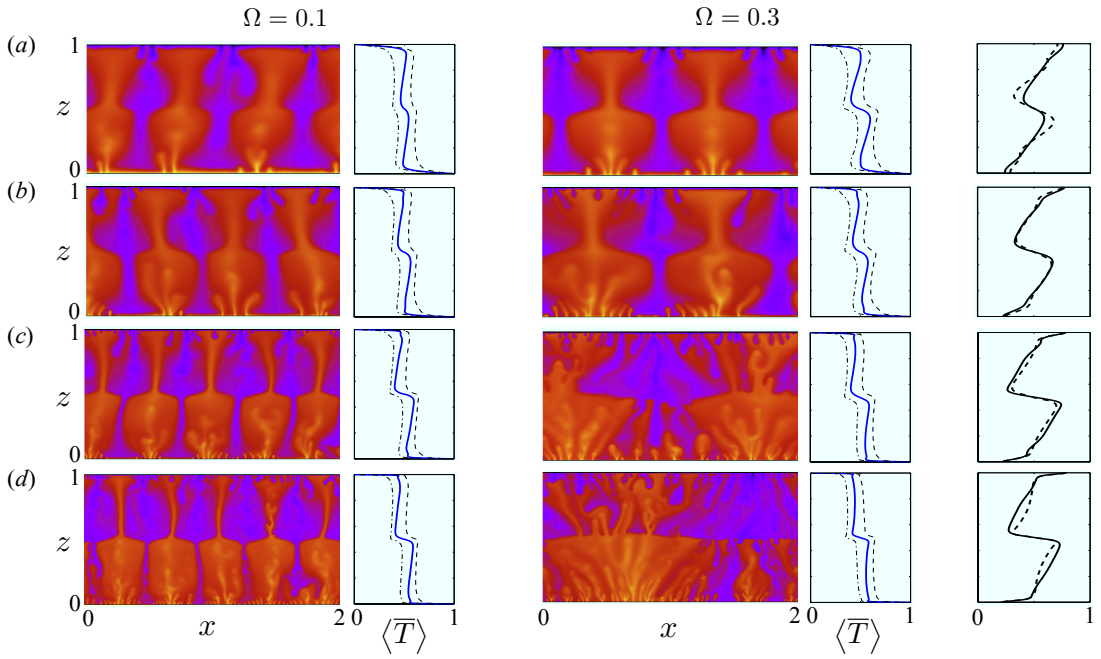


Figure 4.10: Snapshots of the temperature field from reduced simulations for $\Omega = 0.1$ (left) and $\Omega = 0.3$ (right), together with profiles of $\langle \overline{T} \rangle (z)$ (solid lines) and the average temperature of fluid with $w > 0$ (dashed lines) and of fluid with $w < 0$ (dot-dashed lines), for: $(a)$ $Ra = 2500$; $(b)$ $Ra = 5000$; $(c)$ $Ra = 10^4$; and $(d)$ $Ra = 2 \times 10^4$. The right-hand column shows the proportion of the fluid with $w > 0$, for $\Omega = 0.1$ (solid) and $\Omega = 0.3$ (dashed). Although all snapshots are shown over the range $0 \leqslant x \leqslant 2$ for concision, simulations in $(a)$–$(c)$ have aspect ratio $L = 4$, and simulations in $(d)$ have $L = 2$.

We note (with reference to figure 4.9$a$), that $Nu$ increases between $\Omega = 0.1$ and $\Omega = 0.3$ for the lower values of $Ra$ (figure 4.10$a$,$b$), but decreases over this range for the higher values (figure 4.10$c$,$d$). Based on the observations above, the increase in $Nu$ appears to coincide with the increasingly ordered cellular structure, while the absence of such an increase at higher $Ra$ coincides with the presence of protoplumes near the interior layer, which break down the cellular structure and result in a more disordered flow.

It seems likely that one factor which controls whether the flow near the interior layer is unstable to the growth of short-wavelength protoplumes is the distance between the interveaving plumes. It is plausible that the lengthscale for instability should scale with the protoplume lengthscale $\sim Ra^{-1}$ (measured in chapter 2,

figure 2.10). In contrast, as $\Omega \to 0$ the length between the megaplumes is given by the homogeneous scaling of roughly $\sim Ra^{-0.4}$ (2.16). The difference in scaling between $Ra^{-1}$ and $Ra^{-0.4}$ suggests that, as $Ra$ is increased, the flow near $z = 0.5$ should be unstable to the formation of protoplumes at smaller values of $\Omega$, in agreement with the the observations from figure 4.10.

### 4.3.6 Summary of main observations

We have shown that the dynamics of the flow depend only on the ratio $\Omega = h/\Pi$ for $h, \Pi \ll 1$, and a given values of $Ra$ and $L$. We found that the horizontal lengthscale of the flow increases dramatically as $\Omega$ is increased. For small values of $\Omega$, the structure of the flow resembles homogeneous columnar flow. For larger values of $\Omega$, the flow adopts an ordered cellular structure which, for sufficiently large $\Omega$, is unstable to the formation of protoplumes near the interior boundary. For even larger $\Omega$, there is a transition in the dynamics; we surmise that the transition occurs when the advective flux across the inner boundary becomes weaker than the diffusive.

For $Ra = 5000$, we found the unexpected result that the Nusselt number initially increases with $\Omega$, to a maximum at $\Omega \approx 0.25$. For larger values of $\Omega$, $Nu$ decreases. Beyond the transition to the diffusion regime at $\Omega \approx 5$, $Nu$ is independent of $\Omega$. In full simulations with a finite height $h$ of the interior layer, $Nu$ continues to decrease in the diffusion regime as $h$ is increased (figure 4.5).

There are two main differences in this behaviour at different values of $Ra$. First, the initial increase in $Nu$ with $\Omega$ is greater as $Ra$ is decreased, and is weaker as $Ra$ is increased, such that, at $Ra = 2 \times 10^4$, $Nu(\Omega)$ decreases monotonically. Second, as $Ra$ is increased, the formation of protoplumes near the inner boundary appears to occur at a lower value of $\Omega$. Measurements of the decrease in the horizontal wavenumber $k$ over the range of $\Omega$ for which $Nu$ decreases, which are roughly fitted by $k \sim \Omega^{-1/2}$, show no clear dependence on $Ra$ (figure 4.9*b*). Similarly, the value of $\Omega \approx 5$ at which there is a transition in the flow to the diffusion regime appears to be roughly independent of $Ra$.

## 4.4 Simple theoretical models

In order to understand some of the observed behaviour of $Nu(\Omega)$, in this section we develop simple one-dimensional 'toy' models of the statistically steady convective system. These models provide a basis for further study of the dynamical behaviour that we have observed, as discussed in §4.4.3. They involve a balance of the heat flux across the boundary layers at the upper and lower boundaries of the domain and the pressure-driven 'leakage' flux through the interior low-permeability layer, within a one-dimensional horizontally averaged framework.

We derive two simple models of the relationship $Nu(\Omega)$ in each of the regimes identified in §4.3: first, in §4.4.1, for the advection regime ($\Omega \lesssim 5$); and second, in §4.4.2, for the diffusion regime ($\Omega \gtrsim 5$).

For simplicity, in both models, we make the assumption that the horizontally averaged temperature $\overline{T}$ in the upper and the lower layers of the domain is approximately uniform, except in thin boundary regions near $z = 0$, $z = 0.5$ and $z = 1$. We note that this approximation neglects any background stratification in the upper and lower layers; however, as discussed in §4.3.4.1, the apparent observed stratification is largely a reflection of the changing widths of upwelling and downwelling plumes. We therefore set

$$\overline{T} = \Theta(\Omega) \quad \text{in} \quad z > 0.5, \qquad \text{and} \qquad \overline{T} = 1 - \Theta(\Omega) \quad \text{in} \quad z < 0.5, \tag{4.13}$$

as shown schematically in figure 4.11.

We model the flux through the upper and lower layers of the system by a suitable rescaling of the Rayleigh and Nusselt numbers, to relate the flux to that in a homogeneous Rayleigh–Darcy cell. In chapter 2 we found that this flux, $Nu_0(Ra)$, is well described for $Ra \gtrsim 1300$ by

$$Nu_0 = \alpha\, Ra + \beta, \tag{4.14}$$

where $\alpha = 6.9 \times 10^{-3}$ and $\beta = 2.75$. Suitable rescaling can be made as follows. The Rayleigh number is proportional to both a temperature and a height scale, while the Nusselt number is proportional to the same height scale, and inversely proportional to the same temperature scale. In the upper and lower layers, the

driving temperature difference between the boundary and the interior is given by $\Theta(\Omega)$ and the height is $(1-h)/2 \approx 1/2$ in the limit $h \ll 1$. These values can be compared to the homogeneous values of $\approx 1/2$ and 1 for the driving temperature contrast and the height, respectively. The rescaled effective Rayleigh number $R$ and Nusselt number $N$ for the upper and lower cells are thus given by

$$R = 2\Theta\left(\frac{1}{2}\right)Ra = \Theta Ra, \qquad N = \left(\frac{1}{2\Theta}\right)\left(\frac{1}{2}\right)Nu = \frac{Nu}{4\Theta}. \tag{4.15a, b}$$

Under the assumption that $N$ and $R$ are related by (4.14), we deduce the relationship

$$Nu = 4\left(\alpha\Theta^2 Ra + \beta\Theta\right), \tag{4.16}$$

for the convective flux in the upper and lower layers of the domain.

Equation (4.16) is matched with a parameterization of the flux through the thin interior layer, as discussed separately for the advection and diffusion regime below. For the advection regime we work in the limit $h, \Pi \ll 1$, as in the reduced simulations. For the diffusion regime, however, the flux across the interior layer is independent of $\Pi$, and so we develop a model for the flux $Nu(h)$. In the limit $h \to 0$, this model suggests that $Nu \to$ constant, in agreement with the numerical observations from reduced simulations. For both regimes, under the assumption that the dynamics of the flow are mirrored in $z = 0.5$, we consider the flow in $z > 0.5$ only.

### 4.4.1 Advective transport across the interior low-permeability layer

If $\Omega$ is sufficiently small, then fluid can flow relatively easily across the interior layer, and the dominant mechanism for heat transport across the layer is advection. The 'leakage' flux across the layer should therefore scale with $Ra\ w\ T$. We expect that $T$ scales with the temperature difference $\Delta\Theta$ across the interior layer. As we previously observed in §4.3.2, the flow $w$ is driven by the pressure difference $[p]$ across the interior layer, and, from Darcy's law (4.3b), is given by $w \sim [p]/\Omega$. By the symmetry of the system, we might expect that the driving pressure difference $[p]$ across the layer is equal to the horizontal pressure difference

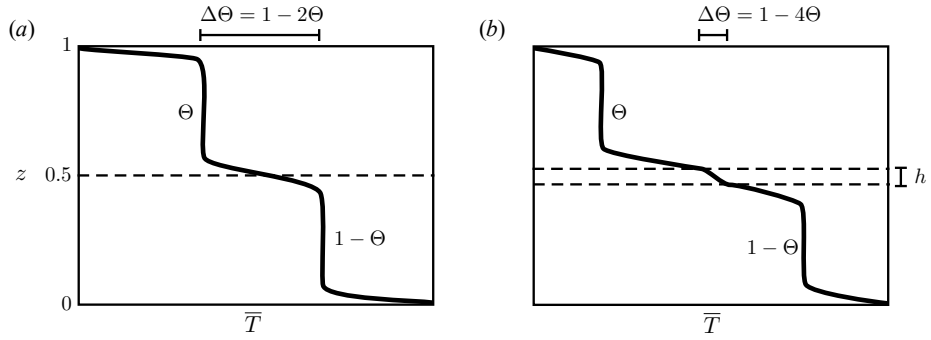


Figure 4.11: A schematic showing profiles of the horizontally averaged temperature $\overline{T}$ in the one-dimensional model setup: $(a)$ for the advection regime in the limit $h, \Pi \ll 1$; and $(b)$ for the diffusion regime. For the diffusion regime in the limit $h, \Pi \to 0$ such that $\Omega$ remains large, $\Theta \to 1/4$.

between upwelling and downwelling plumes on either side of the layer. Under the assumption that the horizontal pressure difference is predominantly hydrostatic, we deduce that $[p] \sim \Delta\Theta$. Therefore, upon substitution of the expression for $\Delta\Theta = 1 - 2\Theta$ (see figure 4.11$a$), the leakage flux is parameterized by

$$Nu = \gamma Ra\, w\, T = \gamma Ra\, \frac{(1-2\Theta)^2}{\Omega}, \tag{4.17}$$

for some constant $\gamma$.

Since the convective flux is the same throughout the domain, we equate (4.16) and (4.17) to generate a quadratic equation for $\Theta(\Omega)$. Only one root of this equation lies in the range $0 \leqslant \Theta \leqslant 1$; this root combined with (4.17) yields an expression for the flux given by

$$Nu(\Omega) = \frac{\gamma}{Ra}\left[\frac{(\alpha Ra + \beta)\,\Omega^{1/2} - \sqrt{\beta^2\Omega + 2\beta\gamma Ra + \alpha\gamma Ra^2}}{\alpha\Omega - \gamma}\right]^2. \tag{4.18}$$

We note that both the numerator and the denominator of (4.18) vanish at $\Omega = \gamma/\alpha$, such that $Nu(\Omega)$ remains well defined.

Figure 4.12 shows a comparison of numerical measurements of $Nu(\Omega)$ and the predictions of (4.18). Based on a rough fit with the data at $Ra = 2\times10^4$, we used a value $\gamma = 0.1$. While the model does not describe the initial increase of $Nu(\Omega)$

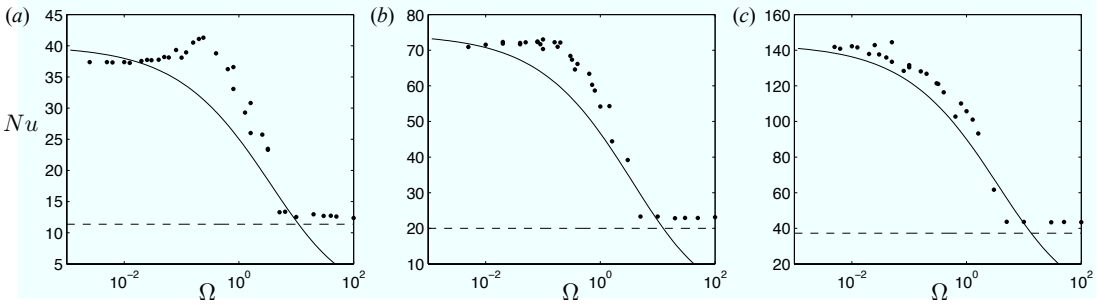


Figure 4.12: A comparison of measurements of $Nu(\Omega)$ from reduced simulations and the predictions of the simple models, in the advection regime (4.18) with $\gamma = 0.1$ (solid lines) and in the diffusion regime (4.21*b*), for: (*a*) $Ra = 5000$; (*b*) $Ra = 10^4$; and (*c*) $Ra = 2 \times 10^4$.

for $Ra < 10^4$, it does gives a rough qualitative fit to the decrease of $Nu$ as $\Omega$ is increased. The predictions appear to underestimate the slope of the decrease in $Nu(\Omega)$ for relatively large values of $\Omega$. Based on a comparison of the shape of the predicted relationship $Nu(\Omega)$ and the measured data, figure 4.12 suggests that the model gives an increasingly good fit as $Ra$ is increased. A discussion of the limitations and possible extensions to this simple model is given in §4.4.3 below.

### 4.4.2 Diffusive transport across the interior low-permeability layer

In §4.3.4, we found that, for sufficiently large values of $\Omega$, the leakage flux is primarily diffusive. In the diffusion regime there is very little flow across the interior layer; the system resembles two homogeneous Rayleigh–Darcy cells placed one on top of the other, and there are boundary-layer regions above and below the interior layer as well as near the upper and lower boundaries of the domain (see figure 4.11*b*).

The flux given by (4.16) must be matched with the diffusive flux across the interior layer, which, if the layer has depth $h$, is given by

$$Nu \approx \frac{\Delta\Theta}{h} = \frac{1 - 4\Theta}{h}, \tag{4.19}$$

(see figure 4.11*b*). The Nusselt number $Nu(h)$ is determined by equating (4.16)

and (4.19), solving the resultant quadratic equation for $\Theta(h)$ (choosing the root in the range $0 < \Theta < 1$), and recombining to give

$$Nu = \frac{1}{\alpha Rah^2}\left[(\alpha Ra + 2\beta)\,h + 2 - 2\sqrt{\alpha\,Ra\,h + (1+\beta h)^2}\right]. \tag{4.20}$$

Predictions of $Nu(h)$ given by (4.20) were included in figure 4.4($a$); they show that $Nu$ decreases as $h$ is increased, and give very good agreement with numerical measurements for $\Pi = 0$.

In the limit $h, \Pi \ll 1$, the interior temperature and Nusselt number from (4.20) reduce to

$$\Theta = \frac{1}{4} - O(h) \qquad \text{and} \qquad Nu = \frac{1}{4}\alpha\,Ra + \beta - O(h). \tag{4.21$a$, $b$}$$

Thus, in the limit $h \to 0$, $Nu$ is a constant, as we observed in numerical measurements of the diffusion regime from reduced simulations (figure 4.5). Predictions of (4.21$b$) give relatively good agreement with these measurements at large $\Omega$ (figure 4.12, dashed lines), although they appear to slightly underestimate the measurements. This small difference is discussed in §4.4.3 below.

We expect $Nu$ to be described by (4.20) and (4.21) when advection through the interior layer is weaker than diffusion. A balance of the advective flux (4.17) and the diffusive flux (4.19) through the interior layer gives a condition for the flow to be in the diffusion regime of $\Pi < (\gamma Ra)^{-1}$. In the limit $h, \Pi \to 0$, however, the condition is instead determined by a comparison of (4.21) and (4.18), which gives

$$\Omega > \frac{\gamma}{\alpha + 4\beta/Ra}. \tag{4.22}$$

Equation (4.22) has only a very weak dependence on $Ra$ at high $Ra$, in agreement with the observation in figure 4.9($a$) that the transition to the diffusion regime in the limit $h, \Pi \ll 1$ occurs at a value of $\Omega$ that is roughly independent of $Ra$. It should be noted that the quantitative predictions of (4.22) are somewhat larger ($\Omega \approx 12.5$ at $Ra = 10^4$ and $\gamma = 0.1$) than the value observed for the transition to the diffusion regime in figure 4.9($a$) of $\Omega \approx 5$.

### 4.4.3 Discussion

The results of figure 4.12 demonstrate that some of the observed features of the relationship $Nu(\Omega)$ can be qualitatively described by simple one-dimensional models, in which the fluxes are parameterized in terms of the average temperatures in each half of domain. However, there are some very notable differences between the model prediction and the numerical measurements in the advection regime; the extent of these differences is perhaps surprising, and would seem to reflect the need to go beyond a simple one-dimensional framework to describe some of the features of the flow that we observed in §4.3.

In the advection regime, the model suggests that the decrease in $Nu(\Omega)$ as $\Omega$ is increased is controlled by a balance between the increased pressure needed to drive plumes through the interior low-permeability layer and the the pressure differences that arises from the buoyancy contrasts between these interleaving plumes. Based on the observations of §4.3, there are a variety of possible extensions of this idea. An important and inherently two-dimensional feature of the flow that we observed in §4.3 is the cellular structure, combined with the asymmetry between upwelling and downwelling plumes and the non-uniform width of these plumes with height. The cellular flow structure appears to be related to the surprising increase in $Nu(\Omega)$ for small $\Omega$, which is not described by our one-dimensional model. Another feature of the flow that is not included in the present model is the presence of protoplumes near the interior layer. We previously observed in §4.3.5 that protoplumes partially break down the cellular structure and reduce the asymmetry between upwelling and downwelling plumes. It is plausible that mixing due to protoplumes would decrease the temperature contrasts between the exchange flow on either side of the interior layer, which would decrease the horizontal pressure differences there, and thus weaken the flow across the layer and reduce the flux. Indeed, figure 4.8 shows that the trend in the measurements of $T_{\text{rms}}$ at $z = 0.5$ with $\Omega$ is disrupted over roughly the range of $\Omega$ for which there are protoplumes near the interior layer. According to this hypothesis, mixing due to protoplumes is responsible for the underestimate of the slope of the curve of $Nu(\Omega)$ in the model, observed in figure 4.12.

In the diffusion regime, the simple model describes the diffusive flux between

two cells in which the dynamics evolve independently of each other. The model has no undetermined parameters, and gives a good prediction of measurements of the flux from full simulations with $\Pi = 0$, and of the constant flux from reduced simulations in the limit $h \to 0$. In both cases, the predictions lie slightly below the measured flux; we anticipate that this small underestimate is related to the implicit assumption in the model that the temperature at the boundaries with the interior layer is uniform. In measurements from reduced simulations, we observed non-zero horizontal fluctuations in $T$ at $z = 0.5$ (figure 4.7$d$), which will induce flow, potentially leading to thinner diffusive boundary layers above and below the interior layer and a larger flux than the model predicts.

The simple models developed above are independent of the dominant horizontal lengthscale of the flow. In figure 4.9($b$), we presented measurements of the dominant horizontal wavenumber $k$ of the flow through the interior layer, which were very roughly fitted by a scaling of $k \sim \Omega^{-1/2}$. A simple argument for this scaling can be developed by a combination of mass conservation and continuity of pressure across the interior layer, as follows. Mass conservation in each half of the domain gives $w \sim u/x \sim ku$, while the balance of pressures near the interior layer, discussed in §4.4.1, gives $w \sim [p]/\Omega$ and $u \sim [p]/x \sim k[p]$. These scalings combine to give $k \sim \Omega^{-1/2}$. Physically, the scaling argument is saying that, as $\Pi$ is decreased or $h$ increased, a larger pressure difference is required to drive flow across the interior layer owing to the increased impedance $\Omega$. The corresponding increase in the horizontal pressure difference between the interleaving plumes, which drives flow across the interior layer, drives larger horizontal velocities in the upper and lower layers, where, by mass conservation, the horizontal lengthscale of the flow must increase. It is important to note that this scaling argument rests on the assumption that $w$ in the upper and lower layers of the domain scales with $w$ through the interior layer, and a theoretical basis for this assumption is not evident. There is some suggestion from the numerical measurements in figure 4.7 that the assumption may be reasonable over the range of $\Omega$ for which the scaling $k \sim \Omega^{-1/2}$ is observed.

In addition to further developments to the modelling of this system, to understand more of the observed features of the flow, there are a number of directions in which this work could be extended. In particular, it would be interesting to

consider the effect of multiple low-permeability layers. It would also be interesting to develop the statistically steady results of this chapter to time-evolving systems of convection from one boundary alone ('one-sided systems'), which have a more direct physical applicability.

## 4.5 Conclusions

We have undertaken a detailed numerical investigation of statistically steady convection at high $Ra$ in a cell containing an interior low-permeability layer of height $h$ and relative permeability $\Pi < 1$. In the limit $h, \Pi \ll 1$, we found that the flow depends only on the parameter $\Omega = h/\Pi$, and that the interior layer can be parameterized by a jump condition for the horizontal velocity at $z = 0.5$. We developed reduced numerical simulations which solved the jump condition, and found good agreement with fully resolved numerical simulations, for a range of values of $h$ and $\Pi$.

In §4.3.4, we examined the structure of the flow for $Ra = 5000$, in the reduced framework $h, \Pi \ll 1$. We found that, for $\Omega \gtrsim 0.05$, the flow develops an ordered cellular structure with a horizontal lengthscale that increases dramatically with $\Omega$. Each cell is roughly half the height of the domain, and comprises a thin vertical plume carrying fluid in one direction and a much wider plume carrying the return flow, together with some 'leakage' of buoyancy across the interior layer. Remarkably, $Nu$ increases as $\Omega$ increases (i.e. as the permeability of the interior layer decreases) in this dynamical regime. For $\Omega \gtrsim 0.3$, the flow is unstable to the formation of protoplumes near the interior layer; the flow becomes less ordered, and $Nu$ decreases. For $\Omega \gtrsim 5$, advection through the interior layer is weaker than diffusion, and the flow structure changes completely to resemble two independent cells placed one on top of the other. We found that the structure of the flow and the associated convective flux are strongly affected by hysteresis, likely owing, at least in part, to restriction imposed on the flow by the horizontal periodicity of the domain.

In §4.3.5, we explored the dependence of this behaviour on $Ra$. We found that the initial increase in $Nu$ with $\Omega$ was more pronounced at smaller $Ra$, and less pronounced at larger $Ra$. We also found that, as $Ra$ is increased, the flow

near the interior layer is unstable to the growth of protoplumes at lower values of $\Omega$. Measurements of the dominant horizontal wavenumber $k$ at $z = 0.5$ suggest that the increase in the horizontal lengthscale with $\Omega$ roughly fits a scaling of $k \sim \Omega^{-1/2}$, with no clear dependence on $Ra$.

In §4.4, we developed one-dimensional models that describe the the behaviour of $Nu(\Omega)$, for both the advection regime and the diffusion regime. These simple models give a rough qualitative description of the decrease in $Nu(\Omega)$ with $\Omega$ and of the transition to the diffusion regime, but also display a number of differences from the measurements, which raises interesting questions for further modelling of the system, as discussed in §4.4.3.

In this numerical study, we have observed a number of surprising features of the flow in the presence of a thin low-permeability layer. Two observations are particularly striking: the dramatic increase in the horizontal lengthscale of the flow with $\Omega$, and the unexpected increase in $Nu$ with $\Omega$ for some values of $Ra$. These observations could have important consequences in physical settings. In particular, the ability to engineer an increase in the transfer of buoyancy in a porous convective system by the simple addition of a thin lower-permeability layer could be of significant industrial value.

# Appendix

## 4.A Discussion of the assumption of uniform porosity

Throughout this paper we make the assumption that the porosity $\phi$ is uniform throughout the domain, and is thus independent of the permeability $K$. Typical models of the relationship $K(\phi)$ (such as the Kozeny–Carman model) suggest that the porosity scales with roughly the cube root of the permeability (Bear, 1988), such that changes in the porosity are likely to be much weaker than changes in the permeability.

Here we briefly consider the qualitative effect of a lower porosity in the thin low-permeability interior layer. Suppose that the porosity of the upper and lower layers is $\phi_1$, while that of the interior layer is $\phi_2 < \phi_1$. The flow $\boldsymbol{u}$ is determined by the solution of the Poisson equation (4.3b), and is thus not directly dependent on the porosity. Under the assumption that the flow through the interior layer is not dominated by time-dependent dynamics, the advective flux through the layer, which scales with $wT$, is not significantly affected by a decrease in the porosity. The diffusivity, however, is multiplied by the porosity (see (4.1d)), and so the diffusive flux would be scaled by a factor of $\phi_2/\phi_1$. Thus, we might anticipate that a lower porosity in the interior layer would not have an appreciable effect on the flux in the advection regime, but would lead to a lower flux in the diffusion regime. As a result, the transition between advection and diffusion regimes would likely occur at a larger value of $\Omega$. A simple parameterization of the effect of a lower porosity in the interior layer could be incorporated into our model of the flux in the diffusion regime (§4.4.2), by including a factor of $\phi_2/\phi_1$ in (4.19), which is equivalent to the rescaling $h \to h(\phi_1/\phi_2)$.

# Chapter 5

# Shutdown of convection in a porous medium I: fixed interface

The material contained in both this and the following chapter has been published in the *Journal of Fluid Mechanics*, under the title 'Convective shutdown in a porous medium' (Hewitt *et al.*, 2013*a*). This chapter contains the first half of the paper. The paper was selected to be the subject of a Focus on Fluids review article (Pritchard, 2013), and figure 6.5(*a*) was adapted for the front-cover picture of the journal.

## 5.1 Introduction

In chapter 2, we explored in detail the flow in a Rayleigh–Darcy cell, which provides a canonical system for the study of convection. The Rayleigh–Darcy cell is a 'two-sided' system, in which there is convective transport away from both the upper and lower boundaries. The system therefore attains a statistically steady state, which allows both for examination of the dynamical structures and emergent patterns of the flow, and for accurate characterization of the convective flux.

Natural convective systems in porous media tend instead to be driven by a source of buoyancy on one boundary alone. We refer to such systems as 'one-sided'. There are fundamental questions relating to the differences and similarities of the dynamics between one-sided and two-sided convective systems, some of

which we address in this chapter and the next. For clarity, when we consider one-sided systems we will assume throughout that the convective flow is downwards, away from an active upper boundary. All the other boundaries of the domain are assumed to be impermeable and perfectly insulating. Furthermore, in contrast to the previous chapters of this dissertation, we consider systems in which convection is driven solely by compositional density differences, such that the density $\rho^*$ of the fluid is a function of the concentration of solute $C^*$ only. It should be noted, however, that the governing equations are equally applicable both to convection from a buoyant source at the base of the domain, and to thermal convection, provided that heat transfer in the solid phase of the medium can be neglected (as discussed in §1.2).

This chapter and the next are closely linked, and, for clarity, are introduced together. The principal objective of this chapter is to examine the relationship between two-sided and one-sided convection with a fixed upper boundary. Then, in chapter 6, we will extend these ideas to examine different physically motivated one-sided systems, each of which comprises two fluid layers with a moving interface (such as in the case of sequestered $CO_2$ and brine).

Previous work on the two-dimensional Rayleigh–Darcy cell was discussed in §1.3. This work has focused on examining the dimensionless heat (or solute) flux through the cell, as described by the Nusselt (or Sherwood) number $Nu$, and the corresponding dynamical structures of the flow, as functions of the Rayleigh number $Ra$. In chapter 2, we examined the flow in a Rayleigh–Darcy cell in the 'high-$Ra$' regime ($Ra \gtrsim 1300$). We recall that the dynamical structure in this regime is dominated by vertical columnar 'megaplumes' that extend across the interior of the domain, and are driven by entrainment and mixing of small 'protoplumes' near the upper and lower boundary. Numerical measurements of $Nu$ were extremely well described by a function of the form $Nu = \alpha Ra + \beta$, for constant $\alpha$ and $\beta$ (see §2.3).

In contrast to the two-sided, statistically steady Rayleigh–Darcy configuration, the dynamics and the buoyancy flux in a one-sided convective system evolve over time. Many previous studies of one-sided convective systems have focused on the conditions required for the onset of convection, which presents significant theoretical challenges as the diffusive base state is both time-dependent and non-

linear. Various theoretical studies (Riaz *et al.*, 2006; Xu *et al.*, 2006; Hassanzadeh *et al.*, 2006; Slim & Ramakrishnan, 2010) have been complemented by direct numerical investigations (Riaz *et al.*, 2006; Hassanzadeh *et al.*, 2007) and laboratory experiments (Fernandez *et al.*, 2002; Backhaus *et al.*, 2011; Slim *et al.*, 2013) that explore the onset of convection.

After onset, the convective flow is dominated by large dense plumes which merge and coarsen as they descend. These descending plumes are fed by the entrainment of smaller plumes near the upper boundary, which are themselves generated episodically by short-wavelength instabilities in the boundary layer. The system evolves independently of the depth of the domain until the largest plumes reach the lower boundary. There have been a number of numerical studies for $Ra \lesssim O(10^3)$ which examine the evolution of the dynamics and the merging of descending plumes before they interact with the lower boundary (Pau *et al.*, 2010; Hassanzadeh *et al.*, 2007). Slim *et al.* (2013) performed experiments in a Hele-Shaw cell for $100 < Ra < 1700$, and categorized the evolution of the system from the onset of convection in detail. In a recent study, Slim (2013) explored the same evolution numerically. Further experimental studies by Neufeld *et al.* (2010) for $5 \times 10^4 < Ra < 6 \times 10^5$ in a quasi-2D porous medium, and by Backhaus *et al.* (2011) for $6 \times 10^3 < Ra < 9 \times 10^4$ in a Hele-Shaw cell, provided measurements of the convective flux after the onset of convection.

When the descending plumes reach the lower boundary, the domain begins to fill up with dense fluid. Once this dense fluid reaches the upper boundary, the dynamics of the system change and the convective flux begins to decrease. The qualitative behaviour of the flux in this 'shutdown' regime has been observed in numerical simulations by Hassanzadeh *et al.* (2007) for $Ra < 1000$, although they provided no theoretical analysis of the system. Slim *et al.* (2013) presented experimental results in this regime for $100 < Ra < 1700$, and derived a phenomenological model which describes the evolution of the flux based on an *ad hoc* parameterization of the typical boundary-layer depth. We are not aware of any studies that explore the shutdown regime, in which the convective flux steadily decreases, for $Ra > 1700$.

In this chapter and the next, we focus on the evolution of the dynamics and the convective flux during the shutdown regime for $Ra > O(10^3)$. In this chap-

ter, we show that the evolution of the flux in this one-sided problem can be directly calculated using measurements of the convective flux from a Rayleigh–Darcy cell. We develop a simple theoretical 'box' model for this system that uses these measurements to predict the timescales for shutdown, and compare the results to high-resolution numerical simulations. Furthermore, we find that the dynamical structure of the flow in the shutdown regime exhibits a remarkable similarity to that in a Rayleigh–Darcy cell: the flow is dominated by vertical columnar 'megaplumes' that extend across the height of the domain, and the lateral spacing of these plumes increases as the average concentration increases and the system shuts down, in excellent quantitative agreement with measurements from a Rayleigh–Darcy cell. Motivated by previous experimental systems (Neufeld *et al.*, 2010; Backhaus *et al.*, 2011) with a nonlinear density curve, we also examine how the rate of shutdown depends on the form of the density $\rho^*(C^*)$ by considering a power-law equation of state.

In chapter 6, we will develop these ideas to model convective systems comprising two fluid layers, with an interface that that is free to move, as discussed in more detail in §6.1.

## 5.2 Overview of physical systems for chapters 5 and 6

In this chapter and the next, we explore three different model systems for one-sided convection in a porous medium, each with different physical applications (figure 5.1). The systems are distinguished primarily by different properties of the active interface at the top of the convecting region: the first system is a 'fixed-interface' system, in the sense that the interface is stationary and is located at a fixed upper boundary; the second and third systems are 'free-interface' systems, in the sense that the active interface is free to move and divides the convecting region below from a non-convecting region of fluid above. The second and third systems are distinguished by whether the fluids on either side of the interface are immiscible or miscible, as discussed below.

The first system is the 'fixed-interface' system, in which the convective flux

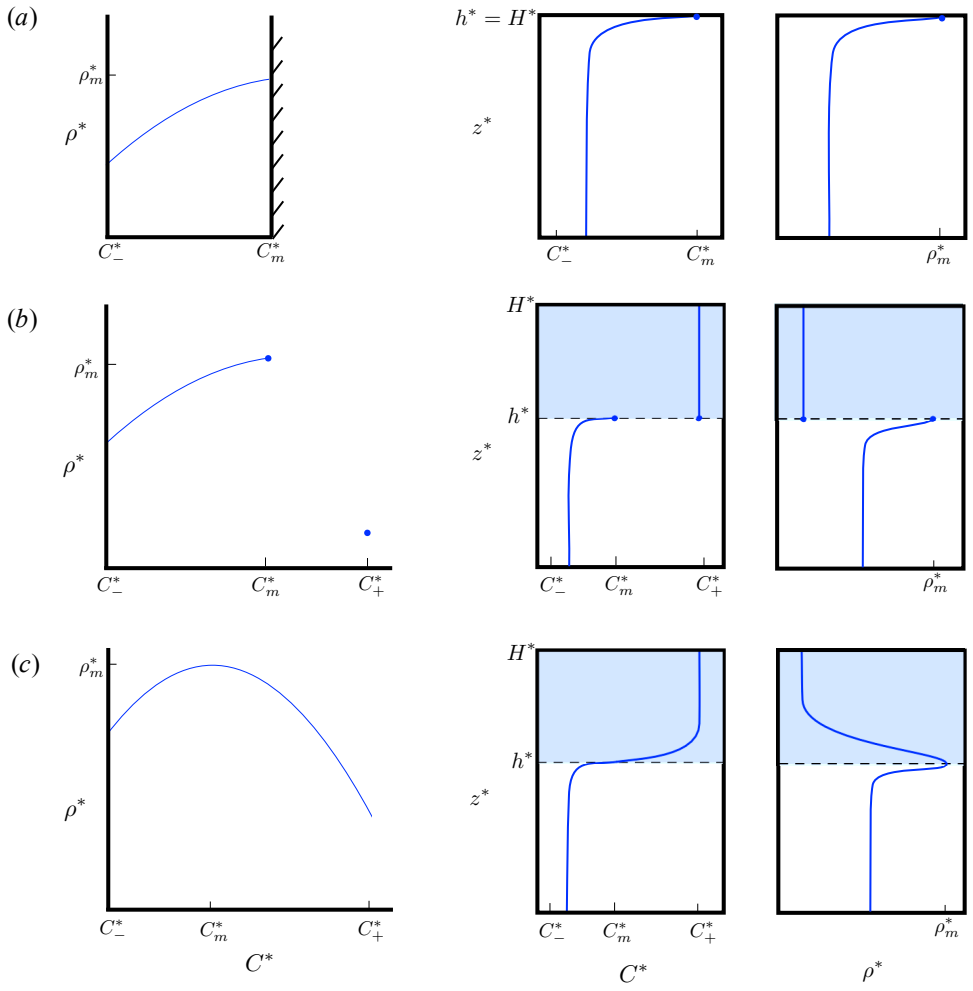


Figure 5.1: A schematic diagram showing typical equations of state $\rho^*(C^*)$, vertical concentration profiles $C^*(z^*)$, and vertical density profiles $\rho^*(z^*)$, for each of the three physical systems outlined in the text (§5.2). In each case the maximum density $\rho^*_m$ is attained at concentration $C^*_m$, the interfacial height is given by $z^* = h^*$, and the domain has constant depth $H^*$: $(a)$ the 'fixed-interface' system, with a stationary upper boundary $z^* = h^* = H^*$ held at concentration $C^*_m$; $(b)$ the 'immiscible' (free-interface) system, in which fluid with concentration $C^*_+$ overlies fluid with initial concentration $C^*_-$, and the upper fluid is partially soluble in the lower; $(c)$ the 'miscible' (free-interface) system, in which the two fluids are fully soluble, and the interfacial height $z^* = h^*$ is given by the isopycnal of maximum density.

away from an interface does not significantly change its height. There are a broad range of geophysical systems for which this is an excellent approximation, including the convection of saline groundwater driven by evaporation at the upper surface (Duffy & Al-Hassan, 1988; Wooding *et al.*, 1997*a*,*b*), and the extraction of geothermal energy driven by underground heat sources (Cheng, 1978; Goldstein *et al.*, 2011). We consider a fluid that initially contains a dissolved solute at some concentration $C_-^*$. The upper boundary of the domain is held at a fixed larger concentration $C_m^*$. We consider a density curve that increases monotonically from $\rho^*(C_-^*)$ to $\rho_m^* = \rho^*(C_m^*)$. A typical density curve for such a system is shown schematically in figure 5.1($a$), together with vertical profiles of the concentration and density. Diffusion of solute across the upper boundary forms a dense solution which is unstable to downwards convection. Over time, the concentration increases from $C_-^*$ towards $C_m^*$, and convection gradually shuts down.

The second and third systems form two different sorts of 'free-interface' system, in which the convective flux away from an interface causes the interface to move. These are typically two-component systems, which initially comprise a light fluid A overlying a dense fluid B. Dissolution of A into B creates fluid that is more dense than pure B. The system is thus unstable to convection, and the active interface between the two layers moves as A dissolves into B and convection transports the dense solution down into the lower layer. The concentration $C^*$ describes that of the solution of A in B, with pure A having concentration $C_+^*$, and pure B having concentration $C_-^* < C_+^*$. Mathematically, this is related to the classical Stefan problem (see *e.g.* Hill 1987), and our approach to the modelling is similar to that used for convection in a (non-porous) fluid layer below a melting interface (e.g. Huppert & Sparks 1988*a*,*b*; Huppert 1989).

We consider two qualitatively different free-interface systems, which correspond to immiscible and miscible fluids respectively. In the 'immiscible' system, A is only partially soluble in B, and, for simplicity, we assume that B is not at all soluble in A. The density is largest ($\rho^* = \rho_m^*$) at the maximum concentration of A in B, denoted by $C_m^*$. The concentration $C^*$ cannot lie in the range $C_m^* < C^* < C_+^*$, and, as such, there is a discontinuity in the concentration and density fields at the interface, which divides pure A above from a solution of A

in B below. This behaviour can be seen in figure 5.1($b$), which shows a typical density curve for the immiscible system, together with vertical profiles of the concentration and density.

In contrast, in the 'miscible' system A and B are fully soluble, and the equation of state $\rho^*(C^*)$ is continuous, with a maximum at some intermediate concentration $C^*_m$ as shown schematically in figure 5.1($c$). There is a qualitative distinction here from the immiscible system, in that there is not a genuine interface between different fluids when the fluids are miscible. Instead, we define the interface to be equal to the contour of maximum density ($\rho^* = \rho^*_m$). This isopycnal separates stably stratified fluid above from unstably stratified fluid below, and is therefore an interface in the sense that it lies between regions of dynamically different fluid behaviour.

Both immiscible and miscible systems have important applications, most pertinently to the subject of $CO_2$ sequestration. Supercritical $CO_2$ and brine are immiscible, with $CO_2$ being only $3-5\%$ soluble by weight in brine under typical storage conditions (van der Meer, 2005). In contrast, many experimental analogues of sequestration systems are based on mixtures of glycol and water, and form miscible systems (e.g. Neufeld *et al.* 2010; Backhaus *et al.* 2011).

In this chapter and the next, we develop a series of mathematical models which describe the different physical systems that we have introduced above. In this chapter, we examine the 'fixed-interface' system. In chapter 6, we examine both immiscible and miscible free-interface systems; first, under the assumption that the interface remains flat, and second, when this assumption is relaxed and the interface is free to deform. The layout of chapter 6 is discussed in §6.1.

The layout of this chapter is as follows. In §5.3, we present the governing equations, non-dimensionalization, and numerical scheme used to model these different one-sided systems. In §5.4, we present the results of high-resolution numerical calculations of the fixed-interface system. Motivated by these results, in §5.5 we derive a simple theoretical 'box' model of this system, which describes the shutdown of the solute flux over time using measurements of $Nu(Ra)$ from a Rayleigh-Darcy cell. We compare the theoretical and numerical results in §5.6. We also show, in §5.7, that the dynamical structure of the flow in the one-sided system can be accurately predicted by measurements from a Rayleigh–Darcy cell.

Finally, in §5.8, we summarize the main results.

## 5.3 Governing equations for chapters 5 and 6

### 5.3.1 Dimensional equations

In common with the previous chapters of this dissertation, we consider the flow of a Boussinesq fluid in a two-dimensional, homogeneous, isotropic porous medium, with horizontal and vertical co-ordinates $x^*$ and $z^*$ respectively. We assume that the flow $\boldsymbol{u}^* = (u^*, w^*)$ obeys Darcy's law and is incompressible,

$$\boldsymbol{u}^* = -\frac{K}{\mu}\left(\boldsymbol{\nabla} p^* + \rho^* g \hat{\boldsymbol{z}}^*\right), \qquad \boldsymbol{\nabla}\cdot\boldsymbol{u}^* = 0, \tag{5.1$a$, $b$}$$

where $K$ is the permeability of the porous medium and $\mu$ is the fluid viscosity, both of which are assumed to be constant, $p^*$ is the pressure field, $g$ is the acceleration due to gravity, and $\hat{\boldsymbol{z}}^*$ is a unit vector in the positive $z^*$ direction. Unlike in previous chapters, the density $\rho^*$ is a function of the local concentration $C^*$. The concentration $C^*$ evolves in time $t^*$ by advection and diffusion,

$$\phi\frac{\partial C^*}{\partial t^*} = -\boldsymbol{u}^*\cdot\boldsymbol{\nabla} C^* + \phi D\nabla^2 C^*, \tag{5.2}$$

where $\phi$ is the porosity of the porous medium and $D$ is the diffusivity, both again assumed to be constant. We recall that these equations are equally applicable to thermal convection, provided heat transfer in the solid phase of the medium can be neglected (see §1.2).

We consider here the boundary and initial conditions for both fixed-interface systems, which are the subject of this chapter, and free-interface systems, which are the subject of chapter 6. The fixed-interface system has a stationary active upper boundary. The domain has height $h_0^*$ and width $L^*$, and the upper boundary has an imposed constant concentration $C^*|_{z^*=h_0^*} = C_m^*$ and no vertical velocity $w^*|_{z^*=h_0^*} = 0$. The lower and side boundaries have zero mass and buoyancy fluxes,

$$w^* = \frac{\partial C^*}{\partial z^*} = 0 \text{ at } z^* = 0, \qquad u^* = \frac{\partial C^*}{\partial x^*} = 0 \text{ at } x^* = 0, L^*. \tag{5.3$a$, $b$}$$

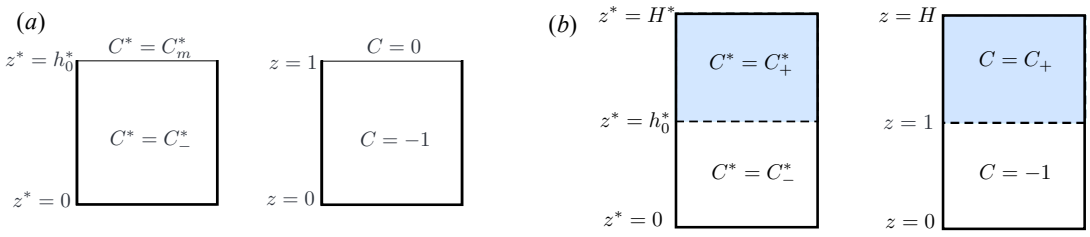


Figure 5.2: A schematic showing the initial conditions in both dimensional and dimensionless variables: $(a)$ the fixed-interface system with a stationary upper active boundary, which is the subject of this chapter; $(b)$ free-interface systems (either immiscible or miscible) with an interfacial height that evolves in time, which are the subject of chapter 6.

The medium is initially saturated with fluid at a concentration $C_-^* < C_m^*$. The initial and boundary conditions for this system are shown schematically in figure 5.2$(a)$, and the equation of state is discussed below.

Free-interface systems (both immiscible and miscible) have an active interface that is located in the interior of the domain, and is free to move. The domain has a constant depth $H^*$ and width $L^*$, with zero mass and buoyancy fluxes on every boundary,

$$w^* = \frac{\partial C^*}{\partial z^*} = 0 \text{ at } z^* = 0, H^*, \qquad u^* = \frac{\partial C^*}{\partial x^*} = 0 \text{ at } x^* = 0, L^*. \qquad (5.4a, b)$$

The medium is initially saturated with fluid in two layers (figure 5.2$b$): a lower layer of concentration $C_-^*$, and an upper layer of concentration $C_+^* > C_-^*$. The density of the lower layer $\rho_-^* = \rho^*(C_-^*)$ is greater than the density of the upper layer $\rho_+^* = \rho^*(C_+^*)$, and, as such, the system is stable to large-scale overturning. The initial height of the interface between the layers is given by $z^* = h_0^*$. For $t^* > 0$, the interfacial height is given by $z^* = h^*(x^*, t^*)$, which is defined to be the contour of maximum density $\rho^* = \rho_m^*$. The details of how the location of the interface is determined over time in each of the different model frameworks that we employ are discussed in §6.2 and §6.3.

For both fixed-interface and free-interface systems, we consider general power-

law equations of state,

$$\rho^* = \rho^*_m \left[1 - b\,(C^*_m - C^*)^n\right], \tag{5.5}$$

where $b > 0$ is a constant coefficient and $n$ is a positive integer. The maximum density, given by the constant $\rho^*_m$, is attained at concentration $C^*_m$. For the fixed-interface system, the concentration $C^*$ is always less than $C^*_m$, and so $\rho^*(C^*) \leqslant \rho^*_m$ irrespective of $n$. For immiscible free-interface systems, the concentration above the interface is fixed at $C^* = C^*_+$, while below the interface the concentration is again always less than $C^*_m$. For miscible free-interface systems, however, (5.5) holds for $C^* > C^*_m$, and so we require $n$ to be an even (positive) integer in order to satisfy $\rho^*_+ < \rho^*_-$. Representative equations of state for each system are shown in figure 5.1. In this paper we focus primarily on either linear ($n = 1$) or quadratic ($n = 2$) equations of state.

### 5.3.2 Dimensionless equations

For all the systems considered, we define a density scale $\Delta\rho^* = \rho^*_m b(C^*_m - C^*_-)^n$ to be the difference between the maximum density and the initial density of the lower layer, and a convective velocity scale $U^* = Kg\Delta\rho^*_m/\mu$. We also define the dimensionless interfacial height $h$, concentration $C$ and density $\rho$ to be

$$h = \frac{h^*}{h^*_0}, \qquad C = \frac{C^* - C^*_m}{C^*_m - C^*_-}, \qquad \rho = 1 + \frac{\rho^* - \rho^*_m}{\Delta\rho^*}. \tag{5.6$a, b, c$}$$

The dimensionless concentration below the interface is then negative, and $C = 0$ at the interface where the density is maximum ($\rho = 1$). We scale lengths with the initial interfacial height $h^*_0$, velocities with $U^*$, pressures with $\mu U^* h^*_0/K$, and times with the convective time scale $T^* = \phi h^*_0/U^*$.

Rescaling in this way gives dimensionless governing equations

$$\boldsymbol{u} = -\left[\boldsymbol{\nabla} P - (-C)^n \hat{\boldsymbol{z}}\right], \tag{5.7}$$

$$\boldsymbol{\nabla} \cdot \boldsymbol{u} = 0, \tag{5.8}$$

$$\rho = 1 - (-C)^n \,, \tag{5.9}$$

$$\frac{\partial C}{\partial t} = -\boldsymbol{u} \cdot \boldsymbol{\nabla} C + \frac{1}{Ra_0} \nabla^2 C, \tag{5.10}$$

with a reduced pressure $P = p + z/[b(C_m^* - C_-^*)^n]$, and an initial Rayleigh number

$$Ra_0 = \frac{h_0^* U^*}{\phi D} = \frac{h_0^* K g \Delta\rho^*}{\phi D \mu}. \tag{5.11}$$

For the fixed-interface system, the dimensionless initial condition is $C(x, z, t = 0) = -1$, and the upper boundary condition is $C|_{z=1} = 0$. For free-interface systems, the dimensionless initial concentration profile is given by

$$C(x, z, t = 0) = \begin{cases} -1 & \text{for } 0 \leqslant z \leqslant 1, \\ C_+ & \text{for } 1 < z < H, \end{cases} \tag{5.12}$$

as shown schematically in figure 5.2.

### 5.3.3 Numerical method

As in previous chapters, the requirement of incompressibility (5.8) can be satisfied by introducing a streamfunction $\psi$, with $(u, w) = (\psi_z, -\psi_x)$, and we can eliminate pressure by taking the curl of (5.7), to give

$$\nabla^2 \psi = -\frac{\partial}{\partial x} (-C)^n \,. \tag{5.13}$$

Equations (5.10) and (5.13) were solved numerically. The numerical method is briefly outlined here, and discussed in more detail in appendix A, §A.2.2. We anticipated a thin diffusive boundary layer below the interface $z = h(x, t)$ and, in order to ensure that the dynamics near the interface are well resolved, we used a vertical co-ordinate transformation $\zeta = f[z, \overline{h}(t)]$. For the free-interface systems, this transformation is adaptive, and is recalculated once the interface has moved a sufficient distance to require it. The horizontal and temporal resolution are uniform.

We solved the Poisson equation (5.13) using a spectral method in the horizontal direction, and a compact fourth-order finite-difference operator for the vertical derivatives. The diffusion and advection operators in the transport equation (5.10) were discretized using standard second-order finite differences and flux-conservative techniques respectively, and the equation was solved using an alternating-direction implicit method (Press *et al.*, 1989). The boundary conditions were imposed in such a way as to ensure that the numerical scheme retained second-order accuracy (see appendix A for details).

### 5.3.4 The flux

We have non-dimensionalized the variables with respect to the convective time scale $T^* = \phi h_0^*/U^*$. For the fixed interface, the dimensionless diffusive solute flux through the upper boundary is therefore given by $Ra_0^{-1}\,\partial C/\partial z|_{z=1}$ (from 5.10). However, we are aiming to compare the one-sided system with the Rayleigh–Darcy cell, where the dimensionless flux is more commonly defined with respect to the diffusive time scale (as in, for example, standard definitions of the Nusselt number used throughout this dissertation; see (2.12)). It is thus helpful to consider a rescaled flux, which we define to be the actual dimensionless flux scaled by the flux $Ra_0^{-1}$ that would be given by diffusion down a unit linear concentration gradient in the absence of convection. The horizontally averaged rescaled flux $F(t)$ is therefore given by

$$F(t) = \frac{1}{L}\int_0^L \left.\frac{\partial C}{\partial z}\right|_{z=1} \mathrm{d}x. \tag{5.14}$$

Throughout this chapter, we measure and model the rescaled flux $F(t)$.

## 5.4 Numerical results

For the remainder of this chapter, we consider a fixed-interface system, in which the active interface is located at the stationary upper boundary $z = 1$. We begin with the results of high-resolution numerical calculations of the fixed-interface system. Numerical snapshots of the concentration field $C(x, z, t)$ are shown in

figure 5.3, together with the horizontally averaged concentration profile $\overline{C}(z,t) = L^{-1}\int_0^L C\,\mathrm{d}x$ at different times, for a linear equation of state ($n = 1$) and an initial Rayleigh number $Ra_0 = 10^4$. The corresponding average solute flux $F(t)$ (figure 5.4) will be discussed in detail at the end of this subsection.

Initially, a stable diffusive boundary layer grows below the upper boundary. After a critical time $t_c \sim Ra_0^{-1}$ (see, for example, Riaz *et al.* 2006), the boundary layer becomes unstable to short-wavelength instabilities leading to downward convection (figure 5.3*a*). At this point both the flux from the upper boundary and the convective dynamics are independent of the location of the lower boundary. At some time $t_1$, the first generation of convecting plumes reaches the base of the domain (figure 5.3*b*), while at some later time $t_2$, the return flow from this interaction reaches the upper boundary and the flux begins to decrease. For $t > t_2$ the system enters a different, 'shutdown', regime in which the solute flux $F(t)$ decreases as the interior of the domain becomes steadily more concentrated with solute. The times $t_1$ and $t_2$ are controlled both by the diffusive onset time scale $t_c \sim Ra_0^{-1}$ and the $O(1)$ convective time scale. Since $Ra_0 \gg O(1)$, we expect the convective time to dominate: thus $t_1$ can be assumed to be independent of $Ra_0$, and $t_2 \approx 2t_1$. We find numerically that $t_1 \approx 7.5$ and $t_2 \approx 15$, in broad agreement with the experimental results of Slim *et al.* (2013). For $t > t_2$, the horizontally averaged concentration $\overline{C}(z,t)$ is approximately independent of $z$ away from the boundary layer, and $\overline{C}$ increases steadily over time (figures 5.3*c* and *d*). These observations underpin the theoretical modelling in §5.5.

The dynamics in the shutdown regime, $t > t_2$, are dominated by persistent, descending 'megaplumes' interleaved with a columnar return flow that rises towards the upper boundary. Instabilities in the thin boundary layer at the upper boundary drive the growth of small vigorous 'protoplumes', which carry dense fluid from the boundary layer into the larger descending megaplumes. As the interior becomes more concentrated, the dynamics of the flow become less vigorous; the depth of the boundary layer increases as the density contrast with the interior decreases; and the (differing) horizontal length scales associated with both protoplumes and megaplumes increase. The dynamical structure of the flow appears qualitatively very similar to that of the upper half of a Rayleigh–Darcy cell in the high-$Ra$ regime (see chapter 2). This similarity is discussed in §5.5.1.

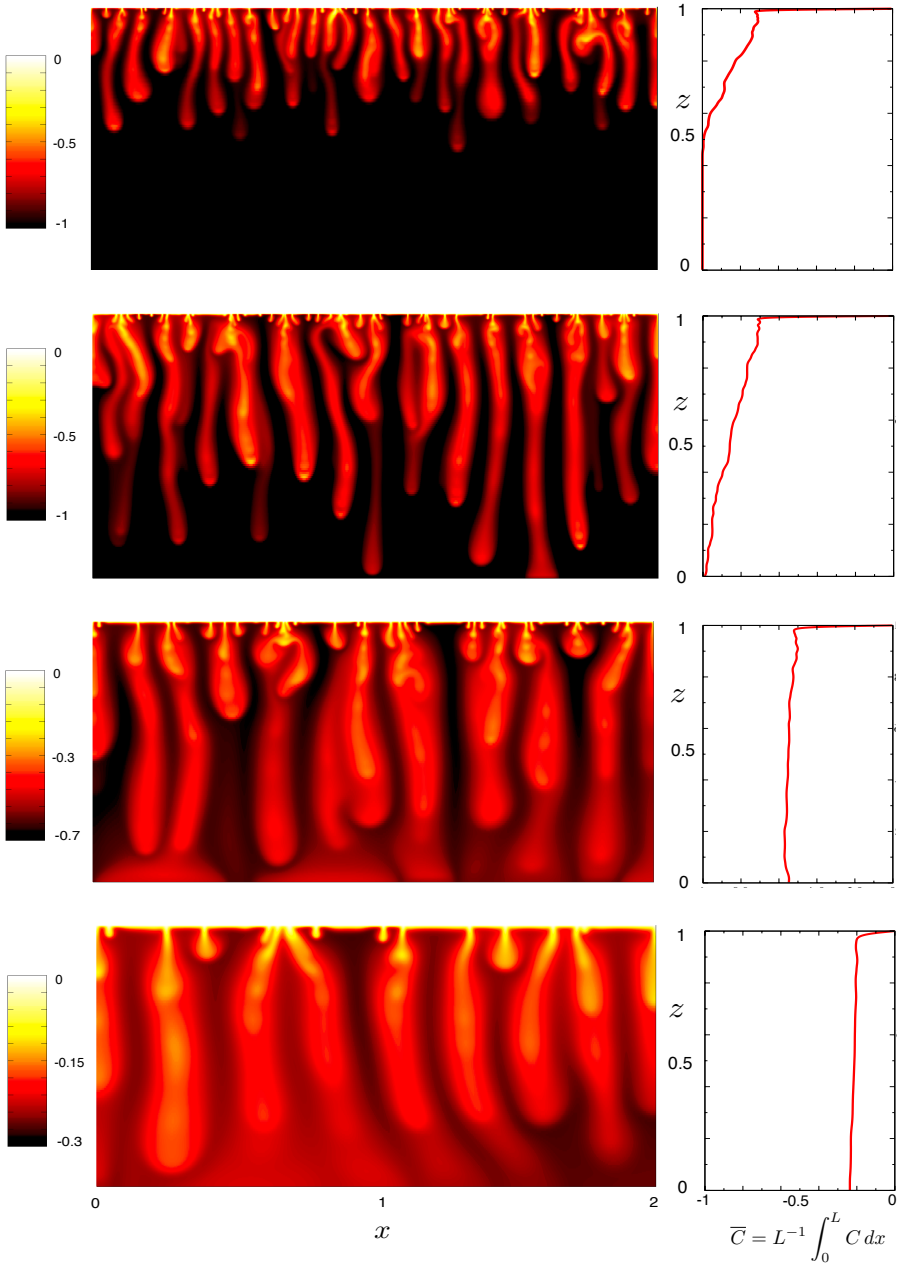


Figure 5.3: Snapshots of the concentration field $C$ in a fixed-interface system, from numerical simulations, for $n = 1$, $Ra_0 = 10^4$, and aspect ratio $L = 2$, together with plots of the horizontally-averaged concentration profile $\overline{C}(z,t) = L^{-1} \int_0^L C \, \mathrm{d}x$: $(a)$ time $t = 4$, before the first generation of plumes has reached the base of the domain; $(b)$ $t = 8 \approx t_1$, when the descending plumes first reach the base; $(c)$ $t = 32$, in the shutdown regime; $(d)$ $t = 128$. The horizontally averaged concentration profile in $(c)$ and $(d)$ is approximately uniform away from the upper boundary. The horizontal spacing of the downwelling plumes increases over time. Note the different colour scales on the left.

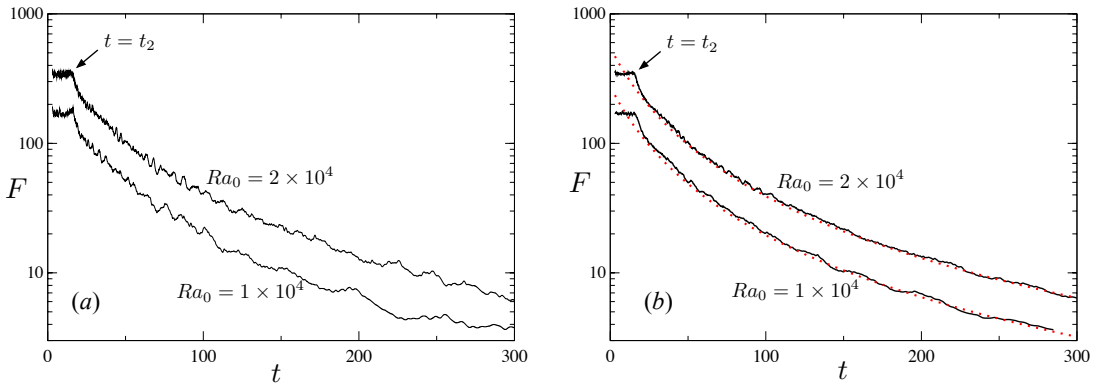


Figure 5.4: The horizontally averaged solute flux $F(t)$ (5.14), for a linear equation of state $n = 1$, aspect ratio $L = 2$, and $Ra_0 = 1 \times 10^4$ and $Ra_0 = 2 \times 10^4$ as marked: $(a)$ measurements from one numerical simulation, showing the variability of $F$; and $(b)$ measurements ensemble-averaged over eight numerical simulations (solid), together with the theoretical predictions (5.28) (dotted) as discussed in §5.5. The transition to the shutdown regime at $t = t_2$ is marked.

The horizontally averaged solute flux (5.14) exhibits rapid chaotic fluctuations about a time-varying mean. Measurements of other variables from our numerical calculations also show some chaotic variation about time-varying average values. We typically ensemble-average our numerical results to reduce the fluctuations and to give clearer measurements for comparison with the theoretical modelling. The variables used in the theoretical sections of this paper refer to the mean values. The number of repeat simulations used in an ensemble-average is given in the caption of the relevant figure.

Figure 5.4 shows numerical measurements of the horizontally averaged flux $F(t)$. The chaotic variation discussed above can be observed in measurements from a single simulation (figure 5.4$a$). Ensemble-averaged measurements (figure 5.4$b$) show that the flux initially fluctuates about an approximately constant value. Once the first generation of plumes have reached the lower boundary, and the domain has filled up with denser fluid, the flux decays slowly in the shutdown regime $t > t_2$.

## 5.5 Theoretical box model

The numerical calculations showed that the horizontally averaged interior concentration is approximately uniform for $t > t_2$ (figures 5.3*c* and *d*), apart from in a thin boundary layer near the upper boundary. This observation provides the motivation for the development of a simple box model, using a well-mixed approximation. We assume that, outside the thin boundary layer, the horizontally averaged concentration is independent of $z$, so that

$$\overline{C} = \Theta(t) \leqslant 0. \tag{5.15}$$

As $\Theta(t)$ increases towards zero, the strength of convection decreases. Based on the definition of the Rayleigh number in (5.11), we define a time-dependent Rayleigh number $Ra(t)$ to be proportional to the current density difference between the upper boundary ($C = 0$) and the interior ($C = \Theta(t) \leqslant 0$). Thus

$$Ra(t) = Ra_0 \left|\Theta(t)\right|^n. \tag{5.16}$$

We further define a time-dependent Nusselt number $Nu(t)$, by scaling the flux $F(t)$ up to a unit concentration difference, which gives

$$Nu(t) = \frac{F(t)}{|\Theta(t)|}. \tag{5.17}$$

We expect $Nu(t)$ to be given by some function of the current Rayleigh number, so that $Nu(t) = \mathcal{N}[Ra(t)]$. The functional form of $\mathcal{N}(Ra)$ is discussed in §5.5.2.

We integrate the transport equation (5.10) over the whole domain, and use the boundary conditions to obtain

$$\frac{d}{dt}\int_0^1\int_0^L C \,\mathrm{d}x\,\mathrm{d}z = \frac{1}{Ra_0}\int_0^L \left.\frac{\partial C}{\partial z}\right|_{z=1} \mathrm{d}x. \tag{5.18}$$

Using (5.14) and the definition of the horizontally averaged concentration $\overline{C}(z,t)$,

(5.18) can be rewritten as

$$\frac{d}{dt}\int_0^1 \overline{C}\,\mathrm{d}z = \frac{F}{Ra_0}. \tag{5.19}$$

Since under the well-mixed approximation (5.15) we are neglecting the area of the thin boundary layer, (5.19) can be combined with (5.15) and (5.17) to give

$$\frac{d\Theta}{dt} = \frac{|\Theta|}{Ra_0}\mathcal{N}\left[Ra(t)\right]. \tag{5.20}$$

Equation (5.20) gives a theoretical prediction for the evolution of the shutdown regime, which we can solve for a given form of the Nusselt number $\mathcal{N}(Ra)$.

The model applies for $t > t_2$, and so (5.20) can be solved together with an initial condition for the interior concentration $\Theta(t_2)$. In fact, solutions can be extrapolated back to $t < t_2$, and (5.20) can thus be solved with an initial condition $\Theta(t_0) = -1$, where $t_0 < t_2$ is a virtual origin that allows for the differing dynamics of the system before it enters the shutdown regime. We find numerically that $t_0 = 0$ provides a very good approximation.

### 5.5.1 Relationship to the two-sided Rayleigh–Darcy cell

As noted earlier, the dynamical structure of one-sided flow in the shutdown regime (figure 5.3*c* and *d*) appears qualitatively very similar to half of the convective profile observed in a two-sided Rayleigh–Darcy (RD) cell (chapter 2). We now show that the Nusselt number $\mathcal{N}_{RD}(Ra)$ measured in a RD cell is quantitatively applicable to shutdown in the one-sided system.

We consider first, for simplicity, the case of a linear equation of state ($n = 1$). Suppose a statistically steady RD cell has boundary conditions of constant concentration $C = 0$ on the upper boundary and $C = -1$ on the lower, and an average concentration $C^i_{RD} = -1/2$ in the interior. As $n = 1$, the density difference $\Delta\rho_{RD}$ between the upper boundary and the interior is given by $\Delta\rho_{RD} = -C^i_{RD} = 1/2$. In contrast, while the one-sided system also has a boundary condition of $C = 0$ on the upper boundary, it has a condition of no solute flux through the lower boundary, and an average interior concentration $C^i = \Theta(t)$. The density difference

between the upper boundary and the interior is therefore given by $\Delta\rho = |\Theta(t)|$.

We compare the two systems by rescaling $Ra(t)$ to take account of the different boundary conditions and density differences between the upper boundary and the interior. Firstly, because of the different lower boundary conditions, we suggest that the one-sided system is related to the upper half of a RD cell of double the depth. Secondly, in order that the density difference should agree in the two systems, we require the total density difference across the RD cell to be scaled by a factor $\Delta\rho/\Delta\rho_{RD} = 2|\Theta|$. The factor $\Delta\rho = |\Theta|$ is already included in the definition of $Ra(t)$ (5.16), and we therefore define the effective Rayleigh number $Ra_e$ for the equivalent RD cell to be $Ra_e = 4Ra(t)$.

For the general case with a nonlinear equation of state ($n > 1$), we can perform a similar analysis. However, there are two differences. Firstly the interior concentration $C^i_{RD}$ of the Rayleigh–Darcy cell is a function of $n$, as discussed in appendix 5.A. Secondly, the dimensionless density difference is not simply equal to the concentration difference, but is given by $\Delta\rho_{RD} = |C^i_{RD}|^n$ and $\Delta\rho = |\Theta|^n$. Therefore, the effective Rayleigh number is given by

$$Ra_e = r(n)Ra(t), \qquad \text{where} \qquad r(n) = \frac{2}{\Delta\rho_{RD}}, \tag{5.21a, b}$$

as, again, the factor $\Delta\rho = |\Theta|^n$ is already included in the definition of $Ra(t)$ (5.16). In appendix 5.A we provide numerical estimates of $C^i_{RD}(n)$, and show that it can be well approximated by the empirical formula $C^i_{RD} = -(n+1)^{-1/n}$ for $n \leqslant 5$. Thus, $\Delta\rho_{RD}(n) = 1/(n+1)$, and the constant premultiplying factor $r(n)$ reduces to

$$r(n) = 2\,(n+1)\,. \tag{5.22}$$

### 5.5.2 The functional form of the Nusselt number

In a RD cell, the time-averaged Nusselt number $Nu$ is a function of the Rayleigh number $Ra$ only, and is given by the form $\mathcal{N}_{RD}(Ra)$. In chapter 2, we found that $\mathcal{N}_{RD}$ asymptotically scales linearly with $Ra$. We also recall that the numerical measurements of $\mathcal{N}_{RD}(Ra)$ for $1300 < Ra < 4\times10^4$ were extremely well fitted by

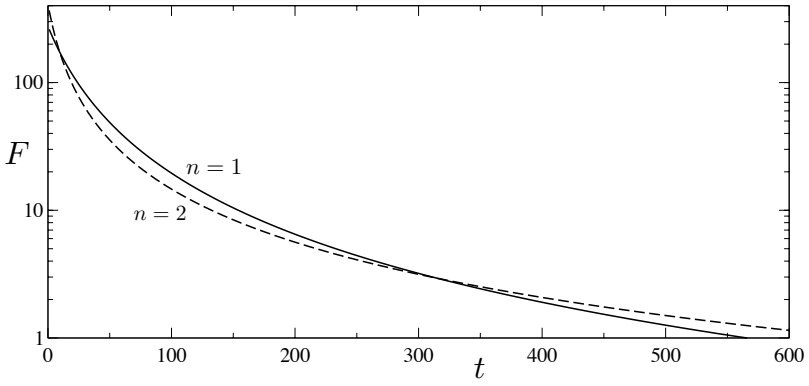


Figure 5.5: The solute flux $F(t)$ given by (5.28) for $Ra_0 = 10^4$, $n = 1$ (solid) and $n = 2$ (dashed), illustrating that the initial decrease of the flux is faster at larger $n$, while the long-time decay is slower and the flux is predicted to scale with $t^{-(n+1)/n}$.

an equation of the form

$$\mathcal{N}_{RD}(Ra) = \alpha\, Ra + \beta, \tag{5.23}$$

(cf. (2.14)), where $\alpha \approx 6.9 \times 10^{-3}$ and $\beta \approx 2.75$ are constants.

### 5.5.3 Analytic solution of the box model

The effective Rayleigh number $Ra_e = r\, Ra_0\, |\Theta|^n$, given by (5.16) and (5.21$a$), can be combined with (5.23) to give an expression for the Nusselt number in the one-sided system:

$$\mathcal{N}[Ra(t)] = \mathcal{N}_{RD}[Ra_e], \tag{5.24}$$

$$= \alpha\, r\, Ra_0\, |\Theta(t)|^n + \beta. \tag{5.25}$$

We use (5.25) to integrate (5.20) analytically. As discussed above, we take an initial condition $\Theta(t_0) = -1$, where $t_0 < t_2$ is a virtual time origin. The solution is given by

$$\Theta(t) = -\gamma^{1/n} \left[(1+\gamma)\, \mathrm{e}^{\alpha\gamma n r (t-t_0)} - 1\right]^{-1/n}, \tag{5.26}$$

where $\gamma = \beta/(\alpha r Ra_0)$.

If $Ra_0$ is sufficiently large ($Ra_0 \gg 10^3$) then $\gamma \ll 1$. In the limit $\gamma \to 0$, which

corresponds to the simple asymptotic linear scaling $\mathcal{N} = \alpha\, r\, Ra$ in (5.25), (5.26) reduces to

$$\Theta(t) = -\left[1 + \alpha\, n\, r\ (t - t_0)\right]^{-1/n}, \tag{5.27}$$

and the solute flux $F(t)$, given by (5.17), becomes

$$F(t) = \alpha\, r\, Ra_0\, |\Theta|^{n+1} = \alpha\, r\, Ra_0\, [1 + \alpha\, n\, r\, (t - t_0)]^{-(n+1)/n}. \tag{5.28}$$

Thus, in the limit of large $Ra_0$ ($\gamma \to 0$), the evolution of the interior concentration $\Theta(t)$ becomes independent of $Ra_0$, and the flux $F(t)$ is proportional to $Ra_0$ (as we might expect from the Nusselt number scaling), but otherwise evolves independently of $Ra_0$.

An important feature of these results is the length of time it takes for the convective flux to shut down. The rate at which the flux $F$ decreases is controlled by $\alpha$, the constant in the Nusselt number relationship (5.23). Since $\alpha \ll 1$, the time scales for the shutdown of convection are much greater than the $O(1)$ convective time scale.

The dependence on the equation of state (5.9) of both the flux and the interior concentration is different at early and late times (figure 5.5). Initially, the flux decreases more rapidly at larger values of $n$. This behaviour can be seen from leading-order expansions of (5.27) and (5.28) (with $t_0 = 0$), which show that

$$\Theta = -\left[1 - \alpha\, r\, t + O(\alpha^2 t^2)\right], \qquad F = \alpha\, r\, Ra_0\left[1 - (n+1)\alpha\, r\, t + O(\alpha^2 t^2)\right]. \tag{5.29a, b}$$

Therefore, using (5.22), to leading order $d\Theta/dt \sim 2\alpha\,(n+1)$ and $dF/dt \sim -4\alpha^2\,(n+1)^3$, both of which increase in magnitude with $n$. However, at late times (5.27) and (5.28) are dominated by different scalings with time: the model predicts that the interior concentration $\Theta(t)$ increases towards zero like $t^{-1/n}$, and the flux $F(t)$ decays like $t^{-(n+1)/n}$. Therefore, the increase of the interior concentration and the resulting decrease of the flux are both ultimately slower at larger $n$.

These differences can be understood by the shape of the density curve $\rho(C) = 1 - (-C)^n$ (5.9) for different values of $n$. At larger $n$, the gradient of the density curve near $C = -1$ is larger, and therefore the density difference $|\Theta|^n$ which

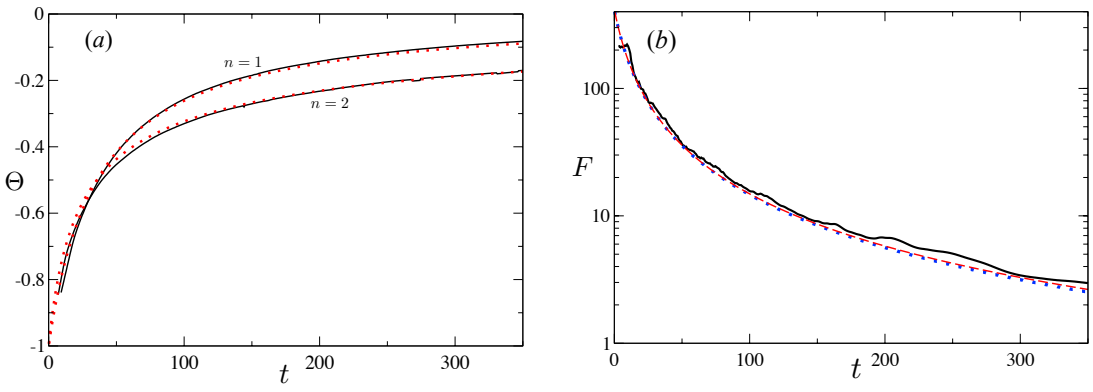


Figure 5.6: Measurements from full numerical calculations (solid) together with theoretical predictions, for $Ra_0 = 10^4$ and aspect ratio $L = 2$: $(a)$ the interior concentration $\Theta(t)$, ensemble-averaged over four calculations, for $n = 1$ and $n = 2$ as marked, together with the theoretical predictions from (5.26) (dotted); $(b)$ the solute flux $F(t)$ for $n = 2$, ensemble-averaged over four calculations, together with the theoretical prediction from (5.17) and (5.26) (dashed), and the theoretical prediction in the asymptotic limit $\gamma \to 0$ from (5.28) (dotted). Numerical measurements of $F(t)$ for $n = 1$ are shown in figure 5.4.

drives convection initially decreases more rapidly. However, the different scaling behaviour of $\rho(C)$ near to the stationary point $C = 0$ means that the long-time scaling of $F(t)$ and $\Theta(t)$ has a weaker exponent at larger $n$.

## 5.6 Comparison of the box model and numerical results

In this section we compare the analytic solutions with numerical measurements. We find empirically that $t_0 = 0$ gives good agreement with the numerical results, and therefore we use this value throughout.

The interior average concentration $\Theta(t)$ is measured in the numerical simulations by defining a time-dependent boundary-layer depth, below which the concentration is averaged in both spatial directions. Figure 5.6$(a)$ shows numerical measurements and theoretical predictions of $\Theta(t)$, for both a linear ($n = 1$) and a quadratic ($n = 2$) equation of state. The theoretical predictions from the box model (5.26) give very good agreement with the full numerical solutions.

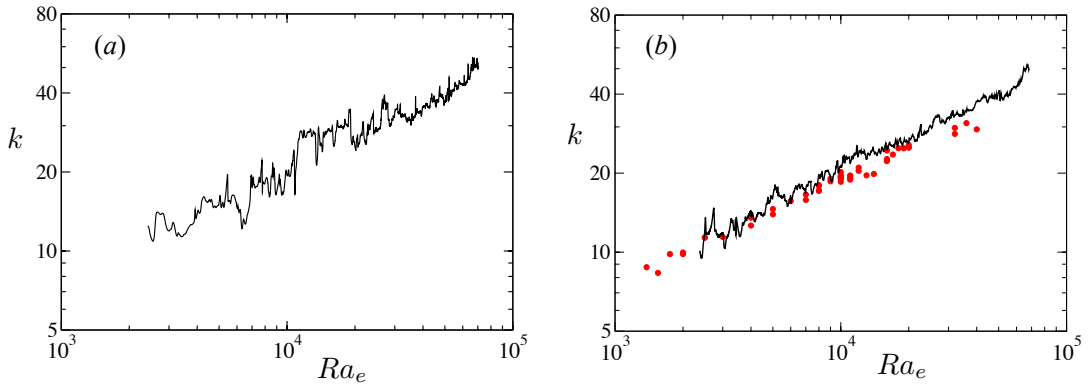


Figure 5.7: Numerical measurements of the average wavenumber $k$ of the downwelling megaplumes, for a linear equation of state $n = 1$, an aspect ratio $L = 2$, and $Ra_0 = 2\times10^4$, measured at $z = 0.5$ and plotted against the effective Rayleigh number $Ra_e = 4Ra_0|\Theta|$ (5.21): $(a)$ measurements from one simulation, showing the typical variability of $k$; and $(b)$ measurements ensemble-averaged over eight simulations (solid line), together with direct measurements of $k(Ra_e)$ in a RD cell (points) (adapted from figure 2.8).

Figure 5.6$(b)$ shows numerical measurements of the solute flux $F(t)$ for a quadratic equation of state ($n = 2$). The theoretical solution derived from (5.26) and the simpler asymptotic solution (5.28) are also shown. These solutions are almost indistinguishable from each other except at late times. Both solutions give excellent agreement with the numerical results.

These figures show that simple one-dimensional box models give a very good description of the evolution of the system in the shutdown regime. We have also shown that the results from a RD cell can be used both qualitatively and quantitatively to describe the average behaviour of the flux in the shutdown regime, and the corresponding evolution of the interior concentration $\Theta$. Moreover, these results suggest that the simple asymptotic linear scaling $\mathcal{N} = \alpha\, r\, Ra$, with $\alpha = 6.9\times10^{-3}$ and $r(n)$ given by (5.22), is a very good approximation provided $Ra_0 > 10^3$.

## 5.7 Dynamical structure of shutdown: the horizontal wavenumber

The correspondence between one-sided and two-sided convection is further strengthened by a comparison of the dynamical structure of the flow. Figure 5.3 shows that in the shutdown regime the flow is dominated by long descending megaplumes, with an average horizontal wavenumber that decreases over time. Based on the discussion above, we might expect the average horizontal wavenumber $k(t)$, which will depend on the time-dependent Rayleigh number $Ra(t)$, to be in agreement with the equivalent dependence $k(Ra_e)$ from a RD cell.

We measured the average horizontal wavenumber $k(t)$ by taking the Fourier transform of the concentration profile at $z = 0.5$, and calculating the average value of $k$ from the Fourier spectrum. Figure 5.7 shows this measured $k$ as a function of $Ra_e = r\,Ra(t)$, together with numerical results from chapter 2; figure 2.8 for $k(Ra_e)$ in a RD cell. The good agreement seen in this figure provides further evidence that the one-sided system can be quantitatively compared to the upper half of a RD cell, and that the dynamical structures of the shutdown regime are well described by the results from a RD cell.

## 5.8 Conclusions

In this chapter, we have shown that measurements of the Nusselt number $Nu(Ra)$ from the statistically steady two-sided Rayleigh–Darcy cell can be used to accurately predict the shutdown of the flux $F(t)$ in one-sided convective systems. We have shown that the relationship $Nu(Ra) = \alpha Ra + \beta$, found in chapter 2, not only qualitatively describes the decay of the flux $F(t)$ in the one-sided shutdown system, but can also be used to give very good quantitative agreement with the results of numerical calculations.

Furthermore, we have found that the dynamical structure of the flow in the shutdown regime can be accurately described by the structures of a Rayleigh–Darcy cell: the shutdown regime is dominated by downwelling megaplumes with an average horizontal wavenumber $k(t)$, which decreases over time in quantitative

agreement with the measurements of the wavenumber $k(Ra)$ from a Rayleigh–Darcy cell.

We also characterized the effect of different power-law equations of state $\rho = 1-(-C)^n$ on the flux of solute, and thus on the time scale for shutdown. We have found that, while the rate of shutdown is initially more rapid for larger values of $n$, at late times the flux decreases more slowly. The initial linear rate of decrease of the flux scales like $(n+1)^3$, while at long times the flux decreases like $t^{-(n+1)/n}$. The time scale for shutdown ($\sim \alpha^{-1}$) is, irrespective of the form of the equation of state, much greater than the convective time scale ($\sim 1$). This observation is a result of the relative 'inefficiency' of the flux, as described by the small coefficient $\alpha$ in the relationship for the Nusselt number in a Rayleigh–Darcy cell (5.23).

In chapter 6, we develop this work by examining the shutdown of convection in 'free-interface' systems, which comprise two fluid layers with an interface that can move as a result of convection across it.

# Appendix

## 5.A Discussion of the average interior concentration in a Rayleigh–Darcy cell

We consider a two-dimensional Rayleigh–Darcy cell in a porous medium, containing a fluid that satisfies a dimensionless power-law equation of state $\rho = 1-(-C)^n$, as in (5.9). The cell has periodic (or no-flux) boundary conditions on the side walls, and fixed concentrations on the upper and lower boundaries,

$$C(x, z = 1) = 0, \tag{5.30}$$

$$C(x, z = 0) = -1. \tag{5.31}$$

We consider the system in statistically steady state.

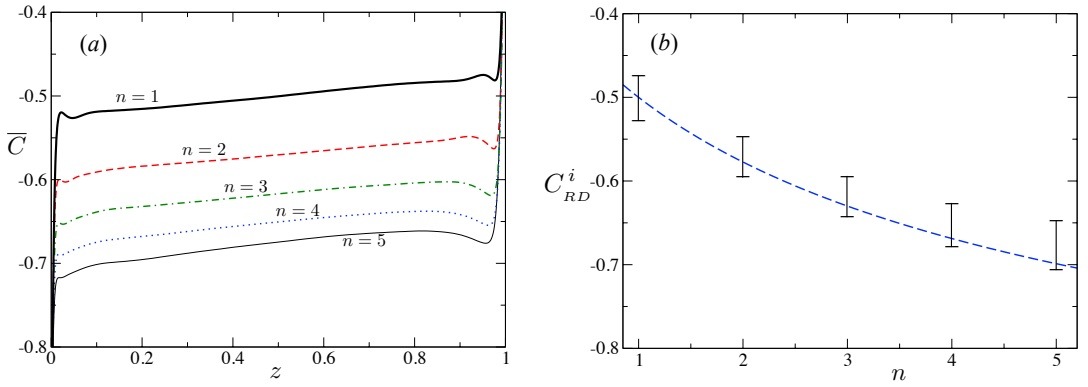


Figure 5.8: Numerical measurements from a Rayleigh–Darcy cell, with $Ra = 10^4$: $(a)$ the average concentration $\overline{C}(z)$ for different values of $n$ as marked; $(b)$ estimated range of the interior concentration $C^i_{RD}(n)$ in the linear interior region, taken from the measurements in $(a)$, together with an approximate analytic fit $C^i_{RD} = -(n+1)^{-1/n}$ (dashed).

In chapter 2, we presented numerical results for the case of a linear equation of state ($n = 1$)[1]. We showed that, close to the upper and lower boundaries of the domain, the horizontally averaged concentration profile $\overline{C}(z)$ varies rapidly. However, in the interior of the domain $\overline{C}(z)$ has a small linear gradient that decreases as the Rayleigh number $Ra$ increases. In the limit $Ra \to \infty$, the average concentration in the interior tends to a constant value, $C^i_{RD} = -1/2$.

We have also carried out numerical calculations of (5.10) and (5.13) in a Rayleigh–Darcy cell for $1 \leqslant n \leqslant 5$, at Rayleigh number $Ra = 10^4$. Measurements of the interior concentration $\overline{C}(z)$ from these calculations are shown in figure 5.8$(a)$. Based on the results for $n = 1$ discussed above, we make the assumption for $n > 1$ that the gradient of $\overline{C}(z)$ in the interior of the domain also decreases as $Ra$ increases, and that, as $Ra \to \infty$, the average concentration in the interior tends to a constant value $C^i_{RD}(n)$. By extrapolating the linear interior gradient of $\overline{C}(z)$ for each value of $n$ from our measurements in figure 5.8$(a)$, we generate estimates for the range of possible values of $C^i_{RD}(n)$, as shown in figure 5.8$(b)$. We find that an approximate analytic fit lying within this range is given by $C^i_{RD} = -(n+1)^{-1/n}$, which is also shown in figure 5.8$(b)$. This curve

[1]In that chapter, concentration $C$ was replaced by temperature $T$; as discussed in §1.2, the governing equations for thermal and compositional convection are taken to be identical

provides a reasonable approximation for $n < 5$, which includes the physically important cases, $n = 1$ and $n = 2$. We use this approximate form for $C^i_{RD}$ throughout the paper.

# Chapter 6

# Shutdown of convection in a porous medium II: free interface

The material contained in this chapter forms the second half of the paper 'Convective shutdown in a porous medium' (Hewitt *et al.*, 2013*a*), which has been published in the *Journal of Fluid Mechanics*.

## 6.1 Introduction

In chapter 5, we explored in detail the shutdown of convection in a one-sided 'fixed-interface' system, as defined in §5.2, and demonstrated the close link between such a one-sided system and the two-sided Rayleigh–Darcy cell. In this chapter, we will develop these ideas to model convective systems comprising two fluid layers, in which the flux of solute across an interface causes that interface to move. We examine the dynamics and evolution of these systems using a combination of simple theoretical box models, high-resolution numerical simulations, and laboratory experiments. These tools allow us to investigate and understand the similarities and differences between a variety of physical systems, as described in §5.2.

These different physical systems comprise two fluids that can be either immiscible or miscible (see §5.2): in an immiscible system, the upper fluid is only partially soluble in the lower, and (by assumption) the lower is not at all soluble

in the upper; while in a miscible system, the upper fluid is fully soluble in the lower. For both immiscible and miscible systems, dissolution of the upper fluid into the lower causes a change in the density of the solution, which drives convection. Typical equations of state, average concentration profiles, and average density profiles for immiscible and miscible systems can be seen in figures 5.1($b$) and ($c$).

In this chapter, we develop two different mathematical models to describe free-interface systems. In §6.2, we consider both immiscible and miscible systems under the assumption that the moving interface can be approximated as remaining flat. Therefore, the interfacial height $h$ is a function of time alone. This assumption allows us to use the results of the previous chapter to derive theoretical box models of each system, which are compared with direct numerical measurements. For the immiscible system (§6.2.1), we make the additional modelling assumption that the pore space is always fully saturated: there is no capillary retention of fluid in the pores of the medium, and as such the interface remains 'sharp'. The reader is reminded that, in the miscible system (§6.2.2), the 'interface' is defined by the isopycnal of maximum density (see §5.2). In §6.2.3, we summarize the main results of this section, and compare the two systems.

In §6.3, we relax the assumption of a flat interface, and present experimental and numerical results for the miscible system when the interface is free to deform. The experimental system consists of water overlying propylene glycol in a Hele-Shaw cell. Solutions of these fluids have a density curve that is qualitatively similar to that shown in figure 5.1($c$). We find that the effects of interfacial deformation and entrainment can be considerable in the miscible system. In contrast, in §6.3.3 we argue that interfacial deformation is likely to be negligible in the immiscible system.

In §6.4, we summarize the main results of this paper, and discuss the implications for the shutdown of convection in different physical settings. Estimates based on this work of the typical time scales for shutdown in current $CO_2$ sequestration sites will be discussed in §8.2.

The relevant governing equations, variables, and non-dimensionalization for free-interface systems were introduced in §5.3. We recall that the system is initially stratified in two layers (figure 5.2$b$), with a lower layer $0 < z < 1$ of

concentration $-1$ and an upper layer $1 < z < H$ of concentration $C_+ > 0$. The maximum density is attained at $C = 0$. The density is given as a function of the concentration by (5.9).

## 6.2 Free-interface systems ($a$): Flat interface

If the interface is assumed to remain flat, then the interfacial height is a function of time alone, and is given by $z = h(t)$, with $h(0) = 1$.

As in §5.3.4, we consider the flux scaled by the diffusive flux in the absence of convection. Under the assumption of a flat interface, the scaled horizontally averaged flux $F(t)$ across the interface is given by

$$F(t) = \frac{1}{L}\int_0^L \left.\frac{\partial C}{\partial z}\right|_{z=h(t)} \mathrm{d}x. \tag{6.1}$$

The evolution of the interfacial height $h(t)$ can be calculated from conservation of solute over the entire domain, which gives

$$\int_0^H \int_0^L C(x,z,t)\,\mathrm{d}x\,\mathrm{d}z = L\left[-1 + (H-1)\,C_+\right]. \tag{6.2}$$

The right-hand side of (6.2) is the result of evaluating the integral at $t = 0$.

### 6.2.1 Immiscible system

When the two fluids are immiscible (and, by assumption, the lower fluid is insoluble in the upper), the concentration $C_+$ above the interface $z > h(t)$ remains constant, as does the corresponding density $\rho_+ < 0$. Hence global conservation of solute (6.2) reduces to

$$\int_0^{h(t)} \overline{C}\,\mathrm{d}z = -1 + [h(t) - 1]\,C_+. \tag{6.3}$$

#### 6.2.1.1 Theoretical box model

Following the analysis of §5.5, we use a well-mixed approximation for the interior of the system in $z < h(t)$: we assume that, below a thin boundary layer, the horizontally averaged concentration $\overline{C}(z,t)$ is independent of $z$, and is given by

$$\overline{C} = \Theta(t) \leqslant 0. \tag{6.4}$$

Starting from the definition of the initial Rayleigh number (5.11), we now define the time-dependent Rayleigh number $Ra(t)$ to be

$$Ra(t) = Ra_0 \, |\Theta(t)|^n \, h(t), \tag{6.5}$$

which accounts for the changes in concentration and depth of the convecting layer. We further define a time-dependent Nusselt number $Nu(t)$, by scaling the horizontally averaged flux $F$ up to a unit concentration difference and height, which gives

$$Nu(t) = \frac{h(t)F(t)}{|\Theta(t)|}. \tag{6.6}$$

The Nusselt number is given by the functional form $Nu(t) = \mathcal{N}[Ra(t)]$, as discussed in §5.5.2, and the flux $F(t)$ is given by (6.1).

As in §5.5, we integrate the transport equation (5.10) over the lower layer $z \leqslant h$, and use the boundary conditions together with (6.1) to obtain

$$\frac{d}{dt} \int_0^{h(t)} \overline{C} \, \mathrm{d}z = \frac{F}{Ra_0}. \tag{6.7}$$

Under the well-mixed approximation (6.4), contributions to the area integral in (6.7) from the thin boundary layer below the interface are neglected. Equations (6.4), (6.6), and (6.7) can be combined to give

$$h \frac{d\Theta}{dt} = \frac{|\Theta|}{h \, Ra_0} \mathcal{N}\left[Ra(t)\right]. \tag{6.8}$$

Equation (6.8) can be compared to (5.20), which is the equivalent governing equation for the fixed-interface box model.

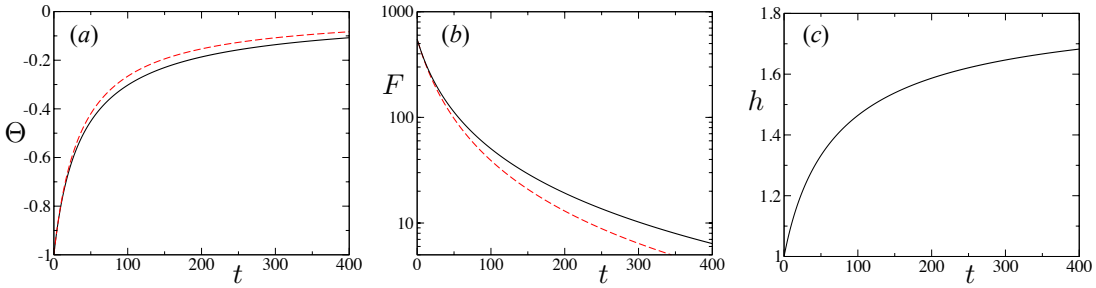


Figure 6.1: Theoretical results for the immiscible system with $n = 1$, $C_+ = 1.2$, $t_0 = 0$, and $Ra_0 = 2 \times 10^4$: $(a)$ the average concentration $\Theta(t)$ given implicitly by (6.12) (solid), together with the prediction for a stationary interface given by (5.27) (dashed); $(b)$ the solute flux $F(t)$ given by (6.13) (solid), together with the prediction for a stationary interface given by (5.28) (dashed); $(c)$ the interfacial height $h(t)$ given by (6.10) and (6.12).

The well-mixed approximation (6.4) can also be combined with global conservation of solute (6.3) to give

$$h\Theta = -1 + (h-1)\,C_+, \tag{6.9}$$

which can be rearranged to obtain the interfacial height,

$$h(t) = \frac{C_+ + 1}{C_+ + |\Theta(t)|}. \tag{6.10}$$

One could solve (6.8) and (6.10) numerically using any functional form of the Nusselt number $\mathcal{N}(Ra)$, including the numerical parameterization in (5.25). We have shown in chapter 5 that the asymptotic linear scaling $\mathcal{N}(Ra) = \alpha\, r\, Ra$, where $\alpha = 6.9 \times 10^{-3}$ and $r(n)$ is defined in (5.22), provides a very good approximation to (5.25) if $Ra > 10^3$, and we therefore use this scaling here. Equations (6.8) and (6.10), together with this linear scaling, give a simple ordinary differential equation for $\Theta$,

$$\left(\frac{C_+ + 1}{C_+ + |\Theta|}\right)\frac{d\Theta}{dt} = \alpha\, r\, |\Theta|^{n+1}. \tag{6.11}$$

Equation (6.11) describes the evolution of $\Theta(t)$ in the shutdown regime, $t > t_2$. In a similar manner to the analysis of §5.5, we extrapolate solutions back to $t < t_2$, and apply an initial condition $\Theta(t_0) = -1$, where $t_0 < t_2$ is a virtual origin. The

solution to (6.11) is then given implicitly by

$$\sum_{k=1}^{n}\left[\frac{C_+^k}{k\,\Theta^k}\left(1-|\Theta|^k\right)\right]+\ln\left[\frac{C_++|\Theta|}{|\Theta|\,(1+C_+)}\right]=-\frac{\alpha\,r(-C_+)^{n+1}}{1+C_+}\,(t-t_0)\,. \quad (6.12)$$

The height of the interface $h(t)$ is related to the interior concentration $\Theta(t)$ by (6.10). Using (6.6), the flux $F(t)$ is related to $\Theta(t)$ by

$$F=\alpha\,r\,Ra_0\,|\Theta|^{n+1}\,. \quad (6.13)$$

Figure 6.1 shows solutions calculated from (6.12) for $\Theta(t)$, $F(t)$, and $h(t)$. The concentration $\Theta(t)<0$ increases monotonically towards $\Theta(t\to\infty)=0$, while the corresponding interfacial height $h(t)$ increases monotonically towards $h(t\to\infty)=h_\infty=1+1/C_+$, independent of $n$. In the limit of large $C_+$, which physically corresponds to the limit $(C_+^*-C_m^*)\gg(C_m^*-C_-^*)$, equation (6.12) reduces to the solution for a stationary interface (5.27), and the height $h$ of the interface remains approximately constant for all time. For any value of $C_+$, the evolution of the system is ultimately given by the solution for a fixed interface (5.27) (up to an additional factor of $1/h_\infty$ multiplying $t-t_0$), since $h\to h_\infty$ at long times.

The predictions for a stationary interface from §5.5 are also shown for $\Theta$ and $F$ in figures 6.1($a$) and ($b$). Given the relatively large change in the interfacial height $h$ over time (figure 6.1$c$), it is surprising that the interior concentration $\Theta$ (figure 6.1$a$) does not display a significant difference to the prediction for a stationary interface. This observation is related to the differences in the solute flux (figure 6.1$b$) between the predictions for a moving and a stationary interface: while the area of the domain below the interface ($\propto h$) is greater in the former case than in the latter, the flux $F$ across the interface is also greater, and therefore the interior concentration $\Theta$ is not significantly different. For larger values of $C_+$ (not shown here), we find that the solutions of (6.11) increasingly resemble those for a stationary interface.

The dependence of $\Theta$ and $F$ on $n$ is also qualitatively similar to that for a stationary interface, which was discussed in §5.5.3. The interior concentration and the flux again have long-time behaviour $\Theta\sim t^{-1/n}$ and $F\sim t^{-(n+1)/n}$ to leading order, and the initial decay of the flux is again more rapid for larger $n$.

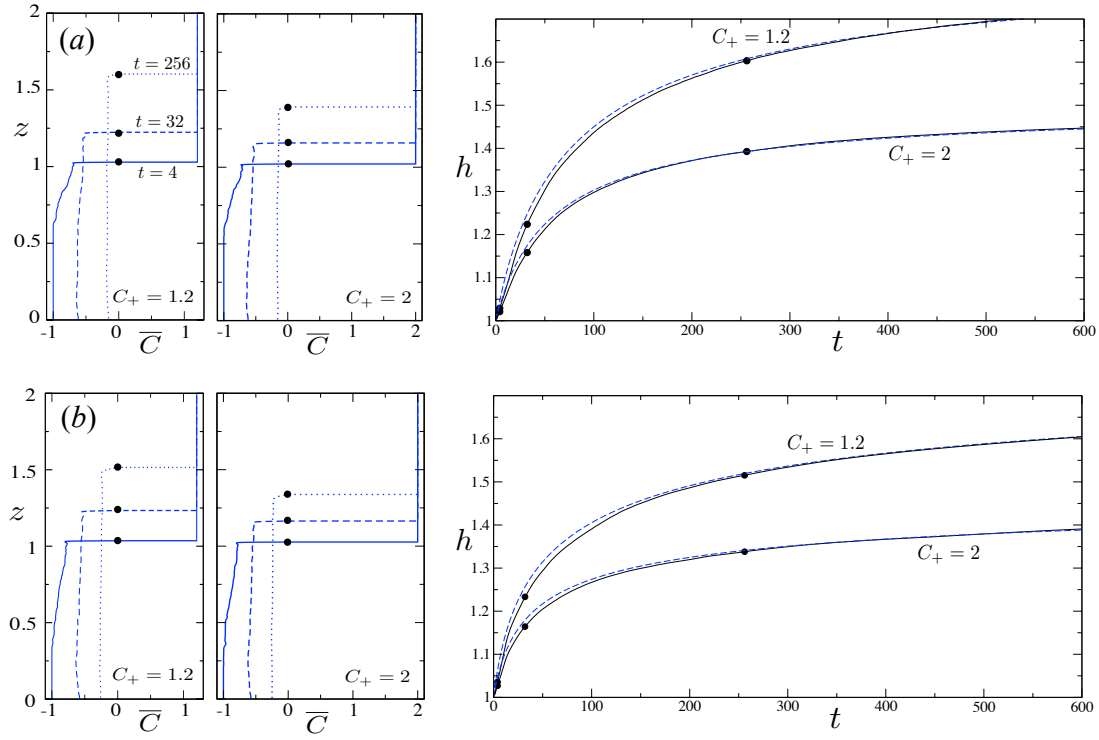


Figure 6.2: Numerical measurements for the immiscible system with a flat interface for $Ra_0 = 2 \times 10^4$, and domain width $L = 2$ and height $H = 2$, showing the horizontally averaged concentration $\overline{C}(z,t)$ at times $t = 4$ (solid), $t = 32$ (dashed), and $t = 256$ (dotted), and the interfacial height $h(t)$: $(a)$ linear equation of state $n = 1$; and $(b)$ quadratic equation of state $n = 2$. Dashed lines show the theoretical predictions for the interfacial height $h(t)$ from box models. The dots on the left-hand figures show the location of the interface, and correspond to the dots on the right-hand figures. Each subfigure shows results for both $C_+ = 1.2$ and $C_+ = 2$, as marked.

#### 6.2.1.2 Numerical results

We solved the full governing equations for the flat-interface immiscible system numerically as outlined in appendix A. These equations are (5.10) and (5.13) for the convecting region $z < h(t)$, subject to boundary conditions $C = 0$ and $w = 0$ imposed at a flat interface $h(t)$, which is determined from (6.3).

Figure 6.2 shows measurements of the horizontally averaged concentration $\overline{C}(z,t)$ and the interfacial height $h(t)$ for both linear ($n = 1$) and quadratic ($n = 2$) equations of state. The upwards retreat of the interface is approxi-

mately linear at early times ($t < t_2$), while the downwelling plumes are descending through unmixed fluid. Once the system enters the shutdown regime ($t > t_2$), the behaviour of $h(t)$ changes. The interface moves more slowly for larger values of $C_+$, as there is more solute per unit volume in the upper layer. The corresponding profiles of $\overline{C}(z,t)$ show that the interior of the domain is well mixed for $t > t_2$, in agreement with the behaviour below a fixed interface (chapter 5) and with the well-mixed assumption (6.4). The predictions of the theoretical box model for the interfacial height $h(t)$, which is based upon this well-mixed assumption, are also shown in figure 6.2, and give very good agreement with the numerical simulations.

### 6.2.2 Miscible system

When the two fluids are miscible, the relatively low concentration below the moving interface can affect the concentration field above the interface by diffusion. Since, by assumption, the interface $z = h(t)$ remains flat, the concentration $C$ is independent of $x$ for $z \geqslant h$. In this region, the governing transport equation (5.10) therefore reduces to a one-dimensional partial differential equation describing vertical diffusion away from the moving interface $h(t)$. In the frame of reference moving with the interface, (5.10) becomes

$$\frac{\partial C}{\partial t} - \frac{dh}{dt}\frac{\partial C}{\partial z} = \frac{1}{Ra_0}\frac{\partial^2 C}{\partial z^2}. \tag{6.14}$$

#### 6.2.2.1 Theoretical box model

The development of a theoretical box model for the miscible system follows similar reasoning to that for the immiscible system §6.2.1.1. The horizontally averaged interior concentration $\Theta(t) \leqslant 0$ (6.4), the time-dependent Rayleigh number $Ra(t)$ (6.5), and the time-dependent Nusselt number $Nu(t)$ (6.6) are all as defined in §6.2.1.1. The evolution equation for the average interior concentration $\Theta(t)$ is again given by (6.8).

Unlike the immiscible system, the concentration above the interface does not remain constant. Instead, it evolves by diffusion (6.14), and varies over some length scale between $C = 0$ at the interface and $C = C_+$ (as shown schematically

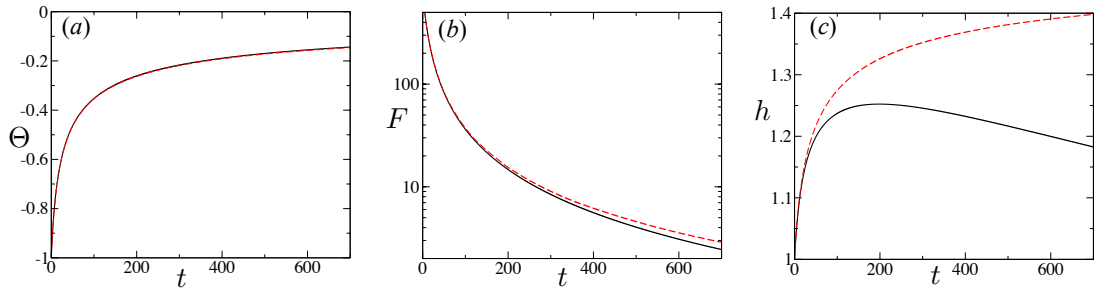


Figure 6.3: Theoretical predictions for the immiscible (dashed) and miscible (solid) systems, with $n = 2$, $C_+ = 2$, $t_0 = 0$, and $Ra_0 = 2 \times 10^4$: $(a)$ the average concentration $\Theta(t)$, for which the two predictions are almost indistinguishable; $(b)$ the solute flux $F(t)$; $(c)$ the interfacial height $h(t)$, which has qualitatively different late-time behaviour in the two systems.

in figure 5.1$c$). In order to generate a simple box model that approximates the solution of (6.14), we define a diffusive boundary-layer depth

$$\delta(t) = \frac{2}{C_+} \int_h^H (C_+ - C)\ \mathrm{d}z, \tag{6.15}$$

which is an integral measure of the length scale of the concentration profile in $z > h$. We then approximate (6.14) by assuming that the evolution of $\delta$ can be described by a simple ordinary differential equation of the form

$$\frac{d\delta}{dt} = \frac{a_1}{Ra_0\,\delta} - a_2 \frac{dh}{dt}, \tag{6.16}$$

where $a_1$ and $a_2$ are numerical coefficients. Equation (6.16) is motivated by the physical balances that control the boundary-layer depth $\delta$: the first term on the right hand side of (6.16) describes the diffusive growth of a boundary layer with a flux proportional to the diffusivity $Ra_0^{-1}$ and the concentration gradient, while the second term describes the advection of the interface.

The constants $a_1$ and $a_2$ in (6.16) are chosen so that the total solute $\delta C_+/2$ contained in the boundary layer gives a good approximation to that in the full solution of (6.14). We find $a_1$ and $a_2$ by comparing solutions of (6.16) with analytic solutions of (6.14) in two limits. In the limit where $dh/dt$ is negligible, the pure-diffusion solution of (6.14) has the form $C \sim \mathrm{erf}[(z-h)\sqrt{Ra_0/4t}]$, and

(6.16) gives $\delta = \sqrt{2a_1 t/Ra_0}$. Similarly, in the steady limit in which advection balances diffusion, the solution of (6.14) has the form $C \sim \exp\left[-\dot{h}\, Ra_0\, (z-h)\right]$, where $\dot{h} = dh/dt$, while (6.16) gives $\delta = a_1/a_2 \dot{h} Ra_0$. We use (6.15) to equate each of these solutions at leading order, which gives $a_1 = 8/\pi$, and $a_2 = a_1/2 = 4/\pi$.

Including the contribution from the diffusive upper boundary layer, global conservation of solute (6.2) gives

$$h\left(C_+ + |\Theta|\right) = (1 + C_+) - \frac{\delta C_+}{2}. \tag{6.17}$$

After rearranging (6.8), (6.16), and (6.17), we extract coupled evolution equations for the concentration $\Theta$, the height of the interface $h$, and the diffusive boundary layer depth $\delta$,

$$\frac{d\Theta}{dt} = \frac{|\Theta|\,\mathcal{N}}{h^2 Ra_0}, \tag{6.18}$$

$$\left(|\Theta| + C_+ - \frac{a_2 C_+}{2}\right)\frac{dh}{dt} = -\frac{a_1 C_+}{2\delta\, Ra_0} + \frac{|\Theta|\,\mathcal{N}}{h\, Ra_0}, \tag{6.19}$$

$$\left(|\Theta| + C_+ - \frac{a_2 C_+}{2}\right)\frac{d\delta}{dt} = \frac{a_1\left(C_+ + |\Theta|\right)}{\delta\, Ra_0} - \frac{a_2\,|\Theta|\,\mathcal{N}}{h\, Ra_0}. \tag{6.20}$$

Equations (6.18)–(6.20) give a theoretical prediction for the evolution of shutdown in a miscible flat-interface system. We integrate these equations numerically using the functional form $\mathcal{N}(Ra)$ in (5.25).

The solutions for the interior concentration $\Theta$ and the flux $F$ from this model (figures 6.3*a*,*b*) are almost indistinguishable from those for the immiscible system. However, the interfacial height $h$ for the miscible system exhibits qualitatively different behaviour at long times (figure 6.3*c*). The diffusion of solute above the interface slows the upward motion of the interface, and eventually leads to a decrease in the isopycnal that defines $h$. Equation (6.19), together with (6.6), give an equation for $dh/dt$, which shows that the height of the interface will decrease when

$$F < \frac{a_1 C_+}{2\delta}, \tag{6.21}$$

*i.e.* the height of the interface will decrease when the flux of solute into the lower layer ($F$) is less than the diffusive flux into the upper layer ($\sim C_+/\delta$).

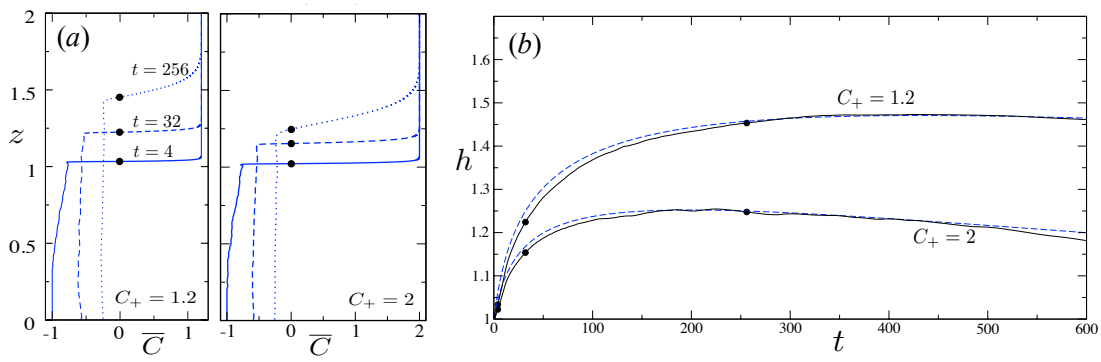


Figure 6.4: Numerical measurements for the miscible system with a flat interface, for $Ra_0 = 2 \times 10^4$, domain width $L = 2$ and height $H = 2$, and a quadratic equation of state $n = 2$: $(a)$ the horizontally averaged concentration $\overline{C}(z,t)$ at times $t = 4$ (solid), $t = 32$ (dashed), and $t = 256$ (dotted); and $(b)$ the interfacial height $h(t)$. Dashed lines show the theoretical predictions for the interfacial height $h(t)$ from box models. The dots in $(a)$ show the location of the interface, and correspond to the dots in $(b)$. Each subfigure shows results for both $C_+ = 1.2$ and $C_+ = 2$, as marked.

In a finite system with no-flux boundaries, the final steady state must have a uniform concentration $C_\infty$, which is determined by conservation of solute (6.2) to be

$$C_\infty = \frac{-1 + (H-1)\,C_+}{H}. \tag{6.22}$$

If $C_\infty < 0$, then the interface $z = h(t)$ must reach the upper boundary $z = H$, and (6.21) is never satisfied. Conversely, if $C_\infty > 0$ the interface must eventually descend, and approaches the base of the domain by diffusion. From (6.22), $C_\infty > 0$ if $H > 1 + 1/C_+$. This condition is satisfied for all the results presented in this paper.

#### 6.2.2.2 Numerical results

We solved the full governing equations for the miscible system numerically (see appendix A). These equations are (5.10) and (5.13) for $z < h(t)$, and (6.14) for $z > h(t)$, together with conservation of solute (6.2), and the flat-interface assumption $w = 0$ at $z = h(t)$.

Figure 6.4 shows measurements of the horizontally averaged concentration

$\overline{C}(z,t)$ and the interfacial height $h(t)$, with a quadratic equation of state $n = 2$. As in the case of the immiscible system (figure 6.2), the rate of upwards retreat of the interface is approximately constant for $t < t_2$, and then decreases once the system enters the shutdown regime ($t > t_2$). Unlike the immiscible system, however, the concentration field above the interface evolves in time (figure 6.4*a*). This evolution becomes very significant at long times, and results in an eventual decrease of the interfacial height $h(t)$ (figure 6.4*b*). The time at which the interface begins to descend decreases with increasing $C_+$, as predicted by (6.21). The predictions of the box model are also shown in figure 6.4*b*, and accurately capture both the slowing of the interface and its eventual descent.

### 6.2.3 Conclusions for immiscible and miscible systems with a flat interface

The results in figures 6.2 and 6.4 show that the theoretical box models give excellent predictions for the shutdown of free-interface systems, under the assumption that the interface remains flat. These figures also highlight the main difference between the immiscible and miscible systems: the long-time evolution of the interfacial height $h(t)$, which continually increases in the immiscible system, but eventually decreases in the miscible system. Given this qualitative difference in the interfacial behaviour, it is remarkable that the solute flux $F(t)$ and the interior concentration $\Theta(t)$ are so similar between the two systems (figure 6.3). The timescales for the shutdown of convection in the two systems are therefore roughly equal, even though observations of the interfacial height $h(t)$ might suggest otherwise. In the limit of large $C_+$, we find that the predictions of the box models for these free-interface systems can be well approximated by the solution in §5.5 for a fixed interface.

These results apply when the assumption of a flat interface is appropriate. In the next section, we examine miscible systems with a deformable interface, and show that the removal of the flat-interface approximation can lead to very different rates of shutdown.

## 6.3 Free-interface systems (*b*): Deformable interface

In this section we relax the flat-interface assumption. Therefore, the interface is free to 'deform', and solute can be entrained across it.

In §6.3.1 we present numerical results for the miscible system. In §6.3.2, to test the validity of the numerical results in a physical system, we compare with measurements from an experimental miscible system in a Hele-Shaw cell. In §6.3.3, we consider the validity of the flat-interface approximation for miscible systems and discuss the anticipated effects of a deformable interface on immiscible systems.

### 6.3.1 Numerical results for the miscible system

We solved the governing equations (5.10) and (5.13) over the whole domain, with an initial condition given by (5.12) and a quadratic equation of state ($n = 2$) (see appendix A for numerical details). As discussed in §5.2, the interfacial height $z = h(x,t)$ is defined by the contour of maximum density $\rho = \rho_m$, which is a function of horizontal position. We therefore define the average interfacial height $z = \overline{h}(t)$ to be the height at which the horizontally averaged density is maximum (which corresponds to the height at which $\overline{C}(z,t) = 0$).

Snapshots of the concentration field (figure 6.5*a*) show that there can be significant interfacial deformation in the miscible system. The extent of the deformation decreases with increasing $C_+$. The dominant wavelength of the deformed interface appears to be set by the lateral spacing of the descending megaplumes. The average interfacial height $\overline{h}(t)$ and the interior concentration $\Theta(t)$ are compared with predictions from the miscible box model under a flat-interface approximation in figures 6.5($b$) and ($c$). Both variables increase significantly more rapidly than the box model predicts, which suggests that the total solute flux $F(t)$ is initially much greater than with a flat interface. Measurements of $F(t)$ from the numerical simulations (not shown here) suggest that the initial flux is approximately 3 times larger than with a flat interface when $C_+ = 1.2$, and approximately 2 times larger when $C_+ = 2$.

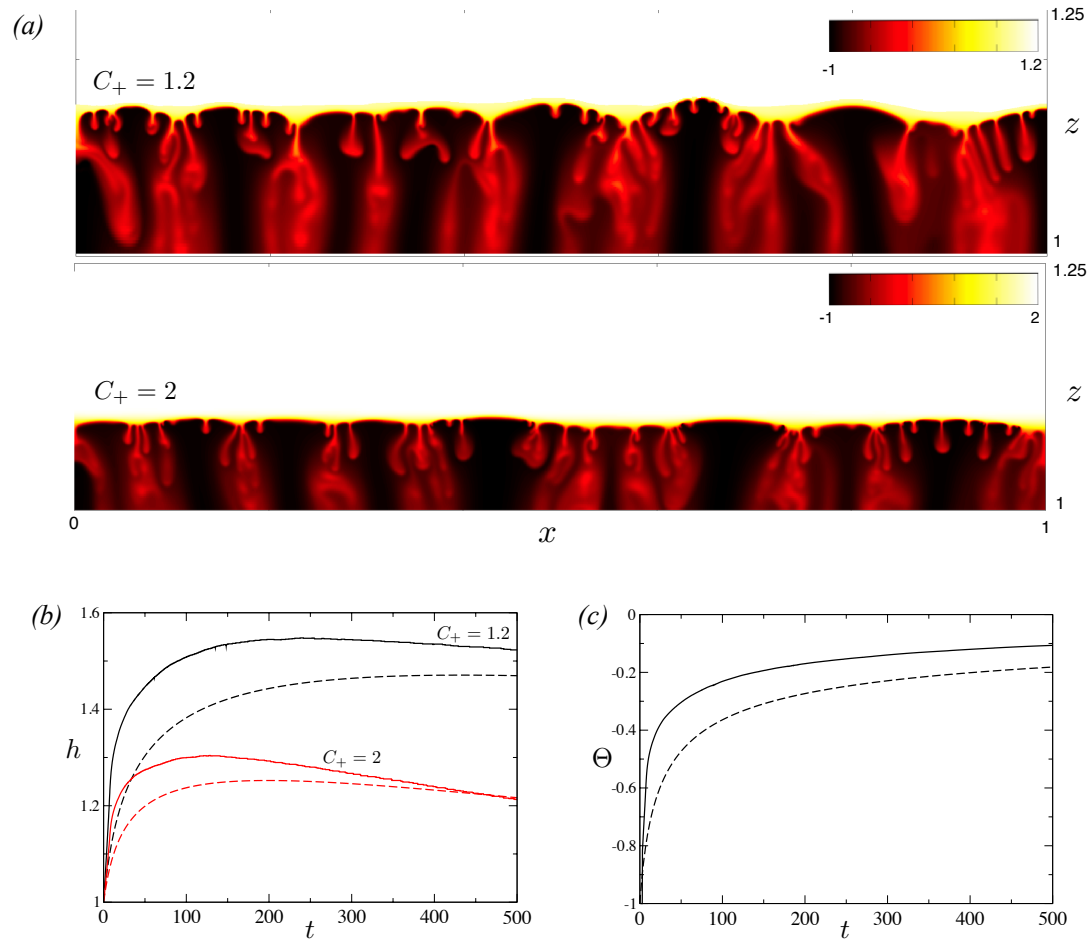


Figure 6.5: Numerical results at $Ra_0 = 2 \times 10^4$, domain width $L = 2$ and height $H = 2$, and a quadratic equation of state $n = 2$: $(a)$ snapshots of the concentration profile at $t = 5$, for $C_+ = 1.2$ and $C_+ = 2$, showing significant deformation of the interface; $(b)$ the average interfacial height $\overline{h}(t)$ (solid) for $C_+ = 1.2$ and $C_+ = 2$, together with the height predicted by the miscible theoretical box model (dashed); $(c)$ the interior concentration $\Theta(t)$ (solid) for $C_+ = 1.2$, together with the prediction of the miscible theoretical box model (dashed).

### 6.3.2 Experimental results for the miscible system

In order to explore the effects of a deformable interface further, and to corroborate the numerical results of §6.3.1, we conducted an experiment in a Hele-Shaw cell using two miscible fluids: propylene glycol (PPG) and water. Backhaus *et al.* (2011) used these fluids to examine the onset of convection and the evolution

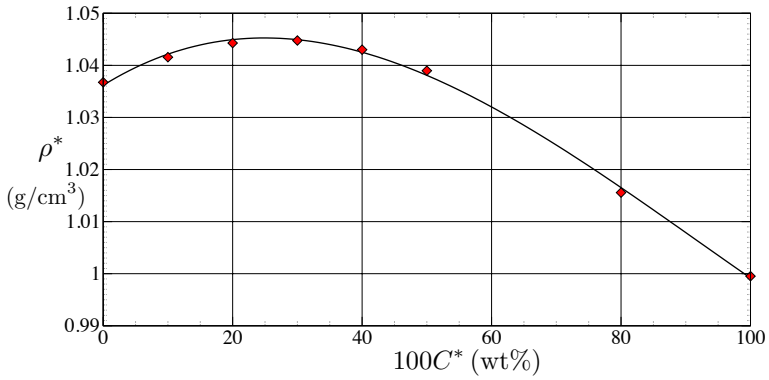


Figure 6.6: Relationship between density and concentration for the propylene glycol–water system. Concentration $C^* = 1$ corresponds to pure water. Symbols denote measurements made in a densitometer, of which the curve is a cubic fit $\rho^* = f^*(C^*) = \rho^*_- \, (1 + 0.077\, C^* - 0.173\, C^{*2} + 0.062\, C^{*3})$, with $\rho^*_- = 1.036\,\mathrm{g/cm^3}$.

of the initial convective plumes. Neufeld *et al.* (2010) used a similar system, composed of water with a mixture of methanol and ethylene-glycol, to examine the convective flow for $t_c < t < t_2$. Here, in contrast, we examine the long-time evolution of the system in the shutdown regime.

The experimental system consists of two glass sheets, separated by a shim of thickness $l = 0.41\,\mathrm{mm}$. The cell has width $L^* = 40\,\mathrm{cm}$ and height 80 cm. The flow in the gap satisfies Darcy's law (5.1*a*), with an effective permeability $K = l^2/12 = 1.4 \times 10^{-4}\,\mathrm{cm^2}$ and porosity $\phi = 1$. PPG, of density $\rho^*_- = 1.0367\,\mathrm{g/cm^3}$, filled the lower layer of the cell up to a depth $h^*_0 = 32.5\,\mathrm{cm}$. The PPG was overlain by a layer of water, of density $\rho^*_+ = 0.9995\,\mathrm{g/cm^3}$, up to a total depth $H^* = 66\,\mathrm{cm}$. We define the concentration $C^*$ to be the proportion of water by weight, so that the concentration of pure PPG is $C^*_- = 0$ and that of water is $C^*_+ = 1$. Measurements of the density for different concentrations are shown in figure 6.6, together with a cubic fitting equation $\rho^* = f^*(C^*)$. The maximum density is obtained at $C^*_m \approx 0.25$, and is given by $\rho^*_m = 1.0451\,\mathrm{g/cm^3}$. The diffusivity of PPG in water varies a little with concentration, but is roughly constant between $C^*_- = 0$ and $C^*_m = 0.25$, with an approximate value $D = 2.5 \times 10^{-6}\,\mathrm{cm^2/s}$ (Wang *et al.*, 2010).

We measured the average interfacial height $\overline{h^*}(t)$ and the interior concentration $\Theta^*(t)$ by the addition of blue dye to the water. The ambient temperature varied by less than $2^\circ$ C for the duration of the experiment ($\approx 3$ weeks). The

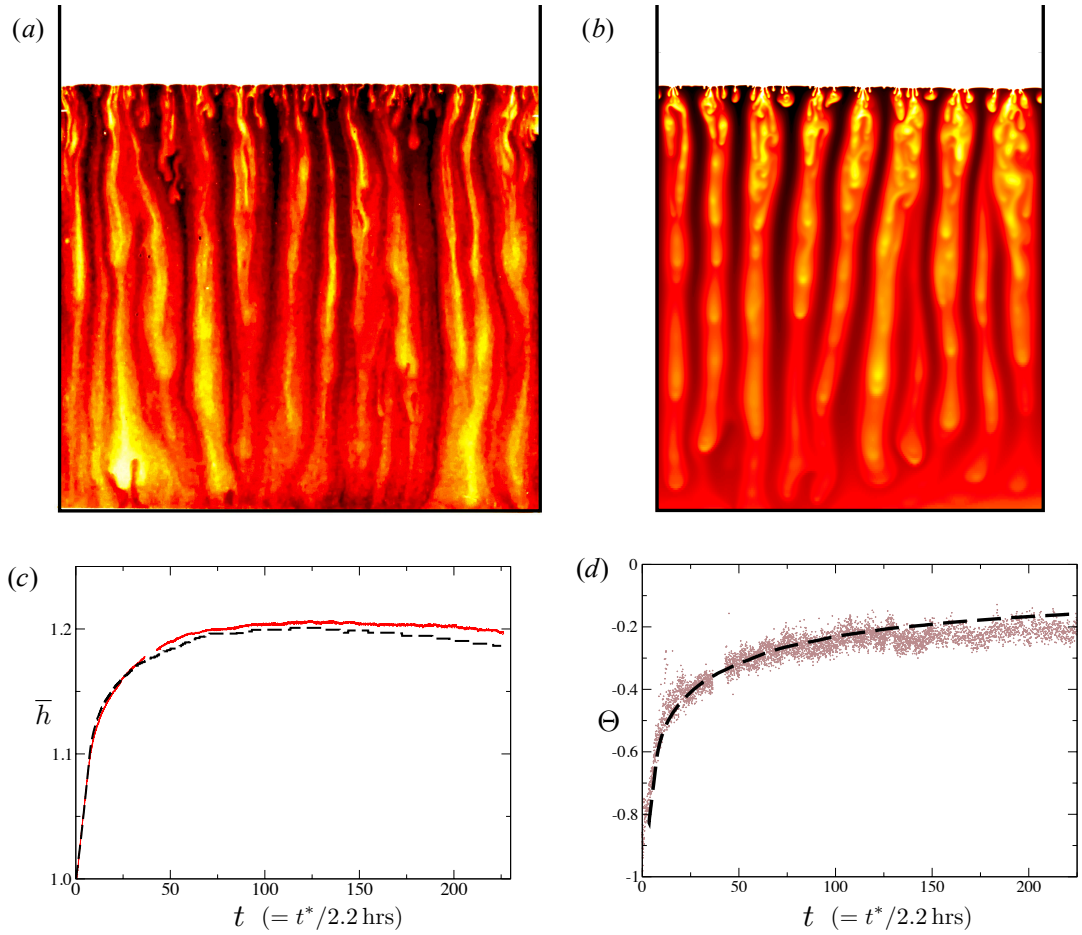


Figure 6.7: Comparison of experimental and numerical results: $(a)$ an image-processed snapshot of the lower half of the experimental setup, at time $t = 8$ ($t^* \approx 18$ hours), which roughly marks the transition to the shutdown regime; $(b)$ a snapshot from the numerical calculations described in the text, with domain width $L = 1$ and height $H = 2$, at time $t = 8$; $(c)$ the dimensionless average height of the interface $\overline{h}(t)$, from the experiment (solid) and from the numerical calculations (dashed); $(d)$ the interior concentration $\Theta(t)$, from the experiment (scattered points) and from numerical calculations (dashed line).

experiment was set up by injecting both fluids into the cell from the top: the cell was first filled with the layer of PPG, which was allowed to settle; the overlying layer of water was then added over a period of some tens of seconds. Setting the experiment up in this way led to some initial local mixing and interfacial deformation, the effects of which decayed over about 10 mins; from then onwards

the flow was dominated by downwelling fingers spread uniformly across the cell, and the interface was horizontal, except for the local deformation. This time over which the start-up transients decayed is much less than the time taken for the plumes to reach the base of the cell ($t_1^* \approx 8 - 9$ hours).

We also performed numerical simulations to compare with the experimental results (figure 6.7). In order to make a fair comparison, we estimate the effects of two physical processes in the experimental system. Firstly, the viscosity of aqueous PPG depends strongly on concentration. Pure PPG has viscosity $\mu \approx 0.05$ Pa s, while the solution with the maximum density has viscosity $\mu \approx 0.015$ Pa s (Sun & Teja, 2004). Therefore the average viscosity below the interface will decrease over time as the average concentration increases. Secondly, experimental measurements of the velocity of the downwelling plumes suggest that Taylor dispersion (Taylor, 1953) will act to increase the effective diffusivity by a factor of $2 - 3$. An estimate of both of these effects, together with the parameters presented above, gives an initial Rayleigh number $Ra_0 \approx 2 \times 10^4$, and a convective time scale $T^* \approx 2.2$ hours. The numerical simulations used this initial value of $Ra_0$, together with the equation of state $\rho = f(C)$ (figure 6.6) and an upper concentration $C_+ = 3$.

In order to give a simple approximation of the change of viscosity over time, we assume that the relevant viscosity scale is given by the average viscosity of all the fluid below the interface, and that the viscosity varies linearly with $1/\Theta^*(t)$. Since $Ra_0$ is inversely proportional to the viscosity, the value of the Rayleigh number $Ra_0$ in the simulations was changed over time, such that it increased linearly with the average concentration $\Theta(t)$. This simple approximation is not intended to reproduce the exact evolution of the experimental system, but rather to provide a reasonable qualitative estimate of the effects of viscosity variation.

The dynamical structure of the flow and the profile of convection in the experimental system are very similar to those in the numerical simulations (figures 6.7a and *b*). The average interfacial height $\overline{h}(t)$ and the interior concentration $\Theta(t)$ (figures 6.7*c* and *d*) similarly show excellent agreement between the experimental and numerical measurements. The transition to the shutdown regime can be observed at $t_2 \approx 8$ by the change in behaviour of the average interfacial height $\overline{h}$ (figure 6.7*c*): before this time the upward retreat of the interface is approximately

linear. At much later times, both the experimental and numerical measurements show that the interface slows down and eventually the height starts to decrease.

The initial linear upward retreat of the interface agrees qualitatively with the numerical observations in §6.2.2.2, and the eventual decrease of the interface agrees qualitatively with the predictions from the miscible box model in §6.2.2.1. We note, however, that the time $t_2 \approx 8$ is much earlier than the predictions and numerical measurements of $t_2$ in §6.2, because of the enhanced solute flux through the deformable interface here.

### 6.3.3 Discussion of systems with a deformable interface

The above results show that the effects of a deformable interface can be very significant for the miscible system. The excellent agreement between the numerical and experimental results with a deformable interface corroborates this observation.

We suggest that the removal of the flat-interface assumption leads to a significantly larger solute flux for two main reasons. Firstly, interfacial deformation results in the sloping of isopycnals below the interface, which leads to a baroclinic generation of lateral flow along the sloping boundary layer, and so an enhancement of the diffusive flux through the interface. (The simple increase in the length of the interface due to deformation is too small to account for the significant increase in flux.) Secondly, there is a contribution to the flux from material transport: positively buoyant fluid from above the interface can be entrained down across the interface. As the fluid loses solute by diffusion to its surroundings, its density increases because of the non-monotonic equation of state, and it continues to descend. It is difficult to quantify the relative importance of these two effects to the increase of the solute flux

The interface deforms due to the competing effects of the stabilizing density gradients above the interface and the density gradients between upwelling and downwelling plumes that drive convection below the interface. If the stabilizing density gradient is much greater than the driving density gradients, then we expect both the interfacial deformation and any entrainment across the interface to be small. This prediction is given credence by the numerical results of §6.3.1,

which show that the interfacial deformation, and the corresponding enhancement of the solute flux, are less at larger values of $C_+$. These observations suggests that the approximation of a flat interface is likely to be more appropriate for larger $C_+$ in the miscible system.

We have not examined the immiscible system with a deformable interface in this paper. In order to model this system numerically, we would need a different approach from that used in the rest of this dissertation, as the free interface would need to be tracked in both space and time, and the domain over which the equations were to be solved would no longer have a flat upper boundary.

We can, however, consider the expected effects of a deformable interface in an immiscible system. At the interface, there is a constant stable density jump $1+|\rho_+|$, which is always greater than the typical density differences ($< 1$) between upwellings and downwellings that drive convection. We therefore anticipate that the interface will remain approximately planar, and that the approximation of a flat interface will be appropriate for immiscible systems, particularly if $|\rho_+|$ is large. This observation highlights an important difference between the immiscible and miscible systems.

## 6.4 Conclusions

One-sided porous convection at high Rayleigh number bears many of the dynamical signatures of the statistically steady two-sided Rayleigh–Darcy cell. We have used this observation to develop theoretical box models which describe the shutdown of complex one-sided convective systems, by coupling the evolution of the interior concentration with the flux through the boundary layer. These theoretical models, together with our numerical and experimental tools, have allowed for the examination of a variety of different physically motivated systems, in which the active interface is either fixed or is free to move.

In this chapter, we used the techniques developed in chapter 5 to consider two different free-interface systems, comprising immiscible or miscible fluids. In §6.2, we examined both of these systems under the assumption that the interface, as defined in §5.2, remained flat. Our models predict very similar behaviour for the flux over time between the immiscible and miscible systems. In the limit of large

$C_+$, the models can be very reasonably approximated by the solution for a fixed interface. Physically, this limit corresponds to the case when the concentration of maximum density $C_m^*$ is much closer to the concentration of the lower layer $C_-^*$ than to that of the upper $C_+^*$.

We have shown, however, that the evolution of the interfacial height $h(t)$ in the two systems is qualitatively different at long times: in the immiscible system the height increases for all time, while in the miscible system it eventually decreases, provided $H$ is sufficiently large, even although the flux of solute across the interface into the lower layer remains positive. This observation provides an important difference when comparing the two systems, as discussed below.

In §6.3, we relaxed the assumption of a flat interface. We presented numerical simulations of the miscible system, which show that the interfacial height eventually decreases, in qualitative agreement with the predictions of our theoretical box model. However, the solute flux is much larger than the box model predicts. This observation was corroborated by experimental results from a Hele-Shaw cell, which show excellent agreement with full numerical simulations. We suggest that the enhancement of the flux in the miscible system is due to entrainment across the interface and sloping isopycnals below the interface, as discussed in §6.3.3. These effects are the result of a balance between the stabilizing density gradients above the interface and the driving density gradients between the interleaving plumes below the interface.

In immiscible systems, however, these density gradients are not comparable, as there is a stabilizing discontinuity in the density $(1 + |\rho_+|)$ across the interface which will dominate, particularly if $|\rho_+|$ is large. Therefore, we anticipate that the interface will remain approximately planar and entrainment across it will be negligible, in agreement with the assumptions of a flat interface.

The relative applicability of the flat-interface approximation, and the long-time behaviour of the interfacial height $h(t)$, each provide an important difference between the immiscible and miscible systems, and suggest that care should be taken when modelling immiscible systems with a miscible analogue, or vice versa. For example, Neufeld *et al.* (2010) and Backhaus *et al.* (2011) each use miscible experimental systems to model the convective dissolution of $CO_2$ in a deep saline aquifer, which is an immiscible system. In the miscible experimental systems, we

anticipate that the effects of interfacial deformation and entrainment would lead to a significant enhancement ($\approx 200-300\%$) of the solute flux. In contrast, in the $CO_2$ sequestration system, the stabilizing density difference between supercritical $CO_2$ and brine ($\sim 300\,\mathrm{kg/m^3}$) is very much larger than the density contrasts that drive convection ($\sim 10-20\,\mathrm{kg/m^3}$), and therefore we anticipate that interfacial deformation and entrainment would be negligible.

Under the assumption that capillary retention in the pore space can be ignored, and thus that the interface is 'sharp', the convective dissolution of $CO_2$ can be well described by our immiscible box model with a moving flat interface and a linear equation of state $n = 1$, presented in §6.2.1. In addition, since $CO_2$ is only very weakly soluble in brine ($3-5\%$ by weight), the value of $C_+$ for this system would be very large ($\sim 20-30$), and the flux would be well approximated by the solution for a fixed interface (5.28). In dimensional form, the total horizontally averaged solute flux for the fixed-interface system with $n = 1$ is given by

$$F^*(t) = \frac{4\alpha\,\phi\,h_0^* T^* \left(C_m^* - C_-^*\right)}{\left(T^* + 4\alpha\,t\right)^2}, \tag{6.23}$$

where $T^*$ is the convective time scale, given by $T^* = \phi h_0^* \mu/(Kg\Delta\rho_m^*)$, and $\alpha = 6.9 \times 10^{-3}$. In §8.2, we consider an illustrative example of convection in a high-permeability, and use (6.23) to estimate typical time scales for shutdown in $CO_2$ sequestration systems.

The models presented in these two chapters describe the shutdown of convection in a range of systems with different physical applications. Our theoretical, numerical and experimental results characterize the evolution of shutdown and the decay of the convective flux over time. The theoretical one-dimensional box models that we have derived provide analytically tractable tools that accurately capture the governing physics of the different convective systems. These simple models describe the relevant time scales of shutdown, and, for the free-interface systems studied in this chapter, the motion of the active interface.

# Chapter 7

# Three-dimensional Rayleigh–Darcy convection at high Rayleigh number

## 7.1 Introduction

Thus far in this dissertation we have been concerned with two-dimensional flow. The numerical study of three-dimensional porous convection remains largely unexplored, except at low values of $Ra$, primarily owing to the high numerical cost required to fully resolve calculations. In this chapter, we present what is, to our knowledge, the first numerical investigation of statistically steady three-dimensional high-Rayleigh-number convection in a porous medium. This chapter forms a three-dimensional analogue of much of the work in chapter 2, and, as we shall see, reveals a number of similarities, and some interesting differences, between two-dimensional and three-dimensional Rayleigh–Darcy convection at high $Ra$.

The majority of previous numerical studies of three-dimensional Rayleigh–Darcy convection, which date from over 30 years ago, focussed on steady convection for $Ra \lesssim 300$. The onset of convection, as in a two-dimensional cell, is at $Ra = Ra_{\text{crit}} = 4\pi^2 \approx 40$, and the most unstable mode is purely two dimensional (i.e. with zero wavenumber in the third dimension). The onset of convection with

a fully three-dimensional mode is at $Ra = 4.5\pi^2 \approx 45$ (Holst & Aziz, 1972); however, the two-dimensional mode continues to give a larger heat flux for $Ra \lesssim 97$ (Straus & Schubert, 1979). For $97 \lesssim Ra \lesssim 300$, the heat flux is maximised by a steady three-dimensional planform (Schubert & Straus, 1979), although multiple possible steady states exist for the flow in this range (Straus & Schubert, 1981). Schubert & Straus (1979) reported that the flow becomes unsteady for $Ra \gtrsim 300$. Some of the dynamics of the unsteady flow for $Ra \lesssim 740$ were investigated by Kimura *et al.* (1989); these are briefly discussed in §7.3.1 below. We are not aware of any numerical studies of the statistically steady system that explore the dynamics of the flow for $Ra > 740$.

Statistically steady three-dimensional convection has also been investigated in experimental work. Elder (1967) reports some experimental results using a variety of porous media, while, in a detailed set of experiments, Lister (1990) measured both the heat flux and the dominant planform of statistically steady convection. Both authors examined a range of values of $Ra$, from onset up to $Ra = O(1000)$. The convection was driven by a temperature contrast applied across the domain, and so it is likely that heat transfer to the solid phase had a significant effect at large values of $Ra$. Lister (1990) observed that the planform of convection for $Ra \gtrsim 1000$ consisted of 'a significant number of dendritic downwellings', which fed into larger plumes; his measurements suggested that the lateral scale of the large plumes decreased roughly like $(Ra + c)^{-0.5}$, for a constant $c$.

Other studies have explored transient porous convection in three-dimensions In particular, Pau *et al.* (2010) presented numerical simulations of the startup of 'one-sided' convection, comprising downwelling convection from a dense source on an upper boundary into a deep domain, in both two and three dimensions. They identified that the flux in three dimensions was roughly 25% higher than in two dimensions. A similar recent numerical study by Fu *et al.* (2013) explored the dynamics of one-sided convection for $Ra \leqslant 6400$, and identified cellular structures of plumes near the upper boundary, that coarsened over time and entrained heat into larger downwelling fingers. They suggested that the cellular structures near the upper boundary had a lengthscale that decreased linearly with $Ra$.

In this chapter, we present a numerical study of statistically steady high-$Ra$ convection in a three-dimensional Rayleigh–Darcy cell. We explore in detail the

dynamics of the flow and the variation of the flux, as described by the Nusselt number $Nu$, over the range $1500 \leqslant Ra \leqslant 2\times10^4$, using high-resolution numerical simulations. Many of the questions that motivated the two-dimensional study in chapter 2, concerning both the flux (and whether the 'classical' linear scaling $Nu \sim Ra$ is attained) and the dynamical structure of the flow, have evident analogues here.

In §7.2, we outline the governing equations, mathematical formulation, and numerical scheme (the latter is discussed in more detail in appendix A, §A.3). In §7.3.1, we briefly describe the features of the flow for $4\pi^2 \leqslant Ra \lesssim 1500$. In §7.3.2, we explore in detail the dynamical structure of the flow and the corresponding relationship $Nu(Ra)$ in the 'high-$Ra$' regime, over the range $1500 \leqslant Ra \leqslant 2\times10^4$. Many of the questions that motivated the two-dimensional study in chapter 2 have evident analogues here. In particular, our measurements strongly suggest that the classical linear scaling $Nu \sim Ra$ (discussed in chapter 2) is attained asymptotically. In addition, we show that a steady 'heat-exchanger' framework provides an increasingly good description as $Ra \to \infty$ of the interior flow in the three-dimensional cell. Measurements of the dominant horizontal wavenumber $k(Ra)$ are roughly fitted by $k \sim Ra^{0.54}$.

In §7.4, we summarize and discuss the main results of this work.

## 7.2 Governing equations and numerical scheme

We consider Boussinesq flow $\boldsymbol{u} = (u, v, w)$ in a three-dimensional, homogeneous and isotropic porous medium. The flow is incompressible and satisfies Darcy's law. The equation of state $\rho(T)$ is linear, and the temperature field $T$ evolves by advection and diffusion. In dimensionless variables, these equations give

$$\boldsymbol{\nabla} \cdot \boldsymbol{u} = 0, \tag{7.1a}$$

$$\boldsymbol{u} = -\left(\boldsymbol{\nabla} p + T\hat{\boldsymbol{z}}\right), \tag{7.1b}$$

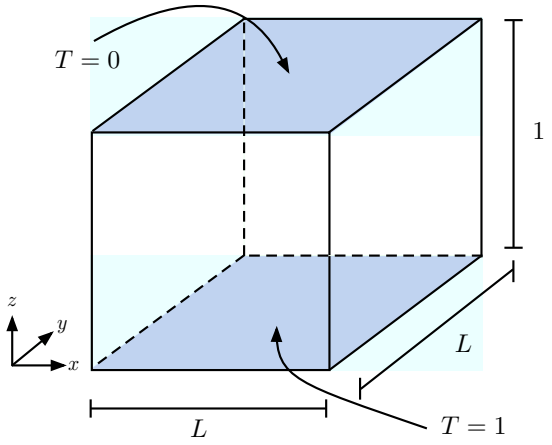


Figure 7.1: A schematic of the dimensionless three-dimensional Rayleigh–Darcy cell under consideration. All boundaries other than the upper and lower boundaries are periodic.

$$\frac{\partial T}{\partial t} = -\boldsymbol{u} \cdot \boldsymbol{\nabla} T + \frac{1}{Ra} \nabla^2 T, \tag{7.1c}$$

where $Ra$ is the Rayleigh number, given, as in (2.10), by

$$Ra = \frac{\Delta \rho g K H}{\phi \kappa \mu}, \tag{7.2}$$

and $\Delta\rho$ is the driving density difference between the upper and lower boundaries of the domain, $g$ is the gravitational acceleration, $K$ is the permeability, $H$ is the height of the domain, $\phi$ is the porosity, $\kappa$ is the thermal diffusivity, and $\mu$ is the viscosity, all of which are assumed to be constant.

The cell has height $z = 1$, with boundary conditions on the upper and lower boundaries of the cell given by

$$w = 0,\ T = 1 \quad \text{on} \quad z = 0, \qquad w = T = 0 \quad \text{on} \quad z = 1. \tag{7.3}$$

The domain is periodic in the two horizontal directions, with period $L$ (figure 7.1).

The average dimensionless flux is given by the Nusselt number,

$$Nu = \langle nu(t) \rangle = \left\langle \frac{1}{L^2} \int_0^L \int_0^L - \left. \frac{\partial T}{\partial z} \right|_{z=0} \mathrm{d}x\, \mathrm{d}y \right\rangle, \tag{7.4}$$

where $nu(t)$ is the instantaneous Nusselt number.

We satisfy incompressibility (7.1a) by the introduction of a vector potential $\boldsymbol{\Psi} = (\psi_x, \psi_y, \psi_z)$, which obeys

$$\boldsymbol{u} = \boldsymbol{\nabla} \times \boldsymbol{\Psi} = \left( \frac{\partial \psi_z}{\partial y} - \frac{\partial \psi_y}{\partial z}, \frac{\partial \psi_x}{\partial z} - \frac{\partial \psi_z}{\partial x}, \frac{\partial \psi_y}{\partial x} - \frac{\partial \psi_x}{\partial y} \right). \tag{7.5}$$

The vector potential $\boldsymbol{\Psi}$ is defined by (7.5) only up to the addition of $\nabla\xi$, for any scalar $\xi$. To constrain this gauge freedom, we consider the curl of (7.1b), which, together with the definition of $\boldsymbol{\Psi}$ in (7.5), gives

$$\boldsymbol{\nabla} \times \boldsymbol{u} = \nabla (\nabla \cdot \boldsymbol{\Psi}) - \nabla^2 \boldsymbol{\Psi} = \left( \frac{\partial T}{\partial y}, -\frac{\partial T}{\partial x}, 0 \right). \tag{7.6}$$

In order to generate a set of simple Poisson equations for the components $\psi_{x,y,z}$ of the vector potential (similar to the Poisson equation for the streamfunction $\psi$ in two-dimensions; see §2.2), we set the gauge condition to be

$$\nabla \cdot \boldsymbol{\Psi} = 0, \tag{7.7}$$

(cf. the Lorentz gauge condition in electrodynamics). Equation (7.6) then reduces to

$$\nabla^2 \psi_x = -\frac{\partial T}{\partial y}, \qquad \nabla^2 \psi_y = \frac{\partial T}{\partial x}, \qquad \nabla^2 \psi_z = 0. \tag{7.8$a$, $b$, $c$}$$

It is straightforward to show (see, e.g., E & Lui 1997) that the gauge condition (7.7) is satisfied throughout the domain provided that is is satisfied on the boundaries. Since the domain is periodic in both $x$ and $y$, both the gauge condition (7.7) and the velocity boundary conditions in (7.3) are satisfied by setting

$$\psi_x = \psi_y = \frac{\partial \psi_z}{\partial z} = 0, \quad \text{on} \quad z = 0, 1. \tag{7.9$a$, $b$, $c$}$$

Equations (7.8$c$) and (7.9$c$) combine to give $\psi_z = 0$ everywhere. The velocity $\boldsymbol{u}$ is therefore determined by the Poisson equations for $\psi_x$ and $\psi_y$ given by (7.8$a$,$b$), with boundary conditions given by (7.9$a$,$b$).

We solved (7.1c) and (7.8$a$,$b$) numerically. The numerical scheme is briefly outlined here, and discussed in detail in appendix A, §A.3. As with the two-

dimensional simulations of chapter 2, we used a coordinate transformation $\zeta(z)$ to fully resolve the thin diffusive boundary layers near the upper and lower boundaries of the domain. The Poisson equations (7.8*a,b*) were solved using fast Fourier transforms for the $x$ and $y$ derivatives, and second-order finite differences for the vertical derivatives. The transport equation (7.1c) was solved using an unconditionally stable three-dimensional alternating-direction implicit method devised by Brian (1961). As in two dimensions, we spatially discretized the diffusion terms using second-order finite differences, and we used a flux-conservative approach for the advection operator. We used a midpoint method for the time derivatives to give second-order temporal accuracy. We parallelized the numerical scheme using a hybrid of both open multi-processing (OpenMP) and message-passing interface (MPI) specifications.

For all the simulations presented in this chapter, the initial condition was given by a linear vertical temperature gradient $T(x, y, z) = 1 - z$, with a small and spatially random perturbation.

## 7.3 Results

The primary focus of this chapter is to explore three-dimensional flow in the 'high-$Ra$' regime, which, for the purposes of this chapter, we define as $Ra \gtrsim 1500$ (see §7.3.2 below). In order to provide a context for these results, we begin in §7.3.1 with a very brief outline of the dynamics of the flow for $Ra \lesssim 1500$. For this range of $Ra$, the system exhibits an array of interesting dynamical structures, bifurcations, and pattern-formation, as discussed below, which warrant a more systematic study; such a study is left for future work. In § 7.3.2, we investigate the 'high-$Ra$' regime in detail.

### 7.3.1 Overview of the flow dynamics for moderate values of $Ra$

Figure 7.2 shows numerical measurements of $Nu(Ra)$ from a three-dimensional cell with aspect ratio $L = 2$. For comparison, measurements from a two-dimensional cell (taken from chapter 2) are also shown. The results show the

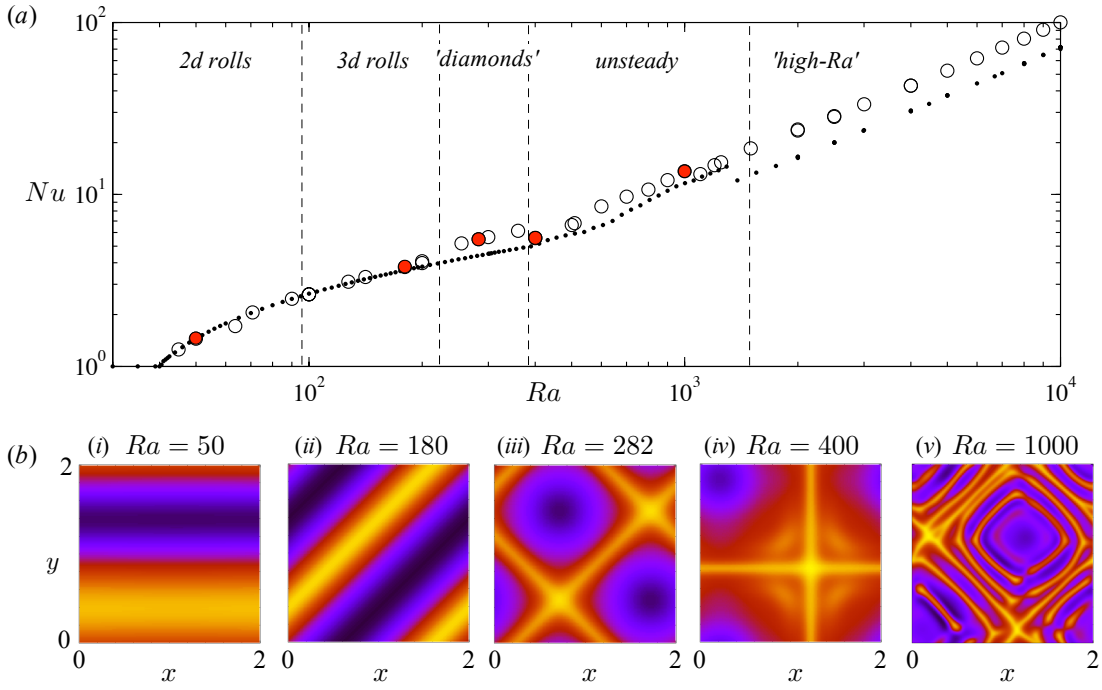


Figure 7.2: (*a*) Measurements of $Nu(Ra)$ (circles) from the onset of convection at $Ra = Ra_{\mathrm{crit}} = 4\pi^2$ to the 'high-$Ra$' regime. All calculations with $Ra < 1500$ have aspect ratio $L = 2$; the calculations for $Ra \geqslant 1500$ are discussed in §7.3.2 below. Measurements from a two-dimensional cell from chapter 2 (dots) are included for comparison. (*b*) Snapshots of the temperature field at depth $z = 30/Ra$, just above the lower boundary, for a selection of values of $Ra$ as marked, corresponding to the red circles in (*a*).

onset of convection at $Ra = Ra_{\mathrm{crit}} = 4\pi^2$. As discussed in the introduction, the planform of the steady flow just above onset is purely two-dimensional (figure 7.2*b,i*). For $Ra \gtrsim 97$, the heat flux is instead maximised by a steady three-dimensional roll (figure 7.2*b,ii*), while for $Ra \gtrsim 250$, a steady 'diamond' planform (figure 7.2*b,iii*) gives a distinctly larger heat flux again. We found that, for $Ra \gtrsim 400$, the steady flow is unstable to a secondary instability; the flow is thus unsteady, and the transition from steady to unsteady flow is marked by a clear decrease in the heat flux[1]. Over the range $400 \lesssim Ra \lesssim 1500$, the flow exhibits a range of dynamical structures and patterns (e.g. figure 7.2*b,iv-v*); the heat flux

[1]Previous authors have suggested that the flow is unsteady for $Ra \gtrsim 300$ (e.g. Schubert & Straus 1979); we found steady solutions in that range, and unsteady flow for $Ra \gtrsim 400$. We have not, however, explored this transition in detail.

appears to be periodic in time for low values of $Ra$ in this range, but becomes chaotic for $Ra \gtrsim 500$. For $Ra \gtrsim 1500$, the system is in the high-$Ra$ regime; the transition to this regime is discussed in §7.3.2 below.

Through examination of a number of simulations (not presented here), we have observed that both hysteresis and aspect ratio play a large part in determining the dynamical structure of the flow; there appear to be multiple steady and quasi-steady states for a given value of $Ra$ and aspect ratio $L$. The transitions between the different regimes identified above are therefore approximate. For example, it can be seen in figure 7.2 that the calculation at $Ra = 63$ has a lower heat flux than the trend in the data would suggest, which is because the system adopted a steady three-dimensional roll planform, rather than the two-dimensional roll planform adopted in each of the calculations at neighbouring values of $Ra$.

Although some of the features of the flow for $Ra \lesssim 1500$ have been previously explored (e.g. Schubert & Straus 1979; Kimura *et al.* 1989), the wealth of pattern formation and series of bifurcations exhibited by the flow over this range certainly warrant more detailed study. In particular, it would be interesting to systematically explore hysteretic effects and the relationship between the aspect ratio of the cell and the flow structure in the unsteady range $Ra \gtrsim 400$. Since the focus of this chapter is to explore the flow in the high-$Ra$ regime, such a study is left for the future.

### 7.3.2 The high-$Ra$ regime

In a two-dimensional cell, the transition to the 'high-$Ra$' regime is marked by a change in the dynamical structure, from unit-aspect-ratio rolls with 'dripping' plumes to columnar exchange flow in a thinner aspect ratio. The transition at $Ra \approx 1300$ is marked by a clear decrease in $Nu$ (see chapter 2). In a three-dimensional cell, such a transition is more difficult to identify. In fact, the high-$Ra$ regime is only rather loosely defined: a plausible description of the transition to the high-$Ra$ regime is that below the transition, the flow comprises a steady planform of convection that is not completely broken down by perturbing instabilities in the boundary layers, whereas above the transition, the steady background flow is completely broken down. Thus, the calculation at $Ra = 1000$ shown in fig-

ure 7.2($b$,$v$) lies below the transition as there is an evident background diamond structure to the flow.

Based on examination of a series of snapshots of the flow in the range $1000 \leqslant Ra \leqslant 2000$, we have found that the transition to the high-$Ra$ regime exhibits significant dependence on aspect ratio (as well as hysteresis). Indeed, for aspect ratio $L = 2$, calculations at $Ra = 1100$ appear to lie above the transition to the high-$Ra$ regime (this can be indirectly observed in figure 7.2 by the slight decrease in $Nu$ between $Ra = 1000$ and $Ra = 1100$). However, for $L = 1$ we have found simulations up to $Ra = 1500$ that still appear to be dominated by a background steady flow that has not been broken down.

Further investigation into the transition to the high-$Ra$ regime is ongoing. In this chapter, however, we take $Ra \approx 1500$ to be the transition, to ensure that all the calculations presented lie in the high-$Ra$ regime.

#### 7.3.2.1 Structure of the flow

Figure 7.3 shows snapshots of the temperature field in the high-$Ra$ regime at three different depths $z$ and three different values of $Ra$, while figure 7.4 shows snapshots from the same simulations at fixed $x = L/2$. The flow has many analogues with the two-dimensional flow discussed in chapter 2; indeed, there are clear visual parallels between the vertical slices in figure 7.4 and the snapshots of the flow in two dimensions (figure 2.2). As in two-dimensions, the flow can be divided into three regions of differing dynamics. The interior region appears to be dominated by roughly vertical and fairly large-scale exchange flow with distinct regions of hot rising fluid and cold sinking fluid. At the upper and lower boundaries of the domain there are thermal boundary layers which are almost too small to distinguish in figure 7.4. Between the boundary layers and the interior flow is a region dominated by the growth and intermittent flushing of long, thin, filamentary structures that arise from time-dependent boundary-layer instabilities (figure 7.3). The filaments are the three-dimensional analogue of two-dimensional protoplumes, and so, for simplicity, we refer to this region as the protoplume region. Vigorous mixing by the filamentary protoplumes drives entrainment into the interior large-scale exchange flow. Visual inspection of figure 7.3 suggests that

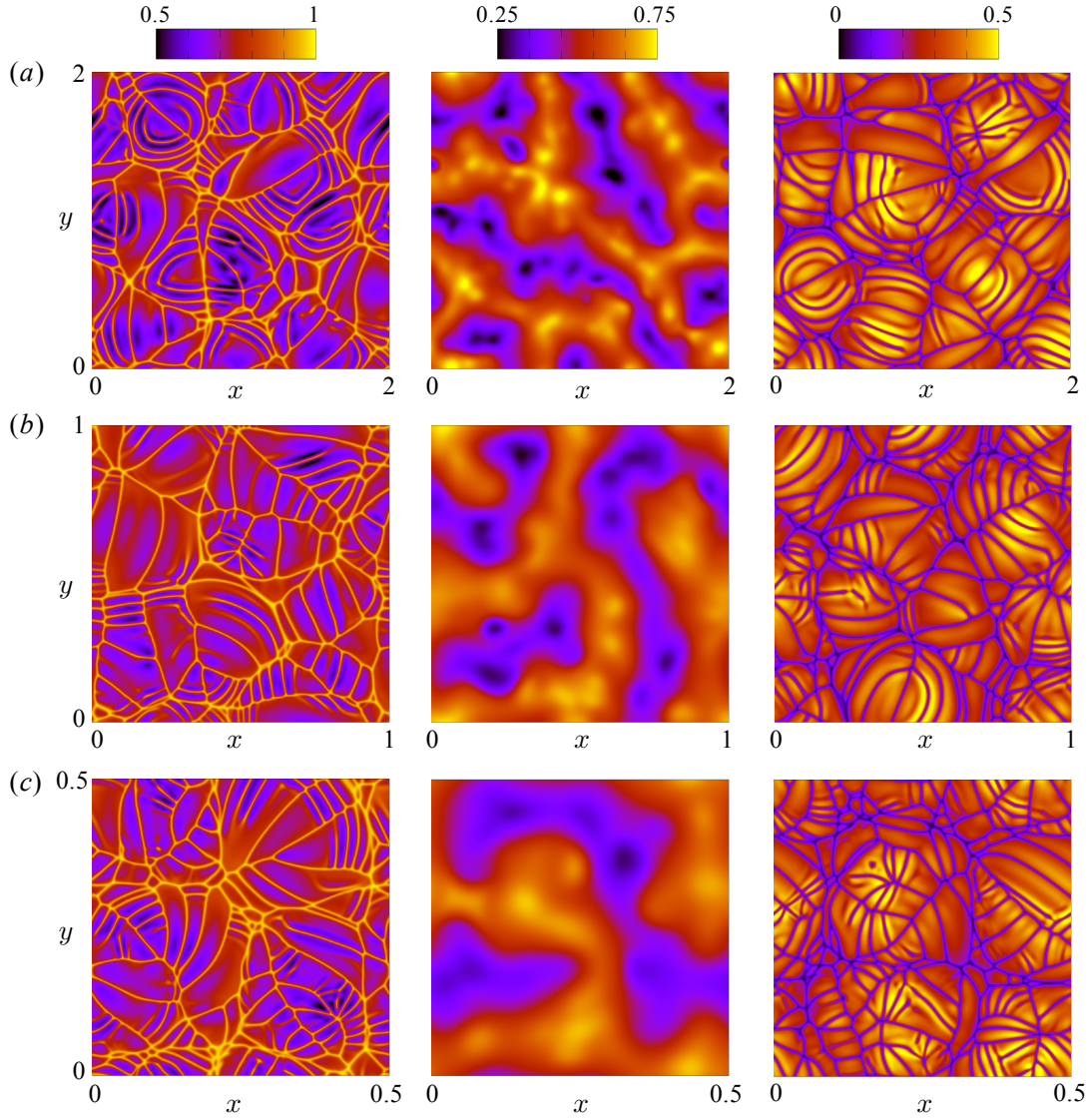


Figure 7.3: Snapshots of the temperature field at heights of $z = 30/Ra$ near to the lower boundary, (left), $z = 0.5$ in the interior of the flow (centre), and $z = 1 - 30/Ra$ near to the upper boundary (right), for: $(a)$ $Ra = 4000$ and $L = 2$; $(b)$ $Ra = 8000$ and $L = 1$; and $(c)$ $Ra = 1.6 \times 10^4$ and $L = 0.5$. Note the different scales on the axes for each subfigure.

the spatial scale of the filamentary plumes near the boundary layers decreases more rapidly with $Ra$ (note the different spatial scales in the figure) than the scale of the dominant wavelength in the interior of the flow (see also §7.3.2.4 below).

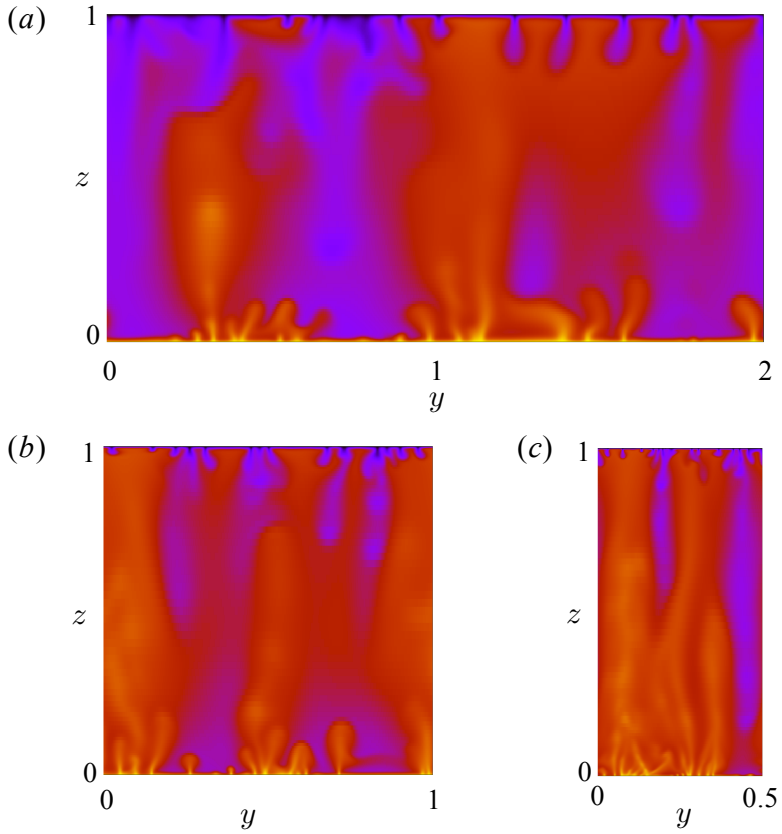


Figure 7.4: Snapshots of the temperature field (from the same simulations as in figure 7.3) at $x = L/2$, for $(a)$ $Ra = 4000$ and $L = 2$; $(b)$ $Ra = 8000$ and $L = 1$; and $(c)$ $Ra = 1.6 \times 10^4$ and $L = 0.5$.

#### 7.3.2.2 The Nusselt number $Nu(Ra)$

In a statistically steady state in the high-$Ra$ regime, the time-dependent Nusselt number, $nu(t)$, exhibits chaotic fluctuations about the time-averaged value $Nu$. The amplitude of the fluctuations is notably smaller than that measured for two-dimensional porous convection at the same values of $Ra$ (figure 7.5), which is likely a reflection of the additional spatial dimension over which the flux is averaged. The time-averaged Nusselt number $Nu = \langle nu \rangle$ is estimated numerically by time-averaging $nu(t)$ until the uncertainty in the mean is less than 0.25%, as discussed in appendix 2.A of chapter 2.

Measurements of $Nu(Ra)$ for different aspect ratios $L$ in the high-$Ra$ regime ($Ra \gtrsim 1500$) are shown in figure 7.6. A least-squares power-law approximation

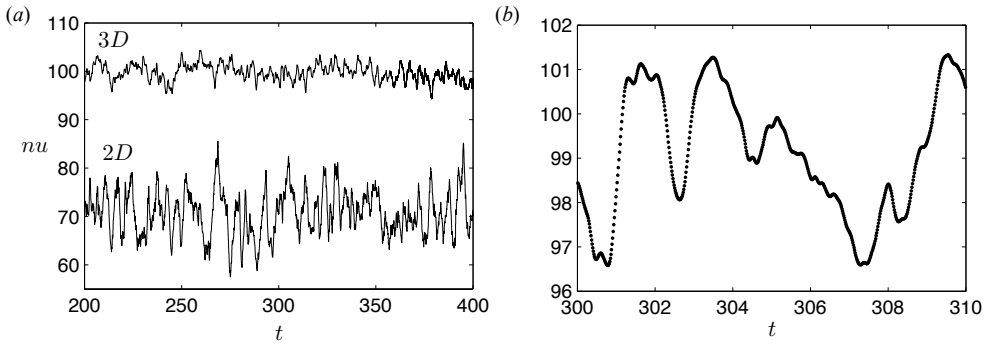


Figure 7.5: The instantaneous Nusselt number $nu(t)$ for $Ra = 10^4$ and $L = 1$: $(a)$ together with $nu(t)$ from two-dimensional simulations at $Ra = 10^4$ (lower line); and $(b)$ individual data points separated by five time steps $\Delta t$, which illustrate the high temporal resolution of the calculations.

to the data is given by $Nu = 0.0163\, Ra^{0.95\pm0.01}$; however, the data is much more accurately fit by an expression of the form

$$Nu = \alpha_3 Ra + \beta_3; \qquad \alpha_3 \approx 9.6 \times 10^{-3}, \quad \beta_3 \approx 4.28. \tag{7.10}$$

Figure 7.5 shows a comparison of the best-fit power-law curve and (7.10). The good fit given by (7.10) strongly suggests that the classical linear scaling $Nu \sim Ra$ is attained asymptotically.

The fit given by (7.10) has an analogous form to the fit found for two-dimensional convection in chapter 2, (2.14). Perhaps the most important observation from these measurements, however, is that the flux $Nu(Ra)$ is much larger than in two dimensions. A comparison of the pre-factor $\alpha_3$ from (7.10) with the pre-factor $\alpha = 6.9 \times 10^{-3}$ from the two-dimensional fit (2.14) shows that the flux in the high-$Ra$ regime is approximately 40% larger in three dimensions.

The slight variation in the measurements shown in figure 7.6 is likely a reflection of some long-timescale variability in the structure of the flow in the interior of the domain. It is possible that the structure, in turn, is slightly affected by mode restriction from the horizontal periodicity of the domain. We return to this point when we investigate the dominant horizontal length scales of the flow in §7.3.2.4 below.

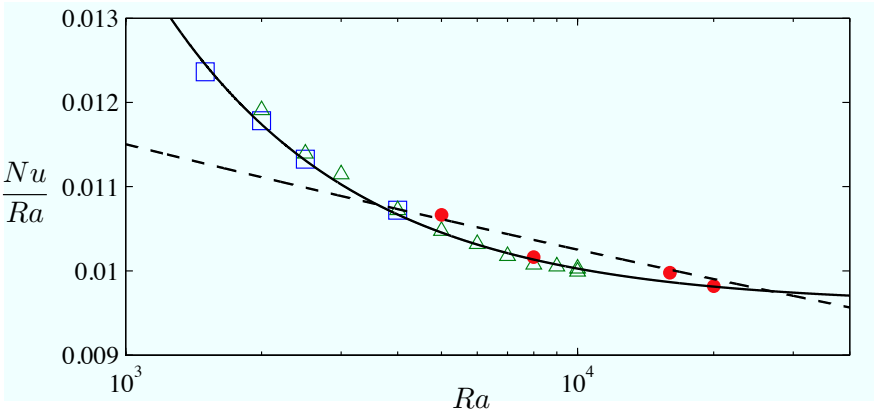


Figure 7.6: The time-averaged Nusselt number scaled by $Ra$, in the high-$Ra$ regime, for aspect ratio $L = 2$ (blue squares), $L = 1$ (green triangles), and $L = 0.5$ (red dots). As in two-dimensions, the best-fit power law $Nu = 0.0163Ra^{0.95}$ (dashed line) does not capture the trend in the data as $Ra$ is increased; instead, a good fit is provided by $Nu = \alpha_3 Ra + \beta_3$ (solid line) for $\alpha_3 = 9.6 \times 10^{-3}$ and $\beta_3 = 4.28$ (7.10).

#### 7.3.2.3 Three-dimensional heat-exchanger solution

Movies of the flow through the interior of the domain reveal that the large-scale exchange flow appears to be almost quasi-steady: the upwelling and downwelling plumes are 'persistent', in that their locations only vary over timescales that are very many times longer than the timescales for flushing of filamentary plumes in the protoplume region.

By analogy with the two-dimensional results in chapter 2, we can write down a simple, steady 'heat-exchanger' solution for buoyancy-driven columnar exchange flow, as a model for the exchange flow in the interior of the domain. Heat-exchanger solutions comprises a steady balance between vertical advection along a background temperature gradient, in columns with a given planform, and horizontal diffusion between the interleaving columns. The simplest such three-dimensional heat-exchanger model, with a square columnar planform, is given by

$$T = \widehat{A} \cos kx \cos ky - \frac{2k^2}{Ra} z, \tag{7.11a}$$

$$u = v = 0, \tag{7.11b}$$

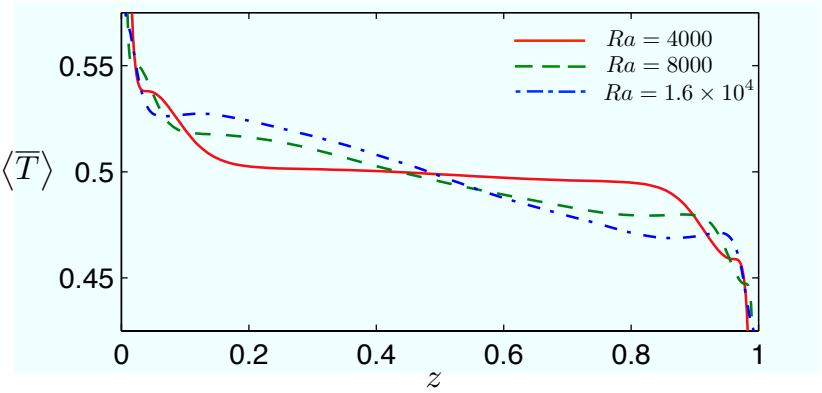


Figure 7.7: The temporally and horizontally averaged temperature profile $\langle \overline{T} \rangle$, for $Ra = 4000$ (red solid), $Ra = 8000$ (green dashed), and $Ra = 1.6 \times 10^4$ (blue dot-dashed). The profiles are approximately linear through the interior of the domain, with a gradient that increases with $Ra$; this is the opposite behaviour to two-dimensional Rayleigh–Darcy convection (figure 2.6).

$$w = \widehat{A} \cos kx \cos ky, \tag{7.11c}$$

and consists of square columns with amplitude $\widehat{A}$ and wavenumber $k$ in both $x$ and $y$ directions.

Using measurements from the numerical calculations, we can examine whether or not a heat-exchanger model of the form given in (7.11) provides a good description of the flow in the interior of the Rayleigh–Darcy cell at high $Ra$. Profiles of the temporally and horizontally averaged temperature $\langle \overline{T} \rangle$ (figure 7.7) show that the background temperature is roughly linear throughout the interior region, in agreement with the prediction of (7.11a). However, unlike in two dimensions, where the gradient decreases with $Ra$ (see figure 2.6), here we observe that the magnitude of the weak negative gradient *increases* as $Ra$ is increased. We return to this observation in §7.3.2.5 below.

We compare the amplitude of the flow from the numerical simulations with the amplitude in the heat-exchanger model by measuring the root-mean-squared (rms) temperature perturbations and velocities, $T_{\mathrm{rms}}$, $w_{\mathrm{rms}}$, $v_{\mathrm{rms}}$, and $u_{\mathrm{rms}}$. Analytic calculation of the rms values from (7.11) shows that, in the heat-exchanger model, $T_{\mathrm{rms}} = w_{\mathrm{rms}} = \widehat{A}/2$ and $u_{\mathrm{rms}} = v_{\mathrm{rms}} = 0$. Numerical measurements of the

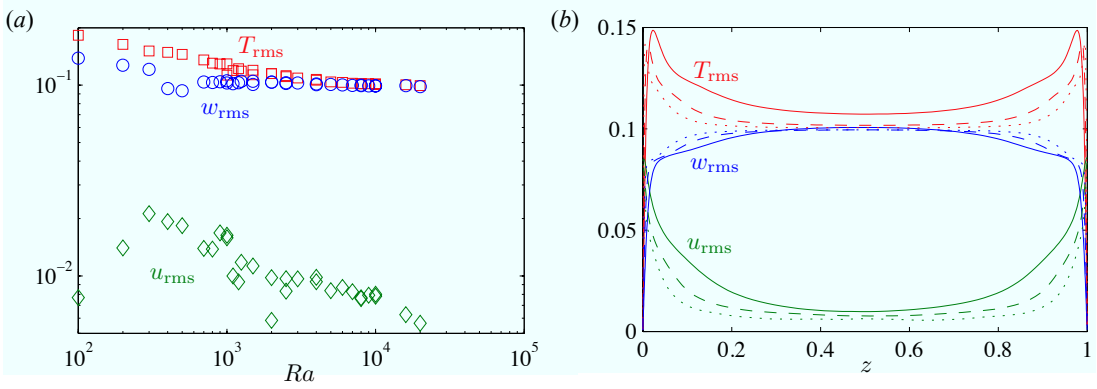


Figure 7.8: Measurements of the temporally averaged rms temperature perturbations $T_{\rm rms}$ and velocities $w_{\rm rms}$ and $u_{\rm rms}$ at $(a)$ $z = 0.5$, against $Ra$; and $(b)$ $Ra = 4000$ and $L = 2$ (solid), $Ra = 8000$ and $L = 1$ (dashed), and $Ra = 1.6\times10^4$ and $L = 0.5$ (dotted), against $z$. Measurements of $v_{\rm rms}$ are indistinguishable from $u_{\rm rms}$, and, for clarity, are not shown.

rms quantities at $z = 0.5$ in the high-$Ra$ regime indicate an increasing agreement with the model predictions as $Ra$ is increased (figure 7.8$a$): the horizontal velocities decrease with $Ra$, and the vertical velocity and temperature appear to tend to the same constant value. This value gives an estimate of $\widehat{A} = 2T_{\rm rms} \approx 0.2$. As a consistency check, this measurement can be used with the heat-exchanger theory to estimate the flux $Nu(Ra)$, as follows. As $Ra \to \infty$, vertical advection dominates the flux through the interior of the domain, and the vertical advective flux given by (7.11) is $Nu = \widehat{A}^2 Ra/4$. Using the measured estimate of $\widehat{A}$ gives a prediction of $Nu \approx 0.01Ra$, which is comfortingly close to the asymptotic prediction from the directly measured relationship (7.10) of $Nu = 9.6\times10^{-3}\,Ra$.

Figure 7.8($b$) shows the vertical variation of the rms measurements at different values of $Ra$. The figure displays the same qualitative features as the equivalent figure for two-dimensional convection (figure 2.7): specifically, the rms quantities are increasingly uniform throughout the interior of the domain as $Ra$ is increased, in agreement with the heat-exchanger model, while near the upper and lower boundaries the rms quantities vary appreciably. The latter observation indicates that the heat-exchanger model breaks down near the boundaries, and is a reflection of the presence of the flushing and entrainment of filamentary protoplumes in those regions.

These measurements all indicate that a heat-exchanger model provides an increasingly good description as $Ra \to \infty$ of the flow throughout the interior region of a three-dimensional Rayleigh–Darcy cell. This observation implies that, as for two-dimensional convection, the interior flow becomes increasingly ordered as $Ra \to \infty$ into columns of steady exchange flow, with a lateral wavenumber $k$. In the following section we present measurements of this wavenumber.

#### 7.3.2.4 The average horizontal wavenumber $k(Ra)$

We extract a measure of the average horizontal wavenumber $k(Ra)$ from the numerical calculations by taking a double Fourier transform of the temperature field. Snapshots of the resultant power spectra as a function of the horizontal wavenumbers $k_x$ and $k_y$ (figure 7.9*a–c*) reveal that the power $P$ depends predominantly on the magnitude of the wavenumber vector, or the 'radial wavenumber' $k_r = \sqrt{k_x^2 + k_y^2}$. This observation implies that the convection is isotropic, both near the upper and lower boundaries and in the interior of the flow. It is clear, from a comparison of power spectra at different values of $Ra$ (figure 7.9*a–c*), that the decay in the power at large wavenumbers has a much stronger scaling with $Ra$ in the protoplumes regions than in the interior of the domain.

We can extract a measure of the average dominant wavenumber $k$ by taking the expected value of $k_r = \sqrt{k_x^2 + k_y^2}$ over two dimensions, and averaging over time, to give

$$k = \left\langle \frac{\int\int \sqrt{k_x^2 + k_y^2}\, P(k_x, k_y)\, \mathrm{d}k_x\, \mathrm{d}k_y}{\int\int P(k_x, k_y)\, \mathrm{d}k_x\, \mathrm{d}k_y} \right\rangle = \left\langle \frac{\int k_r \widetilde{P}(k_r)\, k_r\, \mathrm{d}k_r}{\int \widetilde{P}(k_r)\, k_r\, \mathrm{d}k_r} \right\rangle, \qquad (7.12)$$

where the second equality follows from converting to radial co-ordinates, and setting $\widetilde{P} = \int P\, \mathrm{d}\theta$, where $\theta = \tan^{-1}(k_y/k_x)$. We observed above that measurements of $P$ depend predominantly on $k_r$, rather than on $\theta$, and so we expect $\widetilde{P} \propto P$. Measurements of the radial power $k_r P(k_r)$ show both a clear peak at a relatively small wavenumber, which confirms the presence of a well-defined dominant horizontal lengthscale for the flow, and an exponential decay for larger wavenumbers (figure 7.9*d,e*). The decay in the wavenumber is much slower in the protoplume regime (figure 7.9*e*) than in the interior of the flow (figure 7.9*d*),

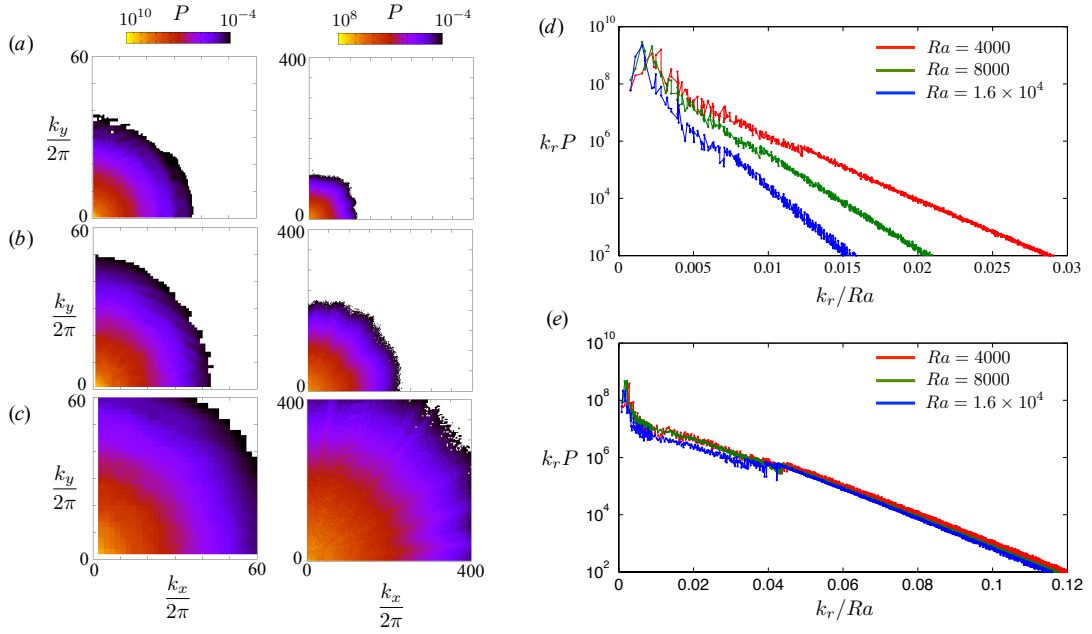


Figure 7.9: Snapshots of the instantaneous power spectra $P(k_x, k_y)$ at $z = 0.5$ (left) and $z = 30/Ra$ in the protoplume region (right), for: $(a)$ $Ra = 4000$ and $L = 2$; $(b)$ $Ra = 8000$ and $L = 1$; and $(c)$ $Ra = 1.6 \times 10^4$ and $L = 0.5$. At both depths, the spectra show no systematic dependence on the angle $\theta = \tan^{-1}(k_y/k_x)$, which suggests that the flow is isotropic. Note the logarithmic colour scale. The radial power $k_r P$ from (7.12) is shown against the radial wavenumber $k_r = \sqrt{k_x^2 + k_y^2}$ scaled by $Ra$, at depths: $(d)$ $z = 0.5$; and $(e)$ $z = 30/Ra$. Both plots show a peak corresponding to the dominant wavenumber of the interior flow; however, at a depth of $z = 30/Ra$ the decay at larger wavenumbers scales with $k_r/Ra$, whereas at $z = 0.5$, the scaling with $Ra$ appears to be much weaker. Note the different scales on the horizontal axis in $(d)$ and $(e)$.

which reflects the presence of the high-wavenumber filamentary structures that dominate the flow there (note the different horizontal scale between these figures). As in the snapshots of the power spectra discussed above, the decay in the radial power exhibits a much weaker scaling with $Ra$ in the interior of the flow (figure 7.9$d$) than in the protoplume region (figure 7.9$e$), where the measurements show a clear scaling of $k_r \sim Ra$.

For computational ease, we measured $k$ using the first equality of (7.12). Measurements of $k(Ra)$ at $z = 0.5$ are shown in figure 7.10$(a)$. A least-squares

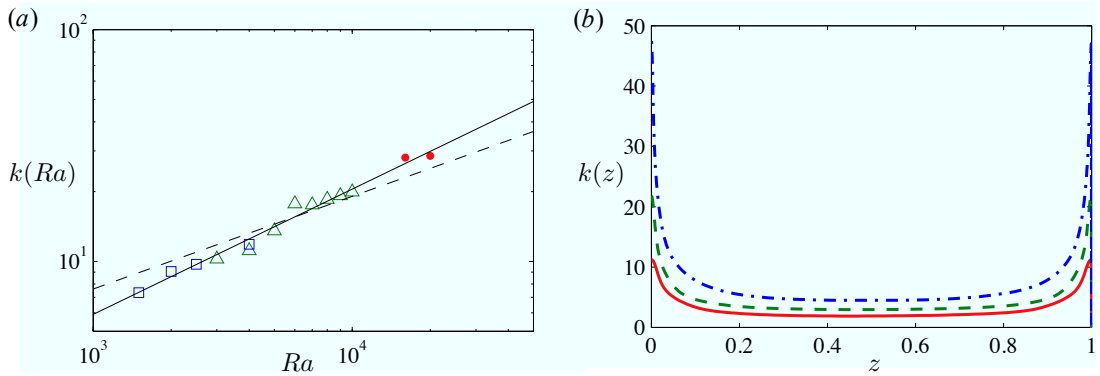


Figure 7.10: Measurements of the dominant horizontal wavenumber $k$. $(a)$ $k(Ra)$ at $z = 0.5$, from simulations with $L = 2$ (blue squares), $L = 1$ (green triangles), and $L = 0.5$ (red dots). The best-fit power law $k \sim Ra^{0.54}$ (7.13) is given by the solid line. The best-fit curve from measurements of $k(Ra)$ for two-dimensional Rayleigh–Darcy convection, given by $k = 0.48Ra^{0.4}$ (2.16), is shown for comparison (dashed line). $(b)$ $k(z)$, for $Ra = 4000$ and $L = 2$ (red solid), $Ra = 8000$ and $L = 1$ (green dashed), and $Ra = 1.6 \times 10^4$ and $L = 0.5$ (blue dot-dashed). The scaling with $Ra$ appears to be roughly linear ($k \sim Ra$) near the boundaries, in contrast to the much weaker scaling in the interior.

power-law fit to the data gives a scaling of

$$k \approx 0.142\, Ra^{0.54}, \tag{7.13}$$

with 95% confidence intervals giving a range of $\pm 0.05$ for the exponent. For comparison, figure 7.10$(a)$ also shows the fitted relationship $k(Ra)$ for two-dimensional porous convection from chapter 2, given by $k = 0.48\, Ra^{0.4}$ (2.16). In magnitude, the two-dimensional and three-dimensional wavenumbers are similar over the range of $Ra$ for which we have measurements; however, the two-dimensional wavenumber displays a discernibly weaker scaling with $Ra$.

The dominant wavenumber $k(z)$ is shown over the whole depth of the domain in figure 7.10$(b)$. These measurements confirm the previous indications of figure 7.9 that the dominant lengthscales of the flow have a much stronger dependence on $Ra$ in the protoplume regions near the upper and lower boundaries than in the interior of the domain. The evidence of figure 7.10$(b)$, together with the decay of the spectra in figure 7.9 and a visual comparison of the snapshots in

figure 7.3, suggests that the dominant lengthscale in the protoplume regions has a scaling of roughly $Ra^{-1}$. This result agrees with previous suggestions for the scaling of these structures in transient ('one-sided') three-dimensional convection (Fu *et al.*, 2013).

An important caveat about the measurements of $k(Ra)$ in the interior of the flow ($z = 0.5$) is the effect of the aspect ratio. At $Ra = 2 \times 10^4$, for example, the domain has aspect ratio $L = 0.5$, and $k/(2\pi) \approx 4.5$. These values indicate that, in a statistically steady state, there were on average between two and three sets of upwelling and downwelling plumes in the interior of the domain. Since these numbers are relatively small, it is possible that mode restriction has some effect on the measured value of $k$.

To investigate this effect, we undertook two calculations at $Ra = 4000$, one with $L = 1$ and one with $L = 2$. The calculations gave a very similar measurement of $k$ (figure 7.10*a*), which suggests that mode restriction is not playing a major role here, although further calculations at non-integer aspect ratios would be needed to confirm this suggestion. At other values of $Ra$ and smaller aspect ratios, we have observed mode restriction: at $Ra = 5000$, for example, the measurement of $k$ for $L = 0.5$ (not included in figure 7.10*a* because of its extremely anomalous value) was more than double that for $L = 1$. Further investigation of calculations at different aspect ratios $L$ is ongoing, to determine the effect of mode restriction on the measurements of $k$.

#### 7.3.2.5 The vertical temperature gradient

Having measured the wavenumber $k$, we are now in a position to understand the intriguing increase with $Ra$ of the magnitude of the linear background temperature gradient, which we observed in figure 7.7. The heat-exchanger framework (7.11) suggests a relationship between the wavenumber $k$ and the background temperature gradient $-2k^2/Ra$. Since the measured exponent for the relationship $k(Ra)$ in (7.13) is greater than 0.5, the theory predicts that the background gradient $\sim k^2/Ra$ should scale with a positive exponent of $Ra$, and so will increase in magnitude as $Ra$ is increased. In contrast, two-dimensional convection gives an exponent less than 0.5 for the relationship $k(Ra)$ (2.16), and so the

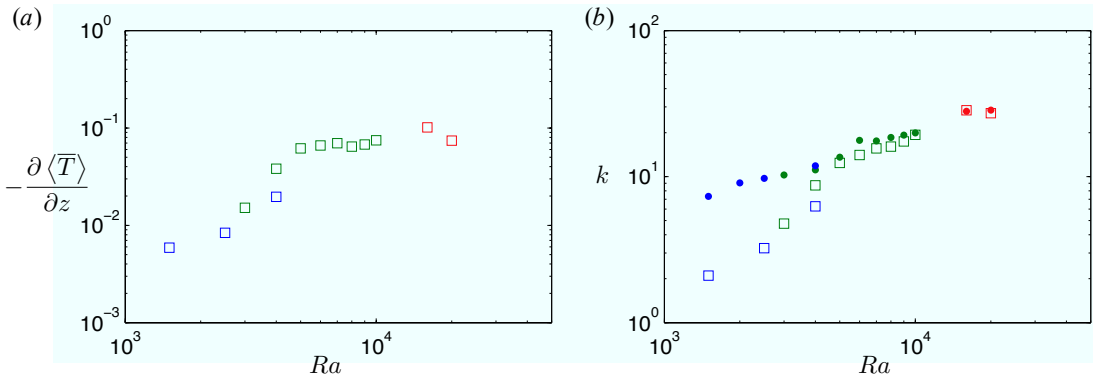


Figure 7.11: $(a)$ Measurements of the negative background gradient $-\partial \langle \overline{T} \rangle / \partial z$. $(b)$ A comparison of direct measurements of the wavenumber $k$ from figure 7.10$(a)$ (dots) and the prediction of $k = \sqrt{(-\partial \langle \overline{T} \rangle / \partial z) Ra/2}$ from the measurements in $(a)$ and the heat-exchanger theory (7.11a) (squares). In each plot, colours denote aspect ratios $L = 2$ (blue), $L = 1$ (green), and $L = 0.5$ (red).

background gradient decreases with $Ra$.

Direct measurements of the negative temperature gradient $-\partial \langle \overline{T} \rangle / \partial z$ confirm the previous observation that the magnitude of the gradient increases as $Ra$ is increased (figure 7.11$a$). There is a suggestion from the data that the rate of increase is slowing at the largest values of $Ra$. We can further verify the applicability of the heat-exchanger framework by comparing measurements of the wavenumber with measurements of the gradient using the expression for the gradient of $-2k^2/Ra$ from (7.11a). A comparison between the two measures (figure 7.11$b$) shows an increased agreement as $Ra$ is increased, which provides further evidence to suggest that the heat-exchanger model gives an increasingly good description of the interior flow.

The possible decrease in the rate of change of the gradient with $Ra$ observed in figure 7.11$(a)$, together with the agreement demonstrated in figure 7.11$(b)$, raises the suggestion that the measured relationship $k(Ra)$ is (7.13) is not a fully asymptotic scaling, and that the wavenumber might have a slightly weaker scaling with $Ra$ as $Ra \to \infty$. Measurements at higher values of $Ra$ would be required to confirm this suggestion. However, the suggestion seems likely, since the heat-exchanger model shows that the background gradient in the interior of the flow would diverge as $Ra \to \infty$, if the measured exponent of $0.54 > 0.5$ were an

asymptotic result.

## 7.4 Conclusions and discussion

In this chapter, we have presented the first measurements of statistically steady three-dimensional convection in a porous medium at high $Ra$. Our measurements of the flux, over the range $1500 \leqslant Ra \leqslant 2 \times 10^4$, are very well fitted by an expression of the form $Nu = \alpha_3 Ra + \beta_3$, for $\alpha_3 = 9.6 \times 10^{-3}$ and $\beta_3 = 4.28$. This fit, which has the same form as the fit of the flux $Nu(Ra)$ in two-dimensional high-$Ra$ porous convection (see chapter 2), strongly suggests that the flux attains the classical linear scaling asymptotically. The flux is roughly 40% larger than the flux for two-dimensional convection; this difference has evident importance for physical applications, where fluxes might be significantly underestimated if a two-dimensional parameterization of the flux is used.

The structure of the flow for $Ra \gtrsim 1500$ is dominated in the interior by persistent exchange flow, with dominant horizontal wavenumber $k$. Instabilities in the thin thermal boundary layers near the upper and lower boundaries give rise to vigorous flushing and mixing of long, thin, filamentary 'protoplume' structures, which drive entrainment into the interior exchange flow. Numerical measurements strongly suggest that the interior flow is increasingly well described by a three-dimensional heat-exchanger model as $Ra$ is increased. The model consists of a steady balance of vertical advection in interleaving columns along a background linear temperature gradient and horizontal diffusion between the columns. We considered a specific heat-exchanger model with a square planform, although it is difficult to discern a distinct horizontal planform of the exchange flow from snapshots of the interior flow (e.g. figure 7.3). The trend of the measurements presented in this chapter, which indicate that the heat-exchanger model provides an increasingly good description of the interior flow as $Ra \to \infty$, suggests that the planform might become more distinct at higher values of $Ra$.

Measurements of the wavenumber and visual inspection of the flow in the filamentary protoplume regime suggest a scaling for the lateral lengthscale of the thin filaments of approximately $Ra^{-1}$. This scaling would agree with the observed scaling for the protoplumes in two-dimensional porous convection (chapter 2). In

the interior of the flow, however, the dominant wavenumber is fairly well described by a scaling of $k \sim Ra^{0.54}$, which is much stronger than the analogous scaling for $k$ in two dimensions. Measurements of the background temperature gradient provided, via heat-exchanger theory, confirmation of these measurements. Further investigation into the effect, if any, of aspect ratio on the measurements of $k$ is ongoing.

We found some suggestion from measurements of a reduction in the measured exponent of 0.54 as $Ra$ is increased. The confirmation of this suggestion would require calculations at higher values of $Ra$ and larger aspect ratios $L$, both of which are currently unfeasible owing to the very high numerical cost required to fully resolve the dynamics on the smallest scales. Without undertaking direct numerical simulations, however, we can still predict that an asymptotic exponent for the relationship $k(Ra)$ of greater than 0.5 seems implausible. This is because, for an exponent greater then 0.5, the effect of horizontal diffusion ($k^2/Ra$) would increase with $Ra$; to balance this increase, the background gradient would also increase, leading ultimately to a reduction in the temperature contrast across the boundary layers at the upper and lower boundaries, and so a reduction in the flux. An interesting question then remains, as to whether $k \sim Ra^{0.5}$ might be the asymptotic scaling, or whether the exponent might reduce further still, towards the scaling observed for two-dimensional convection. Motivated by the results of chapter 3, it is likely that a linear-stability analysis of the three-dimensional heat-exchanger flow might shed light on this question. Such an analysis, discussed at the end of chapter 3, is left for future work.

Some of this work was performed using the Darwin Supercomputer of the University of Cambridge High Performance Computing Service, provided by Dell Inc. using Strategic Research Infrastructure Funding from the Higher Education Funding Council for England and funding from the Science and Technology Facilities Council; these resources are gratefully acknowledged.

# Chapter 8

# Conclusions, and implications for $CO_2$ sequestration

## 8.1 Conclusions

In this dissertation we have studied a range of problems involving convection in a fluid-saturated porous medium at high Rayleigh number $Ra$.

In chapter 2, we presented a detailed numerical investigation of the statistically steady flow in a two-dimensional Rayleigh–Darcy (porous Rayleigh–Bénard) cell at high $Ra$. Rayleigh–Darcy convection undergoes a transition at $Ra \approx 1300$ from predominantly large-scale quasi-periodic rolls to vigorous columnar exchange flow driven by unsteady plume formation in boundary layers. Our measurements of the convective flux, as described by the Nusselt number $Nu$, in this 'high-$Ra$' regime reveal that, contrary to some previous indications, the classical linear scaling $Nu \sim Ra$ is attained asymptotically. The measurements of $Nu(Ra)$ for $1300 < Ra \leqslant 4 \times 10^4$ are extremely well described by $Nu = \alpha Ra + \beta$, for $\alpha = 6.9 \times 10^{-3}$ and $\beta = 2.75$.

The structure of the flow is characterised in the interior by vertical columnar exchange flow of 'megaplumes' across the height of the cell at a (statistically) regular and $Ra$-dependent horizontal wavenumber. Near the boundaries, the flow is instead dominated by short wavelength boundary layer instabilities that drive vigorous protoplume growth and entrainment into the interior megaplume flow.

We found that the interior flow is increasingly well described as $Ra \to \infty$ by a simple, steady, columnar heat-exchanger model with a single horizontal wavenumber $k(Ra)$ and a linear background temperature field. The flow, therefore, becomes increasingly 'ordered' as $Ra$ is increased, in clear contrast to the turbulent interior dynamics of pure-fluid Rayleigh–Bénard convection for $Ra \gg 1$. The dominant horizontal wavenumber $k$ of the interior flow increases as $Ra$ is increased, and numerical measurements of $k(Ra)$ for $1300 < Ra \leqslant 4 \times 10^4$ are roughly fitted by $k \sim Ra^{0.4}$, although there is some suggestion of a weaker scaling at the highest values of $Ra$. An investigation of the dynamics of protoplumes near the upper and lower boundaries of the cell suggested that the columnar wavenumber is not controlled directly by the vigorous dynamics near the boundaries.

In chapter 3, we examined the hypothesis that the columnar flow-structure of high-$Ra$ porous convection is instead determined by the stability of the columnar flow. We tested this hypothesis by examining the linear stability of an unbounded columnar heat-exchanger solution, which is governed by the parameter $A = \widehat{A}Ra/k$, where $\widehat{A}$ is the amplitude of the flow. The flow is always unstable; for $A \lesssim 17.2$ the instability takes the form of a largescale overturning associated with the background unstable linear temperature gradient, while for $A \gtrsim 17.2$, the instability takes the form of vertically propagating pulses on the background columns. By solving a matched asymptotic expansion in the limit of strong columnar flow or large $Ra$ (i.e. $A \gg 1$), we found that the growth rate $\mathrm{Re}\{\sigma\}$ asymptotes to $\mathrm{Re}\{\sigma\} = 0.2308A^{4/9}$ as $A \to \infty$. We used direct numerical simulations to show that the evolution of the instability in the non-linear regime results in a coarsening of the columnar flow.

We applied the results of the stability analysis to the columnar flow in a Rayleigh–Darcy cell, by balancing the time scales for growth of the most unstable perturbation and vertical propagation across the domain. This balance suggests that the columnar flow is unstable for wavenumbers $k$ greater than $k \sim Ra^{5/14}$, as $Ra \to \infty$. A correction to this scaling for non-asymptotic values of $Ra$ predicts a slightly stronger dependence on $Ra$ for $Ra \leqslant 4 \times 10^4$, in good agreement with the trend of the numerical measurements presented in chapter 2. This result supports the hypothesis that the physical mechanism controlling the horizontal scale of columnar convection is the stability of the columnar flow. Under this hypothesis,

the interior flow in a Rayleigh–Darcy cell is forced at small lengthscales ($\sim Ra^{-1}$) by protoplumes near the upper and lower boundaries, but the flow coarsens and the horizontal lengthscales increase until the flow becomes stable, at a lengthscale $\sim k^{-1} \sim Ra^{-5/14}$ as $Ra \to \infty$.

In chapter 4, we examined the implications for high-$Ra$ convection of heterogeneity in the porous medium, specifically when the heterogeneity takes the form of thin low-permeability horizontal layers. We presented a numerical study of statistically steady convection in a Rayleigh–Darcy cell containing a thin low-permeability horizontal layer centred in the middle of the cell. When both the height $h$ and the relative permeability $\Pi$ of the interior low-permeability layer are small, the flow is governed solely by their ratio $\Omega = h/\Pi$, the impedance. We studied the flow in this limit, and analysed the dependence of both the convective flux $Nu$ and the dynamical flow-structure on $\Omega$.

We observed two particularly striking features. First, as $\Omega$ is increased from zero (the limit of homogeneous Rayleigh–Darcy convection), the flow develops a cellular structure and the horizontal lengthscale of the cells increases dramatically. Second, the flux $Nu$ can *increase* as $\Omega$ is increased from zero (i.e. as the permeability of the inner layer is decreased, for fixed $h \ll 1$), before decreasing significantly for larger values of $\Omega$. At $Ra = 2500$, for example, $Nu$ attains a maximum at $\Omega \approx 0.3$ that is roughly 30% larger than the Nusselt number for homogeneous convection. For larger values of $Ra$, the increase in $Nu$ with $\Omega$ is weaker. For larger values of $\Omega$ ($\Omega \gtrsim 5$), there is a transition in the flow structure as the impedance to flow across the interior layer is so large that diffusion becomes the dominant transport mechanism across the layer. We demonstrated that the qualitative decrease of the flux with $\Omega$, and the flux in the diffusive regime, can be described with very simple reduced models. Our observations provide a number of directions for future work, as discussed in §4.4.3 and §4.5.

The work of chapters 2–4 was concerned primarily with statistically steady 'two-sided' convection. In chapter 5 and chapter 6, we developed this work to study 'one-sided' porous convection, driven by a source of density on one boundary only. We developed theoretical and numerical models of the shutdown of convection in one-sided porous systems at high $Ra$. In chapter 5, we revealed a close dynamical relationship between the slowly evolving one-sided shutdown

system and the two-sided Rayleigh–Darcy cell. Our results showed that measurements of $Nu(Ra)$ from a Rayleigh–Darcy cell can be used to give excellent quantitative agreement with the evolution of the flux in the shutdown regime. We used this observation to develop simple reduced theoretical models of the shutdown of convection, which give excellent predictions of the evolution of the convective flux when compared with direct numerical simulations. The dynamical structure of the flow in the shutdown regime is dominated by persistent columnar megaplumes that extend across the height of the domain, and the horizontal spacing of these plumes changes with the evolving average density in very good quantitative agreement with measurements from a Rayleigh–Darcy cell. We extended this work to consider the effect of general power-law equations of state.

In chapter 6, we developed the ideas of the previous chapter to investigate a range of different physical systems. We considered systems comprising two fluid layers, separated by an active interface which can move as a result of the convective flux across it. We separately examined the case of two immiscible fluids and the case of two miscible fluids. Under the assumption that the interface remains flat as it moves, we developed reduced theoretical models of each system, which give excellent agreement with measurements of the evolution of the flux and the height of the interface from direct numerical simulations. In the case of miscible fluids with an interface that is free to deform, we also found good agreement between laboratory experiments in a Hele–Shaw cell and numerical simulations. These investigations showed that the flux could be dramatically enhanced by interfacial deformation. For immiscible fluids like $CO_2$ and water, we argued that interfacial deformation was unlikely to be important owing to the stabilizing density jump at the interface; this observation highlights an important difference between immiscible and miscible systems.

In common with the majority of previous studies of porous convection, the work in chapters 2-6 concerned two-dimensional flow. In chapter 7, we presented the first numerical study of three-dimensional statistically steady convection in a porous medium at high Rayleigh number. We developed fully resolved numerical simulations of the flow in a three dimensional Rayleigh–Darcy cell for $Ra \lesssim 2 \times 10^4$. An overview of the flow for $Ra < 1500$ revealed a range of interesting and largely unexplored convective dynamics, which deserve further study.

In the 'high-$Ra$' regime ($Ra \gtrsim 1500$), measurements of the convective flux were very well described by $Nu = \alpha_3 \, Ra + \beta_3$, for $\alpha_3 = 9.6 \times 10^{-3}$ and $\beta_3 = 4.28$. This fit both implies that the classical linear scaling $Nu \sim Ra$ is attained asymptotically, and also indicates that the convective flux is roughly 40% larger than the corresponding flux in the two-dimensional cell, measured in chapter 2.

There are certain clear analogues between the three-dimensional flow structure in the high-$Ra$ regime and the two-dimensional structure characterized in chapter 2. The statistically steady three-dimensional convective flow for $Ra \gtrsim 1500$ consists of large-scale persistent exchange flow in the interior of the domain. Instabilities in the thin thermal boundary layers near to the upper and lower boundaries of the domain give rise to episodic and highly time-dependent bursts of long, thin, filamentary protoplumes, which drive the interior exchange flow. The interior flow is increasingly well described by a steady heat-exchanger model, characterized by a linear background temperature gradient and a dominant horizontal wavenumber $k$. Numerical measurements of the wavenumber are roughly fitted over the range $1500 \leqslant Ra \leqslant 2 \times 10^4$ by $k \sim Ra^{0.54}$, which gives a distinctly larger exponent that the equivalent expression for two-dimensional convection (roughly $k \sim Ra^{0.4}$; chapter 2). There is some suggestion from the measurements of a reduction in this scaling for larger values of $Ra$, as might also be expected by theoretical considerations (see §7.4).

## 8.2 $CO_2$ sequestration

### 8.2.1 Implications and discussion

The primary motivation for this work, as discussed in §1.1, was to model and understand the convective dissolution of geologically sequestered $CO_2$ in saline aquifers. In this dissertation, we have measured flux laws, analysed the dynamical structure of convection, and developed simple reduced models of convection that can be used in geophysical settings. We consider the implications of some of these results here.

For the sake of this discussion we will use illustrative parameter values from a relatively high permeability aquifer, such as the Utsira sand reservoir at Sleip-

ner (Ennis-King & Paterson, 2005; Bickle *et al.*, 2007). We take: permeability $K = 5 \times 10^{-12}\,\mathrm{m}^2$; porosity $\phi = 0.3$; $g = 10\,\mathrm{m/s}^2$; driving density contrast between dense $CO_2$ solution and brine $\Delta\rho^* = 15\,\mathrm{kg/m}^3$; viscosity of brine $\mu = 5 \times 10^{-4}\,\mathrm{Pa\ s}$; and diffusivity of $CO_2$ $D = 10^{-9}\,\mathrm{m}^2/\mathrm{s}$. The equation of state for $CO_2$ and brine is linear ($n = 1$ in the terminology of chapters 5 and 6). We consider an aquifer of depth $H = 100\,\mathrm{m}$. The convective time scale $T^*$ for this system is given by $T^* = \phi H\mu/(\Delta\rho^* gK) \approx 0.6\,\mathrm{years}$; for comparison, the diffusive time scale is given by $H^2/D \approx 3 \times 10^5\,\mathrm{years}$. The Rayleigh number for this illustrative aquifer, which is the ratio of these time scales, is $Ra \approx 6 \times 10^5$.

In chapter 2, we determined the flux law $Nu = \alpha Ra + \beta$ for two-dimensional statistically steady convection. For $Ra > O(10^4)$, this expression can be very well approximated by setting $\beta = 0$. The horizontally averaged dimensional flux $F^*$ (i.e. the volume flux per unit area) is then given by the expression

$$F^* = \frac{\alpha\, b\, gK \left(C^*_m - C^*_-\right)^2}{\mu}, \tag{8.1}$$

where $b$ is the coefficient in the linear equation of state $\rho(C)$ (5.5). The flux is thus independent of both the height $H$ of the aquifer and the diffusivity $D$. The expression $\left(C^*_m - C^*_-\right)$ denotes the difference in the concentration of $CO_2$ between the dense $CO_2$-saturated solution ($C^*_m \approx 0.05$) and pure brine ($C^*_- = 0$); the fact that this driving concentration difference is small reflects the weak solubility of $CO_2$ in brine ($\sim 5\%$ by weight).

The parameter values above give $F \approx 5 \times 10^{-10}\,\mathrm{m\,s}^{-1}$. Using a density of $700\,\mathrm{kg\,m}^{-3}$, this value gives a mass flux of supercritical $CO_2$ of about 11 thousand tons per year, per kilometre squared of the $CO_2$-brine interface. The typical lengthscales of the flow can also be calculated: based on the parameters above, together with the observed scalings from chapter 2, the width of a megaplume is roughly 3 m, while protoplumes are approximately 5 cm wide.

These estimates are based on measurements from statistically steady two-dimensional two-sided convection. A comparison of measurements of the flux at early times in a one-sided system (e.g. figure 5.4) with measurements from a Rayleigh–Darcy cell (figure 2.4), shows that the flux in the one-sided system is more than double that in the two-sided system; thus, in a (one-sided) unbounded

aquifer, we would expect the values of the flux to be at least double the estimates given above. Moreover, the results are for two-dimensional convection; based on the results of chapter 7, we would expect the flux to be $\approx 40\%$ larger again in a real, three-dimensional, unbounded aquifer.

If, however, the aquifer were closed, the convective flux would shut down over time. The dissolution of $CO_2$ in this situation can be well described by our immiscible box model with a moving flat interface, as discussed in §6.4. Using the values above (with the initial height of the $CO_2$-brine interface at $h_0^* = 100\,\mathrm{m}$), together with the observations in chapters 5 and 6, we would expect the transition to the shutdown regime to occur after roughly $t_2^* \approx 10$ years. The subsequent evolution of the horizontally averaged flux is determined from our box models and given by (6.23), which can be rewritten as:

$$F^*(t) = \frac{4\alpha\, b\, gK \left(C_m^* - C_-^*\right)^2}{\mu \left(1 + 4\alpha\, t/T^*\right)^2}, \tag{8.2}$$

where $T^* = \phi h_0^* \mu/(\Delta\rho^* gK) \approx 0.6\,\mathrm{years}$ is the convective time scale, and $\alpha = 6.9 \times 10^{-3}$. Based on our immiscible box model, after 20 years, the solute flux would have halved. After 75 years, it would be one tenth of its initial value. In this time, the interface would have retreated by nearly 4 metres (4% of the original depth), and about 0.8 million tons of $CO_2$ would have dissolved for every square kilometre of the $CO_2$-brine interface. For comparison, roughly one million tons of $CO_2$ are injected at Sleipner each year. We again note that these results are for two-dimensional convection; based on the results of chapter 7, we would predict that the values of the flux would be $\approx 40\%$ larger in the shutdown regime in a three-dimensional system. We also note that these illustrative results apply to laterally confined aquifers, and, while the physical processes that we examined in chapter 5 and 6 are still relevant, the time scales and dynamics of shutdown in laterally unconfined aquifers may differ substantially.

We can also consider the effects of heterogeneous layering in the medium. Suppose that the exemplar aquifer, of total depth $H = 100\,\mathrm{m}$, contains a thin horizontal layer of depth $h^* = 1\,\mathrm{m}$. The magnitudes of these values are consistent with observations of thin mudstone layers at Sleipner (Bickle *et al.*, 2007). The

permeability of the layers could range from $10-1000$ times smaller than the main aquifer, which gives rise to values of the impedance $\Omega$ in the range $0.1 \lesssim \Omega \lesssim 10$. Neufeld & Huppert (2009) used an example value for the relative permeability at Sleipner of $\Pi \approx 0.05$, which gives $\Omega \approx 0.2$. In this case, our results in chapter 4 suggest that the low-permeability layers would have little negative effect on the rate of dissolution. In contrast, the flux would be considerably lower if the permeability contrast was larger, in which case it is likely that lateral migration along the top of the low-permeability layer or leakage through fractures in the layer would dominate the dynamics (see, e.g. Pritchard *et al.* 2001; Neufeld & Huppert 2009), rather than convection across the layer.

The representative values and time scales given here correspond to high-permeability aquifers like that at Sleipner. Some potential storage sites have permeabilities that are $2-3$ orders of magnitude smaller than that considered here, in which case the flux would be extremely weak; even the transition to the shutdown regime would take thousands of years.

### 8.2.2 Directions

An important future direction for understanding the dynamics of $CO_2$ sequestration systems is the integration of these models of convection into dynamic models of flow in porous media. In particular, current parameterizations of convection assume that the injected $CO_2$ is stationary, whereas, in general, the current will either be rising as a plume or laterally migrating as a gravity current. Since the density difference between supercritical $CO_2$ and brine ($\sim 300\,\mathrm{kg\,m^{-3}}$) that drives this migration is many times stronger than the density difference driving convection ($\sim 10-20\,\mathrm{kg\,m^{-3}}$), it is possible that the motion of the current would have an appreciable effect on the rate of dissolution. The study of convection in the presence of flow (or, analogously, convection forced with an imposed velocity), provides the next step for the modelling presented in here. A fuller understanding of the effect of flow on the strength of convection would allow for a more accurate comparison of the timescales of dissolution with those of spreading (e.g. Lyle *et al.* 2005; Vella & Huppert 2006) or leakage (e.g. Pritchard 2007; Neufeld *et al.* 2011).

In common with previous studies of porous convection, throughout this dissertation we have made the assumption that capillary retention in the pore space can be neglected, and thus that the interface between $CO_2$ and brine is 'sharp'. Capillary retention will have two main effects: first, isolated pockets off $CO_2$ will be retained and trapped in the pores, in the wake of the migrating $CO_2$ current (this effect provides another secure trapping mechanism for $CO_2$; see §1.1 and Hesse & Tchelepi 2008); and second, a 'capillary fringe' of partially saturated $CO_2$ and brine will form at the interface. The extent of the capillary fringe depends on the capillary forces and pore-size distribution of the rock. Golding *et al.* (2011) used measurements of the capillary pressure to estimate that the depth of the partially saturated region lies in the range $0.1 - 100\,\mathrm{m}$ (high-permeability aquifers, which thus have weaker capillary pressures, are likely to have depths towards to lower end of this range). In contrast, the illustrative values quoted above give an estimate of the boundary-layer depth of $O(1)\,\mathrm{cm}$. This comparison suggests that the effects of partial saturation may be important for convective dissolution, and warrant further investigation.

It should be noted that, from the point of view of laboratory experiments, an examination of the interaction between convective dissolution and the effects of partial saturation is not straightforward. Most analogue fluids used in previous experiments of convective dissolution are miscible (such as, for example, the fluids used in chapter 6), and so there are no capillary effects. Similarly, there is no partial saturation in a Hele–Shaw cell, which provides a useful setup for experiments as it is easy to observe the flow. Nevertheless, the development of a viable experimental setup that exhibits both partial saturation and convective dissolution would be useful, since a theoretical approach is also complicated. It is probable that the most promising theoretical approach would involve the modelling of both effects on the pore scale, and the development of a parameterization which could be incorporated into continuum (numerical) models. There are also perhaps some analogues with previous work on evaporation from partially saturated porous media which could be explored.

For a fuller understanding of the effect of dissolution on sequestered $CO_2$, comparison with reservoir-scale experiments and field observations is also required. The complex geometry and heterogeneity of most aquifers indicates that care

must be taken with models developed for idealised systems, and comparison with field data provides a meaningful check on the accuracy of model predictions. Such comparison for simple models of spreading under gravity has been ongoing using seismic data at the Sleipner site (Bickle *et al.*, 2007; Boait *et al.*, 2012). It would be interesting to extend the modelling of this dissertation to compare the effects of dissolution more directly with field measurements, both from natural $CO_2$ reservoirs (Gilfillan *et al.*, 2009) and from sequestration sites like Sleipner.

# Appendix A

# Numerical Method

The governing equations for Boussinesq convection in an ideal porous medium are given by Darcy's law, incompressibility, and a transport equation for the density field. In this appendix, we discuss the techniques used throughout this dissertation to solve these equations numerically. All the numerical code was written in the Fortran 90 programming language.

Throughout the appendix, superscript indices with index $n$ refer to temporal discretization with timestep $\Delta t$, while the subscript indices $i$, $j$, and $k$ refer to spatial discretization in the $x$, $y$, and $z$ directions, respectively.

## A.1 Two-dimensional Rayleigh–Darcy convection

As discussed in chapter 2, the governing equations for two-dimensional Rayleigh–Darcy convection with a linear equation of state are given by

$$\nabla^2 \psi = -\frac{\partial T}{\partial x}, \tag{A.1}$$

$$\frac{\partial T}{\partial t} + \boldsymbol{\nabla} \cdot \boldsymbol{u} T = \frac{1}{Ra} \nabla^2 T, \tag{A.2}$$

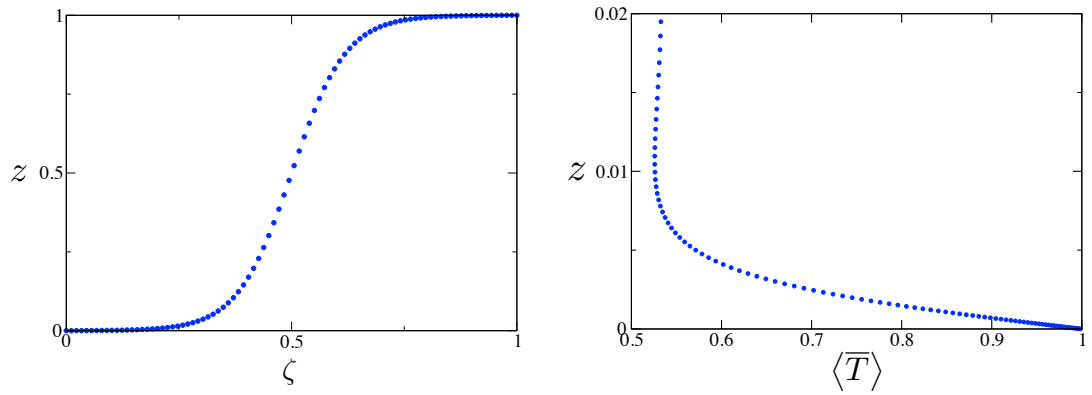


Figure A.1: $(a)$ The coordinate transformation $z(\zeta)$ for $Ra = 2 \times 10^4$. The grid points shown are separated by five (uniform) vertical steps $\Delta\zeta$. $(b)$ The horizontally and temporally averaged temperature profile $\langle\overline{T}\rangle$ for $Ra = 2 \times 10^4$ near to the lower boundary $z = 0$, showing the high density of grid points in the boundary layer.

(cf. §2.2). The boundary conditions on the upper and lower boundaries of the domain are given by

$$T = 1,\ w = 0 \quad \text{at} \quad z = 0, \qquad \text{and} \qquad T = 0,\ w = 0 \quad \text{at} \quad z = 1, \qquad (A.3a, b)$$

and the domain is periodic at $x = 0, L$.

In this section, we discuss the numerical methods used to solve (A.1)–(A.3).

### A.1.1 Coordinate transformation and grid spacing

Based on a balance between advection and diffusion in (A.2), the diffusive boundary-layer depth is expected to scale with $Ra^{-1}$. At high $Ra$, we therefore anticipate extremely thin vertical boundary layers at the upper and lower boundaries, in contrast with much larger vertical scales throughout the interior of the domain. In order to accurately resolve the boundary layers with a vertically uniform grid, we would therefore over-resolve the interior. We dramatically reduced the computational cost of the calculations by using a vertical coordinate transformation $\zeta(z)$ which maps points from the boundary layer into the interior.

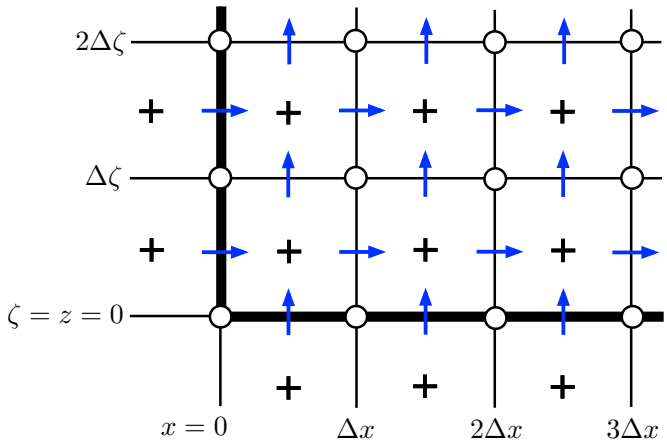


Figure A.2: A schematic showing the location of the discretized variables on a regular grid in $(x, \zeta)$ coordinates. The temperature $T$ is calculated at the centre of every grid square, signified by a plus, while the streamfunction $\psi$ is calculated on the vertices, signified by a circle. The velocity vectors are calculated at the edges of the grid squares, signified by blue arrows. The edge of the domain $x = z = 0$ is shown in bold.

The transformation from $\zeta \in [0, 1]$ to $z \in [0, 1]$ is given by

$$z = \frac{1}{2}\left[1 + \frac{\tanh\left[\eta\left(\zeta - 1/2\right)\right]}{\tanh\left(\eta/2\right)}\right], \tag{A.4}$$

where $\eta$ is an adjustable parameter. For a given value of $Ra$, $\eta$ is defined implicitly by the requirement that

$$\left.\frac{\partial T}{\partial \zeta}\right|_{z=0} \approx O(1). \tag{A.5}$$

An example of this coordinate transformation $z(\zeta)$ with $\eta \approx 8.3$ for $Ra = 2 \times 10^4$ is shown in figure A.1($a$). The extremely high spatial resolution that we are able to employ in the boundary layers is demonstrated in figure A.1($b$), which shows the horizontally averaged temperature profile near to the bottom boundary.

The governing equations (A.1) and (A.2) are transformed analytically to $(x, \zeta)$ coordinates and then solved on a uniform rectangular grid using horizontal and (transformed) vertical resolution $\Delta x$ and $\Delta\zeta$ respectively. The temperature and streamfunction are calculated on a staggered grid in $(x, \zeta)$ coordinates (see fig-

ure A.2). This discretization both arises naturally from the flux-conservative numerical method that we employ, which is discussed below, and it also aids the implementation of the boundary conditions. The temperature field is calculated at the centre of every grid square, which equates to points with coordinates $([n+1/2]\Delta x, [m+1/2]\Delta\zeta)$ for integer $n$ and $m$. The streamfunction is calculated at the vertices of the grid, which equates to points with coordinates $(n\Delta x, m\Delta\zeta)$. In order to implement second-order boundary conditions for the temperature field, we also store an additional temperature point half a grid cell outside the domain on every side, as shown in figure A.2.

### A.1.2 The Poisson equation

The Poisson equation (A.1) was solved using a fast-Fourier transform in the horizontal ($x$) direction, and a simple tridiagonal finite difference method in the vertical. This technique is useful for periodic problems without rapid variation between gridpoints, and is cheaper and quicker than relaxation methods.[1]

After taking the Fourier transform and changing variables to $\zeta(z)$, (A.1) becomes

$$\frac{\partial\zeta}{\partial z}\frac{\partial}{\partial\zeta}\left(\frac{\partial\zeta}{\partial z}\frac{\partial\widetilde{\psi}}{\partial\zeta}\right) - k^2\widetilde{\psi} = -\mathrm{i}k\widetilde{T}, \tag{A.6}$$

where a tilde signifies a Fourier transform in the $x$ component, and $k$ is the horizontal wavenumber. Given $\widetilde{T}(k,z)$, (A.6) is discretized using standard second-order finite difference operators, $\widetilde{\psi}(k,z)$ is determined by inverting the resulting tridiagonal equation, and the solution $\psi(x,z)$ is determined by an inverse Fourier transform of $\widetilde{\psi}$. Therefore, given the temperature field $T$ at time $t$, we can calculate $\psi$, and so the velocity, at time $t$.

The standard real Fourier transform enforces periodic boundary conditions on the flow at $x = 0, L$. Alternatively, boundary conditions of zero heat flux (as in chapters 5 and 6) can be enforced by using a Fourier sine transform, in which case the single spatial derivative on the right-hand side of (A.6) is given by a

[1] We also developed a successive over-relaxation (SOR) method and a multi-grid method to solve the Poisson equation, but, based on a comparison of speed, accuracy and ease of implementation, particularly with respect to the periodic boundary conditions, we used a spectral method in all the simulations presented in this dissertation.

cosine transform.

### A.1.3 The transport equation

Equation (A.2) was discretized using an alternating-direction implicit (ADI) method (e.g. Press *et al.* 1989), centred on the half time-step to give second-order accuracy in time. The temporal discretization takes the semi-implicit form

$$\frac{T^{n+1}-T^n}{\Delta t} = \frac{1}{2}\boldsymbol{\nabla}\cdot\left(\boldsymbol{u}^{n+1/2}\left[T^{n+1}+T^n\right]\right)+\frac{1}{2Ra}\nabla^2\left(T^{n+1}+T^n\right)+O(\Delta t^2). \quad \text{(A.7)}$$

The diffusion terms in (A.7) were spatially discretized using standard second-order finite-difference operators. The advection operator was discretized using a flux-conservative representation, which matches the advective fluxes into and out of grid squares and retains second-order spatial accuracy by using the velocities at the boundaries of the grid cells (as in figure A.2). The spatial discretization of the advection operators thus takes the form

$$\left[\frac{\partial}{\partial x}\left(uT\right)\right]_i = \frac{1}{\Delta x}\left[u_{i+1/2}\left(\frac{T_{i+1}+T_i}{2}\right)-u_{i-1/2}\left(\frac{T_i+T_{i-1}}{2}\right)\right]+O(\Delta x^2), \quad \text{(A.8)}$$

$$\left[\frac{\partial}{\partial z}\left(wT\right)\right]_k = \frac{1}{\Delta\zeta}\left(\frac{\partial\zeta}{\partial z}\right)_k\left[w_{k+1/2}\left(\frac{T_{k+1}+T_k}{2}\right)-w_{k-1/2}\left(\frac{T_k+T_{k-1}}{2}\right)\right]+O(\Delta\zeta^2). \quad \text{(A.9)}$$

The ADI scheme involves the recasting of (A.7) into two coupled discrete equations, each of which is implicit in one spatial direction and explicit in the other. The equations were solved by inverting a cyclic tridiagonal matrix in the $x$ direction, and a regular tridiagonal matrix in the $\zeta$ direction. The ADI scheme is unconditionally stable, and the time step $\Delta t$ was selected to satisfy the Courant condition, as discussed in §A.1.6 below.

### A.1.4 Combining the equations

There are various methods for calculating $\boldsymbol{u}^{n+1/2}$ given the temperature and velocity at previous time-steps. For the sake of compactness, we used a midpoint method rather than an extrapolation method like Adams-Bashforth. The midpoint method updates $T^n$ to $T^{n+1}$ as follows. First, the velocity field $\boldsymbol{u}^n$ is calculated using (A.6). Second, this velocity field is used as an approximation of $\boldsymbol{u}^{n+1/4}$ in the transport equation (A.7) with half the time-step, to give an approximation of the temperature at the half time-step $T^{n+1/2}$. Third, this temperature field is used to calculate the velocity at the half time-step $\boldsymbol{u}^{n+1/2}$ using (A.6) again. Finally, given the velocity at the half time-step, (A.7) is used to evolve the original temperature field $T^n$ forward one time-step to give $T^{n+1}$.

### A.1.5 Boundary conditions

The arrangement of grid points shown in figure A.2 means that the vertical velocity $w$ is stored at points along the upper and lower boundaries of the domain, so that is is very straightforward to impose no-flow boundary conditions there. The fixed-temperature boundary conditions at these boundaries in (A.3) are slightly more complicated to impose, as the temperature is not calculated exactly on the boundary (see figure A.2). In order to retain second-order spatial accuracy, we use a quadratic extrapolation of the nearest three grid points to the boundary. For example, if we desire $T = \Xi$ at $z = 0$ in the simple case of no vertical coordinate transformation ($\zeta = z$), quadratic extrapolation gives

$$T_{-1/2} = -2T_{1/2} + \frac{T_{3/2} + 8\Xi}{3} + O(\Delta z^2). \tag{A.10}$$

In the general case with a coordinate transformation ($z \neq \zeta$), we can generate a similar, but more involved, expression for the temperature $T_{-1/2}$.

Since all the heat flux into the domain is diffusive, the heat flux at the upper or lower boundary is easily measured using the temperature points on either side of the boundary. For example, the heat flux at the lower boundary is given by

$$\left.\frac{\partial T}{\partial z}\right|_{z=0} = \left.\left(\frac{\partial \zeta}{\partial z}\right)\right|_{z=0} \frac{T_{1/2} - T_{-1/2}}{\Delta \zeta} + O(\Delta z^2). \tag{A.11}$$

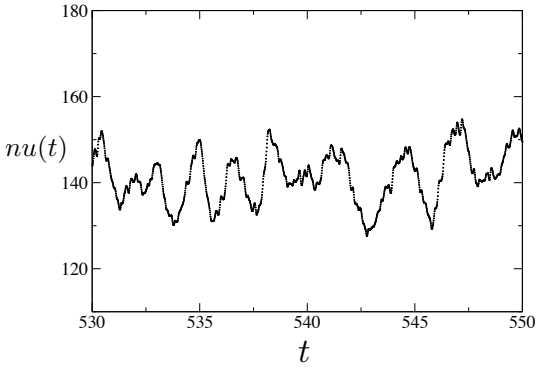


Figure A.3: The time-dependent Nusselt number $nu(t) = L^{-1} \int \partial T/\partial z|_{z=0}$ d$x$ at $Ra = 2 \times 10^4$. The data points shown are separated by ten time-steps $\Delta t$.

### A.1.6 Verification of numerical scheme

We have compared our solutions of both (A.6) and (A.7) against known analytic solutions of the Poisson and transport equations, to confirm that the code gives second-order spatial and temporal errors. With the full combined code, we have observed the well-known onset of convection at $Ra = 4\pi^2$, and found good agreement with weakly non-linear theory for slightly larger values of $Ra$ (Nield & Bejan, 2006). We have recovered the results of Graham & Steen (1994) for moderate values of $Ra \leqslant 1300$, and of Otero *et al.* (2004) for $Ra < 10^4$, as shown in figure 2.4 in chapter 2.

In the high-$Ra$ regime, the smallest horizontal scales are found in thin boundary-layer instabilities (protoplumes), and the horizontal resolution is chosen to ensure that the thinnest points of these structures contain at least ten grid points. These horizontal scales appear to decrease like $Ra^{-1}$ (see chapter 2, §2.4.2). For all but the highest decade of $Ra$ data, we have confirmed that our results are sufficiently well resolved by doubling both the horizontal and vertical ($\zeta$) resolution and recovering statistically identical results. For the highest decade, we used a resolution that is consistent with the observed spatial scalings at lower values of $Ra$, giving us confidence that all our results are well resolved. Typical values of the horizontal and (transformed) vertical discretization range from $\Delta x = (256)^{-1}$ and $\Delta\zeta = (180)^{-1}$ at $Ra = 2500$, to $\Delta x = (4096)^{-1}$ and $\Delta\zeta = (450)^{-1}$ at $Ra = 4 \times 10^4$.

The time-step $\Delta t$ is chosen to be smaller than the Courant time scale $\Delta x/\max|\boldsymbol{u}|$, which corresponds to the physical requirement that fluid is not advected further than one grid cell in one time step. At $Ra_0 = 2 \times 10^4$, the time step was $\Delta t = (1400)^{-1}$. Figure A.3 shows the time-dependent Nusselt number $nu(t)$ at $Ra = 2 \times 10^4$; the points shown are separated by ten time steps, and the fluctuations are well resolved.

## A.2 Extensions of numerical scheme in two-dimensions

In this section we outline the manner in which the numerical scheme discussed above can be extended to model the different systems that we have considered in this dissertation.

### A.2.1 Convection with a low-permeability layer: chapter 4

In chapter 4, we developed the numerical scheme discussed above to model high-$Ra$ convection in a Rayleigh–Darcy cell with a low-permeability interior layer in the region $z_1 < z < z_2$. We developed both 'full simulations', in which the interior layer was fully resolved, and 'reduced simulations', in which the interior layer was parameterized by a jump condition for the horizontal velocity (4.12).

The basic numerical scheme is very similar to that described above; the main difference lies in the choice of coordinate transformation $\zeta(z)$ needed to resolve both the dynamics at the upper and lower boundary layers, and the dynamics near to the interior layer. For the 'full simulations', we used a rather convoluted coordinate transformation from $\zeta \in [0,1]$ to $z \in [0,1]$ of the form

$$z(\zeta) = \frac{\mathcal{T}\left(\zeta, 0.25+\nu, \eta_1\right) + \mathcal{T}\left(\zeta, 0.75-\nu, \eta_1\right) + \varepsilon\mathcal{T}\left(\zeta, 0.5, \eta_2\right)}{\mathcal{T}\left(1, 0.25+\nu, \eta_1\right) + \mathcal{T}\left(1, 0.75-\nu, \eta_1\right) + \varepsilon\mathcal{T}\left(1, 0.5, \eta_2\right)}, \tag{A.12}$$

where

$$\mathcal{T}(x, y, \eta) = \tanh\left[\eta\left(x-y\right)\right] + \tanh\left(\eta y\right), \tag{A.13}$$

and $\eta_1$, $\eta_2$, $\nu$ and $\varepsilon$ are specified parameters that depend on the height $h$ and Rayleigh number $Ra$, and were chosen to ensure sufficient grid points lay in both the boundary layers near $z = 0$ and $z = 1$, and the regions near $z = z_1$ and $z = z_2$.

For the 'reduced simulations', we used a simpler transformation of the form

$$z(\zeta) = \frac{\mathcal{T}(\zeta, 0.25 + \nu, \eta) + \mathcal{T}(\zeta, 0.75 - \nu, \eta)}{\mathcal{T}(1, 0.25 + \nu, \eta) + \mathcal{T}(1, 0.75 - \nu, \eta)}, \tag{A.14}$$

where $\mathcal{T}$ is defined in (A.13), and $\eta$ and $\nu$ are again parameters that control the stretching, and depend on $\Omega$ and $Ra$. The parameters were chosen to ensure the dynamics near $z = 0$, $z = 0.5$, and $z = 1$ are fully resolved.

In the reduced simulations, we solved a jump condition for the horizontal velocity at $z = 0.5$, given by

$$\Omega \frac{\partial w}{\partial x} = [u]_{z=0.5_-}^{z=0.5_+}. \tag{A.15}$$

In order to incorporate (A.15) into the numerical scheme, it can be written in terms of the streamfunction $\psi$. The horizontal Fourier transform of the resultant equation takes the form

$$\Omega k^2 \, \widetilde{\psi} = \left.\frac{\partial \widetilde{\psi}}{\partial z}\right|_{z=0.5_+} - \left.\frac{\partial \widetilde{\psi}}{\partial z}\right|_{z=0.5_-}. \tag{A.16}$$

Equation (A.16) replaces the usual transformed Poisson equation (A.6) for the value of $\widetilde{\psi}$ at $z = 0.5$. Numerically, the expression for $\widetilde{\psi}_k$ at $z = 0.5$ is replaced by the discretized form of (A.16), which depends on $\widetilde{\psi}_{k\pm1}$; the system thus remains tridiagonal and can be solved as before. In addition, since temperature $T$ is continuous at $z = 0.5$, the transport equation can be solved across the whole domain, just as in §A.1.3.

### A.2.2 One-sided convection: chapters 5 and 6

In chapters 5 and 6, we developed numerical schemes to describe both fixed-interface and free-interface one-sided convection, with immiscible fluids and a

flat interface, and miscible fluids and both flat and deformable interfaces.

In chapter 5, the governing equations (5.10) and (5.13) were solved throughout the domain $0 \leqslant z \leqslant 1$. Similarly, in §6.3 the same equations were solved throughout the domain $0 \leqslant z \leqslant H$. In §6.2, however, the equations (5.10) and (5.13) were solved below the interface $0 \leqslant z \leqslant h(t)$ only, in order to impose a flat interface at $z = h(t)$. Above the interface, the concentration either remains constant (immiscible system) or satisfies a one-dimensional advection-diffusion equation (6.14) (miscible system).

As in previous chapters, in order to accurately resolve the dynamics near to the interface $z = h$, we used a vertical-coordinate transformation $\zeta(z, h)$. In chapter 5 and in §6.2, the transformation from $\zeta \in [0, h]$ to $z \in [0, h]$ was given by

$$z = \frac{h}{2}\left[1 + \frac{\tanh\left[\eta\left(\zeta - h/2\right)\right]}{\tanh\left[\eta\, h/2\right]}\right], \tag{A.17}$$

where $\eta(Ra_0)$ is a stretching parameter that was chosen to ensure that sufficient points lay in the boundary layer below the interface. In §6.3, the governing equations were solved over the whole domain, and the interface was located in the interior. A more complex transformation was required to accurately resolve the boundary layers on either side of the interface, without dramatically increasing the computational cost. We employed a transformation of the form

$$z = \frac{H}{A_1 + A_2}\left\{A_1\,\frac{\tanh\left(a_1\,\eta\,\zeta\right)}{\tanh\left(H\,a_1\,\eta\right)} + A_2\left[1 + \frac{\tanh\left(a_2\,\eta\,\left[\zeta - H\right]\right)}{\tanh\left(H\,a_2\,\eta\right)}\right]\right\} \tag{A.18}$$

where $\eta(Ra_0)$ is again a constant stretching parameter, and $A_1$, $A_2$, $a_1$ and $a_2$ are specified functions of the average interfacial height $\overline{h}(t)$, which were chosen to increase the resolution in a region centred on $z = \overline{h}$, and wider than the range of any interfacial deformations. To reduce the computational cost, the transformation $\zeta[z, \overline{h}(t)]$ was not re-calculated at every time step, but only when the interface $z = \overline{h}$ had moved a sufficient distance to require it. After each calculation of a new vertical discretization $\zeta(z, \overline{h})$, the variables were mapped from the previous discretization to the new grid using quadratic interpolation.

The governing equations (5.10) and (5.13) were again solved using a fast-Fourier transform and an ADI method, as described above in §A.1.2 and (A.1.3).

In §6.2 (free-interface systems with a flat interface), the location of the interface $h(t)$ was found by global conservation of solute (6.2) at each time step. For the miscible system with a flat interface (§6.2.2), the one-dimensional transport equation (6.14) was solved at each time step using standard second-order finite-difference operators on a uniform grid above the interface.

## A.3 Three-dimensional Rayleigh–Darcy convection

In chapter 7, we presented results for three-dimensional Rayleigh–Darcy convection in the high $Ra$ regime. The governing equations consist of two Poisson equations for the non-zero components of the vector potential $\boldsymbol{\Psi} = (\psi_x, \psi_y, 0)$, and a transport equation for the temperature $T$ (see §7.2). These equations, introduced in (7.8*a*,*b*) and (7.1c), respectively, are given by

$$\nabla^2\psi_x = -\frac{\partial T}{\partial y}, \qquad \nabla^2\psi_y = \frac{\partial T}{\partial x}, \qquad \frac{\partial T}{\partial t} = -\boldsymbol{u}\cdot\boldsymbol{\nabla}T + \frac{1}{Ra}\nabla^2 T. \quad (A.19a, b, c)$$

The velocity $\boldsymbol{u} = (u, v, w)$ is given from $\boldsymbol{\Psi}$ by

$$(u, v, w) = \boldsymbol{\nabla}\times\boldsymbol{\Psi} = \left(-\frac{\partial\psi_y}{\partial z}, \frac{\partial\psi_x}{\partial z}, \frac{\partial\psi_y}{\partial x} - \frac{\partial\psi_x}{\partial y}\right). \qquad (A.20)$$

The boundary conditions on the upper and lower boundary of the domain are given by

$$\psi_x = \psi_y = 0\, T = 1 \quad \text{on} \quad z = 0, \qquad \psi_x = \psi_y = T = 0 \quad \text{on} \quad z = 1, \qquad (A.21)$$

which the cell is periodic in both $x$ and $y$ directions, with period $L$.

### A.3.1 Coordinate transformation and grid spacing

As for two-dimensional convection, we employed a vertical coordinate transformation $\zeta(z)$ to fully resolve the thin diffusive boundary layers near to $z = 0, 1$. The transformation was identical to that used for the two-dimensional simulations,

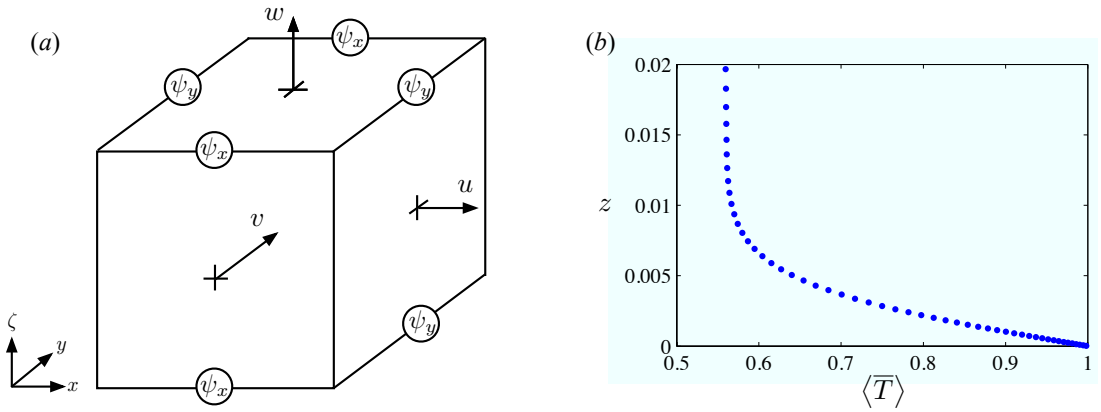


Figure A.4: $(a)$ A schematic showing one cuboid of the numerical grid, with the locations at which $\psi_x$ and $\psi_y$ are calculated. The components of the velocity, given by (A.20), are thus determined at the centre of each face of the cuboid as shown. The temperature is calculated at the centre of each cuboid. $(b)$ Measurements of the average temperature $\langle\overline{T}\rangle$ near to the lower boundary, which demonstrate the the boundary layer is well resolved.

discussed in §A.1.1.

The governing equations (A.19) were transformed to $(x, y, \zeta)$ coordinates and discretized on a uniform cuboidal grid. The three variables $(\psi_x, \psi_y, T)$ are calculated on a staggered grid, which is a requirement of the flux-conservative scheme and helps to facilitate implementation of the boundary conditions: the temperature is calculated at the centre of each grid cuboid, while $\psi_x$ and $\psi_y$ are calculated around the cuboid in such a manner that $u$, $v$ and $w$ are determined in the centre of the relevant faces of the cuboid (see figure A.4$a$). The boundary conditions for $\psi_x$ and $\psi_y$ on $z = 0, 1$ from (A.21) are straightforward to impose with this staggered layout.

### A.3.2 The equations

The two Poisson equations (A.19$a$,$b$) were solved using fast-Fourier transforms in both the $x$ and $y$ directions, and second-order finite differences to discretize the resultant tridiagonal system in the $\zeta$ direction.

The transport equation (A.19$c$) was solved using a three-dimensional ADI scheme, following Brian (1961), which is discussed below. As in §A.1.3, the dif-

fusion operator was discretized using standard two-dimensional finite difference operators. The advection operator was discretized using a flux-conservative formulation, such that the velocity into and out of every grid cell is calculated (as in figure A.4).

Second-order ADI methods are closely related to second-order semi-implicit (Crank–Nicholson) methods (Douglas, 1962; Press *et al.*, 1989). Given an equation like (A.19*c*), an ADI method involves the recasting of the equation into multiple coupled discretized equations, each of which is implicit in some spatial directions and explicit in others. By reformulating these equations back into one equation, it can be shown that the set of ADI equations is equivalent, up to second order in $\Delta t$, to the semi-implicit discretization of the original equation.

While the ADI scheme is unconditionally stable in two spatial direction, in three dimensions it is not, necessarily. In particular, the 'natural' three-dimensional ADI scheme, which has three coupled discretized equations, each of which advances an interval $\Delta t/3$ and is implicit in one direction and explicit in the others, is only conditionally stable, and the requirements of stability give a restrictively small value of $\Delta t$. There are, however, a multitude of possible sets of coupled discrete equations that, when combined, give the same semi-implicit equation up to second order in $\Delta t$. This fact has given rise to a number of different three-dimensional ADI schemes, which have different stability properties. The method that we have used is unconditionally stable, and is attributable to Brian (1961) and Douglas (1962).

As in two dimensions, we used a midpoint method to determine the velocity at the half time step, and so to retain second-order accuracy for the time derivative. We parallelized the code using a hybrid scheme involving both open multi-processing (OpenMP) and message-passing interface (MPI) specifications.

### A.3.3 Verification of numerical scheme

We verified our numerical scheme by reproducing published measurements of $Nu(Ra)$ for low values of $Ra$. We observed the onset of convection with a two-dimensional mode at $Ra = Ra_c = 4\pi^2$ (Holst & Aziz, 1972). We recovered the results of Schubert & Straus (1979) for $Ra < 300$, including the transition at

$Ra \approx 97$ to fully three-dimensional convection.

As discussed above in §A.1.6, we chose a horizontal resolution to fully resolve the smallest horizontal scales, which appear to decrease like $Ra^{-1}$. The vertical scale was chosen to ensure that multiple grid points lay inside the thin boundary layers near the upper and lower boundaries of the domain, the depth of which is also anticipated to scale with $Ra^{-1}$. We tested simulations with both double and half the horizontal resolution $Ra = 2000$, and with both larger and smaller vertical resolutions, and we recovered statistically identical results. Although, to reduce the numerical cost, we used slightly fewer points in the vertical direction than for the two-dimensional simulations discussed in §A.1, the simulations remain very well resolved in the vertical direction (see figure A.4*b*). Typical values of the horizontal and (transformed) vertical discretization range from $\Delta x = \Delta y = (128)^{-1}$ and $\Delta\zeta = (130)^{-1}$ at $Ra = 1000$, to $\Delta x = \Delta y = (1024)^{-1}$ and $\Delta\zeta = (200)^{-1}$ at $Ra = 10^4$.

# References


Ahlers, G., Grossmann, S. & Lohse, D. 2009 Heat transfer and large scale dynamics in turbulent Rayleigh-Bénard convection. *Rev. Mod. Phys.* **81**, 503–537. 10, 16, 31, 37

Backhaus, S., Turitsyn, K. & Ecke, R.E. 2011 Convective instability and mass transport of diffusion layers in a Hele-Shaw geometry. *Phys. Rev. Lett.* **106**, 104501. 16, 38, 109, 110, 113, 146, 152

Bear, J. 1988 *Dynamics of Fluids in porous Media*. Dover. 4, 5, 104

Beaumont, D.N. 1981 The stability of spatially periodic flows. *J. Fluid Mech.* **108**, 461–474. 43

Bickle, M., Chadwick, A., Huppert, H.E., Hallworth, M.A. & Lyle, S. 2007 Modelling carbon dioxide accumulation at Sleipner: Implications for underground carbon storage. *Earth Planetary Sci. Lett.* **255**. 76, 184, 185, 188

Boait, F. C., White, N. J., Bickle, M. J., Chadwick, R. A., Neufeld, J. A. & Huppert, H. E. 2012 Spatial and temporal evolution of injected $CO_2$ at the Sleipner Field, North Sea. *J. Geophys. Res.* **117**, 2156–2202. 76, 188

Brian, P.L.T. 1961 A finite-difference method of high-order accuracy for the solution of three-dimensional transient heat conduction problems. *AIChE Journal* **7**, 367–370. 160, 200, 201

Busse, F.H. & Joseph, D.D. 1972 Bounds for heat transport in a porous layer. *J. Fluid Mech.* **54**, 521–543. 16

Calzavarini, E., Lohse, D., Toschi, F. & Tripiccione, R. 2005 Rayleigh and Prandtl number scaling in the bulk of Rayleigh-Bénard turbulence. *Phy. Fluids* **17**, 0055107. 16

Castaing, B., Gunaratne, G., Heslot, F., Kadanoff, L., Libchaber, A., Thonae, S., Wu, X.-Z., Zaleski.S. & Zanetti, G. 1989 Scaling of hard thermal turbulence in Rayleigh-Bénard convection. *J. Fluid Mech.* **204**, 1–30. 16

Chavanne, X., Chillà, F., Castaing, B., Hébral, B., Chabaud, B. & Chaussy, J. 1997 Observation of the ultimate regime in Rayleigh-Bénard convection. *Phys. Rev. Lett.* **79**, 3648–3651. 16

Cheng, P. 1978 Heat transfer in geothermal systems. *Adv. Heat Transfer* **14**, 1–105. 2, 112

Cherkaouim, A.S.M. & Wilcock, W.S.D. 1999 Characteristics of high Rayleigh number two-dimensional convection in an open-top porous layer heated from below. *J. Fluid Mech.* **394**, 241–260. 2

Corson, L.T. 2011 Maximising the heat flux in steady unicellular porous media convection. In *Proceedings of the 2011 Geophysical Fluid Dynamics summer program, Woods Hole Oceanographic Institution*, pp. 389–412. 38, 65

Cross, M.C. & Hohenberg, P.C. 1993 Pattern formation outside of equilibrium. *Rev. Mod. Phys.* **65**, 851–1112. 1

Doering, C.R. & Constantin, P. 1996 Variational bounds on energy dissipation in incompressible flows: III. Convection. *Phys. Rev. E* **53**, 5957–5981. 16

Doering, C.R. & Constantin, P. 1998 Bounds for heat transport in a porous layer. *J. Fluid Mech.* **376**, 263–296. 16

Douglas, J. 1962 Alternating direction methods for three space variables. *Numerische Mathematik* **4**, 41–63. 201

Drazin, P.G. 2002 *Introduction to Hydrodynamic Stability*. CUP. 59

Duffy, C.J. & Al-Hassan, S. 1988 Groundwater circulation in a closed desert basin: Topographic scaling and climatic forcing. *Water Resour. Res.* **24**, 1675–1688. 112

E, W. & Lui, J.G. 1997 Finite difference methods for 3d viscous incompressible flows in the vorticity-vector potential formulation on nonstaggered grids. *J. Comp. Phys.* **138**, 57–82. 159

Elder, J.W. 1967 Steady free convection in a porous medium heated from below. *J. Fluid Mech.* **27**, 29–48. 156

Ennis-King, J.P. & Paterson, L. 2005 Role of convective mixing in the long-term storage of carbon dioxide in deep saline formations. *SPE J.* **10** (3), 349–356. 184

Ennis-King, J.P., Preston, I. & Paterson, L. 2005 Onset of convection in anisotropic porous media subject to a rapid change in boundary conditions. *Phys. Fluids* **17**, 84107–84115. 76

Fernandez, J., Kurowski, P., Petitjeans, P. & Meiburg, E. 2002 Density-driven unstable flows of miscible fluids in a Hele-Shaw cell. *J. Fluid Mech.* **451**, 239–260. 109

Fowler, A.C. 1985 The formation of freckles in binary alloys. *IMA J. Appl. Math.* **35**, 159–174. 2

Friedlingstein, P., Houghton, R.A., Marland, G., Hackler, J., Boden, T.A., Conway, T.J., Canadell, J.G., Raupach, M. R., Ciais, P. & Le Quere, C. 2010 Update on $CO_2$ emission. *Nature Geosci.* **3**, 811–812. 3

Fu, X., Cueto-Felgueroso, L. & Juanes, R. 2013 Pattern formation and coarsening dynamics in three-dimensional convective mixing in porous media. *Phil. Trans. R. Soc. A* (in press). 38, 67, 156, 173

Gilfillan, S.M.V., Sherwood Lollar, B., Holland, G., Blagburn, D., Stevens, S., Schoell, M., Cassidy, M., Ding, Z., Zhou, Z.,

Lacrampe-Couloume, G. & Ballentine, C.J. 2009 Solubility trapping in formation water as dominant $CO_2$ sinks in natural gas fields. *Nature* **458**, 614–618. 4, 188

Golding, M.J., Neufeld, J.A., Hesse, M.A. & Huppert, H.E. 2011 Two-phase gravity currents in a porous medium. *J. Fluid Mech.* **678**, 248–270. 4, 187

Goldstein, B., Hiriart, G., Bertani, R., Bromley, C., Gutiérrez-Negrín, L., Huenges, E., Muraoka, H., Ragnarsson, A., Tester, J. & Zui, V. 2011 *IPCC Special Report on Renewable Energy Sources and Climate Change Mitigation*, chap. 4: Geothermal Energy. CUP. 112

Graham, M.D. & Steen, P.H. 1994 Plume formation and resonant bifurcations in porous-media convection. *J. Fluid Mech.* **272**, 67–89. 2, 11, 16, 20, 65, 195

Hassanzadeh, H., Pooladi-Darvish, M. & Keith, D.W. 2006 Stability of a fluid in a horizontal saturated porous layer: effect of non-linear concentration profile, initial and boundary conditions. *Transp. Porous Media* **65**, 193–211. 109

Hassanzadeh, H., Pooladi-Darvish, M. & Keith, D.W. 2007 Scaling behaviour of convective mixing, with application to geological storage of $CO_2$. *AIChE Journal* **53**, 1121–1131. 109

He, X., Funfchilling, D., Nobach, H., Bodenschatz, E. & Ahlers, G. 2012 Transition to the ultimate state of turbulent rayleigh-benard convection. *Phys. Rev. Lett.* **108**, 024502. 16

Hesse, M.A., Orr F.M. & Tchelepi, H.A. 2008 Gravity currents with residual trapping. *J. Fluid Mech.* **611**, 35–60. 4, 187

Hewitt, D.R., Neufeld, J.A. & Lister, J.R. 2012 Ultimate regime of high Rayleigh number convection in a porous medium. *Phys. Rev. Lett.* **108**, 224503. 15

Hewitt, D.R., Neufeld, J.A. & Lister, J.R. 2013*a* Convective shutdown in a porous medium at high Rayleigh number. *J. Fluid Mech.* **719**, 551–586. 107, 133

Hewitt, D.R., Neufeld, J.A. & Lister, J.R. 2013*b* Stability of columnar convection in a porous medium. *J. Fluid Mech.* (in press). 37

Hidalgo, J.J., Fe, J., Cueto-Felgueroso, L. & Juanes, R. 2012 Scaling of convective mixing in porous media. *Phys. Rev. Lett.* **109**, 264503. 38

Hill, J.M. 1987 *One-dimensional Stefan problems: an introduction*. Longman. 112

Holst, P.H. & Aziz, K. 1972 Transient three-dimensional natural convection in confined porous media. *Int. J. Heat Mass Transfer* **15**, 73–90. 156, 201

Holyer, J.Y. 1981 On the collective instability of salt fingers. *J. Fluid Mech.* **110**, 195–207. 39

Holyer, J.Y. 1984 The stability of long, steady, two-dimensional salt fingers. *J. Fluid Mech.* **147**, 169–185. 39

Howard, L.N. 1964 Convection at High Rayleigh number. In *Applied Mechanics, Proc. 11th Intl Cong. Appl. Math.* (ed. H Görtler), pp. 1109–1115. 16

Huppert, H.E. 1989 Phase changes following the initiation of a hot turbulent flow over a cold solid surface. *J. Fluid Mech.* **198**, 293–319. 112

Huppert, H.E. & Sparks, R.S.J. 1988*a* The generation of granitic magmas by intrusion of basalt into continental crust. *J. Petro.* **29** (3), 599–624. 112

Huppert, H.E. & Sparks, R.S.J. 1988*b* Melting the roof of a chamber containing a hot, turbulently convecting fluid. *J. Fluid Mech.* **188**, 107–131. 112

Huppert, H.E. & Turner, J.S. 1981 Double-diffusive convection. *J. Fluid Mech.* **106**, 299–329. 39

Jordan, D.W. & Smith, P. 1999 *Nonlinear Ordinary Differential Equations*, 3rd edn. Great Clarendon Street, Oxford, OX2 6DP: OUP. 43

Joseph, D.D., Nield, D.A. & Papanicolaou, G. 1982 Nonlinear equation governing flow in a saturated porous medium. *Water Resour. Res.* **18**, 1049–1052. 6

Kadanoff, L.P. 2001 Turbulent heat flow: Structures and scaling. *Physics Today* **54**, 34–39. 1

Kimura, S., Schubert, G. & Straus, J.M. 1989 Time-dependent convection in a fluid-saturated porous cube heated from below. *J. Fluid Mech.* **207**, 153–189. 156, 162

Kimura, S., Schubert, G. & Strauss, J.M. 1986 Route to chaos in porous-medium thermal convection. *J. Fluid Mech.* **166**, 305–324. 11, 16

Kongsjorden, H., Kdrstad, O. & Torp, T.A. 1997 Saline aquifer storage of carbon dioxide in the Sleipner project. *Waste Management* **17**, 303–308. 3

Kraichnan, R.H. 1962 Turbulent thermal convection at arbitrary Prandtl number. *Phys. Fluids* **5**, 1374–1389. 16

Lapwood, E.R. 1948 Convection of a fluid in a porous medium. *Math. Proc. Cam. Phil. Soc.* **44**, 508–521. 10, 15

Lister, C.R.B. 1990 An explanation for the multivalued heat transport found experimentally for convection in a porous medium. *J. Fluid Mech.* **214**, 287–320. 156

Lohse, D. & Toschi, F. 2003 Ultimate state of thermal convection. *Phys. Rev. Lett.* **90**, 034502. 16

Lyle, S., Huppert, H. E., Hallworth, M.A., Bickle, M. & Chadwick, A. 2005 Axisymmeteric gravity currents in a porous medium. *J. Fluid Mech.* **543**, 293–302. 186

McKibben, R. & O'Sullivan, M.J. 1980 Onset of convection in a layered porous medium heated from below. *J. Fluid Mech.* **96**, 375–393. 76

McKibben, R. & O'Sullivan, M.J. 1981 Heat transfer in a layered porous medium heated from above. *J. Fluid Mech.* **111**, 141–173. 76

McKibben, R. & Tyvand, P.A. 1983 Thermal convection in a porous medium composed of alternating thick and thin layers. *Int. J. Heat Mass Transfer* **26**, 761–780. 76

Metz, B., Davidson, O., de Coninck, H.C., Loos, M. & Meyer, L. 2005 *IPCC Special Report on Carbon Dioxide Capture and Storage*. CUP. 2, 3, 4

Monkhouse, F.J. 1970 *Principles of Physical Geography*. University of London Press. 75

Morris, K.A. & Shepperd, C.M. 1982 The role of clay minerals in influencing porosity and permeability characteristics in the Bridport sands of Wytch Farm, Dorset. *Clay Minerals* **17**, 41–54. 75

Neufeld, J.A., Hesse, M.A., Riaz, A., Hallworth, M.A., Tchelepi, H.A. & Huppert, H.E. 2010 Convective dissolution of carbon dioxide in saline aquifers. *Geophys. Res. Lett.* **37**, 22404. 16, 38, 109, 110, 113, 147, 152

Neufeld, J.A. & Huppert, H.E. 2009 Modelling carbon dioxide sequestration in layered strata. *J. Fluid Mech.* **625**, 353–370. 186

Neufeld, J.A., Vella, D., Huppert, H.E. & Lister, J.R. 2011 Leakage from gravity currents in a porous medium. Part I. A localized sink. *J. Fluid Mech.* **666**, 391–413. 4, 186

Nield, D.A. & Bejan, A. 2006 *Convection in Porous media*, 3rd edn. Springer. 1, 10, 15, 44, 76, 195

Notz, D. & Worster, M.G. 2009 Desalination processes of sea ice revisited. *J. Geophys. Res.* **114**, C05006. 2

Orr Jr., F.M 2009 Onshore geologic storage of $CO_2$. *Science* **325**, 1656 – 1658. 2, 3, 4

Otero, J., Dontcheva, L.A., Johnston, H., Worthing, R.A., Kurganov, A., Petrova, G. & Doering, C.R. 2004 High-Rayleigh-number convection in a fluid-saturated porous layer. *J. Fluid Mech.* **500**, 263–281. 11, 16, 20, 23, 31, 65, 81, 195

Pau, G.S.H., Bell, J.B., Pruess, K., Almgren, A.S., Lijewski, M.J. & Zhang, K. 2010 High-resolution simulation and characterization of density-driven flow in $CO_2$ storage in saline aquifers. *Adv. Water Resour.* **33**, 443–455. 38, 67, 109, 156

Phillips, O.M. 2009 *Geological Fluids Dynamics*. CUP. 5, 75

Plasting, S.C. & Kerswell, R.R. 2003 Improved upper bound on the energy dissipation rate in plane Couette flow: The full solution to Busse's problem and the Constantin-Doering-Hopf problem with one-dimensional background field. *J. Fluid Mech.* **477**, 363–379. 16

Press, W.H., Flannery, B.P., Teukolsky, S.A. & Vetterling, W.T. 1989 *Numerical Recipes (Fortran)*, 1st edn. CUP. 118, 193, 201

Pritchard, D. 2007 Gravity currents over fractured substrates in a porous medium. *J. Fluid Mech.* **584**, 415–431. 4, 186

Pritchard, D. 2013 Sinking inside the box. *J. Fluid Mech.* **722**, 1–4. 107

Pritchard, D., Woods, A. & Hogg, A.J. 2001 On the slow drainage of a gravity current moving through a layered porous medium. *J. Fluid Mech.* **459**, 207–216. 186

Radko, T. & Smith, D.P. 2012 Equilibrium transport in double-diffusive convection. *J. Fluid Mech.* **692**, 5–27. 39

Riaz, A., Hesse, M.A., Tchelepi, H.A. & Orr Jr., F.M 2006 Onset of convection in a gravitationally unstable diffusive layer in porous media. *J. Fluid Mech.* **548**, 87–111. 109, 119

Robinson, J.L. & O'Sullivan, M.J. 1976 A boundary-layer model of flow in a porous medium at high Rayleigh number. *J. Fluid Mech.* **75** (3), 459–467. 11

Schmitt, R.W. 2012 Finger puzzles. *J. Fluid Mech.* **692**, 1–4. 39

Schubert, G. & Straus, J.M. 1979 Three-dimensional and multicellular steady and unsteady convection in fluid-saturated porous media at high rayleigh numbers. *J. Fluid Mech.* **94**, 25–38. 156, 162, 201

Siggia, E.D. 1994 High Rayleigh number convection. *Ann. Rev. Fluid Mech.* **26**, 137–168. 10, 16

Simmons, C.T., Fenstemaker, T.R. & Sharp, J, M Jr. 2001 Variable-density groundwater flow and solute transport in heterogeneous porous media: approaches, resolutions and future challenges. *J. Contaminant Hydrology* **52**, 245–275. 76

Slim, A.C. 2013 Solutal convection regimes in a two-dimensional porous medium. *J. Fluid Mech.* (under review). 109

Slim, A.C., Bandi, M.M., Miller, J.C. & Mahadevan, L. 2013 Dissolution-driven convection in a Hele-Shaw cell. *Phys. Fluids* **25**, 024101. 38, 109, 119

Slim, A.C. & Ramakrishnan, T.S. 2010 Onset and cessation of time-dependent, dissolution-driven convection in porous media. *Phys. Fluids* **22**, 124103. 109

Stein, C, A. 1995 *Global Earth physics: a handbook of physical constants*, chap. Heat flow of the Earth. AGU. 2

Stern, M.E. 1969 Collective instability of salt fingers. *J. Fluid Mech.* **35**, 209–218. 39

Sternlof, K.R., Karimi-Fard, M., Pollard, D.D. & Durlofsky, L.J. 2006 Flow and transport effects of compaction bands in sandstones at scales relevant to aquifer and reservoir management. *Water Resour. Res.* **42**, W07425. 76

Straus, J.M. & Schubert, G. 1979 Three-dimensional convection in a cubic box of fluid-saturated porous material. *J. Fluid Mech.* **91**, 155–165. 156

Straus, J.M. & Schubert, G. 1981 Modes of finite-amplitude three-dimensional convection in rectangular boxes of fluid-saturated porous material. *J. Fluid Mech.* **103**, 23–32. 156

Sun, T. & Teja, A.S. 2004 Density, viscosity and thermal conductivity of aqueous solutions of propylene glycol, diporpylene glycol, and triplropylene glycol between 290K and 460K. *J. Chem. Eng. Data* **49**, 1311–1317. 149

Taylor, G.I. 1953 Dipersion of soluble matter in solvent flowing slowly through a tube. *Proc. R. Soc. Lond. A* **219**, 186–203. 149

van der Meer, B. 2005 Carbon dioxide storage in natural gas reservoirs. *Oil Gas Sci. Technol.* **60**, 527–536. 4, 113

Vella, D. & Huppert, H.E. 2006 Gravity currents in a porous medium on an inclined plane. *J. Fluid Mech.* **555**, 353–362. 186

Vella, D., Neufeld, J.A., Huppert, H.E. & Lister, J.R. 2011 Leakage from gravity currents in a porous medium. Part II. A line sink. *J. Fluid Mech.* **666**, 414–427. 4

Wang, M-H., Soriano, A.N., Caparanga, A.R. & Li, M-H. 2010 Binary mutual diffusion coefficient of aqueous solutions of propylene glycol and dipropylene glycol. *J. Taiwan Inst. Chem. Eng.* **41**, 279–285. 147

Wen, B., Chini, G.P., Dianati, N. & Doering, C.R. 2013 Computational approaches to aspect-ratio-dependent upper bounds and heat flux in porous medium convection. *Phys. Lett. A* (in press). 38

Wen, B., Dianati, N., Lunasin, E., Chini, G.P. & Doering, C.R. 2012 New upper bounds and reduced dynamical modeling for Rayleigh-Bénard convection in a fluid-saturated porous layer. *Commun. Nonlinear Sci. Numerical Sim.* **17**, 2191–2199. 16, 38

Wooding, R.A. 1957 Steady state free thermal convection of liquid in a saturated permeable medium. *J. Fluid Mech.* **2**, 273–285. 6

Wooding, R.A., Tyler, S.W. & White, I. 1997*a* Convection in groundwater below an evaporating salt lake: 1. Onset of instability. *Water Resour. Res.* **33**, 1199 – 1217. 2, 112

Wooding, R.A., Tyler, S.W., White, I. & Anderson, P.A. 1997*b* Convection in groundwater below an evaporating salt lake: 2. Evolution of fingers or plumes. *Water Resour. Res.* **33**, 1219–1228. 2, 112

Xu, X., Chen, S. & Zhang, Z. 2006 Convective stability analysis of the long-term storage of carbon dioxide in deep saline aquifers. *Adv. Water Resour.* **29**, 397–497. 109